

THE UNIVERSITY OF HULL

**INVESTIGATION OF A NOVEL SOLAR  
PHOTOVOLTAIC/LOOP-HEAT-PIPE  
HEAT PUMP SYSTEM**

being a Thesis submitted for the Degree of Doctor of Philosophy

at the University of Hull

by

**Xingxing Zhang**

*MSc University of Nottingham, UK*

*MEng Donghua University, China*

*BEng Donghua University, China*

February 2014



**CONTENTS INDEX**

<b>CONTENTS INDEX .....</b>	<b>I</b>
<b>ABBREVIATIONS.....</b>	<b>V</b>
<b>ABSTRACT .....</b>	<b>VI</b>
<b>PUBLICATIONS .....</b>	<b>VII</b>
<b>ACKNOWLEDGEMENTS .....</b>	<b>X</b>
<b>LIST OF FIGURES .....</b>	<b>XI</b>
<b>LIST OF TABLES.....</b>	<b>XVI</b>
<b>NOMENCLATURE .....</b>	<b>XVIII</b>
<b>CHAPTER 1: INTRODUCTION .....</b>	<b>1</b>
1.1 RESEARCH BACKGROUND .....	1
1.2 RESEARCH OBJECTIVES.....	5
1.3 GENERAL DESCRIPTION OF THE RESEARCH CONCEPT .....	5
1.4 RESEARCH METHODOLOGY .....	6
1.5 RESEARCH NOVELTY .....	9
1.6 THESIS STRUCTURE.....	10
<b>CHAPTER 2: LITERATURE REVIEW .....</b>	<b>13</b>
2.1 CHAPTER INTRODUCTION.....	13
2.2 BASIC CONCEPT AND THEORY, CLASSIFICATION AND PERFORMANCE EVALUATION STANDARDS OF PV/T TECHNOLOGY .....	13
2.2.1 <i>Basic Concept and Theory behind PV/T Operation .....</i>	<i>13</i>
2.2.2 <i>Classification of PV/T Technology.....</i>	<i>19</i>
2.2.3 <i>Performance Evaluation Standards.....</i>	<i>26</i>
2.3 R&D PROGRESS AND PRACTICAL APPLICATIONS OF PV/T TECHNOLOGIES.....	32
2.3.1 <i>Overview of R&amp;D works in the PV/T Field .....</i>	<i>32</i>
2.3.2 <i>Practical Applications of PV/T Technology .....</i>	<i>41</i>
2.3.3 <i>Analysis of the Reviewed Works .....</i>	<i>46</i>
2.3.4 <i>Summary of the Current PV/T Research and its Potential Challenges .....</i>	<i>54</i>
2.4 POTENTIAL OPPORTUNITIES IN THE DEVELOPMENT OF PV/T TECHNOLOGY .....	55
2.4.1 <i>Reducing Thermal Resistance between PV Modules and Thermal Absorbers .....</i>	<i>55</i>
2.4.2 <i>Developing a Heat-pipe-based Thermal Absorber.....</i>	<i>56</i>
2.4.3 <i>Developing a Full Range of Computer Simulation Models.....</i>	<i>58</i>
2.4.4 <i>Evaluating System Performance in Real Climatic Conditions .....</i>	<i>58</i>
2.4.5 <i>Demonstrating System Operation in Practical Buildings.....</i>	<i>58</i>

2.5 DEVELOPMENT OF THE PV/T TECHNOLOGY IN THE PhD PROJECT.....	59
2.6 CHAPTER SUMMARY .....	59
<b>CHAPTER 3: CONCEPTUAL DESIGN OF THE PV/LHP HEAT PUMP</b>	
<b>WATER HEATING SYSTEM .....</b>	<b>62</b>
3.1 CHAPTER INTRODUCTION .....	62
3.2 SYSTEM DESCRIPTION AND WORKING PRINCIPLE .....	62
3.3 PARAMETERS OF THE NEW PV/LHP HEAT PUMP SYSTEM .....	67
3.4 PARAMETRIC DESIGN OF SYSTEM COMPONENTS .....	68
3.4.1 Glazing Cover.....	68
3.4.2 Al-alloy-based PV Layer .....	69
3.4.3 LHP with Fin Sheet.....	70
3.4.4 Flat-plate Heat Exchanger .....	72
3.4.5 Heat Pump.....	73
3.4.6 Electrical Control and Storage Unit.....	74
3.4.7 Insulation Material.....	74
3.5 CHAPTER SUMMARY .....	74
<b>CHAPTER 4: THEORETICAL ANALYSIS AND DEVELOPMENT OF</b>	
<b>THE COMPUTER SIMULATION MODELS.....</b>	<b>76</b>
4.1 CHAPTER INTRODUCTION .....	76
4.2 ANALYTICAL MODEL FOR THE LHP HEAT TRANSFER LIMIT .....	77
4.2.1 Modelling Objective for the LHP Heat Transfer Limit.....	77
4.2.2 Thermal Fluid Theory and the Associated Mathematical Equations of the LHP Heat Transfer Model .....	77
4.2.3 Method and Algorithm for the LHP Heat Transfer Model Development and Operation.....	92
4.2.4 Statistical Analysis.....	95
4.2.5 Validation of LHP Heat Transfer Model by the Published Results .....	95
4.2.6 Model Operation and Result Discussion of LHP Heat Transfer Limit.....	98
4.3 STEADY-STATE MODEL FOR THE CHARACTERISATION OF SYSTEM PERFORMANCE .....	107
4.3.1 Modelling Objective for the System Steady-state Performance.....	107
4.3.2 Thermal Fluid Theory and the Associated Mathematical Equations of the System Steady-state Model .....	107
4.3.3 Method and Algorithm for the Steady-state Model Development and Operation.	122
4.3.4 Validation of the System Stead-state Model by the Published Data .....	124
4.3.5 Model Operation and Result Discussion of the System Steady-state Performance .....	127
4.4 DYNAMIC MODEL FOR THE EVALUATION OF SYSTEM PERFORMANCE .....	127
4.4.1 Modelling Objective for the System Dynamic Performance .....	127
4.4.2 Thermal Fluid Theory and the Associated Mathematical Equations of the System Dynamic Model .....	128

4.4.3 Method and Algorithm for the Dynamic Model Development and Operation.....	140
4.4.4 Validation of the System Dynamic Model by the Published Data .....	143
4.4.5 Model Operation and Results Discussion of the System Dynamic Performance..	143
4.5 CHAPTER SUMMARY .....	144
<b>CHAPTER 5: PROTOTYPE FABRICATION, LABORATORY SCALE</b>	
<b>MEASUREMENT AND STEADY-STATE MODEL VALIDATION....</b>	<b>146</b>
5.1 CHAPTER INTRODUCTION .....	146
5.2 FABRICATION OF THE PROTOTYPE SYSTEM.....	146
5.2.1 Aluminium-alloy-based PV Layer .....	147
5.2.2 Loop Heat Pipe.....	148
5.2.3 Integration of the PV/LHP Module.....	149
5.2.4 System Assembly and Connection.....	150
5.3 EXPERIMENTAL SET-UP UNDER LABORATORY CONDITIONS .....	152
5.3.1 Experimental Instrumentation .....	152
5.3.2 Experimental Procedure.....	153
5.4 RESULTS AND DISCUSSION.....	155
5.4.1 Characterisation of the PV Layer with Different Baseboards using the	
Experimental Results .....	155
5.4.2 Characterisation of the Prototype PV/LHP Heat Pump System and the Steady-state	
Model Validation.....	162
5.5 CHAPTER SUMMARY .....	170
<b>CHAPTER 6: PROTOTYPE PERFORMANCE EVALUATION IN</b>	
<b>REAL CLIMATIC OPERATIONAL CONDITIONS AND DYNAMIC</b>	
<b>MODEL VALIDATION .....</b>	<b>173</b>
6.1 CHAPTER INTRODUCTION .....	173
6.2 EXPERIMENT SET-UP IN REAL CLIMATIC CONDITIONS .....	173
6.2.1 Real-time Experiment – Daily Based.....	173
6.2.2 Real-time Experiment – Hourly Based .....	174
6.3 RESULTS AND DISCUSSION.....	175
6.3.1 Real-time Measurement – Daily Based .....	175
6.3.2 Comparison between the Prototype System and Conventional Solar Energy Systems	
.....	176
6.3.3 Real-time Measurement – Hourly Based and the Dynamic Model Validation .....	178
6.4 CHAPTER SUMMARY .....	187
<b>CHAPTER 7: ENERGY SAVING, ECONOMIC, ENVIRONMENTAL</b>	
<b>AND REGIONAL ACCEPTANCE ANALYSIS .....</b>	<b>190</b>
7.1 CHAPTER INTRODUCTION .....	190
7.2 ANNUAL OPERATIONAL PERFORMANCE.....	190
7.2.1 Weather Profiles and Operational Conditions .....	191

7.2.2 Hourly Predictions of the Prototype System Performance in Shanghai Weather Conditions .....	193
7.2.3 Monthly Predictions for the Prototype System Performance in Three Climatic Weather Conditions .....	198
7.3 LIFE-CYCLE ECONOMIC ANALYSIS .....	204
7.3.1 Capital Cost .....	204
7.3.2 Annual Operational Cost and Saving .....	206
7.3.3 Annual Maintenance Cost .....	208
7.3.4 Cost Payback Period and Life-cycle Net Cost Saving .....	208
7.4 LIFE-CYCLE ENVIRONMENTAL BENEFITS .....	210
7.5 CHAPTER SUMMARY .....	211
<b>CHAPTER 8: CONCLUSION AND FURTHER WORK.....</b>	<b>214</b>
8.1 CONCLUSIONS .....	214
8.2 FURTHER OPPORTUNITIES AND CHALLENGES .....	219
8.2.1 Pilot Demonstration Project.....	219
8.2.2 PV/LHP Stakeholders .....	221
8.2.3 Technical Development .....	222
8.2.4 Evaluation Standards .....	223
8.2.5 Long-term Reliability Measurement .....	223
8.2.6 Market Analysis .....	223
8.2.7 Manufacturing Cost .....	224
8.2.8 Dissemination Activities .....	224
8.2.9 Policy Support .....	224
<b>APPENDIX: REFERENCES .....</b>	<b>225</b>

**ABBREVIATIONS**

<i>ASHP</i>	<i>Air-source heat pump</i>
<i>Al</i>	<i>Aluminium</i>
<i>BDF</i>	<i>Backward differentiation formula</i>
<i>BIPV</i>	<i>Building integrated photovoltaic</i>
<i>CNY</i>	<i>Chinese Yuan</i>
<i>COP</i>	<i>Coefficient of performance</i>
<i>CPT</i>	<i>Cost payback time</i>
<i>EPBT</i>	<i>Energy payback time</i>
<i>EVA</i>	<i>Ethylene-vinyl acetate</i>
<i>FEM</i>	<i>Finite element method</i>
<i>GBP</i>	<i>Great Britain Pound</i>
<i>GHG</i>	<i>Greenhouse gases</i>
<i>GPBT</i>	<i>Greenhouse gas payback time</i>
<i>GSHP</i>	<i>Ground-source heat pump</i>
<i>HVAC</i>	<i>Heating, ventilation and air conditioning</i>
<i>IM</i>	<i>Iterative method</i>
<i>IPVTS</i>	<i>Integrated photovoltaic/thermal system</i>
<i>LCA</i>	<i>Life-cycle assessment</i>
<i>LHP</i>	<i>Loop heat pipe</i>
<i>ODE</i>	<i>Ordinary differential equation</i>
<i>OHP</i>	<i>Oscillating heat pipe</i>
<i>PDE</i>	<i>Partial differential equation</i>
<i>PV</i>	<i>Photovoltaic</i>
<i>PV/e</i>	<i>Photovoltaic/evaporator</i>
<i>PV/FPHP</i>	<i>Photovoltaic/flat-plate heat pipe</i>
<i>PV/LHP</i>	<i>Photovoltaic/loop heat pipe</i>
<i>PV-SAHP</i>	<i>Photovoltaic solar-assisted heat pump</i>
<i>PV/T</i>	<i>Photovoltaic/thermal</i>
<i>RHI</i>	<i>Renewable heat incentive</i>
<i>TPT</i>	<i>Tedlar-Polyester-Tedlar</i>

## ABSTRACT

With the widespread deployment of solar photovoltaic (PV) and thermal devices imminent, this research aims to resolve some engineering barriers to the existing solar photovoltaic/thermal (PV/T) technologies by incorporating an innovative loop heat pipe (LHP) and a typical heat pump. In addition, a coated aluminium-alloy (Al-alloy) sheet replaces the conventional baseboard for the PV cells to improve heat exportation. As a result, this research has developed a novel solar PV/LHP heat pump system to maximise the electrical output of a PV module and generate an additional amount of heat simultaneously.

The overall investigation followed the basic methodology of combined theoretical and experimental analysis, including procedures for a critical literature review, optimal concept design, mathematical derivation, the development of simulation models, prototype fabrication, laboratory-controlled and field testing, simulation model validation and socio-economic analysis. A full range of specialised simulation models was developed to predict the system performance with reasonable accuracy. The proposed LHP device has a maximum heat transfer limit of about 900W. The Al-alloy baseboard improved PV efficiency by nearly 0.26% when compared with a traditional PV baseboard. During the real-time measurement conditions, the mean electrical, thermal and overall energetic/exergetic efficiencies of the PV/LHP module were 9.13%, 39.25% and 48.37%/15.02%, respectively. The basic thermal and advanced system coefficients of performance ( $COP_{th}/COP_{PV/T}$ ) were almost 5.51 and 8.71, respectively. The test results indicated that this system performed better than conventional solar/air energy systems. The feasibility analysis illustrated that this system could generate a substantial amount of energy in subtropical climatic regions, such as Hong Kong. It is cost effective to operate this system in areas with high energy charging tariffs, such as London and Hong Kong.

The research results are expected to configure feasible solutions for future PV/T technologies and develop a new solar-driven heating system. The core technologies may enable a significant reduction in or even elimination of the carbon footprint in the built environment.



## PUBLICATIONS

### Book Chapter

1. Xudong Zhao, **Xingxing Zhang**, Solar Photovoltaic/Thermal Technologies and their Application in Building Retrofitting (Chapter 22), Nearly Zero Energy Building Refurbishment, DOI: 10.1007/978-1-4471-5523-2\_22, *Springer-Verlag London* 2013; 615-658.

### Journal Publications

1. **Xingxing Zhang**, Xudong Zhao, Jingchun Shen, Xi Hu, Xuezhi Liu, Jihuan Xu, Design, Fabrication and Experimental Study of a Solar Photovoltaic/Loop-heat-pipe-based Heat Pump System, *Solar Energy* 2013; 97: 551–568.
2. **Xingxing Zhang**, Jingchun Shen, Xudong Zhao, Jihuan Xu, Xiaotong Yu, Dynamic Performance of a Solar Photovoltaic/Loop-heat-pipe Heat Pump Water Heating System, *Applied Energy* 2014; 114: 335–352.
3. **Xingxing Zhang**, Xudong Zhao, Jihuan Xu, Xiaotong Yu, Characterisation of a Solar Photovoltaic/Loop-heat-pipe Heat Pump Water Heating System, *Applied Energy* 2013; 102: 1229-1245.
4. **Xingxing Zhang**, Xudong Zhao, Jihuan Xu, Xiaotong Yu, Study of the Heat Transport Capacity of a Novel Gravitational Loop Heat Pipe, *International Journal of Low Carbon Technologies* 2013; 8 (3): 210-223.
5. **Xingxing Zhang**, Xudong Zhao, Jihuan Xu, Xiaotong Yu, Review of R&D Progress and Practical Application of the Solar Photovoltaic/Thermal (PV/T) Technologies, *Renewable & Sustainable Energy Reviews* 2012; 16 (01) : 599-617.
6. Xudong Zhao, **Xingxing Zhang**, Saffa Riffat, Yaxin Su, Theoretical Investigation of a Novel PV/e Roof Module for Heat Pump Operation, *Energy Conversion and Management* 2011; 52 (01): 603–614.

7. **Xingxing Zhang**, Yaxin Su, Xudong Zhao, Investigation of a Cogeneration of Cooling/heating-electricity Supply Heat Pump System based on a PV/e Roof Module, *Building Energy & Environment* 2010; 29 (02): 58-61.

### Conference proceedings

8. **Xingxing Zhang**, Xudong Zhao, Jingchun Shen, Case Study of a Pilot-scale Solar Photovoltaic/Thermal (PV/T) System and its Opportunities for Future Deployment, Proceedings of the *International Initiative for a Sustainable Built Environment (iiSBE) 2013*, Guimaraes, Portugal, 30<sup>th</sup> October-1<sup>st</sup> November 2013.
9. **Xingxing Zhang**, Xudong Zhao, Jingchun Shen, Social-economic Benefits of a Novel Photovoltaic/loop-heat-pipe Water Heating System and its Adaptability in Future Building Energy Envelopes, Proceedings of the *International Scientific Conference and Workshops of Building Innovation (INBUD)*, Technical University of Cracow, Poland, 15<sup>th</sup>-18<sup>th</sup> October 2013.
10. **Xingxing Zhang**, Xudong Zhao, Jingchun Shen, Feasibility Study of a Solar Photovoltaic/Loop-Heat-Pipe Heat Pump Water Heating System, Proceedings of the *12<sup>th</sup> International Conference on Sustainable Energy Technologies*, Hong Kong, 26<sup>th</sup>-29<sup>th</sup> August 2013.
11. **Xingxing Zhang**, Xudong Zhao, Jihuan Xu, Xiaotong Yu, Investigation of a Novel Solar Driven Water Heating System with Enhanced Energy Yield for Buildings, Proceedings of the *International Conference for Enhanced Building Operations (ICEBO) 2012*, Manchester, UK, 23<sup>rd</sup>-26<sup>th</sup> October 2012.
12. **Xingxing Zhang**, Xudong Zhao, Characterisation of a Hybrid Photovoltaic/Heat-pump Water Heating System, Proceedings of the *5<sup>th</sup> International Forum on Energy Saving and Environmental Protection Technologies for Air-Conditioning and Refrigeration*, Beijing, China, 13<sup>th</sup>-14<sup>th</sup> June 2012.

## Patents

1. Jihuan Xu, **Xingxing Zhang**, A Novel Water Heating System by Low-temperature Solar Capillary Heat Pipe Assisted with Heat Pump, China patent, CN202119134U, 18/01/2012.
2. **Xingxing Zhang**, Xudong Zhao, Jihuan Xu, Xiaotong Yu, A Novel Gravitational Loop Heat Pipe Used for a Micro Solar Photovoltaic/thermal Cogeneration System, China patent, CN202660776U, 09/01/2013.

## Presentations/posters/showcases

1. Jingchun Shen, **Xingxing Zhang**, Xudong Zhao, Smart City, *Science Showcase 2013 of the University of Hull*, Hull City Hall, UK, 14<sup>th</sup> May 2013.
2. **Xingxing Zhang**, Xudong Zhao, Jihuan Xu, Extract Energy from the Sun – The New Hybrid Solar Solution, *Poster for Postgraduate Research Posters at the University of Hull*, UK, 6<sup>th</sup> February 2013.
3. **Xingxing Zhang** and Jihuan Xu, Application of Renewable Technology in Conjunction with the Solar Thermal at the Hongqiao Business District in Shanghai, *Presentation for the Science and Technology Commission of Shanghai Municipality*, Shanghai, China, 27<sup>th</sup> December 2012.
4. **Xingxing Zhang**, Xudong Zhao, Jihuan Xu, Improving Solar Conversion Efficiency, *Poster for the 2012 UKERC Summer School Poster Competition at the University of Warwick*, Coventry, UK, 17<sup>th</sup>-22<sup>nd</sup> June 2012.
5. **Xingxing Zhang**, Xudong Zhao, Jihuan Xu, Improving the Solar Conversion Ratio, *Poster for the 3<sup>rd</sup> PhD Conference at De Montfort University*, Leicester, UK, 25<sup>th</sup> April 2012.

## ACKNOWLEDGEMENTS

I would like to express my sincere and heartfelt gratitude to my supervisor, Professor Xudong Zhao, for his continuing support and guidance, as well as his patience, motivation, enthusiasm, immense knowledge and enthusiastic involvement throughout the whole process of my PhD research. From the initial to the final stage, his encouragement, advice and assistance have always been with me, and have helped me to complete this PhD subject smoothly. I would also like to thank my external supervisor, Professor Jihuan Xu, for her support and suggestions.

I wish to thank the University of Hull, the Shanghai Pacific Energy Centre (China) and the European Commission Marie Curie Action - International Research Staff Exchange Scheme for their financial support of this project.

I am especially indebted to a supportive technician, Mr Jianding Li, at the Shanghai Pacific Energy Centre for his assistance during the construction and testing of my research prototypes. I would also like to thank Ms Liz Eggleston for proofreading my thesis.

Finally, I wish to thank and dedicate this thesis to my wife and parents for their unselfish, endless love, care and encouragement. I could never have accomplished so much without them.

## LIST OF FIGURES

Fig. 1-1: Energy consumption in residential and commercial buildings .....	2
Fig. 1-2: Contribution of solar thermal energy to EU heat demand by sector....	3
Fig. 1-3: Evolution of PV electricity generation by end-use sector .....	4
Fig. 1-4: Schematic of the PV/LHP heat pump micro-generation system .....	6
Fig. 1-5: Schematic of the research methodology .....	7
Fig. 2-1: Established efficiency-to-temperature relationship .....	14
Fig. 2-2: Network of different solar conversion technologies .....	14
Fig. 2-3: A focused cross section of a typical PV/T module .....	15
Fig. 2-4: Schematic of an absorber plate with dimensions.....	17
Fig. 2-5: Cross sections of air-based PV/T modules .....	20
Fig. 2-6: Cross sections of water-based PV/T modules.....	20
Fig. 2-7: Cross-section of a PV evaporator roof panel .....	21
Fig. 2-8: Schematic of (a) PV/e roof module-based heat pump system and (b) its thermodynamic process in a Pressure-Enthalpy diagram .....	22
Fig. 2-9: Schematic of a conventional heat pipe.....	22
Fig. 2-10: Three types of flat-plate heat pipe with micro-channel array .....	23
Fig. 2-11: PV/flat-plate heat pipe: a) air cooling; b) water cooling.....	23
Fig. 2-12: Schematic of the OHP-BIPV/T module.....	24
Fig. 2-13: A Carnot cycle acting as a heat engine on a Temperature-Entropy diagram .....	27
Fig. 2-14: TWINSOLAR application and its performance curve.....	41
Fig. 2-15: Solar air PV/T products from Conserval Engineering.....	42
Fig. 2-16: PV/T liquid collector – the PVTWIN produced by PVTWINS .....	43
Fig. 2-17: MULTI SOLAR PV/T System produced by Millennium Electric ..	43
Fig. 2-18: X10 PV/T system produced by Absolicon.....	44
Fig. 2-19: Power-Spar produced by Menova Energy .....	44
Fig. 2-20: Harmony HD211 produced by HelioDynamics.....	45
Fig. 2-21: Ventilated PV with heat recovery produced by Secco Sistemi.....	45
Fig. 2-22: Correlation between module efficiencies and external/operational conditions represented by $(T_{fi}-T_a)/I$ .....	47

Fig. 2-23: Correlation between daily testing of efficiency and external/operational conditions represented by $(T_i-T_a)/H_t$ .....	48
Fig. 2-24: Correlation between module efficiencies and external/operational conditions represented by $(T_{mean}-T_a)/I$ .....	49
Fig. 2-25: Variation of full-day testing efficiency versus operating time.....	51
Fig. 2-26: Schematic of a typical LHP and its evaporator .....	57
Fig. 2-27: Schematic of the PV/T module and the systems network .....	57
Fig. 3-1: Schematics of (a) the heat pump-assisted PV/LHP solar water heating system and (b) concept design of the LHP three-way vapour-liquid separation structure.....	64
Fig. 3-2: Concept design of (a) the PV/LHP collector and (b) configuration of the PV layer.....	65
Fig. 3-3: Heat pump thermodynamic cycle in a Temperature-Entropy chart ..	67
Fig. 3-4: Dimensional drawings of (a) the LHP liquid-vapour separation structure and (b) the PV/LHP module.....	72
Fig. 3-5: Schematic of the solar electrical control and storage system .....	74
Fig. 4-1: Schematic of the thermal and hydrodynamic couplings in the LHP ..	78
Fig. 4-2: Wick and pore parameters in the evaporator and condenser .....	83
Fig. 4-3: Frictional coefficients in the rectangular pipes .....	90
Fig. 4-4: Flow chart for calculating the LHP heat transfer limits .....	94
Fig. 4-5: Referenced rig for the LHP thermal measurement [4.7] .....	96
Fig. 4-6: Comparison between the LHP simulation results and the published test data.....	97
Fig. 4-7: Impact of operational temperature on the heat transfer performance of the LHP .....	99
Fig. 4-8: Impact of evaporator diameter on the heat transfer performance of the LHP .....	101
Fig. 4-9: Impact of evaporator length on the heat transfer performance of the LHP .....	102
Fig. 4-10: Impact of evaporator inclination angle on the heat transfer performance of the LHP .....	103
Fig. 4-11: Impact of vapour column diameter on the heat transfer performance of the LHP .....	104

Fig. 4-12: Impact of liquid filling mass on the heat transfer performance of the LHP ..... 105

Fig. 4-13: Impact of evaporator-to-condenser height difference on the heat transfer performance of the LHP ..... 106

Fig. 4-14: Schematic of steady-state solar energy conversion and transfer processes ..... 108

Fig. 4-15: Thermal network of heat loss for a typical double-cover module . 109

Fig. 4-16: Temperature drops and equivalent thermal resistances along the heat transfer path ..... 114

Fig. 4-17: Heat flow pattern at the elemental length ‘ $dx$ ’ on the fin sheet ..... 115

Fig. 4-18: Flow chart for the calculation of steady-state system performance ..... 123

Fig. 4-19: Schematic of the referenced PV-SAHP/HP test rig [4.13] ..... 125

Fig. 4-20: Comparison of steady-state simulation results with the published testing data ..... 126

Fig. 4-21: Schematic of the transient energy balances in the system ..... 128

Fig. 4-22: Grid meshing for the fin sheet along the width..... 132

Fig. 4-23: Technical assessment set-up for the PV/LHP module and its associated system..... 137

Fig. 4-24: Flow chart for the calculation of the dynamic system performance ..... 142

Fig. 4-25: Comparison of the dynamic simulation results with the published testing data ..... 144

Fig. 5-1: Fabrication process of the Al-alloy-based PV layer ..... 147

Fig. 5-2: Fabrication/connection process of the LHP vapour-liquid separation structure ..... 148

Fig. 5-3: Fabrication process of the PV/LHP module ..... 149

Fig. 5-4: Flow chart indicating the fabrication process of the PV/LHP module ..... 150

Fig. 5-5: Experiment rig of the PV/LHP heat pump solar water heating system ..... 153

Fig. 5-6: Laboratory testing rigs of the aluminium-alloy- and TPT-based PV layer ..... 154

Fig. 5-7: Laboratory-based testing rig for the characterisation of the whole system.....	155
Fig. 5-8: Impact of operating time on PV layer with different baseboards.....	156
Fig. 5-9: Impact of solar radiation on PV layer with different baseboards.....	157
Fig. 5-10: Impact of air temperature on PV layer with different baseboards..	159
Fig. 5-11: Impact of air velocity on PV layer with different baseboards.....	160
Fig. 5-12: Impact of mounting solution on PV layer with different baseboards .....	161
Fig. 5-13: Impact of solar radiation on the PV/LHP heat pump system .....	163
Fig. 5-14: Impact of air temperature on the PV/LHP heat pump system.....	164
Fig. 5-15: Impact of air velocity on the PV/LHP heat pump system .....	165
Fig. 5-16: Impact of heat pump evaporation temperature on the PV/LHP heat pump system.....	167
Fig. 5-17: Impact of top glazing covers on the PV/LHP heat pump system...	168
Fig. 5-18: Impact of LHP number on the PV/LHP heat pump system .....	169
Fig. 6-1: On-site outdoor experimental rig.....	174
Fig. 6-2: Real-time variation in solar radiation and air temperature .....	174
Fig. 6-3: Graphic plot of the experimental results for module thermal efficiency .....	176
Fig. 6-4: Comparisons between the PV/LHP heat pump system and (a) independent solar systems and (b) conventional heat pump water heating systems .....	177
Fig. 6-5: Real-time temperature distribution of the system components .....	179
Fig. 6-6: (a) real-time mean temperature of the fin, (b) real-time fin temperature versus fin width, and (c) 3D fin temperature versus both fin width and operating time.....	181
Fig. 6-7: Real-time solar power output and module electrical efficiency .....	182
Fig. 6-8: Real-time solar heat gain and module thermal efficiency .....	183
Fig. 6-9: Real-time module overall energetic and exergetic efficiencies.....	184
Fig. 6-10: Real-time water heat gain and system performance coefficients ...	186
Fig. 7-1: Hourly weather profile of the monthly averages for Shanghai, China .....	191
Fig. 7-2: Monthly averages for solar radiation in three climate regions .....	191
Fig. 7-3: Monthly averages for air temperature in three climate regions.....	192



Fig. 7-4: Monthly diurnal average variation of temperature at the PV layer .	193
Fig. 7-5: Monthly diurnal average variation of module electrical efficiency .	194
Fig. 7-6: Monthly diurnal average variations in module electrical output .....	194
Fig. 7-7: Monthly diurnal average variations in module thermal efficiency ..	195
Fig. 7-8: Monthly diurnal average variations in module thermal output and heat pump condensation capacity .....	196
Fig. 7-9: Monthly diurnal average variations in module exergetic efficiency	197
Fig. 7-10: Monthly diurnal average variations in the heat pump $COP_{th}$ and $COP_{PV/T}$ .....	198
Fig. 7-11: Temperatures of the PV layer in three climate regions.....	199
Fig. 7-12: Energetic efficiencies of the PV/LHP module in three climate regions.....	200
Fig. 7-13: Overall assessment of the prototype system in three climate regions .....	201
Fig. 7-14: Overall energy output of the PV/LHP module in three climate regions.....	202
Fig. 7-15: Condensation capacity of the heat pump in three climate regions.	202
Fig. 7-16: Cost breakdown of the PV/LHP heat pump prototype system .....	205
Fig. 7-17: Annual operating costs of different water heating systems .....	208
Fig. 8-1: Dimensional drawings of the PV/LHP module for the demonstration project .....	219
Fig. 8-2: On-site image of the demonstration project in Shanghai, China .....	220

## LIST OF TABLES

Table 2-1: The characteristics comparison of different PV/T types .....	25
Table 2-2: Cost breakdown and cost payback time of different PV/T systems [2.47] .....	31
Table 2-3: EPBT and CO <sub>2</sub> PBT values for different PV/T systems [2.47] .....	31
Table 2-4: Energy outputs of different SolarVenti models .....	42
Table 3-1: Summary of different parameters for further characterisation .....	68
Table 3-2: Alternative parameters for the glazing covers .....	69
Table 3-3: Design Parameters of the Al-alloy-based PV panel .....	69
Table 3-4: Alternative wick structures in the LHP evaporator .....	70
Table 3-5: Design parameters of the LHP operation.....	71
Table 3-6: Thermodynamic properties of water with operating temperatures..	71
Table 3-7: Design parameters of the flat-plate heat exchanger.....	73
Table 3-8: Sample thermodynamic properties of the R134a refrigerant in the heat pump .....	73
Table 3-9: Thermal resistance of typical insulating materials .....	74
Table 4-1: Design and operation parameters of the referenced LHP [4.7] .....	96
Table 4-2: Impact of wick structure on the heat transfer performance of the LHP .....	100
Table 4-3: Design and operation parameters of the referenced PV-SAHP/HP system [4.13] .....	125
Table 5-1: Photovoltaic characteristics under standard testing conditions .....	148
Table 5-2: Model/capacity of the primary system components .....	151
Table 5-3: List of the experimental testing and monitoring devices.....	152
Table 5-4: List of laboratory experimental testing modes .....	154
Table 6-1: Test results over a consecutive period in real climate conditions .	175
Table 6-2: Average system performances and error analysis results .....	187
Table 7-1: Monthly averages for wind speed in three climate regions (m/s)..	192
Table 7-2: Monthly averages for ground water temperature in three climate regions (°C) .....	193

Table 7-3: Summary of water temperature in the tank under monthly diurnal averages .....	196
Table 7-4: Monthly final tank water temperature in three climate regions ....	203
Table 7-5: Total annual output of the prototype system in three climate regions .....	204
Table 7-6: Capital cost breakdown of the prototype PV/LHP heat pump system .....	204
Table 7-7: Renewables tariffs for the installation of a solar thermal system .	206
Table 7-8: Annual operating costs of different water heating systems .....	207
Table 7-9: Cost payback period and life-cycle net cost saving .....	210
Table 7-10: Environmental benefits of the prototype system.....	211
Table 8-1: Initial test results for the demonstration project.....	221
Table 8-2: Opportunities and challenges for PV/LHP stakeholders.....	222

## NOMENCLATURE

$A$	area ( $m^2$ )	$\varphi$	inclination angle
$c_p$	specific heat at a constant pressure (J/kg-K)	$\Omega$	embodied greenhouse gas
$C$	constant; cost	<b>Subscripts</b>	
$CR$	carbon reduction	$a$	air
$CS$	cost saving	$abs$	absorption
$D$	diameter (m)	$aG$	axial hydrostatic pressure
$Ex$	exergy rate (W)	$b$	baseboard; bubbles
$f$	solar fraction; frictional factor	$bos$	balance of system
$f_{co_2}$	gas/electricity-to-CO <sub>2</sub> ratio	$BL$	boiling limit
$F$	frictional coefficient	$c$	cover; collecting; compressor
$F'$	efficiency factor	$c,max$	maximum capillary
$F_f$	standard fin efficiency	$c,r$	cross area of refrigerant
$F_R$	heat removal factor	$c,t$	condensation energy
$F_{th}$	thermal efficiency factor	$c_1$	internal cover sheet
$g$	gravity acceleration ( $m/s^2$ )	$c_2$	external cover sheet
$h$	heat transfer coefficient (W/m-K)	$CL$	capillary limit
$h_c$	convective heat transfer coefficient (W/m-K)	$e$	electricity; evaporator
$h_{fg}$	latent heat of vaporisation (J/kg)	$ei$	electrical insulation
$h_m$	hour angle (rad)	$el$	electrical
$h_R$	radiative heat transfer coefficient (W/m-K)	$en$	net electricity
$H$	thermal enthalpies (kJ/kg)	$exp$	experiment
$H_h$	height of heat exchanger plate (m)	$EL$	entrainment limit
$I$	solar radiation intensity ( $W/m^2$ )	$f$	fin sheet; groove fin
$k$	thermal conductivity ( $W/m^2-K$ )	$fc$	centre of fin sheet
$K$	extinction coefficient of glass cover	$fe$	edge of fin sheet
$K_p$	wick permeability ( $m^2$ )	$fl$	filled liquid
$L$	length (m)	$fs$	insulation around fin sheet
$L_m$	local latitude	$FL$	liquid filling mass limit

$m$	mass flow rate (kg/s); molecular	$g$	groove
$M$	mass (kg); Mach number	$g,pv$	glass of PV limitation
$n$	mesh number; iteration number	$G$	gravity
$n_g$	ratio of refraction index	$hp$	heat pipe
$N$	number	$hp,in$	heat pipe inner wall
$Nu$	Nusselt number	$hp,o$	heat pipe outer wall
$P$	pressure (Pa)	$hp,w$	heat pipe wall
$P_o$	measured output power (W)	$hx$	heat exchanger
$Pr$	Prandtl number	$hx,hp$	heat exchanger to heat pipe
$PP$	payback period (year)	$hx,in$	heat exchanger inner
$q$	energy rate per unit area ( $W/m^2$ )	$hx,o$	heat exchanger outer
$Q$	energy rate (W)	$hx,r$	refrigerant within heat exchanger
$r$	thermal resistance per area ( $m^2$ -K/W)	$i$	differential length node; inlet; inner layer
$r_{h,s}$	hydraulic radius of wick pore (m)	$k$	differential time node
$r_e$	effective capillary radius (m)	$l$	liquid
$R$	thermal resistance (K/W)	$lf$	liquid film
$Ra$	Rayleigh number	$L$	loss
$Re$	Reynolds number	$m$	mean; module
$R_o$	universal gas constant (kJ/kmol-K)	$mtl$	replacing materials
$R_v$	vapour constant (kJ/kg-K)	$o$	overall; outer layer
$t$	time (s)	$out$	outlet
$T$	temperature (K)	$p$	PV; pressure
$T_{su}$	solar temperature at 6000 K	$PV/T$	PV/thermal
$U$	heat loss coefficient ( $W/m^2$ -K)	$r$	refrigerant
$V$	velocity (m/s)	$rc$	reference temperature
$W$	width (m)	$r,e$	refrigerant evaporator
$x$	width parameter; parameter to the liquid filling mass	$r,l$	liquid refrigerant
$x_r$	refrigerant saturation rate	$r,m$	mean refrigerant
<b>Greek</b>		$rG$	radial hydrostatic pressure
$\alpha$	absorption ratio; width-to-length ratio	$s$	solid

$\beta_p$	PV packing factor	$s, g$	solid groove
$\beta_{PV}$	efficiency temperature coefficient	$sim$	simulation
$\gamma$	vapour specific heat ratio	$s, ms$	solid mesh screen
$r_{//}$	parallel components of unpolarised radiation for smooth surfaces	$s, sp$	solid sintered powder
$r_{\perp}$	perpendicular components of unpolarised radiation for smooth surfaces	$SL$	sonic limit
$\delta$	thickness (m)	$th$	thermal
$\delta_m$	declination angle (rad)	$u$	useful
$\varepsilon$	emissivity; porosity; resistance	$v$	vapour
$E$	energy output	$v, e$	vapour core in evaporator
$\zeta$	exergetic efficiency	$vt$	vapour in three-way fitting
$Z$	reduction of greenhouse gas	$vtl$	vapour transportation line
$\eta$	energetic efficiency	$vtl, in$	inner vapour line
$\theta$	collector slope (rad)	$vtl, o$	outer vapour line
$\theta_e$	contact angle of evaporator (rad)	$VL$	viscous limit
$\theta_1$	incidence angle (rad)	$w$	water
$\theta_2$	refraction angle of direct solar beam (rad)	$wi$	wick
$\mu$	dynamic viscosity (kg/m-s)	$wi, g$	groove wick
$\nu$	kinematic viscosity (m <sup>2</sup> /s)	$wi, ms$	mesh screen wick
$\rho$	density (kg/m <sup>3</sup> )	$wi, sp$	sintered powder wick
$\sigma$	Stefan–Boltzmann constant; surface tension coefficient (N/m)	$wm$	working medium
$\Sigma$	embodied energy	$ws$	insulation of water tank
$\tau$	transmittance	$ws, in$	inner tank insulation
$\tau_{c, a}$	transmittance for absorption	$ws, o$	outer tank insulation

## CHAPTER 1: INTRODUCTION

### 1.1 Research Background

In the context of the recent call from the Copenhagen Summit in 2009, the urgency of global climate change has become fully realised across the world. Extensive fossil fuel consumption by human activities has led to serious atmospheric and environmental problems. Consequently, global warming, greenhouse gas (GHG) emission, climate change, ozone layer depletion and acid rain terminologies have started to appear frequently in the literature. To abate the impacts of the above disasters, many governments in the world have addressed ambitious goals by using new technologies to reduce their energy footprint and CO<sub>2</sub> emissions. As reported by the Copenhagen conference, by 2020, the European Union (EU) further aims to reduce the GHG emitted by 20% to 30% below 1990 levels and China is attempting to reduce CO<sub>2</sub> emission intensity by 40% to 45% below 2005 levels [1.1].

In the EU, the building sector accounts for nearly 30% of industrial employment, contributing about 10.4% of the gross domestic product [1.2]. Hence, the building sector is fully aware of its huge responsibility in being the highest energy consumer in the EU (about 40% [1.3]) and the main contributor to GHG emissions (nearly 36% of the EU's total CO<sub>2</sub> emissions [1.4]). Nowadays, the primary energy demand in built environment mainly comes from electricity and heat, which are usually for hot water, space heating/cooling, ventilation, lighting, etc (**Fig. 1-1**) [1.5]. Thus, reducing the electricity/heat energy demand in buildings and improving their energy efficiencies have become a priority and a challenge, as seen throughout EU research and low-carbon economic plans.

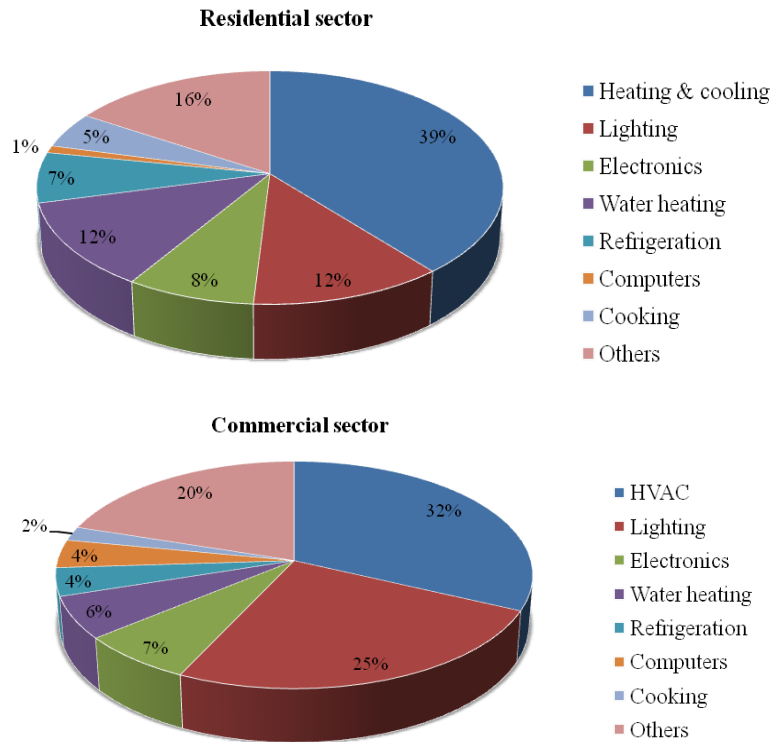


**Fig. 1-1: Energy consumption in residential and commercial buildings**

In 2009, the European Energy Efficient Buildings Association issued its scope and vision document [1.6], stating that ‘by 2050, most buildings and districts could become energy neutral, and have a zero CO<sub>2</sub> emission. A significant number of buildings would become energy positive, thus becoming real power plants, integrating renewable energy sources, clean distributed generation technologies and smart grids at district level’. A high fraction of locally available renewable energy sources in the energy mix will be necessary, in addition to a significantly reduced energy demand by buildings. Among the renewable resources, solar energy comes at the top of the list due to its abundance and its more even distribution in nature than any other renewable energy type, such as wind, geothermal, hydraulic, wave and tidal energies [1.7].

Indeed, solar energy is currently playing a crucial role in the energy supply field for buildings using different conversion methods. Applications of solar energy in terms of solar thermal collectors and PV devices have been emerging on the market for years and still have space for growth, which would be driven by continuous technical advances and increased concerns regarding energy saving and environmental protection.



Solar thermal systems are one of the most cost-effective renewable energy technologies and have an enormous market potential globally. They represent more than 90% of the world-installed solar capacity that has been applied for various purposes, including domestic hot water generation and space heating, solar-assisted cooling, and industrial process heating. The global solar thermal market has been continuously growing since the beginning of the 1990s and, in EU, the solar thermal market tripled from 2002 to 2006 and is still booming. A vision plan issued by the European Solar Thermal Technology Platform indicates that solar thermal energy has the potential to cover 50% of the total heat demand by 2050 (**Fig. 1-2**) [1.8]. The European Solar Thermal Industry Federation (ESTIF) has also predicted that by 2020 the EU will reach a total operational solar thermal capacity of between 91 and 320 gigawatts (GW), thus leading to savings equivalent to at least 5,600 tons of crude oil. By 2050, the EU will eventually achieve 1,200 GW of solar thermal capacity [1.9].

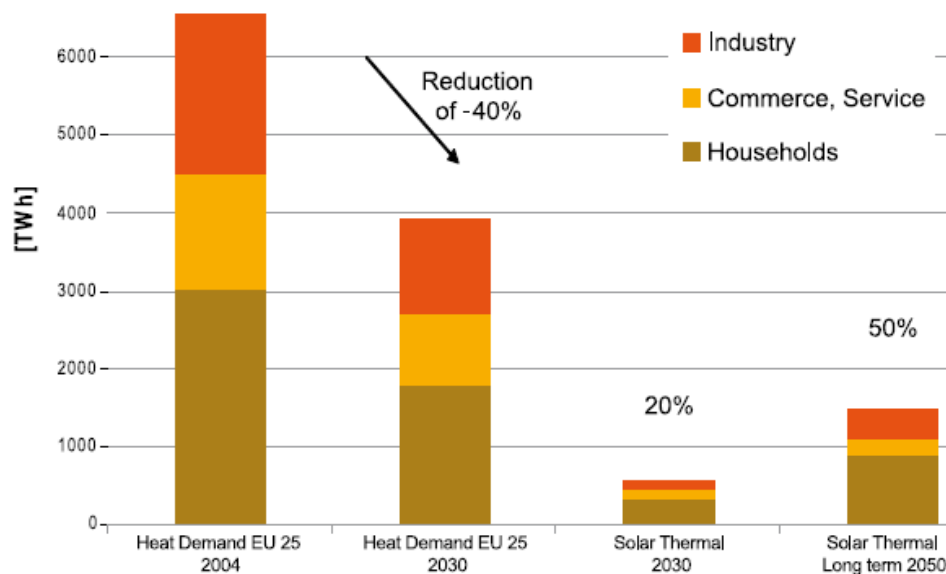


**Fig. 1-2: Contribution of solar thermal energy to EU heat demand by sector**

PV technology is now becoming commercially available and can generate and meet part of electricity demand by solar energy. Although the current capacity of PV installations is still small and provides only 0.1% of the world's total electricity generation, a market review indicates that global PV installations are growing at a 40% average annual rate [1.10]. With continuous technical development, increased installation volume, reduced price and encouraging

legal policies, PV technology will certainly maintain its fast-growing pace and eventually become a significant energy supplier across the world. It was predicted by the International Energy Agency (IEA) in its recent Technology Roadmap - Solar Photovoltaic Energy that PV systems will deliver about 5% of global power needs by 2030 and 11% by 2050, as illustrated in **Fig. 1-3** [1.10]. The accelerated use of PV technology will result in more than 100 giga-tonnes (Gt) of CO<sub>2</sub> emission reduction between 2008 and 2050 [1.10].

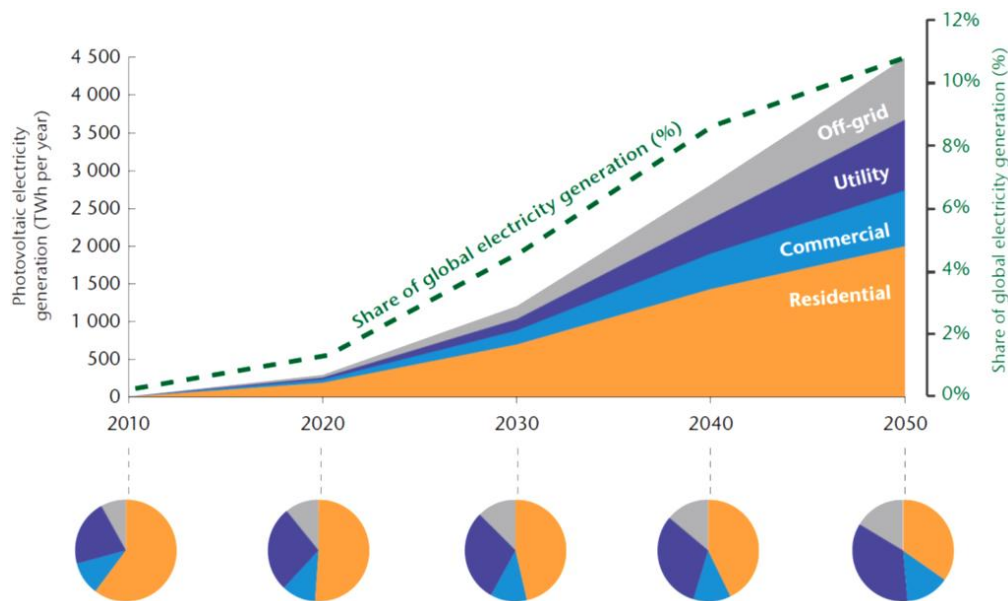


**Fig. 1-3: Evolution of PV electricity generation by end-use sector**

PV/thermal (PV/T) technology allows the dual functions of solar collection in one module with outputs of both electricity and heat. Such synergetic integration of PV and thermal collection not only results in improved PV efficiency [1.11], but also generates more energy per unit area than a stand-alone PV panel or solar collector. Additional characteristics of PV/T technology lie in the potential saving in material use, reduction in installation cost and homogeneous facade appearance [1.11]. It is now becoming a significant solution to yielding more electricity and offsetting heating load freely in contemporary building environments. The market potential of PV/T technology would, therefore, be significantly higher than individual PV and solar thermal systems. This strategic concept will boost the solar energy application, which is absolutely in line with the long-term energy roadmap.

## 1.2 Research Objectives

Although PV/T research has yielded a rich harvest, it still faces some critical challenges, such as low efficiency, insufficient energy supply, leakage risk, and uneven fluid distribution. To overcome these critical barriers, this research had the aim of developing a novel PV/T technology (plus a full package of design/simulation models) incorporating several technical initiatives. To achieve this goal, the research set out six interlinked objectives, as below:

- (1) To carry out an extensive literature study of PV/T technologies, identify the existing technical challenges and suggest potential solutions.
- (2) To design a conceptual PV/T system incorporating the potential initiatives concluded from the literature review.
- (3) To develop a full range of computer simulation models to optimise the configurations of the proposed system and predict its operational performance, including an analytical model for the LHP heat-transfer limitations and steady-state/dynamic performance simulation models for the integrated PV/LHP heat pump system.
- (4) To construct and test a prototype system in laboratory-controlled conditions and validate the steady-state simulation model using the experimental data.
- (5) To evaluate performance of the prototype system in real climatic conditions and validate the dynamic simulation model using the experimental data.
- (6) To establish a socio-economic model to carry out energy saving, economic, environmental and regional acceptance analysis of the integrated PV/LHP heat pump system.

## 1.3 General Description of the Research Concept

The overall concept, as shown in **Fig. 1-4**, is to use an LHP device to cool the PV cells, thus enabling improvement in PV efficiency and, meanwhile, make

feasible use of the absorbed heat through a heat pump for one or more of the following purposes: space heating, hot water supply, desiccant and evaporative cooling, and natural ventilation in buildings. Electricity generation from the PV cells, either exported to the national grid or stored in batteries, will meet the building electrical load and drive the heat pump compressor. The LHP device can passively transfer a large amount of heat for a long distance using its capillary power, thus eliminating the need for a circulation pump. The combination of these concepts is expected to create a low (zero) carbon heating, ventilation and air conditioning (HVAC) and hot water supply system driven by solar energy.

However, in this research, the proposed system would only be designed for basic hot water generation due to the limited project budget, while the other functions could be explored during future investigation.

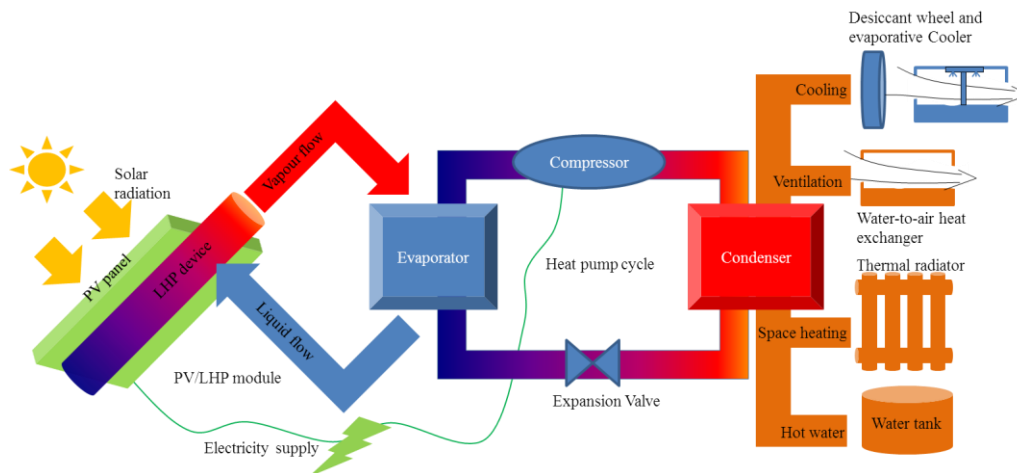
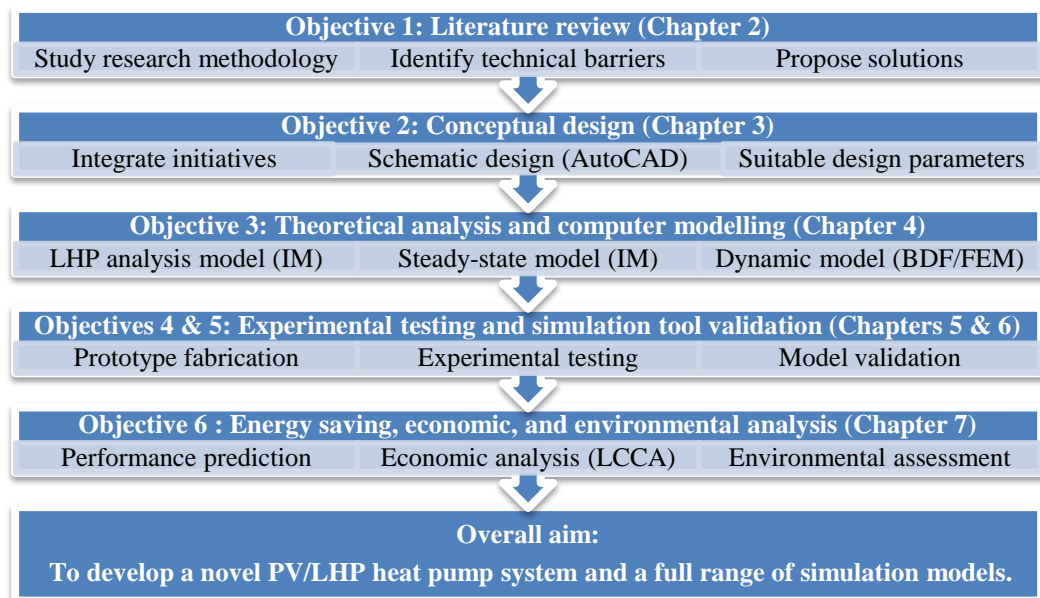


Fig. 1-4: Schematic of the PV/LHP heat pump micro-generation system

## 1.4 Research Methodology

The proposed project involved typical applied research aiming to develop a new PV/LHP heat pump system. It followed the basic procedure of concept formation and its validation/optimisation. The approaches to processing the scientific and technological works were as follows: **(I)** identification of the

nature of PV/T technology to bring forward questions and potential solutions (for objective 1); **(II)** concept design (for objective 2); **(III)** theoretical analysis and computer modelling (for objective 3); **(IV)** experimental testing and simulation model validation (for objectives 4 and 5); and **(V)** energy saving, economic, environmental and regional acceptance analysis (for objective 6). It was obvious that approaches 1 and 2 involved concept formation, while approaches 3, 4 and 5 were linked together to prove or revise the established concept through the integrated efforts of theoretical, experimental and socio-economic analysis (as shown in **Fig. 1-5**). These approaches, correlated to the relevant objectives, are given briefly below.



**Fig. 1-5: Schematic of the research methodology**

❑ **Approach to objective 1 – Investigating the nature of PV/T technology to identify potential questions and corresponding solutions**

This approach would **(1)** identify the basic PV/T operational mechanism and research methodology; **(2)** involve a series of quantitative and qualitative reviews into the research and development (R&D) works and the practical application of existing PV/T technologies; **(3)** identify crucial features, research highlights and technical barriers regarding existing PV/T technologies; and **(4)** propose potential solutions for resolving the technical challenges. This

approach would enable recognition of current PV/T research status and build the foundation for the rest of the objectives.

□ **Approach to objective 2 – Concept design of the proposed technology**

This approach would (1) complete the sketch drawings of the system components and the integrated PV/LHP heat pump system; (2) describe the basic working principle of the proposed concept; and (3) deliver alternative components in terms of material type and geometric size. This approach would generate the system concept and build the foundation for objectives 3, 4 and 5.

□ **Approach to objective 3 – Theoretical analysis and computer simulation models**

This approach would (1) carry out the fundamental mathematical analysis of the energy balances and transfer processes occurring in different system components; (2) develop and operate an analytical computer simulation model on the basis of the iterative method (IM) to investigate the heat transfer limit of the LHP, which would enable (a) the LHP operational performance against different variables to be established, (b) recommendation of the appropriate LHP design and operational parameters, and (c) determination of the optimum geometric sizes and capacities of other system components; (3) develop and operate a steady-state computer simulation model on the basis of the IM to characterise the system performance, which would enable (a) determination of the system performance against different variables, (b) clarification of the optimum system configuration, and (c) recommendation of the appropriate system design and operational parameters; and (4) develop and operate a dynamic computer simulation model by combining the backward differentiation formula (BDF) and finite element method (FEM) to evaluate the system performance, which would enable (a) prediction of the system performance in real climate conditions, (b) prediction of the seasonal system performance, and (c) recommendation of the appropriate climate region for system operation. This approach would enable the refined system design addressed in objective 2 and data validation as well as the socio-economic analysis to be undertaken in regard to the following objectives.

❑ **Approach to objectives 4 and 5 – Experimental testing and computer model validation**

This approach would (1) propose the fabrication methods for the PV/LHP heat pump prototype system in practice and construct it according to the simulation recommendations; (2) characterise the performance of the prototype system under laboratory conditions and verify the steady-state simulation model; and (3) evaluate its operational performance in real climate conditions and verify the dynamic simulation model. This approach would enable verification of the simulation models derived from objective 3 and development of an experimental prototype with a feasible fabrication method in practice.

❑ **Approach to objective 6 – Energy saving, economic, environmental and regional acceptance analysis**

This approach would develop and run the dynamic simulation model to predict the annual operational performance of the prototype system and discuss its socio-economic impacts using the method of life-cycle assessment (LCA). The adaptability of this technology to a number of typical climatic regions would be analysed. This approach would enable evaluation of the potential benefits and impact raised by the proposed technology, including its payback period, life-cycle cost saving, and carbon emission reduction.

### 1.5 Research Novelty

In brief, the research has the following identifiable novel aspects:

- ❑ **Concept:** (1) the LHP device works as a solar thermal absorber; (2) the coated Al-alloy sheet serves as the PV baseboard; and (3) the heat pump controls the PV cells in a low-temperature operation mode.
- ❑ **System structure:** (1) the top-positioned three-way structure is designed for vapour-liquid separation flow in the LHP; (2) configuration of the PV/LHP module is simplified with only one or two LHPs; and (3) the LHP

can passively transport heat for a long distance owing to capillary power that removes the need for a circulation pump in the system.

- ❑ **Methodology:** a full range of computer simulation models has been developed, including an analytical model for LHP heat transfer, steady-state and dynamic models, and a socio-economic model for predicting the integrated system performance.
- ❑ **Simulation method:** the combination of the backward differentiation formula (BDF, also known as Gear's method) and the finite element method (FEM) was adopted to solve the ordinary differential equations (ODE) and parabolic partial differential equation (PDE), respectively, in the transient code by means of MATLAB's ODE and PDE solvers ("*ode15s*" and "*pdepe*") for the efficient output of numerical results.
- ❑ **Fabrication:** a fabrication procedure and technique for the new LHP with a three-way liquid-vapour separation structure have been developed.

## 1.6 Thesis Structure

**Chapter 1 – Introduction:** this briefly describes the research background, significance, objectives, research concept, methodology and novelty.

**Chapter 2 – Literature review:** this involves an extensive review of the existing PV/T technologies, including basic theory, research methodology, evaluation standards, R&D processes and practical applications. The current research status and technical barriers regarding PV/T technologies are examined. As a result, potential opportunities for future development are identified.

**Chapter 3 – Conceptual design:** this describes the basic working principle of the proposed system and creates a schematic design for key components. Alternative structures, materials, geometric and operating conditions of the system are recommended for the further input of theoretical simulation.

**Chapter 4 – Theoretical analysis and computer modelling:** this develops a group of dedicated computer simulation models for the LHP device and the



whole system (both steady state and dynamic) by analysing the fundamental equations of the energy balances, solar transmittance, heat transfer, fluid flow and photovoltaic generation. Through running the simulation model, appropriate LHP design/operational parameters are recommended, and the optimum geometry/capacity of the relevant system components is determined. These results are subsequently applied to the prototype construction and experiment testing.

**Chapter 5 – Prototype system fabrication, laboratory measurement and validation of the steady-state performance model:** this describes the detailed process and method for the fabrication of the prototype system. A series of laboratory-based experiments are set up to evaluate the AL-alloy-based PV layer and validate the steady-state modelling. The results are applied to identify the different factors impacting upon the system performance, which is intended to form the basis for further system optimisation.

**Chapter 6 – Evaluation of the prototype system in real climatic conditions, and validation of the dynamic performance model:** this evaluates the prototype system in outdoor weather conditions throughout a consecutive period of about one week. The test results verify the dynamic simulation model at a reasonable level of accuracy. As a result, a validated dynamic simulation model is ready to predict seasonal system performance.

**Chapter 7 – Energy saving, economic, environmental and regional acceptance analysis:** this discusses the system's annual performance, energy payback periods, and carbon emission reduction for the prototype system in three climate areas. It addresses the potential feasibility of such a system in different regions in comparison with traditional water heaters by assessing both economic and environmental benefits.

**Chapter 8 – Conclusion and further works:** this concludes the main observations from this research. A pilot-scale demonstration of this system is described with the initial test results. Opportunities and challenges are discussed for further development of the technology.

All the above chapters are systematically connected, as indicated in **Fig. 1-5**, to enable achievement of the overall project aim. The new PV/T technology should enable a higher overall solar-energy conversion ratio than either an independent PV panel or a solar thermal collector. This will allow PV/T technology to become a widely applicable system for building heat and power supply. This innovation will have the potential to reduce fossil fuel consumption and CO<sub>2</sub> emission significantly.

## CHAPTER 2: LITERATURE REVIEW

### 2.1 Chapter Introduction

This chapter will carry out a critical review of R&D progress and the practical application of solar PV/T technologies. The major aims are briefly given as follows:

- (1) Present the concept of PV/T technology and the theory behind it.
- (2) Describe the evaluation standards relating to the technical, economic and environmental performance of PV/T systems.
- (3) Illustrate a comprehensive literature review into the R&D works and practical applications of PV/T devices.
- (4) Analyse the review in the categories of PV/T type and research methodology.
- (5) Identify the major features, current R&D status, research highlights and existing technical barriers of various PV/T technologies.
- (6) Discuss the opportunities for further development of PV/T technology.

This part of the work provided the foundation for the entire investigation and helped to: (i) identify the technical barriers existing in current PV/T technology; (ii) establish the scientific methods for PV/T research; (iii) develop new research topics; and (iv) set up the research direction for subsequent chapters.

### 2.2 Basic Concept and Theory, Classification and Performance Evaluation Standards of PV/T Technology

#### 2.2.1 Basic Concept and Theory behind PV/T Operation

PV cells are well known as solar electricity-generating semiconductors and solar efficiency is a critical parameter for justifying their performance, which is largely dependent upon the cells' materials and temperature. Overall, PV electrical efficiency is in the range of 6% to 18%, which is a value measured at

the nominal operating cell temperature (NOCT) ( $0.8 \text{ kW/m}^2$  of solar radiation,  $20 \text{ }^\circ\text{C}$  of ambient temperature, and  $1 \text{ m/s}$  of air velocity) [2.1]. It is well known that the electrical efficiency of a PV cell falls with a rise in its operating temperature, as shown in **Fig. 2-1**. Increasing the temperature of a PV cell by  $1\text{K}$  leads to  $0.4\%$  to  $0.5\%$  reduction in the electrical efficiency for crystalline silicon cell [2.2, 2.3] and  $0.25\%$  for amorphous silicon (a-Si) cell [2.4].

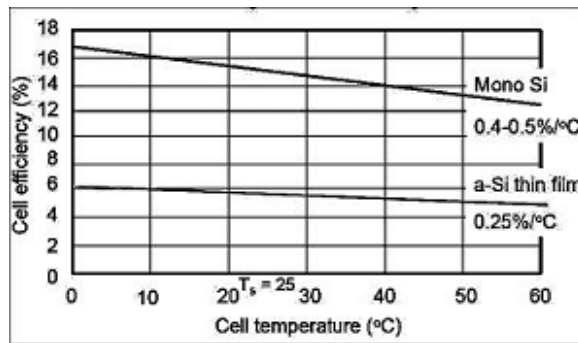


**Fig. 2-1: Established efficiency-to-temperature relationship**

To increase PV electrical efficiency and make full utilisation of solar radiation, it is desirable to remove the accumulated heat from the concealed PV surface and collect the residual heat effectively. PV/T technology has been developed for this purpose, and combines PV cells and heat extraction components in a single module. This subsequently allows cooling of the PV cells, increasing PV electrical efficiency and simultaneously supplying the extracted heat to the end users. Thus, this hybrid solar collector can obtain an enhanced overall solar efficiency and provide an effective method for the utilisation of solar energy. The PV/T device represents a new direction for renewable heating and power cogeneration. **Fig. 2-2** shows the interrelationship between different solar conversion technologies.

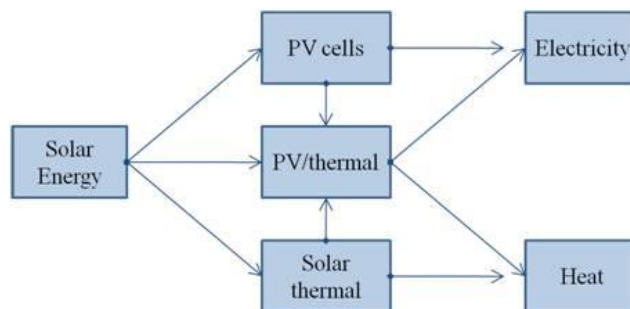


**Fig. 2-2: Network of different solar conversion technologies**

A typical PV/T module is a sandwiched structure comprising several layers: flat-plate clear glazing as the top layer; a layer of photovoltaic cells or a commercial PV lamination beneath the cover with a small air gap; a thermal absorber closely adhered to the PV layer; and a thermally insulated layer located immediately below the flow channels. All the layers are fixed into a frame using adequate clamps and connections. The most basic technique for fabricating a PV/T module is to glue a commercial PV lamination to a thermal absorber. **Fig. 2-3** displays a schematic of a typical PV/T module structure.

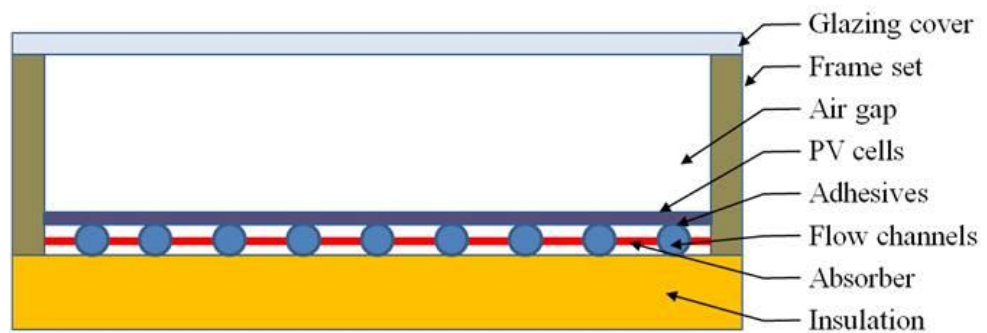


**Fig. 2-3: A focused cross section of a typical PV/T module**

The general concept of PV/T technology was originally addressed by Kern and Russell [2.5] in 1978. For a PV/T module, solar irradiation with a wavelength from 0.6-0.7  $\mu\text{m}$  is absorbed by the PV cells and converted into electricity, whilst the remaining irradiation is mostly transformed in the form of thermal energy. PV/T modules can collect solar energy at different grades (wavelengths), leading to enhanced energy and exergetic efficiency [2.6]. According to Zongdag et al. [2.6] and Zhao [2.7] et al., a PV/T module can collect and convert a higher percentage of solar energy than either an individual PV panel or a thermal collector at the same absorbing area and, therefore, offers the potential to be developed into a low-cost and highly effective heat and power cogeneration system.

A PV/T module is principally derived from the combined functions of a flat-plate solar (thermal) collector and a PV panel. The overall efficiency is the sum of the collector's thermal efficiency and the PV electrical efficiency, which are defined as the ratio of useful system heat gain and electricity gain to the incident solar irradiation striking the collector's absorbing surface

$$\eta_o = \eta_{th} + \eta_e \quad [2-1]$$

where,  $\eta_o$  is the overall efficiency;  $\eta_{th}$  and  $\eta_e$  represent the thermal and the electrical efficiencies respectively.

### (1) Thermal Efficiency

The thermal efficiency of a flat-plate PV/T collector is the ratio of the useful thermal energy to the overall incident irradiation

$$\eta_{th} = \frac{Q_u}{IA_c} \quad [2-2]$$

where,  $Q_u$  is the useful thermal energy (W);  $I$  is the incident irradiation ( $W/m^2$ ) and  $A_c$  is the collecting area of the module ( $m^2$ ).

The heat gathered by the flat-plate PV/T collector could either be given as

$$Q_u = mc_p(T_{out} - T_i) \quad [2-3]$$

where,  $m$  is the mass flow rate of working medium (kg/s);  $c_p$  is the specific heat capacity at a constant pressure of working medium (J/kg-K);  $T_{out}$  and  $T_i$  are the temperatures of the module outlet and inlet (K).

Or could simply be expressed by the difference in the absorbed solar radiation, heat loss and electrical energy produced

$$Q_u = A_c[I(\tau\alpha) - U_L(T_{p,m} - T_a) - q_e] \quad [2-4]$$

where,  $\tau\alpha$  is the transmittance-absorption coefficient of glazing cover;  $U_L$  is the heat loss coefficient ( $W/m^2-K$ );  $T_{p,m}$  and  $T_a$  are the temperatures of the PV module and ambient (K);  $q_e$  is module electrical output per unit area ( $W/m^2$ ).

To allow engineering analysis, equations for a flat-plate solar collector were modified by Hottel and Whillier [2.8] through the inlet temperature ( $T_i$ ) of the fluid to replace the mean absorber temperature ( $T_{p,m}$ ), which has been widely used in the design and evaluation of solar collectors. The equations are correlated to the solar collector configuration, as shown in **Fig. 2-4**.

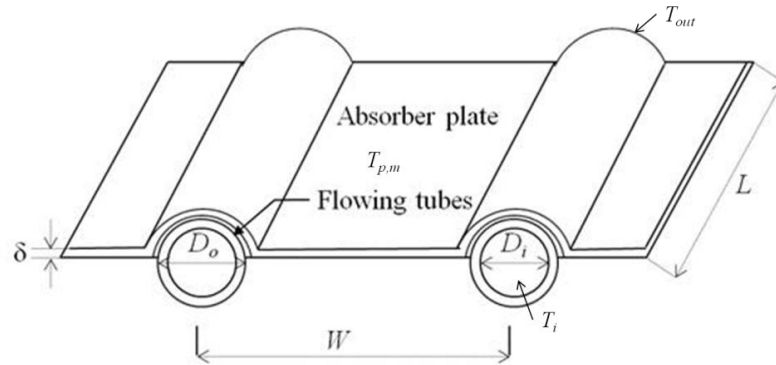


**Fig. 2-4: Schematic of an absorber plate with dimensions**

Hence, the heat gathered by the PV/T collector can be related to the fluid inlet temperature ( $T_i$ ) by

$$Q_u = F_R A_c [I(\tau\alpha) - U_L(T_i - T_a) - q_e] \quad [2-5]$$

where  $F_R$  is the heat removal factor that is connected with the efficiency factor ( $F'$ ) using the following equation

$$\frac{F_R}{F'} = \frac{Ic_p}{U_L F'} \left[ 1 - \exp\left(-\frac{U_L F'}{Ic_p}\right) \right] \quad [2-6]$$

where  $F'$  is a variable dependent upon the type of working medium (e.g., water or air), which has the different expressions as followings due to the different structures of water or air based PV/T modules

$$F' = \frac{1/U_L}{W \left[ \frac{1}{U_L [D_o + (W - D_o)F]} + \frac{1}{C_b} + \frac{1}{\pi D_i h_{wm}} \right]} \quad \text{for water} \quad [2-7]$$

$$F' = \frac{1}{1 + [U_L / (h_{wm} A / A_c + \frac{1}{(1/h_r + 1/h_{wm})})]} \quad \text{for air} \quad [2-8]$$

where,  $W$  is the distance between tubes (m);  $D_o$  and  $D_i$  are the outside and inside diameter of flow tubes (m);  $C_b$  is thermal conductance of the bond between the fin and tube (W/m-K);  $h_{wm}$  is the heat transfer coefficient of working medium;  $A/A_c$  is the ratio of heat transfer area to collector aperture area;  $h_r$  is the equivalent radiation coefficient (W/m<sup>2</sup>-K);  $F$  is the fin efficiency, which could be given by

$$F = \frac{\tanh[\sqrt{(U_L / k\delta)}(\frac{W - D_o}{2})]}{\sqrt{(U_L / k\delta)}(\frac{W - D_o}{2})} \quad [2-9]$$

where,  $k$  is the thermal conductivity of the fin (W/m-K) and  $\delta$  is the fin thickness (m).

## (2) Electrical Efficiency

It is known that the electrical efficiency of a PV module decreases with an increase in the cell's working temperature, and this dependence is [2.9]

$$\eta_e = \eta_{rc} [1 - \beta_{PV} (T_p - T_{rc})] \quad [2-10]$$

where,  $\eta_{rc}$  is the initial electrical efficiency at reference temperature;  $\beta_{PV}$  is the cell efficiency temperature coefficient (1/K);  $T_p$  and  $T_{rc}$  are respectively the PV cell temperature and its reference temperature (K).

Alternatively, in practical applications, the electrical efficiency ( $\eta_e$ ) of a PV module is represented as the ratio of measured output power,  $P_o$  (W), to the overall incident solar radiation:



$$\eta_e = \frac{P_o}{IA_c} \quad [2-11]$$

The generated electrical energy,  $Q_e$  (W), can be expressed as

$$Q_e = P_o = \eta_e IA_c \quad [2-12]$$

### 2.2.2 Classification of PV/T Technology

PV/T modules can be classified into different groups in terms of configuration, cooling medium, temperature level and function. From the cooling medium point of view, there are currently four types of PV/T collector available, which are the devices developed using air, water, refrigerants, and heat pipes.

#### (1) Air-based PV/T Technology

An air-based PV/T module is a solar air heater with an additional PV layer laminated on the top or bottom of a naturally or mechanically ventilated air channel. This PV/T type can be formulated by incorporating an air gap between the PV module's back surface and the building fabric (facade or tilted roof). Usually, this PV/T system is designed for end users who have a demand for hot air, space heating, agricultural/herb drying or increased ventilation, as well as electricity generation. For this module type, air can be delivered from above, below or on both sides of the PV absorber, as shown in **Fig. 2-5**.

#### (2) Water-based PV/T Technology

A water-based PV/T module has a similar structure to a conventional flat-plate solar collector. The absorber is attained with numerous PV cells that are connected in a series or parallel and fixed under serpentine or a series of parallel tubes. Water is forced to flow across the tubes and, if the water temperature remains low, the PV cells will be cooled, thus leading to increased electrical efficiency. In the meantime, the passing water will be heated by absorbing the PV heat and will be delivered to certain heat devices to provide

heating. This part of the water may be consumed or, alternatively, cooled in the heating services and returned to the module to retain heat. Compared to the air-based system, a water-based PV/T system can achieve enhanced cooling effectiveness due to the higher thermal mass of water over air and, therefore, both the thermal and electrical efficiencies of the system will be higher. Zondag et al. [2.10] addressed several water flow patterns for PV/T collectors, i.e., sheet and tube, channel, free flow and two absorber types, which are shown schematically in Fig. 2-6.

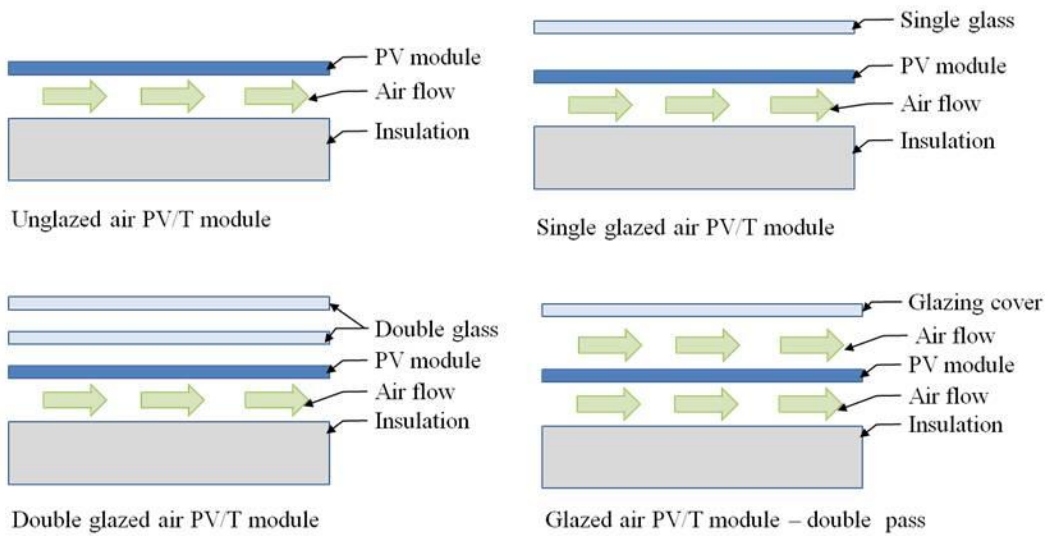


Fig. 2-5: Cross sections of air-based PV/T modules

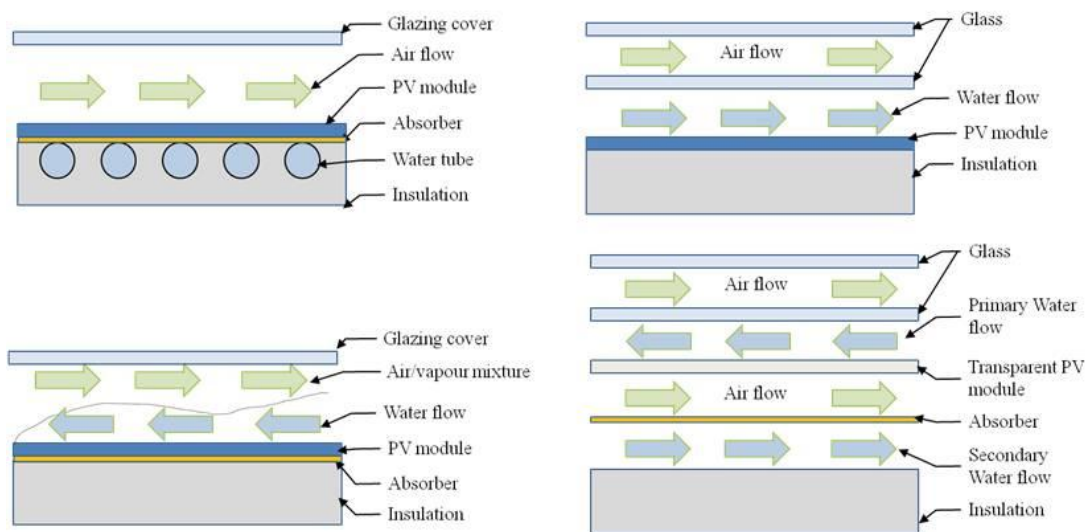


Fig. 2-6: Cross sections of water-based PV/T modules

### (3) Refrigerant-based PV/T Technology

In recent years, refrigerant-based PV/T heat pump systems have been studied. Kern and Russell [2.5] initially proposed a simple PV/T collector connected with a heat pump system and studied the energy saving and economic benefits. Recent study has suggested a novel concept of a PV/T module for heat pump application. This solar technology lays direct expansion evaporation coils underneath the PV modules, which allows a refrigerant to be evaporated when passing through the modules. In this way, the coils act as the evaporation sector of the heat pump, which allows the refrigerant to evaporate at a remarkably low temperature, e.g., 0-20 °C. As a result, the PV cells are cooled to a similar low temperature, which leads to a significant increase in the panel's heat and electrical efficiencies. The compressor of the heat pump increases the pressure of the vapour generated from the panels and delivers it to the condenser to provide heating. In operation, the compressor would be driven by PV-generated electricity, thus creating a solar-powered heat pump independent of fossil fuel energy. **Fig. 2-7** gives a cross-sectional view of a glazed PV evaporator (PV/e) roof panel [2.7], and **Fig. 2-8** shows a schematic of a PV/T-based heat pump system and its thermodynamic process in a Pressure-Enthalpy (P-H) diagram [2.7].

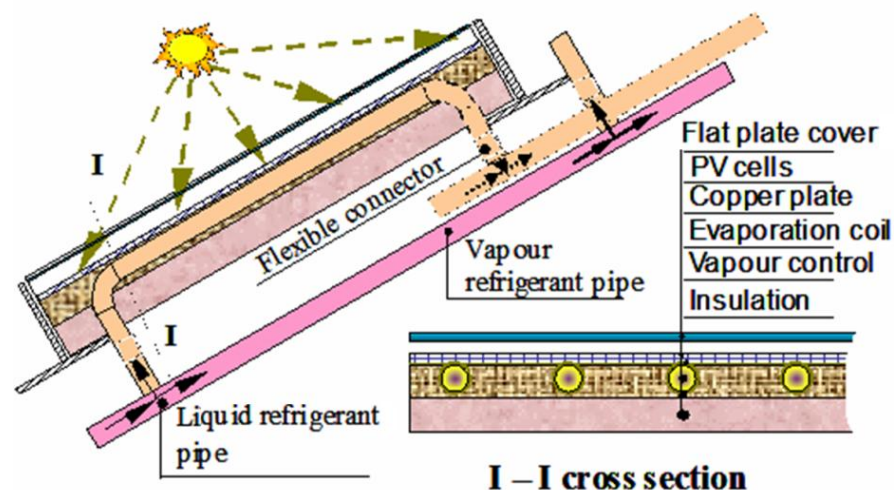


Fig. 2-7: Cross-section of a PV evaporator roof panel

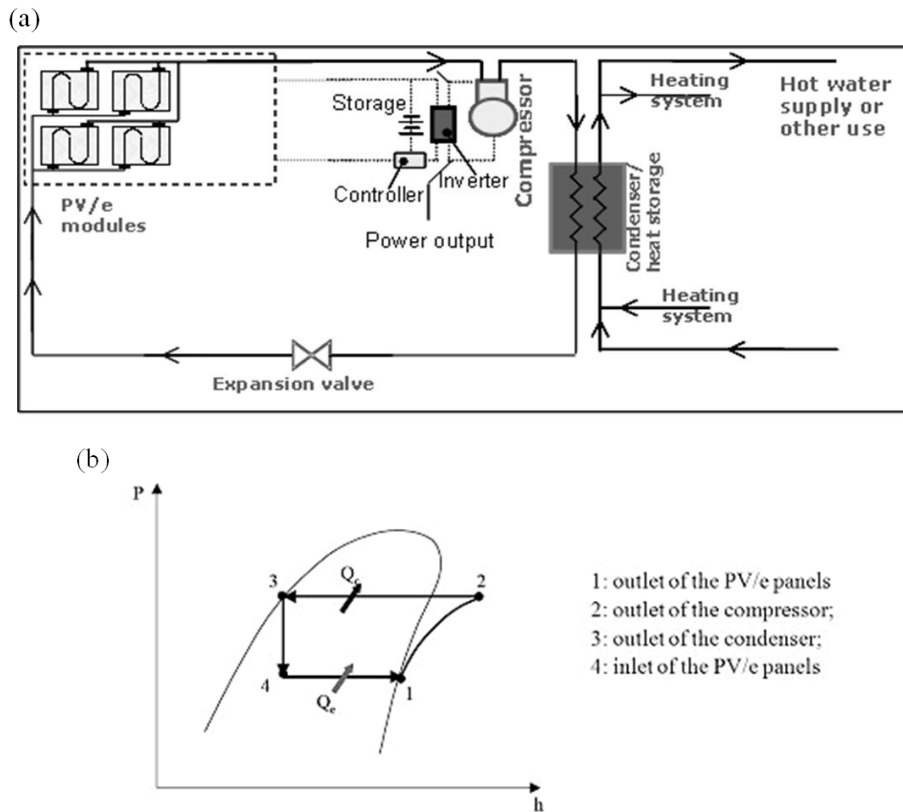


Fig. 2-8: Schematic of (a) PV/e roof module-based heat pump system and (b) its thermodynamic process in a Pressure-Enthalpy diagram

#### (4) Heat-pipe-based PV/T Technology

Heat pipes are considered an efficient heat transfer mechanism that combines the principles of both thermal conductivity and phase transition. A typical heat pipe, as indicated in **Fig. 2-9** [2.11], consists of three sections: an evaporation section (evaporator), an adiabatic section and a condensation section (condenser), and provides an ideal solution for heat removal and transmission.

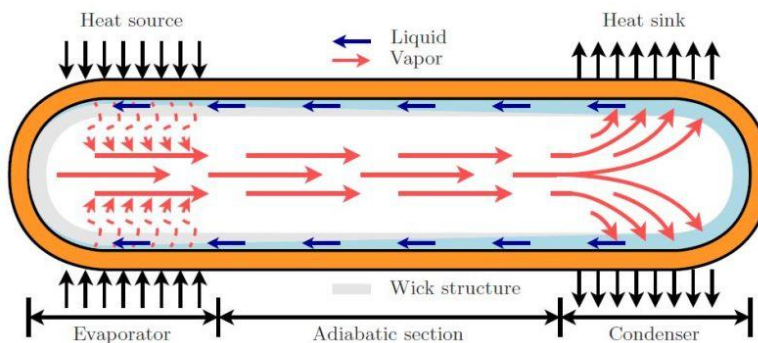
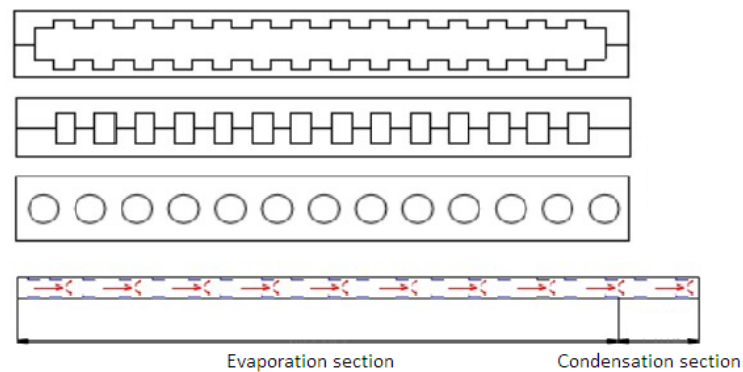
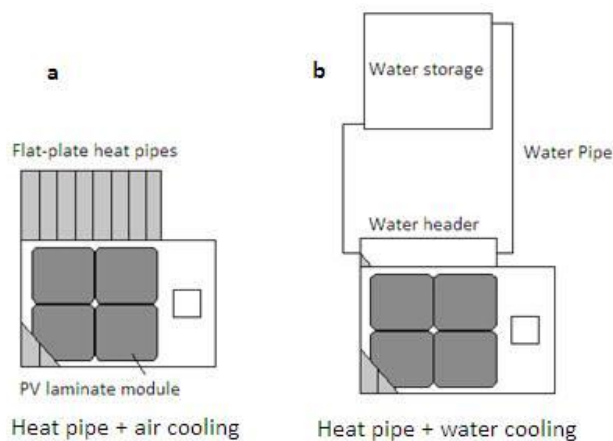


Fig. 2-9: Schematic of a conventional heat pipe

The PV/heat pipe combination has recently been studied. Zhao et al. [2.12-2.14] proposed a PV/flat-plate heat pipe array for the cogeneration of electricity and hot air/water. This prototype module comprises a PV layer and a flat-plate heat pipe containing numerous micro-channel arrays acting as the evaporation section of the heat pipe. The other end of the heat pipe is the condensation section, which releases heat to the passing fluid. The authors claim that the flat-plate geometry was more efficient due to the excellent thermal contact between the PV cells and the heat extraction devices, which results in lower thermal resistance and higher overall solar conversion efficiency. In this way, PV efficiency could increase by 15-30% compared to a standard PV panel if its surface temperature is controlled to around 40-50 °C. The overall solar conversion efficiency of the module tested at around 40%. **Fig. 2-10** [2.12] and **Fig. 2-11** [2.14] show three types of PV/heat pipe modules acting as thermal and power cogeneration units.



**Fig. 2-10: Three types of flat-plate heat pipe with micro-channel array**



**Fig. 2-11: PV/flat-plate heat pipe: a) air cooling; b) water cooling**

Qian et al. [2.15, 2.16] brought a new concept for buildings that integrated a PV/T system utilising an oscillating heat pipe. This system was designed as facade components for transporting heat from concealed PV cells (OHP-BIPV/T), as shown in **Fig. 2-12** [2.22]. The system consists of the oscillating heat pipes, headers, finned tube, graphite conductive layer, metal frame, PV laminate module and insulation. During operation, the working fluid within the metal heat pipes will absorb heat from the PV cells and will then be evaporated into vapour fluid. The vapour will flow up into the finned tube, where it condenses by releasing heat to the passing fluid and returns to the absorber by the effect of gravity and capillary forces.

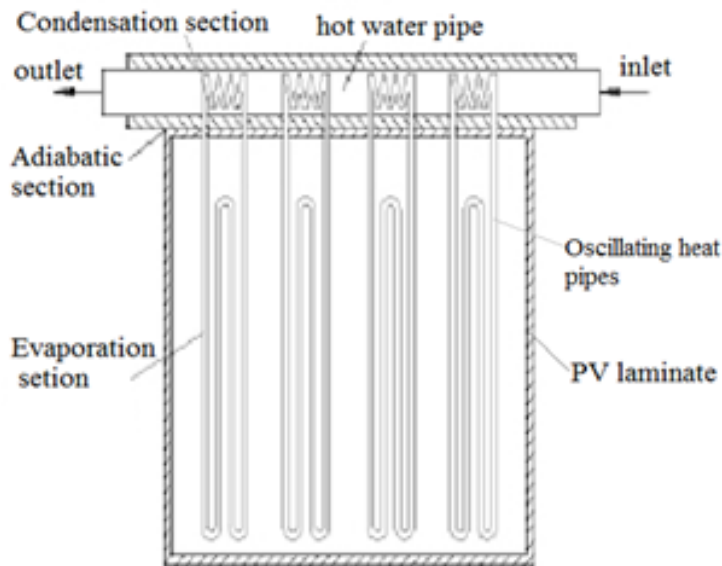


**Fig. 2-12: Schematic of the OHP-BIPV/T module**

### (5) Technical Characteristics of Currently Available PV/T Types

A general comparison of the four currently available PV/T types was made in terms of their technical characteristics. The overall module efficiencies for different PV/T types were calculated with the same external solar/weather conditions (i.e., weather conditions on 22<sup>nd</sup> December in the Midwestern area of the UK) and operational conditions (i.e., 0.01 kg/m<sup>2</sup>-s of mass flow rate, 10% of initial PV efficiency). The calculation models used were as follows: (1) an indoor-simulator (IS) model for air-based PV/T [2.17]; (2) an integrated PV/T system (IPVTS) model for water-based PV/T [2.18]; (3) a PV solar-assisted

heat pump (PV-SAHP) model for refrigerant-based PV/T [2.19]; and (4) a PV/flat-plate heat pipe (PV/FPHP) model for heat-pipe-based PV/T [2.13]. **Table 2-1** gives a specific description of the characterised results.

**Table 2-1: The characteristics comparison of different PV/T types**

PV/T models	Efficiency	Advantage	Disadvantages
IS model for air-based PV/T type [2.17]	24%–47%	<ul style="list-style-type: none"> <li>- Low cost</li> <li>- Simple structure</li> </ul>	<ul style="list-style-type: none"> <li>- Low thermal mass</li> <li>- Large air volume</li> <li>- Poor thermal removal effectiveness</li> <li>- High heat loss</li> </ul>
IPVTS model for water-based PV/T type [2.18]	33%–59%	<ul style="list-style-type: none"> <li>- Low cost</li> <li>- Direct contribution</li> <li>- High thermal mass</li> <li>- Low flow volume</li> </ul>	<ul style="list-style-type: none"> <li>- Still high PV temperature</li> <li>- Unstable heat removal effectiveness</li> <li>- Complex structure</li> <li>- Possible pipe freezing</li> </ul>
PV-SAHP model for refrigerant-based PV/T type [2.19]	56%–74%	<ul style="list-style-type: none"> <li>- Low PV temperature</li> <li>- Stable performance</li> <li>- High efficiency</li> <li>- Effective heat removal</li> </ul>	<ul style="list-style-type: none"> <li>- Risk of leakage</li> <li>- Unbalanced liquid distribution</li> <li>- High cost</li> <li>- Difficult to operate</li> </ul>
PV/FPHP model for heat-pipe-based PV/T type [2.13]	42%–68%	<ul style="list-style-type: none"> <li>- Low PV temperature</li> <li>- Stable performance</li> <li>- High solar efficiency</li> <li>- Effective heat removal</li> <li>- Reduced power input</li> </ul>	<ul style="list-style-type: none"> <li>- High cost</li> <li>- Risk of damage</li> <li>- Complex structure</li> </ul>

In general, the air PV/T type has a poor heat removal performance due to its low thermal mass and less-organized air flow; the water type remains with increasing water temperature and a fall in solar efficiency because of varying water temperatures over operational time and the heat removal effectiveness will actually become poor while at high-temperature operation; the refrigerant type is difficult to handle in operation as pressurisation and depressurisation are required along the system, and risks of leakage and an imbalance in refrigerant distribution remain high during the whole process; the heat-pipe type remains with a large number of pipe arrays and a high cost problem that may affect its wide deployment in practical projects.

### 2.2.3 Performance Evaluation Standards

Several national/regional standards are currently available for evaluating the performance of standard solar thermal and PV devices. For solar thermal devices, the available standards include EN 12975 [2.20, 2.21], EN 12976 [2.22, 2.23], EN 12977 [2.24-2.28], Solar Keymark [2.29], ISO 9806 [2.30-2.32], MCS 004 [2.33] and other national solar thermal themes; for PV devices, the available standards include IEC (61215, 61646, 61730) [2.34-2.37], UL (1703, 1741, 4703) [2.38-2.40], IEEE (1262 and 929) [2.41, 2.42], CE-marking [2.43] and other national electrical codes. No published standards were found to address the performance of PV/T system. Instead, methods for evaluating the PV/T devices were provided in some academic papers. The technical performance of PV/T systems is usually evaluated using several indicative parameters, including overall energetic efficiency, overall exergetic efficiency, primary energy saving efficiency and solar fraction. The economic performance of PV/T systems is measured by the life-cycle cost and cost payback time (CPT). The environmental benefit of a PV/T system is justified using life-cycle carbon saving or energy payback time (EPT) and greenhouse gas payback time (GPBT).

#### (1) Technical Parameters for Performance Evaluation

##### *I. Overall Energy Efficiency*

Overall energy efficiency is the ratio of collected electrical and heat energy to the incident solar radiation striking a PV/T absorber. It comes from the first law of thermodynamics and indicates the percentage of the energy converted from solar radiation. In a PV/T module, the electrical efficiency is much lower than the thermal efficiency and, therefore, the overall energetic efficiency will largely depend on the thermal energy conversion of the system. It should be pointed out that the overall energetic efficiency ignores the difference between heat and electrical energy in terms of energy grade (quality) and is inadequate for justifying the energy performance of PV/T systems.



## II. Overall Exergetic Efficiency

Overall exergetic efficiency takes into account the difference in energy grades between heat and electricity and involves the conversion of low-grade thermal energy into the equivalent high-grade electrical energy using the theory behind the Carnot cycle. The Carnot cycle is a theoretical thermodynamic cycle for converting a given amount of thermal energy into work, or conversely creating a temperature difference by given amount of work. The behaviour of a classical Carnot heat engine is illustrated by a temperature-entropy ( $T$ - $S$ ) diagram in **Fig. 2-13**, in which the thermodynamic state is specified by a point with entropy ( $S$ ) as the horizontal axis and temperature ( $T$ ) as the vertical axis. The Carnot cycle is therefore considered to take place between the working medium inside the PV/T panel (hot reservoir) at temperature  $T_{wm}$  and the ambient temperature (cold reservoir) at temperature  $T_a$ .

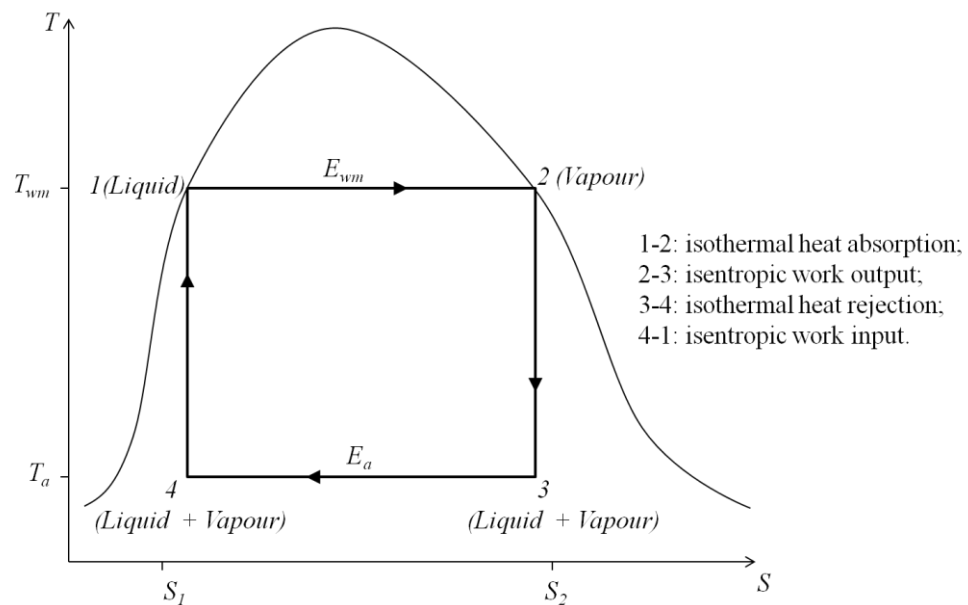


**Fig. 2-13: A Carnot cycle acting as a heat engine on a Temperature-Entropy diagram**

The exergetic efficiency is defined as the ratio of total exergy output to total exergy input

$$\xi_o = \frac{Ex_o}{Ex_{sun}} = \frac{Ex_e + Ex_{th}}{Ex_{sun}} = \xi_e + \xi_{th} \quad [2-13]$$

where,  $Ex_o$ ,  $Ex_{th}$  and  $Ex_e$  are the overall, thermal and electrical exergy output respectively (W);  $Ex_{sun}$  is the total exergy input of solar radiation (W);  $\xi_{th}$  and  $\xi_e$  are the thermal and electrical exergetic efficiency respectively;  $\xi_o$  is the overall exergetic efficiency of PV/T module.

The electrical and thermal exergetic efficiencies are written by following equations respectively

$$\xi_e = \frac{Ex_e}{Ex_{sun}} = \frac{Q_e}{Ex_{sun}} \quad [2-14]$$

$$\xi_{th} = \frac{Ex_{th}}{Ex_{sun}} = \frac{Q_{th}\eta_c}{Ex_{sun}} \quad [2-15]$$

where,  $\eta_c$  is the ideal Carnot efficiency for a heat engine, which is the fraction of the heat energy extracted from the PV/T Panel (hot reservoir) and converted to the electricity (mechanical work), defined as

$$\eta_c = \frac{W_{carnot}}{E_{wm}} = \frac{(T_{wm} - T_a)(S_2 - S_1)}{T_{wm}(S_2 - S_1)} = 1 - \frac{T_a}{T_{wm}} \quad [2-16]$$

where,  $W_{carnot}$  is the work done by the Carnot system (J);  $E_{wm}$  is the heat put into the Carnot system (J); In above equation, the initial temperature of the fluid medium is simply assumed equal to the ambient temperature [2.44] while  $T_a$  is the temperature of the ambient (cold reservoir, K) and  $T_{wm}$  is the final temperature of the working medium (hot reservoir, K);  $S_1$  and  $S_2$  are the minimum and the maximum entropy of heat engine system respectively (J/ K).

In a PV/T system, the overall exergy input of solar radiation is described by

$$Ex_{sun} = \left(1 - \frac{T_a}{T_{sun}}\right) IA_c \quad [2-17]$$

where,  $T_{sun}$  is the solar radiation temperature at 6000 K.

The exergy represents the maximum quantity of work that can be produced by the system in the given environment. Exergetic efficiency considers the energy grade difference between heat and electricity, which is a more rational index for evaluating performance.

### ***III. Primary Energy Saving Efficiency***

Huang et al. [2.18, 2.45] proposed another performance evaluation method to recognise the energy grade difference between heat and electricity: namely, the primary energy saving efficiency ( $E_f$ ), which is given by

$$E_f = \eta_e / \eta_{power} + \eta_{th} \quad [2-18]$$

where,  $\eta_{power}$  is the electrical power generation efficiency for a conventional power plant at 0.38. Huang et al. [2.18] recommended that the primary energy saving efficiency of a PV/T system should be higher than 0.50 to complete a solar hot water system.

### ***IV. Solar Fraction***

From the primary energy saving point of view, solar fraction ( $f$ ) can also be used to evaluate the performance of PV/T systems. It is defined as the fractional ratio of the primary energy saving that a PV/T system can obtain to the overall energy demand, and can be given as

$$f = \frac{1}{2} \times \left( \frac{Q_{load,th} - Q_{aux,th}}{Q_{load,th}} + \frac{Q_{load,e} - Q_{aux,e}}{Q_{load,e}} \right) \quad [2-19]$$

where,  $Q_{load,t}$  and  $Q_{aux,t}$  is the overall thermal load and auxiliary heat required;  $Q_{load,e}$  and  $Q_{aux,e}$  is the total electrical load and auxiliary electricity needed. Kalogirou [2.46] indicated that the solar fraction is lower in the winter months

and higher in the summer months. For a typical hot water supply system, the average solar fraction has a value of 0.49 annually.

In summary, energetic and exergetic efficiencies are the most appropriate indexes for the performance evaluation of PV/T systems, whereas primary energy saving efficiency and solar fraction are occasionally used to evaluate the fossil fuel saving capacity of PV/T systems. In reality, different end users have different energy demands that will somewhat affect the performance of the PV/T systems in use. Choosing an appropriate evaluation method for a specific PV/T installation will need to take both energy supply and demand into consideration.

## (2) Economic and Environmental Measurements

In terms of the economic measures of PV/T, Tripanagnostopoulos et al. suggested the life-cycle cost assessment method, which takes into account the capital cost of system installation and the associated operational and maintenance cost across the system's life cycle [2.47]. Time-related issues such as inflation, tax and company discount rates should also be factors to be considered [2.48]. A simplified approach to the assessment of PV/T economic value is to use cost payback time (in years), which ignores the time-relevant items and maintenance cost and is, therefore, inaccurate. **Table 2-2** [2.47] specifies the cost breakdown and payback issues for various PV/T types.

In terms of the environmental measures of PV/T technology, the most common method is to use the life-cycle carbon emission saving indicator by multiplying the PV/T energy output by the energy-to-carbon conversion factor [2.47]. Tripanagnostopoulos et al. [2.47] and Chow [2.48] also suggested using EPBT and GPBT as the environmental assessment factors. EPBT is the ratio of the embodied energy of the PV/T system to its annual energy output, while GPBT is the ratio of the greenhouse gas embodied by the PV/T system to its reduction of greenhouse gas. The environmental measures of some PV/T devices are presented in **Table 2-3** [2.47].

**Table 2-2<sup>1</sup>: Cost breakdown and cost payback time of different PV/T systems [2.47]**

System cost 30m <sup>2</sup> installation cost payback time (CPBT)	Cost of PV+HRU+REF (€)	Cost of electrical+thermal (€)	Installation cost (€)	Total cost (€)	CPBT for electricity saving (in yr)	CPBT for electricity and gas saving (in yr)
PV	21000	1500	1500	24000	25.8	25.8
PV+REF	22500	1500	1500	25500	22.9	24.1
PV-TILT	21000	1500	900	23400	28.2	26.9
PVT/UNGL-25°C	24000	4500	1500	30000	11.9	18.1
PVT/UNGL-35°C	≥	≥	≥	≥	18.7	23.8
PVT/UNGL-45°C	≥	≥	≥	≥	28.1	29.6
PVT/UNGL+REF-25°C	25500	4500	1500	31500	11.1	17.2
PVT/UNGL+REF-35°C	≥	≥	≥	≥	17.0	22.3
PVT/UNGL+REF-45°C	≥	≥	≥	≥	25.5	28.1
PVT/GL-25°C	27000	4500	1500	33000	10.5	17.6
PVT/GL-35°C	≥	≥	≥	≥	14.5	21.9
PVT/GL-45°C	≥	≥	≥	≥	21.2	27.9
PVT/GL+REF-25°C	28500	4500	1500	34500	10.3	17.2
PVT/GL+REF-35°C	≥	≥	≥	≥	13.9	21.1
PVT/GL+REF-45°C	≥	≥	≥	≥	19.8	26.3
PVT/UNGL-TILT-25°C	24000	4500	900	29400	11.8	18.2
PVT/UNGL-TILT-35°C	≥	≥	≥	≥	18.5	24.2
PVT/UNGL-TILT-45°C	≥	≥	≥	≥	28.2	30.8
PVT/GL-TILT-25°C	27000	4500	900	32400	10.5	17.9
PVT/GL-TILT-35°C	≥	≥	≥	≥	14.2	22.1
PVT/GL-TILT-45°C	≥	≥	≥	≥	20.7	28.2

**Table 2-3: EPBT and CO<sub>2</sub> PBT values for different PV/T systems [2.47]**

System EPBT and CO <sub>2</sub> PBT results	EPBT for replacing electricity only (yr)	CO <sub>2</sub> PBT for replacing electricity only (yr)	EPBT for replacing electricity and gas (yr)	CO <sub>2</sub> PBT for replacing electricity and gas (yr)
PV	2.9	2.7	2.9	2.7
PV+REF	2.7	2.5	2.7	2.5
PV-TILT	3.2	3.1	3.2	3.1
PVT/UNGL-25°C	1.0	0.9	1.2	1.5
PVT/UNGL-35°C	1.9	1.7	2.2	2.4
PVT/UNGL-45°C	3.6	3.3	3.8	3.7
PVT/UNGL+REF-25°C	0.9	0.9	1.2	1.4
PVT/UNGL+REF-35°C	1.7	1.5	2.0	2.2
PVT/UNGL+REF-45°C	3.1	2.9	3.4	3.4
PVT/GL-25°C	0.8	0.8	1.1	1.3
PVT/GL-35°C	1.3	1.2	1.6	1.9
PVT/GL-45°C	2.2	2.0	2.6	3.0
PVT/GL+REF-25°C	0.8	0.8	1.0	1.3
PVT/GL+REF-35°C	1.2	1.1	1.5	1.8
PVT/GL+REF-45°C	2.0	1.9	2.4	2.7
PVT/UNGL-TILT-25°C	1.0	1.0	1.3	1.6
PVT/UNGL-TILT-35°C	1.9	1.8	2.3	2.5
PVT/UNGL-TILT-45°C	3.8	3.5	4.1	4.1
PVT/GL-TILT-25°C	0.8	0.8	1.1	1.4
PVT/GL-TILT-35°C	1.3	1.2	1.6	2.0
PVT/GL-TILT-45°C	2.2	2.0	2.7	3.1

<sup>1</sup> Note: HRU: heat recovery unit; UNGL: unglazed; GL: glazed; REF: stationary flat diffuse reflectors; TILT: tilted installation.

## 2.3 R&D Progress and Practical Applications of PV/T Technologies

### 2.3.1 Overview of R&D works in the PV/T Field

Numerous pieces of research have been carried out to study the performance of different PV/T configurations, optimise their geometric sizes and recommend the most appropriate operational parameters. As a result, a sufficient quantity of experience has been obtained and this is selectively indicated as follows.

Hendrie [2.49] developed a theoretical model for a flat-plate PV/T solar collector and carried out a study into the thermal and electrical performance of air- and liquid-based PV/T solar collectors. He concluded that when the PV modules were not in operation, the air- and liquid-based collectors could achieve peak thermal efficiencies of 42.5% and 40%, respectively. However, when the PV modules were functioning, the air- and liquid-based units obtained slightly lower thermal efficiencies than the previous case, of 40.4% and 32.9%, respectively. In the meantime, the measured peak electrical efficiency of these units was 6.8%.

Florschuetz [2.50] used the well-known Hottel–Whillier [2.8] thermal model for flat-plate solar collectors to analyse the performance of a combined PV/T collector. By slightly modifying the parameters existing in the original computer program, the model was made available for analysing the dynamic performance of the PV/T collector. Assuming that the solar PV electrical efficiency was linearly reduced when the cell's temperature increased, the thermal and electrical efficiencies of the combined PV/T collector were obtained and the results were further analysed to enable development of the correlations between the efficiencies and the various operational parameters of the collectors.

Raghuraman [2.51] developed two one-dimensional analytical models to predict the thermal and electrical performance of both liquid- and air-based flat-plate PV/T collectors. The analysis took into account the difference in temperature of the primary absorber (the PV cells) and the secondary absorber

(a flat-plate thermal absorber), and a number of design were recommended to enable the maximised energy utilisation of the collectors.

Bergene and Lovvik [2.52] developed a dedicated PV/T mathematical model and associated algorithms, enabling quantitative predictions of system performance. The model was established by analysing the energy transfer processes, including conduction, convection and radiation, initiated by Duffie and Beckman [2.9], and the results of the model's operation suggest that the overall efficiency of the PV/T collectors was in the range of 60% to 80%.

Sopian et al. [2.53] developed steady-state models to analyse the performance of both single- and double-pass PV/T air collectors. The models yielded the temperature profiles of the glass cover, plates, and air stream, while the mean plate temperature could be applied to evaluate the efficiency of the PV cells. Performance analysis showed that the double-pass PV/T solar collector produced a better performance than the single-pass module at a normal operational mass flow rate range. In addition, the thermal and the combined thermal and electrical efficiencies increased when the packing factor (defined as the ratio of the PV cell area to the absorber area) decreased, whereas the electrical efficiency of the PV decreased slightly.

Sandnes and Rekstad [2.54] constructed a PV/T unit by using a polymer solar heat collector combined with a single-crystal silicon PV cell. An analytical model derived from the Hottel–Whillier equations was used to simulate the temperature distribution and the performance of both the thermal and PV parts. The simulation results were in agreement with the experimental data. The authors found that increasing the number of solar cells on the absorbing surface would reduce the absorbed energy by the panel (about 10% of incident energy) due to the lower optical absorption of the solar cells compared to the black absorber plate. Further, there was increased thermal resistance at the surface of the absorber and within the fluid, which reduced the collector's heat removal factor,  $F_R$ . Moreover, they concluded that the solar cells' temperature was strongly related to the system inlet-fluid temperature and the collector's heat transport characteristics. The combined PV/T concept could, therefore, be

associated with applications of sufficiently low temperature to give a desired cooling effect.

Tiwari and Sodha [2.55] developed a thermal model for an integrated PV/T solar collector system and compared it with a model of a conventional solar water heater by Huang et al. [2.18]. Based on the energy balance of each component in the system, an analytical expression for the temperature of a PV module and water was derived. The simulations predicted a daily primary energy saving efficiency of around 58%, which was in good agreement with the experimental figure (61.3%) obtained by Huang et al.

Dubey et al. [2.56] developed an analytical model that indicated the electrical efficiency of a PV module with and without cooling flow as a function of climatic and PV physical/operational parameters. Four different PV configurations i.e., case A (glass-to-glass PV module with duct), case B (glass-to-glass PV module without duct), case C (glass-to-Tedlar PV module with duct), and case D (glass-to-Tedlar PV module without duct) were investigated. It was found that the glass-to-glass PV modules with duct gave a greater electrical efficiency and a higher outlet air temperature among all four cases. The annual average efficiencies of the glass-to-glass type PV module with and without duct were reported to be 10.41% and 9.75%, respectively.

Chow [2.57] developed an explicit dynamic model with seven nodes for a single-glazed flat-plate water-heating PV/T collector that was used for system dynamic simulation. This model, derived from control volume finite difference formulation and incorporated with a transport relay subprogram, could provide information on the transient performance, including the real-time thermal/electrical gains, their efficiencies, and the thermal conditions of various components. Further to an extension of the nodal scheme to include multi-dimensional thermal conduction on PV and absorber plates, this model was able to perform a complete energy analysis of the performance of the hybrid solar collector.

Cox and Raghuraman [2.58] explored several useful design features for air-based flat-plate PV/T collectors in order to determine their effectiveness and



interaction on the basis of a computer simulation. They found the air PV/T types were usually less efficient than the liquid ones due to the relatively lower PV cell packing factor, lower solar absorptance, higher infrared emittance and a lower absorber to air heat transfer coefficient. Two methods were recommended to tackle these existing problems: (1) increasing the solar absorptance and (2) reducing the infrared emittance. The results showed that when the packing factor was greater than 65%, a selective absorber could actually reduce the thermal efficiency when a gridded-back cell was applied. The optimum air PV/T configuration was suggested to consist of gridded-back PV cells, a non-selective secondary absorber, and a thermal cover above the PV cells.

Grag and Agarwal [2.59] developed a simulation model to investigate the effect of both the design and operational parameters of a hybrid PV/T air heating system on its performance. It was found that whether or not to use single or double glass covers in a PV/T air heating system largely depended on its design temperatures, as the extra glass cover might lead to larger transmission losses and, beyond some critical point, the single-glass cover could collect more heat than the double glass. The parametric studies indicated that the system efficiency is positively proportional to collector length, mass flow rate and cell density, while it is negatively proportional to the duct depth for both configurations. However, as material cost increases with the number of glass covers, collector length, cell density, duct depth and mass flow rate, the final selection of design parameters and operational variables for a PV/T system must be based on the cost-effectiveness consideration, which was represented by the minimised system life-cycle cost.

Kalogirou [2.46] carried out a computer modelling of the performance of a hybrid PV/T solar water system by using TRNSYS, which is a transient simulation program with typical meteorological year (TMY) conditions for Nicosia in Cyprus. The PV system consisted of a series of PV panels, a battery bank and an inverter, whereas the thermal system consisted of a hot water storage cylinder, a pump and a differential thermostat. The results indicate that the hybrid system would enable an increase in the mean annual PV efficiency

from 2.8% to 7.7% and, meanwhile, cover nearly half the hot water needs in a house, leading to a mean annual overall efficiency of 31.7%. The life-cycle saving of the system was CYP 790.00 (Cyprus Pound) and the payback time was 4.6 years.

Tripanagnostopoulos et al. [2.60] constructed an air-based PV/T solar collector which applied two low-cost approaches to enhance heat transfer between the air flow and the PV surface. A finned metal sheet was attached to the back wall of the air channel to improve heat extraction from the PV modules. Experimental tests were carried out on the air-based PV/T system, which used a 46 W-rated commercial a-Si PV module with a 0.4 m<sup>2</sup> aperture area as the absorber plate. The results showed good agreement between the predicted figures and the measurement data. It was found that the induced mass flow rate and thermal efficiency decreased with a higher ambient (inlet) temperature and increased with a larger tilt angle at a given insulation level. The results also showed that the optimum channel depth was in the range of 0.05 m to 0.1 m for this system. This type of PV/T system is practical, cost effective and suitable for integration within a building with both heat and electricity demands.

Dubey et al. [2.17] designed and constructed a PV/T solar air heater, and investigated its performance in different operational conditions while the parameters remained steady. The experimental system consisted of three PV modules (mono-crystalline silicon solar cells) of glass-to-Tedlar type, each rated at 75 Wp, 0.45 m in width and 1.2 m in length and mounted on a wooden duct. They found that the thermal, electrical and overall efficiency of the solar heater was 42%, 8.4% and 50%, respectively, in the designed laboratory conditions. They also proposed an indoor standard test procedure for thermal and electrical testing of the PV/T collectors connected in series. It was concluded that this test procedure could be used by manufacturers for testing different types of PV modules in order to optimise their geometric sizes.

Shahsavari and Ameri [2.61] designed and tested a direct-coupled PV/T air collector with and without a glass cover in Kerman in Iran. In this study, a thin aluminium sheet suspended in the middle of the air channel was used to increase the heat exchange area and consequently improve the heat extraction

from the PV panels. This PV/T system was tested in natural forced convection conditions (with two, four and eight fans operating). Good agreement between the measurement data and those calculated by the simulation model was achieved. It was concluded that there was an optimal fan number to match the maximum electrical efficiency. Results also indicated that adding a glass cover to photovoltaic panels would lead to increased thermal efficiency and decreased electrical efficiency.

Huang et al. [2.45] studied an integrated PV/T system set-up. A commercial polycrystalline PV module was used to make a PV/T collector, which was part of the system configuration. The test approach for conventional solar hot water heaters was used to evaluate the thermal performance rating of the system. The measurement results indicated that the solar PV/T collector made using a corrugated polycarbonate panel could obtain a primary energy saving efficiency of about 61.3%, while the temperature difference between the tank water and the PV module was around 4 °C.

De Vries [2.62] and Zondag et al. [2.10, 2.63] carried out testing on a PV/T solar boiler with a water storage tank in the Netherland, which indicated that a sheet-and-tube system with cover was the most appropriate PV/T configuration for the purpose of tap water heating. It was reported that the water-based PV/T system could provide good architectural uniformity, and reduce roof space use, as well as the payback period. This PV/T system could achieve annual average solar efficiencies in the range of 34% to 39% for the sheet-and-tube system with cover, and 24% for the same system without cover.

Chow et al. [2.64] conducted an experimental study into a combined centralised photovoltaic and hot water collector wall system that can serve as a water preheater. The collectors were mounted on vertical façades with different operational modes in various seasons. The authors found that natural water circulation was better than forced circulation in their solar collector system. The thermal efficiency was reported at 38.9% and the corresponding electricity conversion efficiency was 8.56% during the late summer in Hong Kong. For the PV/T wall, the space thermal loads can be significantly reduced both in summer and winter, leading to a significant amount of energy savings.

Zhao et al. [2.14] designed two experimental prototypes by integrating a flat-plate heat pipe with mono-crystalline PV cells at an effective area of  $0.0625 \text{ m}^2$ , while the surplus heat was taken away, respectively, via natural air flow and passive water circulation. In comparison with an independent PV system, the PV/T modules were found to be able to achieve enhanced electrical efficiencies of 2.6% and 3% and reduced cell temperatures of  $4.7 \text{ }^\circ\text{C}$  and  $8 \text{ }^\circ\text{C}$ , respectively, for air- and water-based conditions.

Ji et al. [2.65] developed a solar PV/T heat pump system that combined a Rankine refrigeration cycle with a PV/T solar collector. A dynamic model for the PV evaporator was established using a distributed parameter approach to investigate the effect of the refrigerant parameters (e.g., pressure, temperature, vapour quality and enthalpy) on the system's solar efficiencies and the temperature distribution across the evaporator channels. The results indicated that the PV electrical efficiency and evaporator thermal efficiency were around 12% and 50%, respectively, during the test period in Hefei in China.

Ji et al. [2.19] also carried out the testing of the system under a range of operational conditions. The results indicated that the PV-SAHP system had a higher COP figure than the conventional heat pump system and the PV electrical efficiency was also higher. The heat pump COP could achieve 10.4, whilst the average COP value of the traditional heat pumps was around 5.4. Overall, the average PV efficiency was around 13.4%. The highest overall COP figure, taking into account the performance of PVs and evaporators, was around 16.1.

Zhao et al. [2.7] designed a novel PV/e roof module to act as a roof element, electricity generator and the evaporator of a heat pump system. The energy profiles and system operational conditions were analysed and the temperature distribution across the module layers was simulated. This study indicated that the combined system should operate at  $10 \text{ }^\circ\text{C}$  of evaporation and  $60 \text{ }^\circ\text{C}$  of condensation temperature. Borosilicate as a top cover had better thermal performance than polycarbonate and glass, whilst the mono-crystalline photovoltaic cells showed higher electrical efficiency over the polycrystalline and thin films. Under typical Nottingham (UK) operational conditions, the

modules achieved 55% thermal efficiency and 19% electrical efficiency, whilst the module-based heat pump system had an overall efficiency of over 70%. It was also addressed that the integration of the PV cells and evaporation coil into a prefabricated roof would lead to a large saving in both capital and running costs over separate arrangements of the PV panel, heat pump and roof structure.

Apart from the above reports, many other works in this subject were found by the literature study and a few more examples of these are briefed below.

*For air-based PV/T*, Komp and Reeser [2.66] reported the design and installation of a stationary concentrating glazed roof-integrated PV-air collector for an off-grid dwelling. The hybrid collector with fins was intended to enhance the heat transfer between the PV cells and the air; the air was then drawn into the house using a fan in winter and by natural convection in summer. Fudholi et al. [2.67] reported that the drying of agricultural and marine products was one of the most attractive and cost-effective applications for solar PV/T technology. Takashima [2.68] concluded that the surface temperature of PV panels could be reduced when an air gap was above the PV panels to form a thermal collector. Moshtegh and Sandberg [2.69, 2.70] studied the performance of air flow induced by the buoyancy effect and the heat transfer within a vertical channel heated from the PV side wall. The study reported that the induced velocity led to increased heat flux non-uniformity inside the duct and its several impacts depended upon the sizes and geometry of the air exit. Bhargava [2.71] and Parkash [2.72] studied the performance of a single-pass PV/T air collector and analysed the influence of air mass flow rate, the depth of the air channel and the packing factor on the system's overall efficiency. Sopian et al. [2.53] analysed the performance of both single- and double-pass PV/T air collectors using steady-state computer models. The results showed that double-pass PV/T air collectors had higher efficiencies than the single-pass ones but their capital cost was slightly higher. Kelly [2.73] and Tripanagnostopoulos et al. [2.74] suggested several possible approaches to enhance the cooling effect, such as modifying channel geometries to create turbulent flows. Tiwari and Sodha [2.75] indicated that glazed air PV/T collectors had higher thermal efficiency than the paralleled unglazed types,

especially at low temperature conditions where the double-glazing cover was found to be superior to single glazing [2.76]. On the other hand, the glazing cover would slightly reduce the overall performance of a collector owing to unavoidable solar reflection.

**For water-based PV/T**, Agarwal and Grag et al. [2.77, 2.78] designed prototypes for thermo-syphonic and flat-plate PV/T water heaters. Bergene and Lovvik [2.79] then conducted an energy transfer study into a PV/T water system consisting of a flat-plate solar collector and a group of PV cells, which indicated that an overall efficiency of 60% to 80% could be achieved. It was found that the proposed system could be used to preheat domestic hot water. More recently, Zondag et al. [2.10] classified water-based PV/T collectors into four main types: sheet-and-tube collectors, channel collectors, free-flow collectors, and two absorber collectors. Chow et al. [2.64] suggested that implementing the water flow channels beneath a transparent PV module may be a good choice to achieve enhanced solar efficiency. However, the single-glazing sheet-and-tube hybrid PV/T collector was regarded as the most promising design as it has high overall efficiency. Kalogirou and Tripanagnostopoulos [2.46, 2.4] simulated a PV/T water supply and storage system and found that the economic viability of the PV/T water system was much better than the air-based type. Elswijk et al. [2.80] installed a number of large PV/T arrays on residential buildings and reported that the use of PV/T systems would save around 38% in roof area relative to a side-by-side system of PV and solar thermal. Ji et al. [2.81] studied a façade-integrated PV/T collector for residential buildings in Hong Kong. The annual thermal efficiencies were around 48% for thin film silicon and 43% for the crystalline silicon case. In addition, the building-integrated system was able to reduce the cooling requirements of the building substantially due to the reduced heat absorption by the walls.

**For refrigerant/heat-pipe-based PV/T**, Nishikawa et al. [2.82] studied a PV/T heat pump system using R22 as the refrigerant. When the PVs were effectively cooled, the system could achieve a higher COP than a conventional heat pump. Ito et al. [2.83] investigated a similar PV/T heat pump and concluded that when

the condensation temperature was set at 40 °C, the COP of the heat pump could achieve as high as 6.0. Further, Ito et al. [2.84] analysed the effect of a few physical parameters e.g., collector area, and the width, length and thickness of the collector plate on the system's solar efficiency and COP. Zhao et al. [2.12-2.14] initiated a PV/flat-plate heat pipe containing micro-channel arrays to produce electricity and hot air/water simultaneously, as shown in **Fig. 2-11**. Qian et al. [2.15, 2.16] invented a building-integrated photovoltaic/thermal system using an oscillating heat pipe for combined heat and power generation using solar energy. This type of system is shown in **Fig. 2-12**.

### 2.3.2 Practical Applications of PV/T Technology

Although PV/T technology is at the start-up stage, some commercial products or engineering projects involving PV/T application can be found in practice. A number of practical PV/T works are addressed below.

Grammer Solar GmbH in Germany has developed an air-based PV/T solar collector entitled TWINSOLAR, which is designed to preheat ventilation air in buildings with an absorber area in the range of 1.3 m<sup>2</sup> to 12.5 m<sup>2</sup>. The modules can be assembled vertically or horizontally, on the roof or on south-, southeast-, or southwest-facing façades. It was observed that at a maximum solar radiation of 700 W/m<sup>2</sup>, the air temperature increased to 40 °C and nearly 70% of the solar incident energy was converted into thermal energy and transported into the building, as shown in **Fig. 2-14** [2.85].

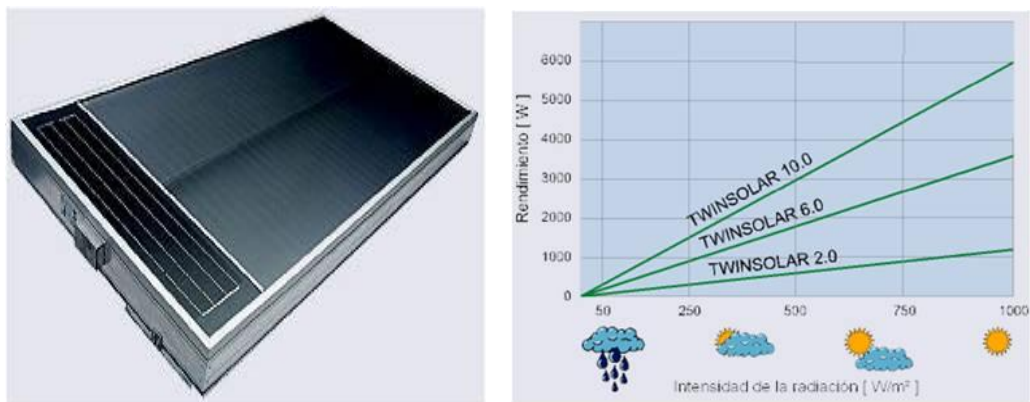


**Fig. 2-14: TWINSOLAR application and its performance curve**

In Denmark, SolarVenti units are mainly used for ventilation, supplementary heating and assisting in air dehumidification. The larger capacity SolarVenti models have a substantial amount of thermal output and can drive a significant amount of air flow due to the buoyancy effect. The thermal energy is captured directly from solar radiation across the spectrum, which could supplement the existing space-heating system in any domestic or commercial building. **Table 2-4** provides the energy outputs for the SolarVenti models [2.86].

**Table 2-4: Energy outputs of different SolarVenti models**

Model	Air volume	Temperature increase	Max Output kW (per hour)	Max Output kW per year (1000 hrs sun)
SV14	60 m <sup>3</sup> Hr	~30 °C	0.6	600
SV30	120 m <sup>3</sup> Hr	~40 °C	1.6	1,600
SV30H	100 m <sup>3</sup> Hr	~40 °C	1.3	1,300

The Canadian company Conserval Engineering Inc. provides SolarWall and rooftop SolarDuct products. The SolarWall is a proprietary solar air-heating system that can heat buildings using the ventilation air, and is usually mounted on walls or roofs for various purposes, including heating for buildings and running agricultural and manufacturing drying processes. The SolarWall is a PV/T combined system that has a significantly lower payback period than a standard PV panel. It can produce up to 400% more usable energy than an individual PV panel. The SolarDuct PV/T is a modular rooftop system with total operational efficiency of above 50%, where the thermal panels have doubled the output from the PV racking system. **Fig. 2-15** indicates the product series available from this company [2.87].

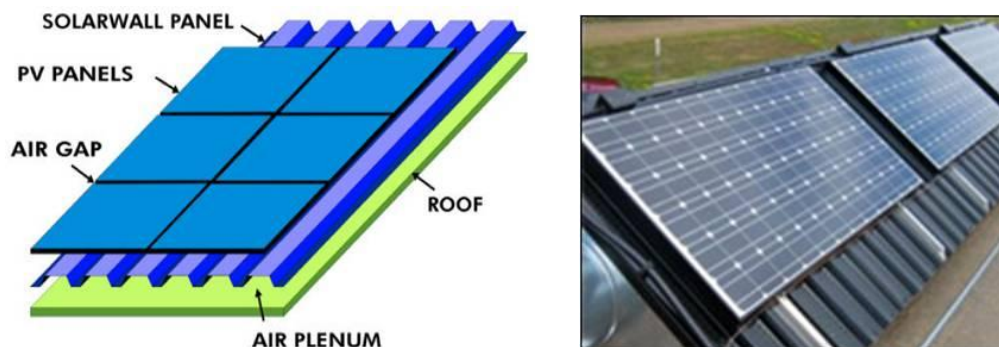


**Fig. 2-15: Solar air PV/T products from Conserval Engineering**



The Dutch-based PVTWINS company has developed PV/T water-heating products for a niche market, as shown in **Fig. 2-16** [2.88]. The PV/T water collectors can be used in individual and integrated domestic hot water systems. This PV/T type can achieve a temperature as high as 90 °C. The electrical yield is measured with 125 Wp/m<sup>2</sup> and the thermal yield is about 1.2 GJ/m<sup>2</sup> per year. The PV/T collectors have three available sizes e.g., 1800 × 1800 mm, 900 × 5600 mm and 1800 × 2400 mm, and are suitable for being integrated into tilted or flat roofs using a common connection method.



**Fig. 2-16: PV/T liquid collector – the PVTWIN produced by PVTWINS**

Israel-based Millennium Electric Ltd has developed a MULTI SOLAR PV/T System that enables the conversion of solar energy into thermal and electrical energy simultaneously using a single hybrid system, as shown in **Fig. 2-17** [2.89]. The Multi Solar System is made of façade/roof tile-like panels which behave as a ‘living’ skin around a building, allowing the flow of water to chill the PV cells, capture heat and store it in an insulated tank, thus enabling the heat control of a living environment. The system can generate 30% higher PV efficiency for domestic electricity.



**Fig. 2-17: MULTI SOLAR PV/T System produced by Millennium Electric**

In terms of PV/T concentrators, there are three leading manufacturers in the world, namely, Absolicon in Sweden, Menova Energy in Canada, and Heliodynamics in the UK. Absolicon has produced the X10 PV/T commercial heat and power system, as shown in **Fig. 2-18** [2.90]. The system consists of a cylinder-parabolic reflector that concentrates ten times the amount of solar light onto the receiver. It is equipped with the latest generation of PV technology and a solar tracking system using electrical custom-designed high-quality linear actuators. The aim is to rotate the X10 concentrator to allow sunlight to be focused onto the cells all the time. The tracking system has a program that can automatically protect the photovoltaic cells from being overheated or from storms. If the temperature exceeds a certain value, the X10 automatically turns the receiver away from the sun.

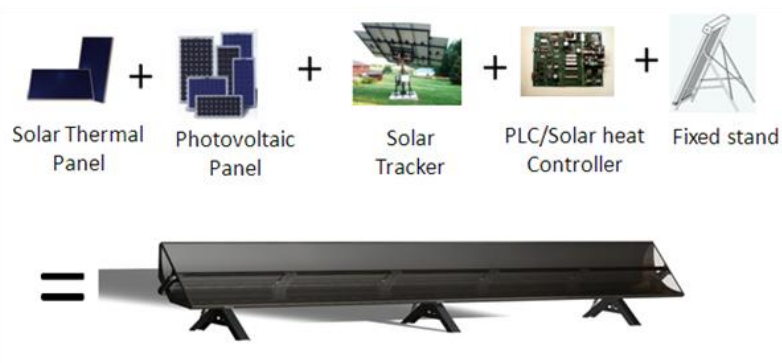


**Fig. 2-18: X10 PV/T system produced by Absolicon**

Menova Energy provides the Power-Spar PV/T concentrator for use in domestic applications, as shown in **Fig. 2-19** [2.91]. The Power-Spar model has been specifically engineered to provide an enhanced performance, even when exposed to extreme winter conditions.



**Fig. 2-19: Power-Spar produced by Menova Energy**

HelioDynamics provides a tracking PV/T Fresnel concentrator, namely the Harmony HD 211, as shown in **Fig. 2-20** [2.91]. It is designed for both flat/sloping roofs and can be pole-mounted over parking areas at the mid-latitudes ( $20^{\circ}$  to  $40^{\circ}$ ).



**Fig. 2-20: Harmony HD211 produced by HelioDynamics**

Ventilated PV with heat recovery is a type of PV/T air collector system that has recently emerged. The system is designed to provide solutions to ventilating PV cells and utilising the PV heat to preheat the ventilation air. Standardised products for this purpose have been manufactured by Secco Sistemi, an Italian PV manufacturer, as shown in **Fig. 2-21** [2.91]. This system type has been used in various engineering projects, including the Fiat Research Centre, the Imagina Studio in Barcelona, and the Professional Training Centre in Casargo.



**Fig. 2-21: Ventilated PV with heat recovery produced by Secco Sistemi**

### 2.3.3 Analysis of the Reviewed Works

A significant quantity of research works related to PV/T technology was found, although the above case-by-case statement may be too scattered to capture the main sense of this subject. To enable clear justification of the research progress and engineering practice in PV/T, the above works were further analysed from two angles: (1) system type and (2) research methodology.

#### (1) Analysis of Research Works in Terms of PV/T Type

In terms of the PV/T types, the research falls into four categories: (1) air-based PV/T; (2) water-based PV/T; (3) refrigerant-based PV/T; and (4) heat-pipe-based PV/T technology. Of these systems, the air- and water-based types are relatively mature and have already been widely used in practical projects. The refrigerant- and heat-pipe-based systems are still at the research/laboratory stage and some technical/economic barriers remain.

##### *I. Air-based PV/T Technology*

Air-based PV/T is one of the most commonly used PV/T technologies and has been developed into commercial units and used in many engineering practices. This type of system usually comprises (1) commercial laminated PV modules; (2) specially-designed air flow channels/ducts; (3) active fans; and (4) air-handling units or air/air heat exchangers [2.85, 2.87]. The most common unit configuration and material is the integrated frameset of an aluminium absorber and lamina-separated channels with either the presence or absence of built-in commercial PV cells [2.85]. The relation between the various solar efficiencies and the external/operational conditions is presented in **Fig. 2-22** [2.17].

In summary, a typical air-based PV/T type can achieve up to 8% electrical efficiency and 39% thermal efficiency [2.17]. Its performance is largely dependent upon air flow speed and temperature. Research relating to this type of PV/T system mainly focuses on (i) studying the most common air flow patterns e.g., buoyancy-driven and forced flow; (ii) determining the optimised channel geometry and sizes to enable the creation of effective turbulence within the channels; and (iii) selecting the proper glazing modes, e.g.,

uncovered or covered with single/double glass sheets. The major problem with the air-based system lies in its relatively poor heat removal effectiveness owing to the low thermodynamic properties of air, such as density, specific heat capacity and thermal conductivity.

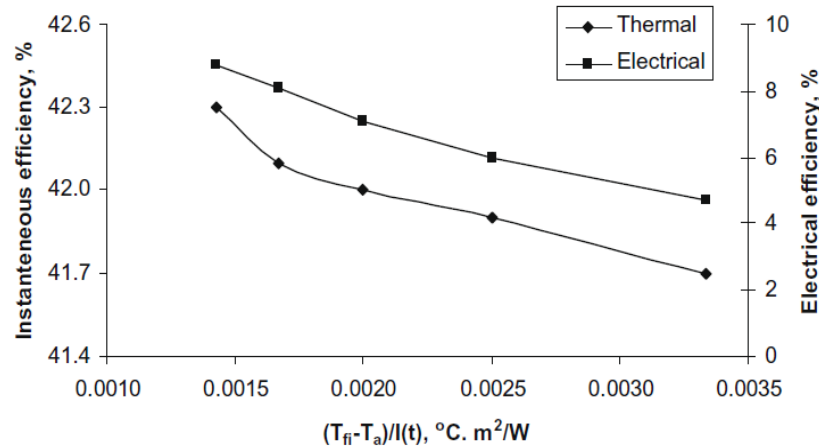


**Fig. 2-22: Correlation between module efficiencies and external/operational conditions represented by  $(T_n - T_a)/I$**

## II. Water-based PV/T Technology

Water-based PV/T is another common solar thermal and power cogeneration device, and has gained in practical use over recent years. Numerous commercial products have emerged on the market and the most impressive examples include the PVTWIN series products by PVTWINS, and MULTI SOLAR by Millennium Electric. The performance of water-based PV/T technology is usually indicated by its electrical and thermal efficiencies, which are found to vary with the water temperature, flow rate, water flow channel geometry and sizes and PV type, as well as external climatic conditions. The most common unit configuration is a PV module with single glazing and a sheet-and-tube absorber integrated in an insulated aluminium frame. This is regarded as the most promising design as it has relatively high overall efficiency and is easy to construct [2.88]. The correlation between the solar efficiencies and the external/operational conditions is given in **Fig. 2-23** [2.18], and was established based on the fixed geometric conditions and PV type.

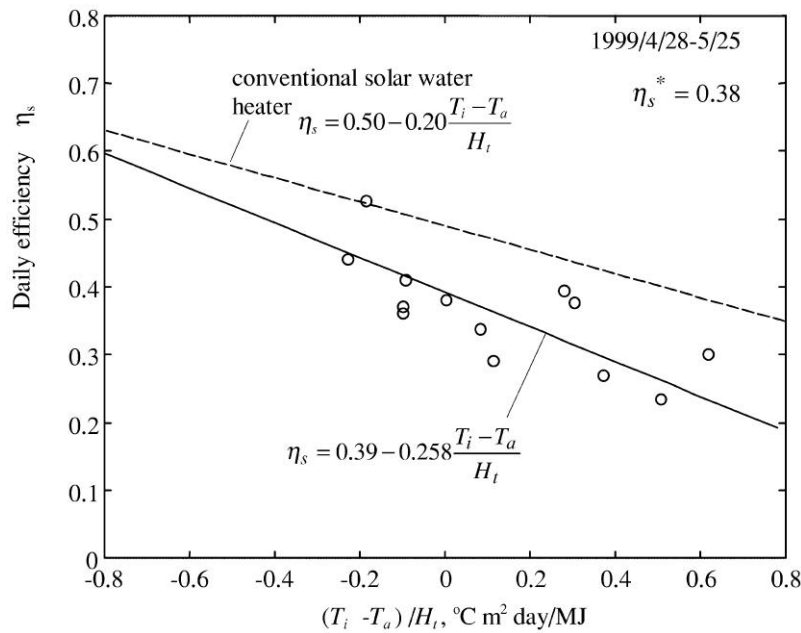


**Fig. 2-23<sup>2</sup>: Correlation between daily testing of efficiency and external/operational conditions represented by  $(T_i - T_a)/H_t$**

In summary, a typical water-based PV/T type can achieve up to 9.5% electrical and 50% thermal efficiency [2.18]. Its performance is largely dependent upon water temperature, flow rate, water flow channel geometry, PV type, and external climatic conditions. Research related to water-based PV/T systems usually focuses on (i) determining appropriate water flow velocity and temperature; (ii) optimising water flow channel geometry and size; and (iii) suggesting configurations for the integrated PV/T panels, including the covers, the PV cells and their connections.

In comparison with an air-based PV/T type, a water-based PV/T system could improve the electrical efficiency of PV modules and, therefore, increase solar heat energy utilisation. However, the improvement is limited due to some inherent technical difficulties. Firstly, the heat removal effectiveness of water is poor in practice as the water continuously rises in temperature over the operating period and fails to improve the solar efficiency when operating at a high water temperature; secondly, additional back-up heating devices (to achieve the required water temperature) would increase the complexity of the

<sup>2</sup> Note:  $H_t$ : daily solar radiation;  $\eta_s$ : characteristic efficiency of solar energy.

system and reduce its efficiency. Further, freezing may be a problem when the system operates in a cold climatic region.

### III. Refrigerant-based PV/T Technology

Refrigerant-based PV/T is a recently emerging technology and research into this subject shows that this type of device could improve the solar utilisation rate significantly over the air- and water-based systems and, therefore, has the potential to replace the two former systems in the near future. The system usually operates in conjunction with a heat pump, and its performance is justified by the electrical and thermal efficiencies of the PV/T modules and the COP of the PV/T heat pump system. These parameters (efficiencies and COP) vary with the flow rate of the refrigerant, its preset evaporation and condensation temperature/pressure, flow channels, geometric sizes, PV type and external climatic conditions. The most common configuration is to attach a PV module to the front surface of an aluminium fin plate with a section of serpentine copper coils between the two layers [2.19, 2.65]. The interrelation between the solar efficiencies and the external/operational conditions is shown in **Fig. 2-24** [2.7], which was developed on the basis of the fixed geometric conditions and PV type.

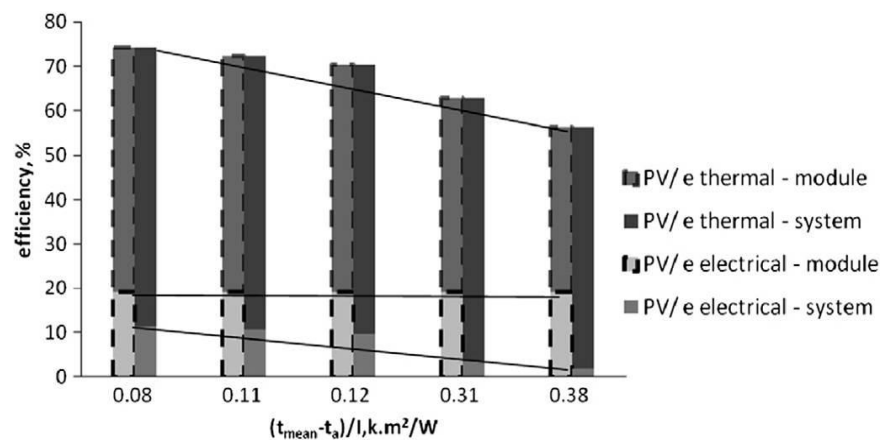


**Fig. 2-24<sup>3</sup>:** Correlation between module efficiencies and external/operational conditions represented by  $(T_{mean} - T_a)/I$

<sup>3</sup> Note: PV/e: photovoltaic/evaporator;  $T_{mean}$ : mean PV temperature;  $T_a$ : air temperature.

In summary, a typical refrigerant-based PV/T type can achieve up to 10% electrical and 65% thermal efficiency [2.19]. Research relating to refrigerant-based PV/T systems usually focuses on (i) determining appropriate refrigerant type, flow rate, evaporation/condensation temperature and pressure; (ii) optimising flow channel geometric sizes; and (iii) suggesting a system configuration, including the panel configuration e.g., covers, PV cells, the combination of PV modules and refrigerant channels, and the connection between the PV/T panels and the heat pump.

In comparison with air-/water-based systems, a refrigerant-based system could significantly improve the electrical efficiency of PV cells and increase solar heat energy utilisation. This initiative represents a step forward in PV cooling technology but its practicality still faces many challenges: for example, the refrigerant piping cycle needs a perfect seal in order to maintain various pressures in different sections to prevent air being sucked into the system during operation, which is very difficult to achieve owing to the large number of welding joints. There are also high risks of refrigerant leakage and the problem of achieving balanced refrigerant distribution across the multiple coils installed in a large PV panel area is technically difficult.

#### ***IV. Heat-pipe-based PV/T Technology***

Heat-pipe-based PV/T is also a relatively new technology and research into this subject is very limited. To date, flat-plate and oscillating heat pipes have been studied for potential use in PV cooling and the results indicate that heat pipes may have the potential to overcome problems existing in a refrigerant-based system, e.g., the possible leakage of refrigerant, an imbalance in the distribution of refrigerant flow, and the difficulty of retaining pressurisation or depressurisation states in different parts of the system.

This system usually operates in conjunction with a heat pump or a heating cycle, and its performance is justified by the electrical and thermal efficiencies of the PV/T module and the heat pipe heat transfer capacity. These performance parameters vary with the structure/material and vacuum degree of the heat pipe, the type of heat pipe working fluid, the temperature and flow rate



of the secondary fluid, PV type and external climatic conditions. The most common unit configuration is a commercial PV module attached to aluminium flat-plate heat pipes while its headers are located in a water manifold. The interrelation between the solar efficiencies and the running time is presented in **Fig. 2-25** [2.13], which was developed on the basis of the fixed geometric conditions and PV type.

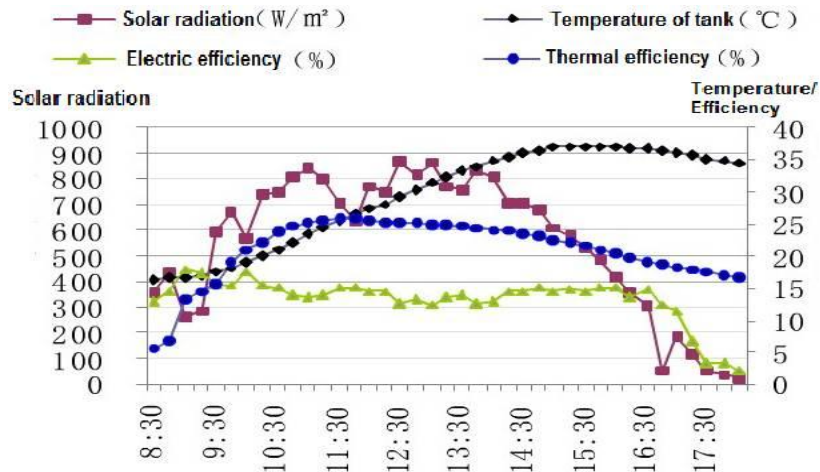


**Fig. 2-25: Variation of full-day testing efficiency versus operating time**

In general, a typical heat-pipe-based PV/T type [2.13] can achieve up to 10% electrical and 58% thermal efficiency. Research relating to heat-pipe-based PV/T systems mainly focuses on (i) determining appropriate heat-pipe structure/material and vacuum degree, heat pipe fluid type and volume, and the flow rate and inlet temperature of the secondary fluid; (ii) optimising heat pipe geometry; and (iii) suggesting a configuration for an integrated PV/T and other heat removing system, including panel configuration, e.g., the covers, PV cells, the combination between the PV modules and heat pipes, and the connection between the PV/T panels and the secondary fluid cycle.

In comparison with a refrigerant-based system, a heat-pipe-based system could achieve an equivalent performance if the heat pipes operate at an adequate temperature. This system may overcome the difficulties that exist in a refrigerant-based system and become the next generation of technology for removing heat from PV cells and effectively utilising this part of the heat. However, this system type also has some disadvantages that require further

resolution, e.g., the high cost of heat pipes and reliable control of heat pipe performance.

## **(2) Analysis of Research Works in Terms of Research Methodology**

In terms of research methodology, the research results can be classified into (i) theoretical analysis and computer modelling, (ii) experimental study, (iii) combined modelling and experimental study, (iv) economic and environmental analysis, and (v) a demonstration of the technology and a feasibility study.

### ***I. Theoretical Analysis and Computer Modelling***

Many pieces of theoretical research have been carried out in terms of a performance study of PV/T modules and the associated heat and power system. These works are dedicated to: (1) revealing the temperature distribution across the various layers of the PV/T modules and the energy (heat and power) conversion mechanism; (2) optimising the structural/geometric parameters of the PV/T modules, including constitution, connection, and geometric shapes and sizes; and (3) recommending the optimum operational conditions, e.g., fluid flow rate, temperature and pressure.

Theoretical works so far have covered (1) simple analytical models addressing heat transfer and heat balance across different parts of the PV/T modules and module-based energy systems [2.49, 2.50]; (2) one-dimensional thermal models derived from a conventional solar thermal flat-plate collector with the inclusion of PV electrical yields [2.51-2.54]; (3) two-/three-dimensional models addressing the energy transfer and distribution across PV/T modules and module-based energy systems [2.63, 2.65]; (4) transient energy models simulating the dynamic characteristics of PV/T modules and module-based energy systems [2.57, 2.72]; and (5) energetic and exergetic analytical models to study the overall energy utilisation performance of integrated systems [2.44, 2.93].

In summary, the established theoretical models have sufficient breadth and depth to reveal the nature of PV/T technology and predict its performance, and

to optimise further the system's configuration and suggest optimum operational conditions. Further work in this methodology category may fall into a dynamic performance study of a system under long-term operational conditions e.g., seasonal and annual schemes.

## ***II. Experimental and Combined Modelling/Experimental Study***

Experimental studies, running from individual modules to whole system schemes, have measured various operational parameters, including temperature, flow, and heat and power conversion rates. The aims are to (1) reveal the practical performance of PV/T components and associated systems under specified operational conditions; (2) examine the reliability and accuracy of established computer models and provide clues for further modification; and (3) establish the correlation between theoretical analysis and practical application.

The experimental and combined modelling/experimental works completed so far cover (1) PV electrical efficiency and its relevance according to various operational parameters, especially PV temperature [2.18, 2.47, 2.55]; (2) the heat removal effectiveness of various cooling media e.g., air, water, refrigerant and heat pipe fluids [2.17, 2.64, 2.19, 2.13]; (3) the temperature and fluid flow characteristics of PV/T modules and module-based energy systems [2.94, 2.95]; (4) the thermal and electrical conversion rates of PV/T modules and their associated energy systems [2.75, 2.96]; (5) comparison between and error analysis of modelling results and experimental data [2.61, 2.65]; and (6) the validation, accuracy analysis, tuning and modification of a computer model [2.55].

In summary, the experimental and combined modelling/experimental works are also very substantial, and have found reasonable agreement with most theoretical results. These works also provide feasible approaches to leading the theoretical findings towards practical applications. Further work may lie in the measurement of system performance under long-term conditions.

### ***III. Economic and Environmental Analysis***

Some research works have focused on the economic and environmental analysis of PV/T technology by comparing its performance against that of independent PV and solar thermal technologies. In terms of economic issues, simple payback time and life-cycle cost are addressed, taking into account primary fossil fuel energy saving and increases in capital cost and maintenance cost needed during system operation. In terms of environmental issues, life-cycle carbon emission reduction, energy payback time and greenhouse gas payback time are calculated to justify the environmental benefits of the system.

Works related to economic and environmental analysis cover (1) PV/T energy-saving potential, its augmented cost, estimated payback time and life-cycle cost saving [2.47]; (2) PV/T life-cycle carbon emission saving, energy payback time and greenhouse gas payback time [2.47]; and (3) comparison between different PV/T configurations, PV and solar thermal alone and separately laid PV and solar-thermal arrangements [2.6, 2.7].

In summary, economic and environmental analysis works are adequate for indicating the performance of PV/T technology in terms of its economic and carbon benefits. Further work may focus on long-term (seasonal and annual) analysis of the system's performance by taking into account the influence of climatic conditions.

### ***IV. Demonstration and Feasibility Study***

Although PV/T technology has been used in many practical projects, there has been very little reporting found that focuses on assessing the long-term performance of PV/T technology under real climatic conditions, and, consequently, the feasibility of the system in practice as a long-term measure has not yet been fully studied.

#### **2.3.4 Summary of the Current PV/T Research and its Potential Challenges**

The established research into PV/T technology so far is substantial and usually aims to (1) reveal the nature of the energy transfer and conversion occurring in

PV/T modules and module-based systems; (2) identify the optimal system type; (3) optimise the structural and geometric parameters of PV/T systems and suggest appropriate operational conditions; (4) build the link between theoretical analysis and practical application; and (5) analyse the economic and environmental benefits of PV/T systems and study their feasibility. All these efforts will contribute to develop a PV/T system that is as efficient as possible for the least cost and with the simplest structure.

Although numerous pieces of research have been carried out in the field of PV/T technology, these systems still face various inherent technical barriers, such as inefficient heat removal effectiveness, the higher temperature of the working fluid, potential freezing, risk of fluid leakage and an imbalance in liquid distribution. Air-based PV/T modules have the least heat removal effectiveness owing to their low thermodynamic attributes. Water-based PV/T modules face barriers of a continuous increase in water temperature over the operating period and freezing potential in cold climates. Refrigerant-based PV/T systems are also not ideal solutions, as they have several practical challenges, including the high risk of refrigerant leakage and uneven refrigerant distribution across multiple coils in a large area. Heat-pipe-based PV/T systems have recently been proposed but still require further investigation. Additional challenges may lie in the long-term reliability of PV/T operations in real climate conditions.

## **2.4 Potential Opportunities in the Development of PV/T Technology**

### **2.4.1 Reducing Thermal Resistance between PV Modules and Thermal Absorbers**

The most common method of fabricating a PV/T module is to glue commercial PV lamination to a thermal absorber. This will normally lead to high thermal resistance between the PV module and the thermal absorber due to the non-conductive Tedlar-Polyester-Tedlar (TPT) baseboard, which will thus reduce the overall PV/T performance. In comparison with a conventional TPT

baseboard, a treated aluminium-alloy (Al-alloy) sheet can be considered an ideal replacement for integration with PV cells, as it has the advantages of much higher thermal conductivity (144 W/m-K versus 0.648 W/m-K), higher solar absorptance (5% versus 2%), lower solar transmittance (0.2% versus 12.8%) and lower reflectance of solar beams in the wavelengths of 340-1100 nm [2.97]. In this thesis, an Al-alloy sheet was utilised for the PV baseboard to accelerate heat transfer at the back of the PV cells.

### 2.4.2 Developing a Heat-pipe-based Thermal Absorber

Existing PV/T types have been found to have a number of disadvantages that prohibit wide application in practice. The opportunity for developing new PV/T technology remains open. A heat-pipe-based system is still in the start-up stage and there is a large area of space to explore. Heat pipes have specific characteristics to overcome some of the technical barriers in existing PV/T technology, such as a large heat transfer capacity, the availability of anti-freezing media, hermetically sealed loops, and homogeneous capillary force. A heat pipe is a perfectly sealed container with no joints and connections; by virtue of trapping a small amount of anti-freezing fluid inside, there is no leakage or freezing during its operation. Heat pipes also have equivalent capillary forces, which allows the entire system to achieve an even fluid distribution.

A loop heat pipe (LHP), as a special type of heat pipe, is famous for its large capacity for remote and passive heat transfer by circulating the working fluid in a closed loop. **Fig. 2-26** illustrates a basic LHP construction. An LHP has a separate configuration of vapour and liquid transportation lines without entrainment between the two-phase flows, which leads to a large heat flux transported across a long distance [2.98-2.101]. Such features enable the wide application of LHPs in the thermal control of satellites, spacecraft, electronics, lighting, and cooling/heating systems [2.102-2.105]. Combining a gravitational LHP and a solar heat collecting system was recently proposed in order to transport solar heat from a building's exterior to its interior [2.106].

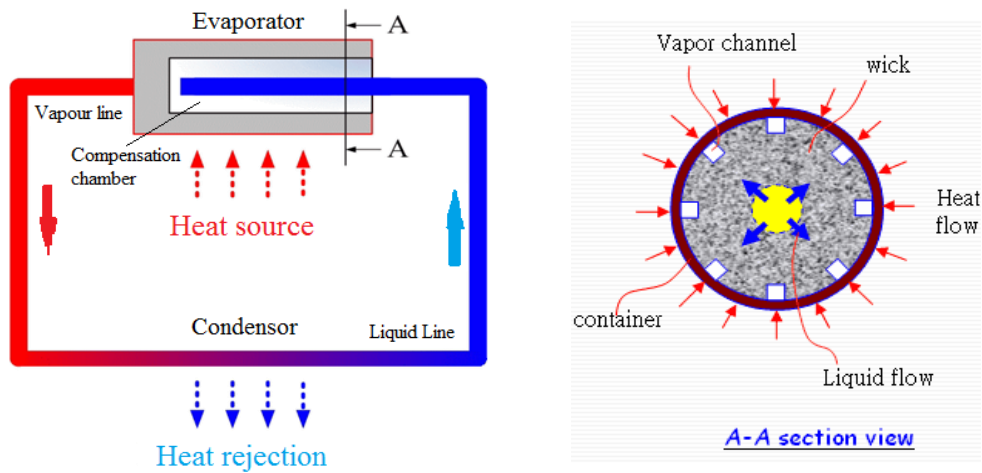


Fig. 2-26: Schematic of a typical LHP and its evaporator

However, conventional gravitational LHPs usually face a common ‘dry-out’ phenomenon on the top wick surface due to the limited capillary force for liquid elevation [2.101]. In this thesis, a novel LHP structure with the top-positioned vapour-liquid separation device was therefore proposed to overcome the above difficulty. This new LHP structure can be placed under the PV layer to form a new modular PV/LHP module. A heat pump was also coupled with a PV/LHP module with the expectation of controlling the PV cells at a relatively low working temperature, which should help to reduce thermal loss from the module to the surroundings and, therefore, increase the total utilisation rate of solar energy for heat and electricity production. **Fig. 2-27** illustrates the relationship between the proposed concept and existing PV/T technologies.

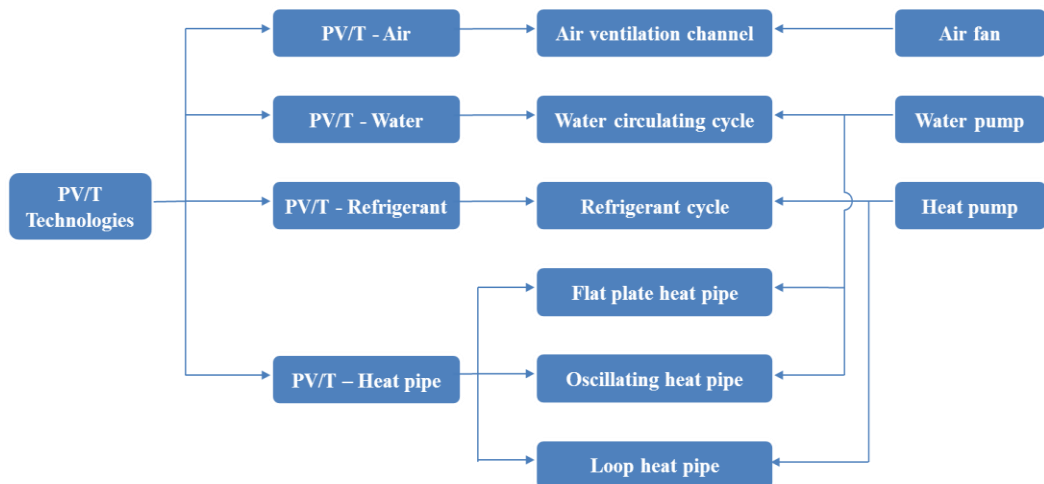


Fig. 2-27: Schematic of the PV/T module and the systems network

### **2.4.3 Developing a Full Range of Computer Simulation Models**

Previous PV/T researchers have normally developed one or two independent simulation models for their investigation. A full range of computer simulation models needed to be developed for a comprehensive investigation of the proposed PV/LHP technology. These models included (1) an analytical model of the heat transfer capacity of the thermal absorber; (2) a steady-state model of the heat transfer and heat balance across different system components; (3) a transient energy model for system dynamic performance; and (4) an analytical model of the life-cycle cost and carbon saving. Such theoretical models were utilised to reveal the nature of the PV/LHP technology, optimise its configuration, enable the recommendation of appropriate operational conditions, evaluate system performance under real climate conditions, and predict the system's economic and environmental benefits.

### **2.4.4 Evaluating System Performance in Real Climatic Conditions**

The steady-state performance of various PV/T systems has been studied comprehensively by a number of researchers from both theoretical and experimental aspects. However, an evaluation of the PV/T systems under real climatic conditions has not yet been fully examined. This work retains certain challenges, however, as there are several uncertain factors, including dynamic weather conditions, thermal adaptability in different climate zones and system robustness. Combined theoretical and experimental study may enable a feasible solution to this study.

### **2.4.5 Demonstrating System Operation in Practical Buildings**

Although PV/T technology has been applied in many practical projects, few reports have been found that focus on the assessment of system performance under operation in real buildings. Further research could be carried out on this point by installing and monitoring PV/T systems in practical buildings. This would allow the assessment of a system's real performance and commercialisation potential. This work could follow up the research outcomes for commercial application.



## 2.5 Development of the PV/T Technology in the PhD Project

In summary, in accordance with the previous research results and future potential opportunities in the development of PV/T technology, this PhD project would address the following aspects: (1) reducing the thermal resistance between the PV panel and the thermal absorber through application of a coated Al-alloy sheet as the PV baseboard; (2) developing a novel LHP as the thermal absorber; (3) developing a full range of computer simulation models, including initial concept design, optimisation of the PV/LHP configuration, evaluation of PV/LHP energy performance and socio-economic analysis of the PV/LHP technology; and (4) investigating the PV/LHP technology under both laboratory and real climatic conditions. These works were intended to achieve the systematic development of a new PV/T technology and cover some of the points missing in the previous research. The research results will contribute a certain added value to the development of PV/T technology.

## 2.6 Chapter Summary

A critical review into R&D works and the practical application of emerging PV/T technology has been carried out. The results of the work helped to understand the current status of PV/T technical development, identify potential difficulties and barriers remaining in this sector, develop potential research topics/directions to improve the performance of PV/T technology, establish associated strategic plans, standards and regulations of PV/T design and installation, and promote its market exploitation throughout the world.

PV/T module has various structures. Currently available PV/T configurations could be classified as air-, water-, refrigerant- and heat-pipe-based types. The technical performance of a PV/T system is usually evaluated by its energetic and exergetic efficiencies, whereas economic performance and environmental benefit are measured by life-cycle cost saving, payback time, life-cycle carbon saving or energy payback time, and greenhouse gas payback time.

Air-based PV/T is one of the most commonly used PV/T technologies and has been developed in commercial units and used in a number of engineering practices. This type of system can achieve up to 8% electrical and 39% thermal efficiency, and its performance is largely dependent on air flow speed and temperature. The major problem with air-based systems lies in their relatively poor heat removal effectiveness owing to the low thermodynamic attributes of air, such as density, specific heat capacity and conductivity.

Water-based PV/T is also a very popular technology and has applied in many practical projects. This type of system can achieve up to 9.5% electrical and 50% thermal efficiency, and its performance is largely dependent upon water temperature and flow rate, and water flow channel geometric shape and size. Compared to air-based systems, water-based systems could improve the electrical efficiency of PV units and increase solar thermal energy utilisation. However, the scope for improvement is limited by inherent technical difficulties, such as rising water temperature during operation and a complex system layout.

Refrigerant-based PV/T technology could improve the solar utilisation rate significantly over air- and water-based systems and, therefore, has the potential to replace the two former systems in the near future. Such systems usually operate in conjunction with a heat pump, and performance is largely dependent upon the type and thermal/physical properties of the refrigerant and the structural/geometric parameters of the refrigerant flow channels. Refrigerant-based PV/T technology can achieve up to 10% electrical and 65% thermal efficiency. This type of system represents a significant step forward in PV cooling technology but its practicality faces several challenges, such as potential refrigerant leakage, an imbalance in refrigerant distribution across the panel coils, and difficulty in pressure maintenance across the operation duration.

Heat-pipe-based PV/T is also a relatively new technology and its operation is often in conjunction with a heat pump or heat cycle. A heat-pipe-based PV/T system can achieve up to 10% electrical and 58% thermal efficiency, and its performance is largely dependent upon the structure/material and vacuum

degree of the heat pipe, the heat pipe working fluid, the inlet temperature and the flow rate of the secondary fluid. This system may overcome the difficulties in a refrigerant-based system and become the next generation of technology for removing heat from PV cells and effectively utilising this part of the heat. However, this type of system also has some disadvantages that require further resolution, e.g., the high cost of heat pipes and the effective control of heat pipe performance.

The established research in PV/T technology is substantial, and usually aims to (1) reveal the nature of the energy transfer and conversion occurring in PV/T modules and module-based systems; (2) identify common system types; (3) optimise the structural/geometric parameters of PV/T systems and suggest appropriate operational conditions; (4) build the link between theoretical analysis and practical application; and (5) analyse the economic and environmental benefits of PV/T systems and study their feasibility. All these efforts have contributed to developing PV/T systems that are as efficient as possible with the least cost and simplest structure.

Although numerous pieces of research have been carried out in the field of PV/T technology, the industry still faces various inherent technical challenges, such as inefficient heat removal effectiveness, increasing temperature of the working fluid, potential freezing, risk of fluid leakage, and an imbalance in liquid distribution. To overcome these technical barriers, opportunities for further development of PV/T technology have been discussed, including (1) reducing thermal resistance between the PV module and thermal absorber; (2) developing a new heat-pipe-based thermal absorber; (3) developing a full range of simulation models; (4) evaluating system performance in real climate conditions; and (5) demonstrating the system in practical buildings.

The review results helped to (1) identify the technical barriers existing in current PV/T technology, (2) establish a scientific methodology for the PV/T research, (3) propose new research opportunities, and (4) build the research direction for subsequent chapters.

## CHAPTER 3: CONCEPTUAL DESIGN OF THE PV/LHP HEAT PUMP WATER HEATING SYSTEM

### 3.1 Chapter Introduction

This chapter proposes a new PV/T concept for hot water generation by incorporating a coated Al-alloy sheet, an innovative LHP device and a heat pump. It is intended to complete the following tasks:

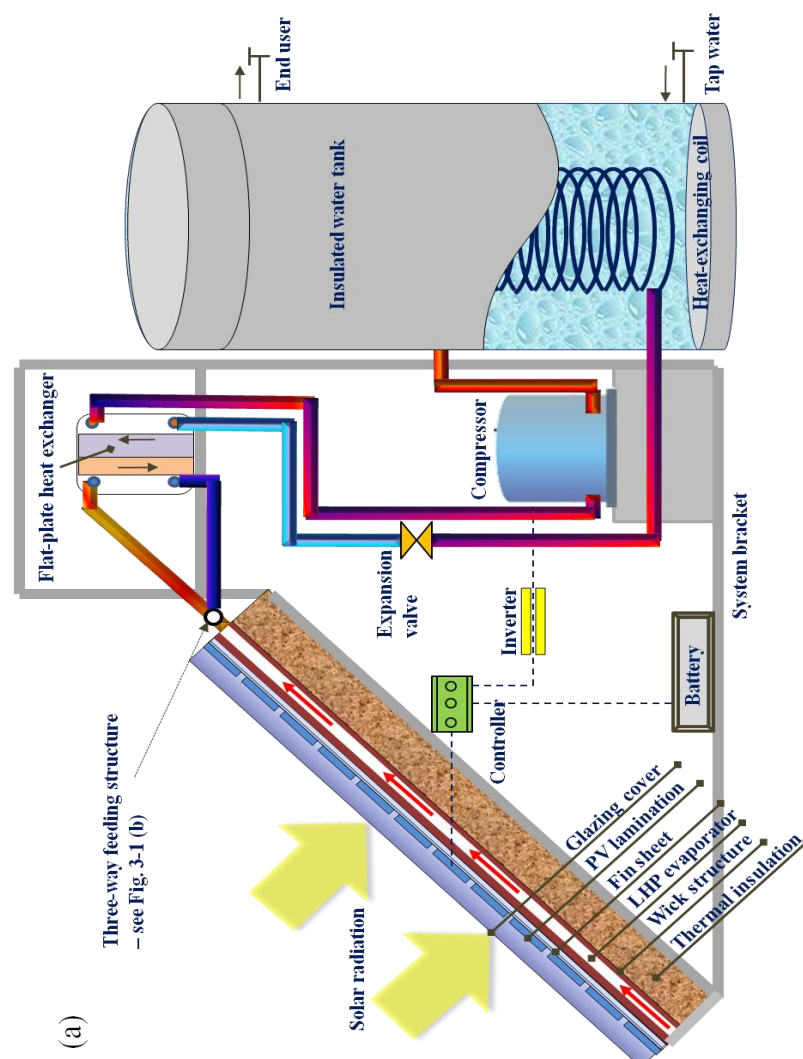
- (1) Present the sketch drawings of the primary system components.
- (2) Describe the basic working principle of the whole system.
- (3) Identify the heat-transfer requirement of LHP absorber for further design, simulation and testing as well as other several parameters relating to the system performance, including design (structure, geometry and materials), and operating and external parameters.
- (4) Provide a parametric design of the different system components for further theoretical analysis, prototype fabrication and experimental testing.

A conceptual design illustrates the precedence for the hypothetical function by the creation of new ideas and builds the fundamental physical structure for the theoretical and experimental investigations in the following chapters.

### 3.2 System Description and Working Principle

The proposed PV/LHP heat pump water heating system is schematically shown in **Fig. 3-1 (a)**. The system comprises a modular PV/LHP collector (entitled 'PV/LHP module'), an electricity control/storage unit, fluid vapour/liquid transportation lines, a flat-plate heat exchanger acting as the condenser for the LHP and the evaporator of the heat pump, a hot water tank, a compressor, a coil-type condenser embedded into the water tank and an expansion valve. The LHP absorber is a specific LHP configured with external fins, internal wicks

and a top-positioned three-way tube (the vapour-liquid separation structure). This pipe enables water evaporation to take place on its inner surface when receiving solar irradiation on the outer surface. To maintain the continuous operation of this process, the top three-way tube is a dedicated design, as shown schematically in **Fig. 3-1 (b)**, for the even distribution of water films across the inner-wall surface of the pipe, thus preventing the ‘dry-out’ potential of water across the wick surface. A piece of ‘ $\lambda$ ’-shaped copper tube with expanded edges is internally connected to a refined three-way copper fitting. When tightly compressing the bottom expander edge against the wick structure, the returned liquid is evenly distributed from the top of the evaporator across the wick surface owing to the equivalent capillary force within the wick structure. The three-way tube, meanwhile, can also deliver the vapour upward to the flat-plate exchanger through the vapour transportation line. This creates a clear separation between the liquid and vapour flows in the heat pipe.



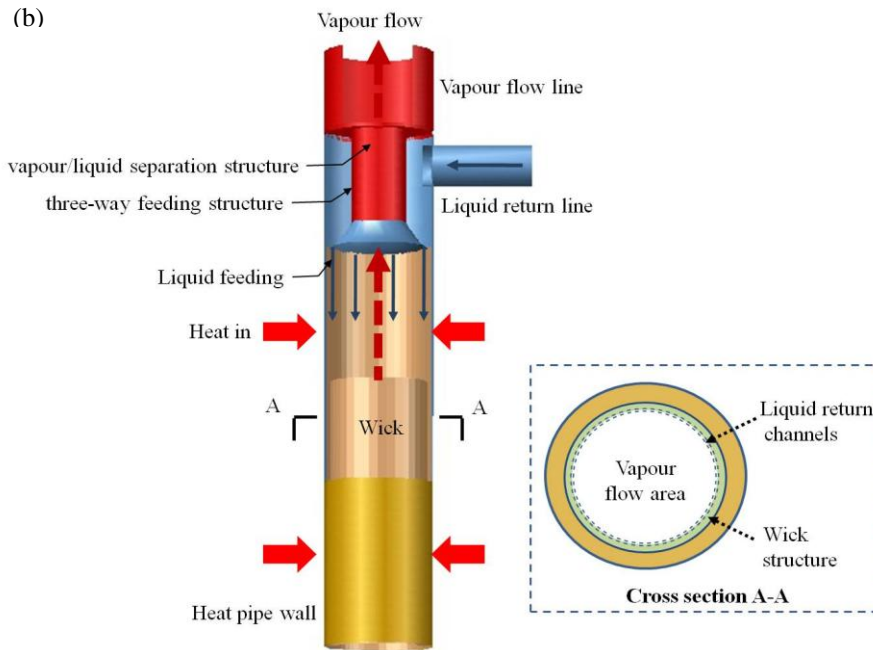


**Fig. 3-1: Schematics of (a) the heat pump-assisted PV/LHP solar water heating system and (b) concept design of the LHP three-way vapour-liquid separation structure**

In the PV/LHP module, the unique LHP device is fitted beneath the PV layer, as shown in **Fig. 3-2 (a)**, in order to extract the heat from the back of PV module and thus reduce the PV cell temperature and increase PV electrical efficiency. During operation, this part of the heat is delivered to the flat-plate heat exchanger through the vapour transportation line, within which heat transfer between the heat pump refrigerant and the heat pipe working fluid occurs. This interaction between the heat pipe fluid and the heat pump refrigerant leads to condensation of the heat pipe working fluid. The condensed liquid returns to the LHP absorber via the liquid transportation line, thus completing the heat pipe fluid circulation. In addition, an Al-alloy sheet coated with anodic oxidation film was also proposed to replace the conventional TPT baseboard of PV cells during the module lamination process in order to increase the overall heat transfer. **Fig. 3-2 (b)** indicates the configuration of the Al-alloy-based PV layer. It consists of clean tempered glass on the top, a group of PV cells in the middle, a treated Al-alloy sheet at the back and two layers of ethylene-vinyl acetate (EVA) sealant to connect all three components.

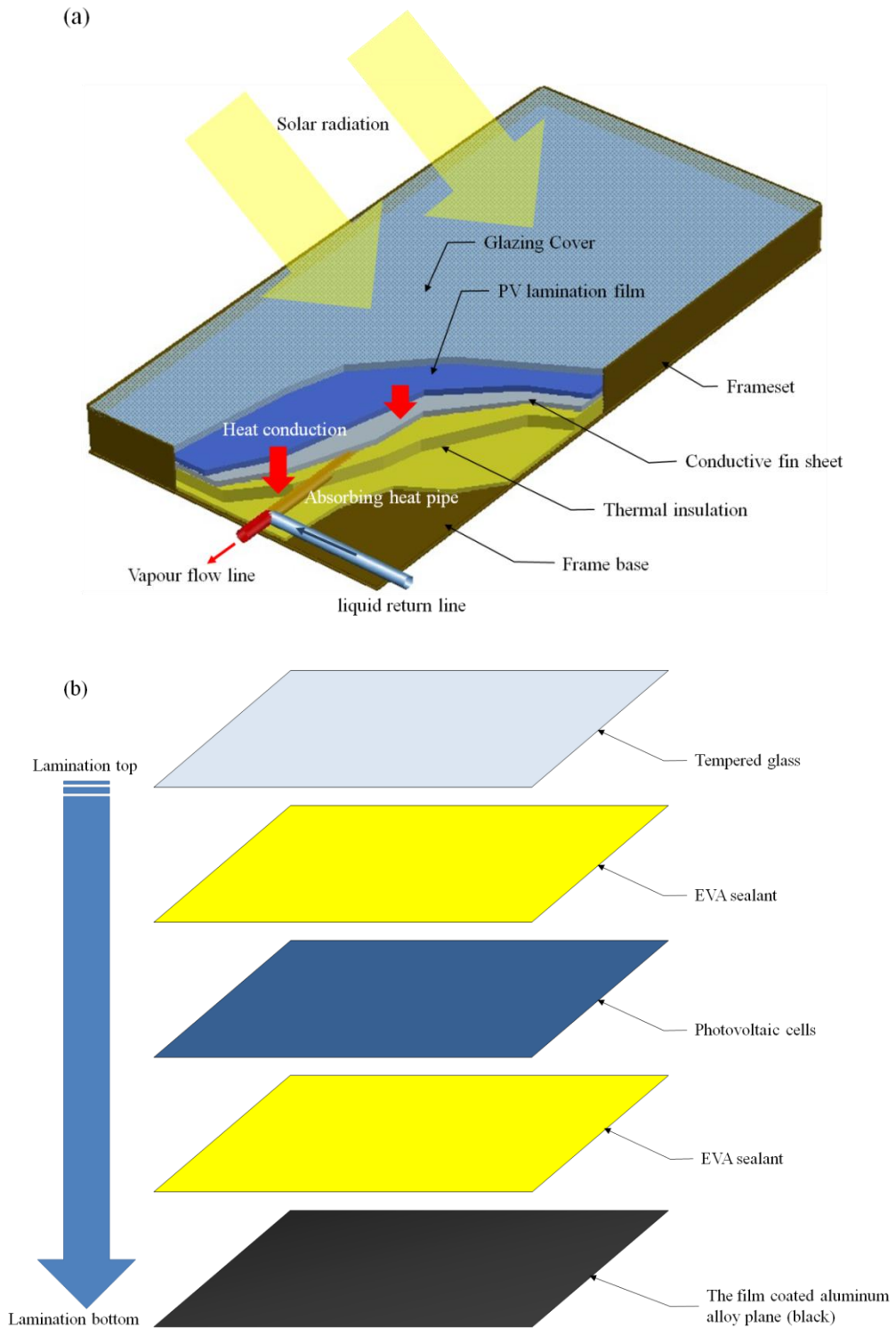


**Fig. 3-2: Concept design of (a) the PV/LHP collector and (b) configuration of the PV layer**

In the heat pump cycle, the liquid refrigerant is vaporised in the heat exchanger, which, under the pressurisation of the compressor, is subsequently converted into higher pressure, supersaturated vapour, and thus transfers heat energy into the tank water via the coil exchanger (condenser for the heat pump cycle),

leading to a temperature rise in the tank water. The heat transfer process within the coil exchanger also leads to the condensation of the high pressure, supersaturated vapour, which, when passing through the expansion valve, is downgraded to a low-pressure liquid refrigerant. This refrigerant undergoes an evaporation process within the flat-plate heat exchanger (the evaporator for the heat pump cycle), thus completing the whole heat pump cycle.

As the essential component of a heat-pump cycle, the mechanical compressor normally has two functions: (1) to deliver refrigerant throughout the heat-pump system and (2) to compress gaseous refrigerant from evaporating pressure to condensing pressure. In practice, once the evaporation and the condensation temperatures are set constantly in a heat pump cycle, the evaporation and the condensation pressures will be fixed accordingly. As a result, the compressor will remain the temperatures and pressures relatively constant, regardless of changing of external conditions, by two alternative methods, i.e. automatically varying the driver speed or simply switching on/off. For instance, as the evaporation temperature grows higher than the settings while receiving the solar radiation continuously, the heat-pump compressor will automatically increase its driving speed to deliver more refrigerant or start up to circulate the refrigerant until the evaporator is cooled down. So essentially speaking, both these two methods is to enable the heat pump ultimately adapted to the external conditions by adjusting the overall mass flow rate of refrigerant (the switching on/off of compressor can also be considered as a special approach to fluctuate the mass flow rate of refrigerant during a certain operation period). The mass flow rate of refrigerant is therefore regarded as the primary parameter that determines the thermodynamic process in the heat pump during the further dynamic simulation and experiments.

A temperature-entropy (T-S) chart based on the thermodynamic cycle of the refrigerant within the heat pump cycle is displayed schematically in **Fig. 3-3**, where the isentropic efficiency is taken into account at the compressor for analysis, as additional power will be consumed in the practical operation.



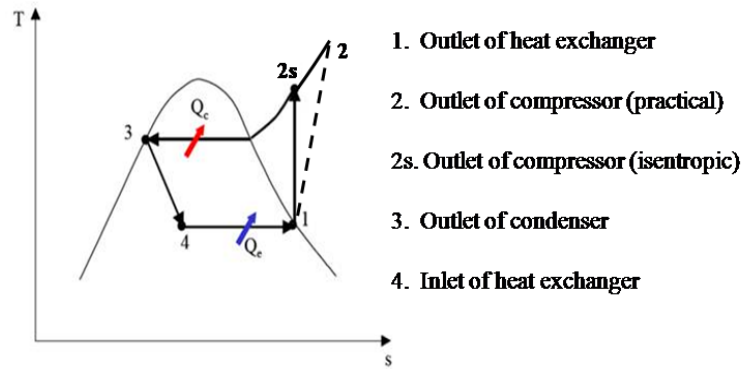


**Fig. 3-3: Heat pump thermodynamic cycle in a Temperature-Entropy chart**

The distinct features of the PV/LHP heat pump system lie in the following: (1) the temperature of the LHP working fluid can be controlled to a lower level through adjustment of the evaporation pressure of the refrigerant in the heat pump cycle; this will lead to reduced PV cell temperature, increased PV electrical and thermal efficiencies, and increased solar output per unit of absorbing surface; (2) the refrigerant temperature/pressure will be increased to the required level using a compressor to enable heat to be transferred from the refrigerant to the hot water; (3) the power desired for compressor operation can be provided by PV-generated electricity if the system is appropriately designed (such as the direct-current powered solar compressors from the Danfoss Company [3.1]), thus creating a low (zero) carbon heating operation. It can be predicted that more or less electricity surplus or deficiency may occur, which could be matched through battery storage or a grid. This system can be installed on a building where the PV/LHP modules could be mounted on the facade or roof. For this application, the heat exchanger could be positioned on the upper side of the modules, while the heat pump is installed inside the building. Alternatively, the system can be installed as an independent heat and power micro-generation unit.

### 3.3 Parameters of the New PV/LHP Heat Pump System

For the new research topic of PV/T technology, a number of parameters were identified for characterisation of the system performance, including: (1) design (structure, geometry and material), (2) operational and (3) external parameters.

These variables were applied for the subsequent theoretical analysis, prototype fabrication and experimental testing, as summarised in **Table 3-1**.

**Table 3-1: Summary of different parameters for further characterisation**

Parameter type	Variables for characterisation	
	Structure	(1) Glazing cover (2) LHP wick type (3) LHP numbers
<b>Design parameters</b>	Geometry	(1) LHP evaporator diameter (2) LHP evaporator length (3) LHP vapour column diameter in three-way fitting (4) LHP evaporator-to-condenser height difference
	Material	(1) PV baseboard
<b>Operating parameters</b>		(1) LHP operational temperature (2) LHP evaporator inclination angle (3) LHP liquid filling mass (4) Heat pump evaporation temperature (5) PV mounting solution
<b>External conditions</b>		(1) Solar radiation (2) Air temperature (3) Air velocity (4) Operating time

### 3.4 Parametric Design of System Components

This section presents the parametric design of the different system components with certain alternative varying ranges, including the glazing cover, PV layer, LHP, fin sheet, flat-plate heat exchanger, heat pump, electrical unit and insulation material. The parametric data will be further applied as the input figures for the modelling and optimisation in subsequent chapters.

#### 3.4.1 Glazing Cover

The glazing cover of the PV/LHP module is significant to the overall absorption of solar energy because it can maximise the amount of solar absorption and minimise heat loss. It also protects the PV/LHP module from external damage. However, increasing the number of glazing covers will have the opposite effect of reducing the input of solar radiation due to the glazing

transmittance. Hence, the relationship between the number of glazing covers and the module energy performance was investigated. There were two different glazing types proposed, as shown below in **Table 3.2**.

**Table 3-2: Alternative parameters for the glazing covers**

Glazing type	Emissivity	Transmittance	Thickness (m)	Conductivity (W/m-k)
Double glazing	0.79	0.85	0.010	1.2
Single glazing	0.89	0.92	0.004	2.4

### 3.4.2 Al-alloy-based PV Layer

In the preliminary design, mono-crystalline PV cells were applied with a total effective absorbing area of  $0.612 \text{ m}^2$ . This layer consisted of 36 ( $4 \times 9$  array) PV cells, each with a size of  $125 \times 125 \times 0.3$  (mm  $\times$  mm  $\times$  mm), and which covered nearly 90% of the baseboard surface. **Table 3-3** gives the design parameters of the PV panel, which had a nominal efficiency of 16.8%. In comparison with a conventional TPT baseboard, the treated Al-alloy sheet can be considered an ideal replacement for integration with PV cells, for it has the advantages of a much higher thermal conductivity (144 W/m-K versus 0.648 W/m-K), a higher solar absorptance (5% versus 2%), a lower solar transmittance (0.2% versus 12.8%) and a lower reflectance of solar beams in the wavelengths of 340-1100 nm [2.97]. The coated Al-alloy sheet was designed to be 0.5 mm thick, which not only served as an electrical insulation device, but also protected the baseboard from corrosion during its life-cycle operation.

**Table 3-3: Design Parameters of the Al-alloy-based PV panel**

Parameters	Nomenclature	Value	Unit
Number of PV cells	$N_{PV}$	36 ( $4 \times 9$ )	-
Packing ratio	$\beta_{PV}$	0.9	-
Nominal efficiency	$\eta_{PV,o}$	16.8	%
Thermal conductivity of Al-alloy	$k_{Al}$	144	W/m-K
Solar absorptance of Al-alloy	$\alpha_{Al}$	5	%
Solar transmittance of Al-alloy	$\tau_{Al}$	0.2	%
Thickness of Al-alloy	$\delta_{Al}$	0.5	mm

### 3.4.3 LHP with Fin Sheet

As the subsequent experiment would be carried out in Shanghai in China, the maximum heat transfer capacity required by the LHP absorber in Shanghai is estimated at about  $730 \text{ W/m}^2$  by assuming the maximum thermal efficiency of 60% of a typical solar thermal collector when the maximum solar radiation striking the south-facing tilted plane reaches nearly  $1328 \text{ W/m}^2$  [3.2].

In the LHP design, the working fluid not only required a high thermodynamic performance, but also an anti-freezing attribute. As a result, a solution of water and glycol (95%/5%) was proposed. A 5 mm thick aluminium  $\Omega$ -type fin sheet wrapped the LHP evaporation section. The LHP wall is a copper material with a high thermal conductivity of  $394 \text{ W/(m-K)}$ . A refined three-way fitting is internally connected with a piece of 'T'-type tube (smaller diameter) serving as the vapour-liquid separation structure. There are three alternative wick structures in this LHP, as shown in **Table 3-4**: screen mesh, sintered powder metal and groove.

**Table 3-4: Alternative wick structures in the LHP evaporator**

Parameters	Nomenclature	Value	Unit
Mesh screen	Wire diameter (layer I)	$D_{owi,ms}$	$7.175 \times 10^{-5}$ m
	Layer thickness (layer I)	$\delta_{owi,ms}$	$3.75 \times 10^{-4}$ m
	Mesh number (layer I)	$N_{owi,ms}$	6299 /m
	Wire diameter (layer II)	$D_{iwi,ms}$	$12.23 \times 10^{-5}$ m
	Layer thickness (layer II)	$\delta_{iwi,ms}$	$3.75 \times 10^{-4}$ m
	Mesh number (layer II)	$N_{iwi,ms}$	2362 /m
	Conductivity	$k_{s,ms}$	394 W/m-K
Sintered powder	Pore diameter	$D_{po,sp}$	$4.47 \times 10^{-5}$ m
	Layer thickness	$\delta_{wi,sp}$	$7.5 \times 10^{-4}$ m
	Porosity	$\varepsilon_{wi,sp}$	0.64 -
	Layer number	$N_{wi,sp}$	1 -
	Conductivity	$k_{s,sp}$	16.3 W/m-K
Rectangular groove	Groove depth	$\delta_{wi,g}$	$7.62 \times 10^{-4}$ m
	Groove width	$W_{wi,g}$	$4.57 \times 10^{-4}$ m
	Groove number	$N_{wi,g}$	44 -
	Conductivity	$k_{s,g}$	394 W/m-K

The liquid fill level is considered to be one-third to one-fourth of the evaporator length [3.3]. The height difference between the LHP condenser and absorber determines the capillary limit due to the gravity effort. The specifications of the loop components are listed in **Table 3-5**.

**Table 3-5: Design parameters of the LHP operation**

Parameters	Nomenclature	Value	Unit
External diameter of evaporator	$D_{hp,o}$	0.014-0.022	m
Internal diameter of evaporator	$D_{hp,in}$	0.012-0.0196	m
Internal diameter of vapour column	$D_{vt}$	0.004-0.018	m
Operating temperature range	$T_v$	20-60	°C
Vacuum pressure in heat pipe	$P_{hp}$	$1.3 \times 10^{-4}$	Pa
Evaporator length	$L_{hp,e}$	1-2	m
Evaporator inclination angle	$\phi_e$	0-90	degree
Evaporator-to-condenser height difference	$H_{hx, hp}$	0.2-1.2	m
Liquid filling mass	$m_{fl}$	0.001-0.045	kg
Transportation line outer diameter	$D_{tl,o} / D_{vtl,o}$	0.022	m
Transportation line inner diameter	$D_{tl,in} / D_{vtl,in}$	0.0196	m
Transportation line length	$L_{tl} / L_{vtl}$	0.65-1.0/0.5-0.9	m
Fin sheet (length/width)	$L_{fin} / W_{fin}$	1.2/0.55	m

**Table 3-6** presents the properties of water at different operating temperature levels [3.4-3.5]. The thermodynamic properties of the water/glycol mixture can be considered to be approximately the same as water when the glycol only accounts for less than 5% of the total liquid volume.

**Table 3-6: Thermodynamic properties of water with operating temperatures**

$T_v$ °C	$h_{fg}$ kJ/kg	$P_v$ Pa	$\rho_v$ kg/m <sup>3</sup> (e-02)	$\rho_l$ kg/m <sup>3</sup>	$k_l$ W/k-m	$\mu_v$ kg/m-s (e-06)	$\mu_l$ kg/m-s (e-04)	$\sigma$ N/m (e-02)
20	2454	2337	1.73	998	0.600	8.84	10.00	7.28
25	2442	3172	2.38	997	0.613	9.03	8.70	7.20
30	2430	4242	3.04	996	0.621	9.22	8.03	7.12
35	2418	5622	4.08	994	0.627	9.42	7.16	7.04
40	2407	7375	5.12	992	0.634	9.62	6.45	6.96
45	2395	9582	6.71	990	0.64	9.82	5.98	6.88
50	2393	12335	8.30	988	0.645	10.00	5.53	6.79
55	2371	15740	10.70	986	0.650	10.20	5.09	6.71
60	2358	19920	13.00	983	0.654	10.40	4.71	6.62

Sample dimensional drawings of the LHP vapour-liquid separation structure and the PV/LHP module are illustrated in **Fig. 3-4**.

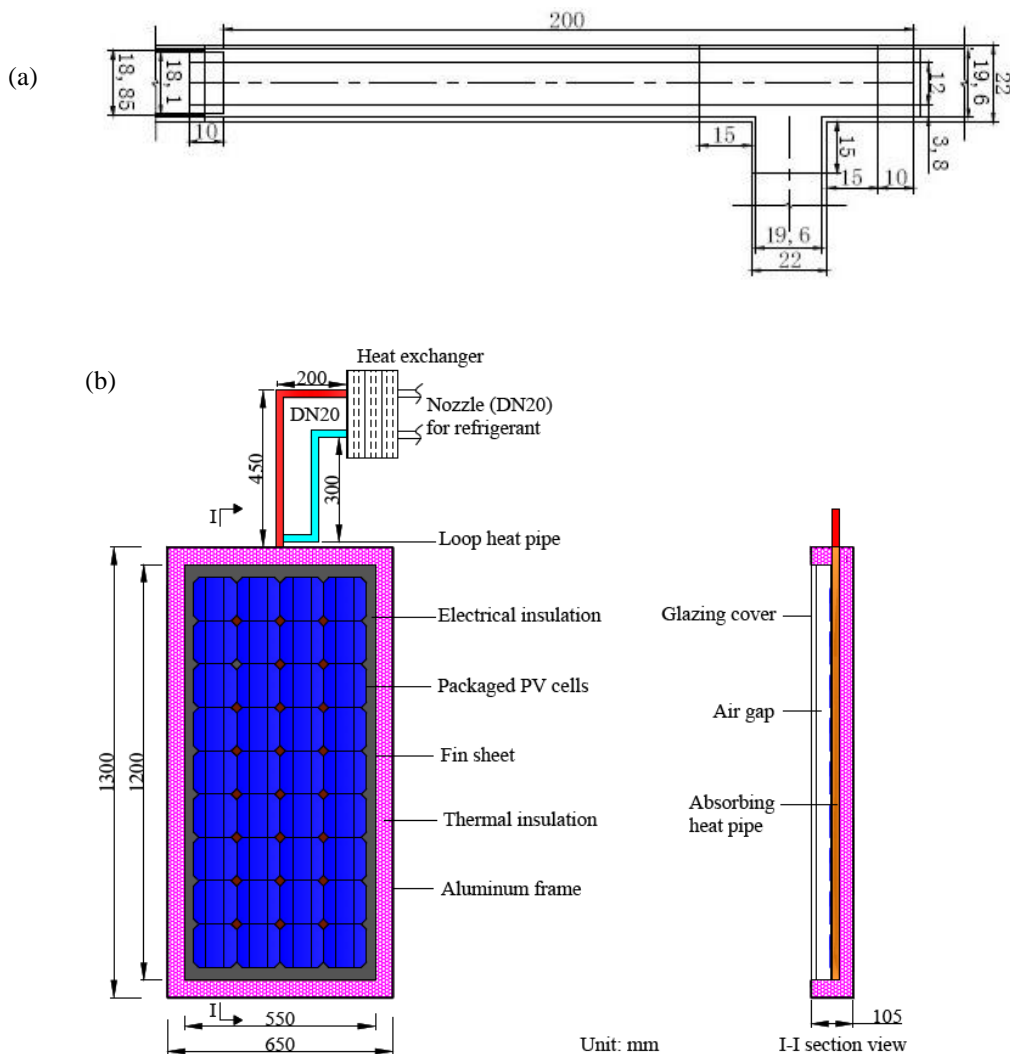


**Fig. 3-4: Dimensional drawings of (a) the LHP liquid-vapour separation structure and (b) the PV/LHP module**

### 3.4.4 Flat-plate Heat Exchanger

A flat-plate heat exchanger is well suited to transferring heat between medium- and low-pressure liquids using layers of plates with a larger surface area. This comprises a series of thin and corrugated thermal plates commonly made of stainless steel, which are compressed together into a frame to form an arrangement of parallel flow channels with alternating hot and cold fluids. The plates are all welded to each other, which reduces the risk of fluid leakage. In comparison to shell-and-tube heat exchangers, plate-heat exchangers require a

lower temperature and smaller size for the equivalent heat exchanged [3.6]. The design of the flat-plate heat exchanger is given in **Table 3-7**.

**Table 3-7: Design parameters of the flat-plate heat exchanger**

Parameters	Nomenclature	Value	Unit
Heat exchanger plate thickness	$\delta_{hx}$	0.00235	m
Heat exchanger plate height	$H_{hx}$	0.206	m
Heat exchanger plate cluster width	$W_{hx}$	0.076	m
Heat exchanger plate cluster length	$L_{hx}$	0.055	m
Heat exchanger number of plates	$N_{hx}$	20	-
Heat exchanger operating temperature range	$T_{hx}$	-160-225	°C
Heat exchanger operating pressure range	$P_{hx}$	0-3.24	MPa

### 3.4.5 Heat Pump

A heat pump is a device that transfers heat energy from a heat source to a heat sink against a temperature gradient through phased changes in the refrigerant. The environmentally friendly R134a was considered as the working fluid in this design. The evaporation and condensation temperatures are set at 0-25 °C and 55 °C, respectively. A water tank with built-in copper heat-exchanging coils is connected to the heat pump, acting as its condenser and hot water storage. The simple thermodynamic properties for each point (1, 2s, 3 and 4 in **Fig. 3-3**) are displayed in **Table 3-8** through the “Allprops” software, which is a special program developed to calculate properties of pure substances (enthalpy, entropy and special heat capacity etc.) for various categories of fluids (cryogenic, hydrocarbons and refrigerant etc.).

**Table 3-8: Sample thermodynamic properties of the R134a refrigerant in the heat pump**

Point	Phase	Pressure (MPa)	Temperature (°C)	Enthalpy(H) (kJ/kg)	Entropy(S) (kJ/kg·K)
1	Vapour	0.5717	20	409.748	1.71804
2s	Vapour	1.4915	58.34	429.449	1.71804
3	Liquid	1.4915	55	279.469	1.26106
4 ( $x^4=0.2853$ )	Liquid/Vapour	0.5717	20	279.469	1.27363

<sup>4</sup> Note:  $x$  means the saturation of refrigerant

### 3.4.6 Electrical Control and Storage Unit

To match the capacity of the PV cells, the electrical control and storage system consisted of a 12 V (10 A) controller, an 800 W DC/AC inverter, a 100 AH (12 V) battery, and connection wires. A schematic of the solar electrical generation system is given in **Fig. 3-5**.

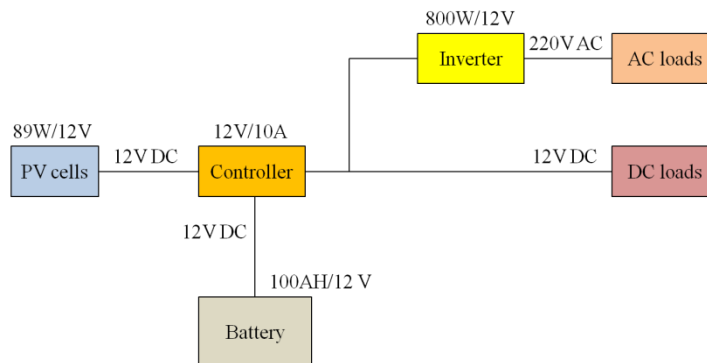


**Fig. 3-5: Schematic of the solar electrical control and storage system**

### 3.4.7 Insulation Material

Insulation materials, such as fibreglass, polyurethane foam and polystyrene board, are applied to minimise the heat loss of the system components. The efficiency of the insulation material is measured by its thermal resistance (R-value). A larger R-value results in higher insulating effectiveness. **Table 3-9** lists the R-values of some insulation materials [3.7].

**Table 3-9: Thermal resistance of typical insulating materials**

Insulating materials	Thermal resistance (K-m <sup>2</sup> /W)
Fibreglass	0.546-0.616
Polyurethane foam	0.986-1.356
Polystyrene boards	0.634-0.933

## 3.5 Chapter Summary

This chapter has described the system concept and its working principles from the aspects of the PV/LHP module, the LHP and the heat pump. The distinct



features of the proposed PV/LHP heat pump system lay in the following: (1) the temperature of the LHP working fluid can be controlled to a lower level through adjustment of the refrigerant evaporation pressure in the heat pump cycle; this would lead to reduced PV cell temperature, increased PV electrical and thermal efficiencies, and increased solar output per unit of absorbing surface; (2) the refrigerant temperature/pressure would be upgraded to the required level using a compressor to enable heat to be transferred from the refrigerant to the hot water; (3) the power desired for compressor operation could be provided by the PV-generated electricity if the system was appropriately designed, thus creating a low (zero) carbon solar heating operation. Any electricity surplus or deficiency could be matched through battery storage or a grid. This system can be installed either on a building facade or as an independent heat and power micro-generation unit.

A number of parameters desired for further characterisation of the system performance were summarised, including the design (structure, geometry and material) and the operational and external parameters. The chapter also presented the parametric design of the different system components with certain alternative varying ranges, including the glazing cover, PV layer, LHP, fin sheet, flat-plate heat exchanger, heat pump, electrical unit and insulation material. As the subsequent experiment would be carried out in Shanghai, China, the maximum heat transfer capacity required by the LHP absorber should be over  $730 \text{ W/m}^2$  (the baseline for further LHP simulation). These parametric data will be applied as the input figures for the modelling and optimisation in subsequent chapters.

## CHAPTER 4: THEORETICAL ANALYSIS AND DEVELOPMENT OF THE COMPUTER SIMULATION MODELS

### 4.1 Chapter Introduction

Based on the established conceptual design, this chapter reports the theoretical analysis and development of the associated computer simulation models. The theories are coupled with the energy balance equations within different parts of the system, including transient solar transmittance, heat transfer, fluid flow and photovoltaic generation. The main works achieved are described in this chapter as follows:

- (1) Three theoretical models were built, respectively, for the LHP heat transfer limits and the system steady-state and dynamic performance.
- (2) The iterative method (IM), backward differentiation formula (BDF or Gear's method) and finite element method (FEM) were applied to solve the mathematical models by means of computer.
- (3) A group of computer-based simulation models were subsequently developed to simulate the performance of the LHP device and the integrated PV/LHP heat pump system
- (4) These simulation models were preliminarily validated by the published test data, indicating that reasonable accuracies could be achieved in predicting the performance of the LHP device and integrated PV/LHP heat pump system.
- (5) Operation of the simulation models led to the optimisation of the geometric configurations and a recommendation for the most appropriate operational conditions for both the LHP device and the entire system.

This part of the work facilitated the foundation of the prototype fabrication and experimental testing, which will be addressed in Chapter 5 and Chapter 6.

## 4.2 Analytical Model for the LHP Heat Transfer Limit

### 4.2.1 Modelling Objective for the LHP Heat Transfer Limit

As the LHP serves as the crucial heat-exchanging device in the integrated system, it will directly affect PV working efficiency and the overall amount of heat absorbed from the solar sources. Analysis of the LHP heat transfer limit was thus required prior to the investigation of the integrated system. Once the maximum LHP heat transfer value was determined, the size and capacity of other system components could be determined. Development of an analytical model for the LHP device enabled (a) maximum heat transfer capacity of the LHP device at the given geometric setting and operational condition; (b) determination of the LHP operational performance against different variables; (c) recommendation of an appropriate LHP design and operational parameters; and (d) determination of the optimum geometric sizes and capacities of other system components.

### 4.2.2 Thermal Fluid Theory and the Associated Mathematical Equations of the LHP Heat Transfer Model

A schematic showing the LHP operation is displayed in **Fig. 4-1**. The LHP device incorporates a unique three-way fitting with an expander to provide homogeneous and swift liquid distribution across the evaporator wick surface. This three-way fitting enables the connection of the LHP evaporator and vapour/liquid transporting lines. With tight compression of the expander edge against the wick, liquid will be evenly distributed across the wick surface. The speed of the liquid film drop will be automatically controlled by the interior vapour pressure, which will be affected by external heat input. Ideally, the liquid flowing across the wick can be instantly evaporated without or with little reservation at the bottom of the LHP evaporator during operation, which will help maximise the heat transport capacity of the LHP. This configuration can create an even distribution of the liquid across the evaporator wick surface, which will result in enhanced heat transfer capacity over conventional LHP systems.

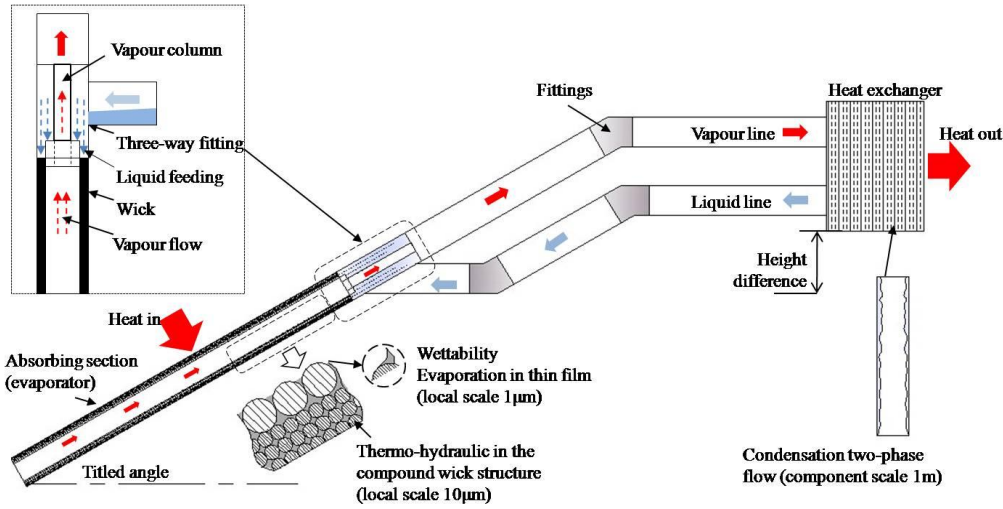


Fig. 4-1: Schematic of the thermal and hydrodynamic couplings in the LHP

In this section, six limits will be discussed in determining the LHP heat transport capacity, i.e., the viscous, sonic, entrainment, capillary, boiling and liquid filling mass limits. The minimum values of these limitations are the actual restraint on the system heat transfer. The magnitudes of these limits are directly related to the thermal properties of the working fluids, wick structures, heat pipe dimensions, and operating conditions, which will be discussed in the following sections.

### (1) Viscous Limit, $Q_{VL}$

At low-temperature operation, the viscous forces dominate the performance of vapour flow. This limit reflects the level of vapour flow for carrying heat [2.100]. Bussel et al. [4.1] initially developed an equation for the viscous limit

$$Q_{VL,e} = \frac{\pi D_{v,e}^4 h_{fg} \rho_v P_v}{256 \mu_v L_e} \quad [4-1]$$

where,  $Q_{VL,e}$  is the viscous limit at the absorbing section (W);  $D_{v,e}$  and  $L_e$  are the diameter (m) and length (m) of vapour space in the absorbing section;  $h_{fg}$ ,  $\rho_v$ ,  $\mu_v$  and  $P_v$  are the thermodynamic properties of the vapour at certain operating temperature respectively, which are the latent heat of vaporization (J/kg),

density ( $\text{kg/m}^3$ ), dynamic vapour viscosity ( $\text{kg/m-s}$ ), and corresponding saturated vapour pressure (Pa).

This expression could be further applied to other LHP components by replacing the evaporator's parameters (diameter and length) with the respective characteristic parameters, e.g., the vapour column in the three-way fitting ( $Q_{VL,vt}$ ), the vapour transporting line ( $Q_{VL,vtl}$ ) and the heat exchanger ( $Q_{VL,hx}$ ). The minimum value among these items will be the ultimate viscous limit ( $Q_{VL}$ )

$$Q_{VL} = \min(Q_{VL,e}, Q_{VL,vt}, Q_{VL,vtl}, Q_{VL,hx}) \quad [4-2]$$

**(2) Sonic Limit,  $Q_{SL}$**

At higher temperature operation, the Mach number of the vapour will increase significantly. Particularly when the vapour velocity is close to the sonic or supersonic level, the compression state of the vapour should be taken into consideration to evaluate its heat transfer capacity. A heat pipe may be choked by high-speed vapour flow, which would limit the total heat transfer capacity in the pipe. This limit for the evaporator is given by [2.100]

$$Q_{SL,e} = \left( \frac{\pi D_{v,e}^2 \rho_v h_{fg}}{4} \right) \left[ \frac{\gamma_v R_v T_v}{2(\gamma_v + 1)} \right]^{0.5} \quad [4-3]$$

where,  $Q_{SL,e}$  is the sonic limit at the absorbing section (W);  $\gamma_v$  is the vapour specific heat ratio whose magnitude is 4/3 for polyatomic working liquid (water);  $T_v$  is the average vapour temperature (K) in the absorbing section;  $R_v$  is the vapour constant (kJ/kg-K), given by:

$$R_v = \frac{R_0}{m} \quad [4-4]$$

where,  $R_0$  is the universal gas constant ( $R_0 = 8.314\text{kJ/kmol}\cdot\text{k}$ );  $m$  is the molecular weight of the vapour ( $m = 18$  for water).

The sonic limit may also occur in places where vapour flow exists, including the vapour column in the three-way fitting ( $Q_{SL,vt}$ ), the vapour transporting line ( $Q_{SL,vtl}$ ) and the heat exchanger ( $Q_{SL,hx}$ ). These figures can be attained by substituting the evaporator's parameters with characteristic parameters. The final sonic limit ( $Q_{SL}$ ) can be determined by the minimum value, expressed as

$$Q_{SL} = \min(Q_{SL,e}, Q_{SL,vt}, Q_{SL,vtl}, Q_{SL,hx}) \quad [4-5]$$

As observed from the equations, wick geometry and structure will not affect the sonic limit, while the vapour core diameter and the characteristic properties of the working fluid will impose an influence on the heat transfer. For most LHP operations, the effect of the sonic limit is temporary, and will disappear when the operational temperature moves to a higher level [4.2].

### (3) Entrainment Limit, $Q_{EL}$

The opposite flow directions of liquid and vapour may result in shear force at the liquid-vapour interface. When the vapour velocity is sufficiently high, the liquid will be torn from the wick surface and entrained into the vapour [2.100]. Entrainment can lead to a sudden substantial increase in fluid circulation and, consequently, the immediate drying out of the wick at the evaporator, which will decrease the heat transport capacity of conventional heat pipes. In this LHP operation, since the liquid and the vapour flow separately in the three-way fitting and transporting lines, the entrainment limit may only happen in the evaporator and heat exchanger. Such a benefit could largely reduce the flow resistance and increase the associated heat transport capacity. The expression of this limit at the evaporator is given as [2.100]

$$Q_{EL,e} = \left( \frac{\pi D_{v,e}^2 h_{fg}}{4} \right) \left[ \frac{\sigma \rho_v}{2r_{h,s}} \right]^{0.5} \quad [4-6]$$

where,  $\sigma$  is the surface tension coefficient of water (N/m);  $r_{h,s}$  is the hydraulic radius of wick surface pore (m), for a *screen mesh* wick which is given by

$$r_{h,s} = \left( \frac{1}{N_{wi,ms}} - D_{wi,ms} \right) / 2 \quad [4-7]$$

where,  $N_{wi,in}$  and  $D_{w,ms}$  are mesh number (1/m) and wire diameter of the inner screen layer (m).

For a *sintered powder wick*, the hydraulic radius of a surface pore is

$$r_{h,s} = D_{po,sp} / 2 \quad [4-8]$$

where,  $D_{po,sp}$  is the pore diameter in the sintered powder wick structure (m).

For an *open rectangular groove* wick, the pore hydraulic radius is

$$r_{h,s} = w_g \quad [4-9]$$

where,  $w_g$  is the groove width (m).

For the entrainment limit in an LHP condenser, the same equation can be applied by substituting the evaporator's parameters (diameter, hydraulic radius) with the structural parameters of the heat exchanger and the hydraulic radius of liquid film. Hence, the smaller of the limit values between the evaporator and the heat exchanger ( $Q_{EL,hx}$ ) will be the eventual entrainment limit ( $Q_{EL}$ ), defined by

$$Q_{EL} = \min(Q_{EL,e}, Q_{EL,hx}) \quad [4-10]$$

#### (4) Capillary Limit, $Q_{CL}$

The capillary limit represents the ability of heat pipe wicks to carry over the maximum liquid flow. A heat pipe has a higher heat transport capacity with a

larger volume of liquid pumped by wicks [4.3]. During heat pipe operation, the maximum capillary pumping head ( $\Delta P_{c,max}$ , Pa) must be greater than or at least equal to the total pressure drops along the heat pipe. The pressure drops consist of three aspects [2.100]: the viscous and inertial drop in the vapour ( $\Delta P_v$ , Pa); the viscous drop in the liquid ( $\Delta P_l$ , Pa); and the gravitational head ( $\Delta P_G$ , Pa), which contains radial and axial hydrostatic pressure drops ( $\Delta P_{rG}$  and  $\Delta P_{aG}$ ). For this particular operation, where the heat pipe fluid is mainly driven by gravity, the overall gravitational head is positive. The pressure relationship is

$$\Delta P_{c,max} + \Delta P_G \geq \Delta P_v + \Delta P_l \quad [4-11]$$

### ***I. Maximum Capillary Head ( $\Delta P_{c,max}$ )***

The capillary pressure power across a curved liquid-vapour interface achieves the maximum value when the contact angle in the evaporator ( $\theta_e$ ) equals zero and in the condenser ( $\theta_c$ ) is  $\pi/2$  (see **Fig. 4-2**). The maximum capillary pressure for such LHP operations is given by [2.100]

$$\Delta P_{c,max} = \frac{2\sigma \cos(\theta_e)}{r_e} \quad [4-12]$$

where,  $r_e$  is the effective capillary radius (m) which has the different expressions with wick structures, for a ***compound mesh screen*** wick

$$r_e = \frac{1}{2N_{owi,ms}} \quad [4-13]$$

where,  $N_{wi,o}$  is the mesh number of the outer screen layer (1/m).

For a ***sintered powder*** wick, the effective capillary radius is

$$r_e = \frac{0.41D_{po,sp}}{2} \quad [4-14]$$



For an *open rectangular grooves* wick, the effective capillary radius is

$$r_e = w_g \quad [4-15]$$

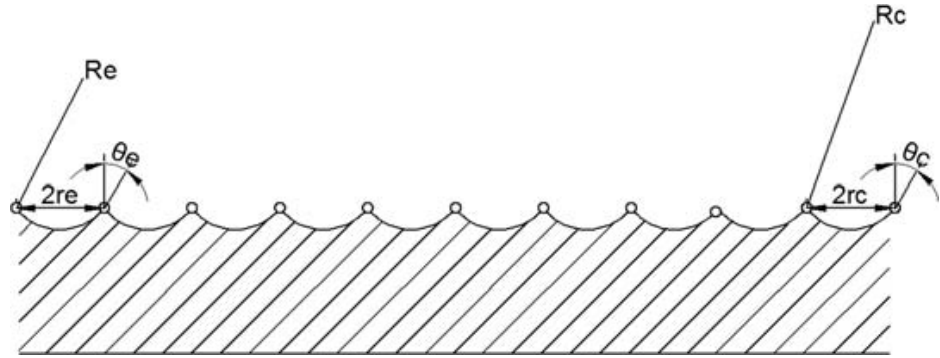


**Fig. 4-2: Wick and pore parameters in the evaporator and condenser**

Zhao [4.3] recommended that the contact angle ( $\theta$ ) should be about  $\pi/3$  for any heat pipe application. Imura et al. [4.4] suggested that the theoretical capillary force should be multiplied by a correction ratio of  $2/3$  for a mesh-screen wicked heat pipe design. These correction factors are necessary for the determination of the actual capillary power of this LHP during practical design.

## II. Gravity Pressure Head ( $\Delta P_G$ )

If a heat pipe works at a gravitational field and the circumferential communication of liquid in the wick is possible, the radial hydrostatic pressure drop has to be considered, and is the effort of liquid rising in a direction perpendicular to the heat pipe axis against the force of gravity, expressed by

$$\Delta P_{rG} = -\rho_l g D_{v,e} \cos \phi \quad [4-16]$$

where,  $\rho_l$  is the liquid density ( $\text{kg/m}^3$ );  $\phi$  is the collector title angle (rad). For an open-groove wick structure, the radial hydrostatic pressure drop is equal to zero, as the circumferential communication of liquid in this wick structure is impossible. The positive axial hydrostatic pressure head of the liquid column is

generated by the overall height difference between the heat pipe condenser and the bottom of the evaporator. This pressure difference is

$$\Delta P_{aG} = \rho_l g (H_{hx} / 2 + H_{hx-hp} + L_e \sin \phi) \quad [4-17]$$

where,  $H_{hx}$  is the height of the heat exchanger plate (m);  $H_{hx-hp}$  is the height difference between the heat exchanger and the top of absorbing heat pipes (m).

Thus, the overall gravity head is

$$\Delta P_G = \Delta P_{aG} - \Delta P_{rG} \quad [4-18]$$

### III. Vapour Pressure Drop ( $\Delta P_v$ )

A vapour pressure drop ( $\Delta P_v$ ) occurs in four LHP parts, including the evaporator ( $\Delta P_{v,e}$ ), the vapour column of the three-way fitting ( $\Delta P_{v,vt}$ ), the vapour transportation line ( $\Delta P_{v,vtl}$ ), and the condenser section ( $\Delta P_{v,hx}$ )

$$\Delta P_v = \Delta P_{v,e} + \Delta P_{v,vt} + \Delta P_{v,vtl} + \Delta P_{v,hx} \quad [4-19]$$

*i. Vapour Pressure Drop in the Evaporator ( $\Delta P_{v,e}$ ), the Vapour Column of the Three-way Fitting ( $\Delta P_{v,vt}$ ), and the Vapour Transportation Line ( $\Delta P_{v,vtl}$ )*

The vapour pressure gradient at the evaporator can be written as [2.100]

$$\Delta P_{v,e} = F_{v,e} L_e Q_{CL} \quad [4-20]$$

where,  $Q_{CL}$  is the capillary limit (W);  $F_{v,e}$  is the vapour frictional coefficient in the absorbing section, given by

$$F_{v,e} = \frac{8C_{v,e} (f_{v,e} \text{Re}_{v,e}) \mu_v}{\pi D_{v,e}^4 \rho_v h_{fg}} \quad [4-21]$$

where,  $C_{v,e}$  and  $f_{v,e}$  are the characteristic parameter and the friction factor in the absorbing section, which can be determined once the local axial Reynolds number and Mach number are defined. These expressions are given below

$$\text{Re}_{v,e} = \frac{4Q_{CL}}{\pi D_{v,e} \mu_v h_{fg}} \quad [4-22]$$

$$M_{v,e} = \frac{4Q_{CL}}{\pi D_{v,e}^2 \rho_v h_{fg} (R_v T_v \gamma_v)^{0.5}} \quad [4-23]$$

Kraus and Bar-Cohen [4.5] gave the full expression of  $C_{v,e}$  and  $f_{v,e}$  with different conditions

$$\text{Re}_{v,e} \leq 2300, M_{v,e} \leq 0.2, \quad [4-24]$$

$$(f_{v,e} \text{Re}_{v,e}) = 16, C_{v,e} = 1.00$$

$$\text{Re}_{v,e} \leq 2300, M_{v,e} > 0.2, \quad [4-25]$$

$$(f_{v,e} \text{Re}_{v,e}) = 16, C_{v,e} = \left(1 + \left(\frac{\gamma_v - 1}{2}\right) M_{v,e}^2\right)^{-0.5}$$

$$\text{Re}_{v,e} > 2300, M_{v,e} \leq 0.2, \quad [4-26]$$

$$(f_{v,e} \text{Re}_{v,e}) = 0.038, C_{v,e} = \text{Re}_{v,e}^{0.75}$$

$$\text{Re}_{v,e} > 2300, M_{v,e} > 0.2, \quad [4-27]$$

$$(f_{v,e} \text{Re}_{v,e}) = 0.038, C_{v,e} = \left(1 + \left(\frac{\gamma_v - 1}{2}\right) M_{v,e}^2\right)^{-0.75} (\text{Re}_{v,e})^{0.75}$$

The vapour pressure gradient at the vapour column in the three-way fitting ( $\Delta P_{v,vt}$ ) and vapour transportation line ( $\Delta P_{v,vtl}$ ) can be similarly carried out using the equations from [4-20] to [4-27] by substituting the evaporator's parameters (i.e., diameter and length of the vapour flow) with the respective characteristic parameters in each vapour core space of the LHP.

*ii. Vapour Pressure Drop in the Condenser Section ( $\Delta P_{v,hx}$ )*

As the vapour channels in the heat exchanger have the same structure/geometry and are connected in parallel with the same amount of vapour passing across, the vapour pressure drop in one plate could represent a pressure loss in the whole condenser section. For a single plate, the vapour pressure drop is [4.6]

$$\Delta P_{v,hx} = F_{v,hx} \left( \frac{H_{hx}}{2} \right) \left[ \frac{Q_{CL}}{(N_{hx}/2) - 1} \right] \quad [4-28]$$

where,  $N_{hx}$  is the number of heat exchanger plates;  $F_{v,hx}$  is the vapour frictional coefficient in the heat exchanger, which can be similarly determined through equations [4-21] to [4-27] by substituting the evaporator's hydraulic diameter with the characteristic diameter of the vapour space in the heat exchanger.

**IV. Liquid Pressure Drop ( $\Delta P_l$ )**

A liquid pressure drop ( $\Delta P_l$ ) also occurs in four parts, i.e., the condenser section ( $\Delta P_{l,hx}$ ), the liquid transportation line ( $\Delta P_{l,ttl}$ ), the liquid feeding inlet ( $\Delta P_{l,lt}$ ) of the three-way fitting, and the evaporating section ( $\Delta P_{l,e}$ ). The overall liquid pressure drop is, therefore, defined by

$$\Delta P_l = \Delta P_{l,hx} + \Delta P_{l,ttl} + \Delta P_{l,lt} + \Delta P_{l,e} \quad [4-29]$$

*i. Liquid Pressure Drop in the Condenser Section ( $\Delta P_{l,hx}$ )*

The liquid pressure drop in each heat exchanger plate channel can represent a total liquid pressure drop in the condenser. For a single-plate channel, the liquid pressure drop can be described using Darcy's Law [2.100]

$$\Delta P_{l,hx} = F_{l,hx} \left( \frac{H_{hx}}{2} \right) \left[ \frac{Q_{CL}}{(N_{hx}/2) - 1} \right] \quad [4-30]$$

where,  $F_{l,hx}$  is the liquid frictional coefficient in the heat exchanger, defined as

$$F_{l,hx} = \frac{4\mu_l}{\pi(D_{hx}^2 - D_{lf}^2)\rho_l h_{fg}} \quad [4-31]$$

where,  $D_{hx}$  and  $D_{lf}$  are respectively the hydraulic diameters of plate (m) and liquid film in the heat exchanger (m);  $\mu_l$  is the dynamic viscosity of the working liquid (kg/m-s).

ii. *Liquid Pressure Drop in the Liquid Line ( $\Delta P_{l,tl}$ ) and the Three-way Fitting ( $\Delta P_{l,tl}$ )*

The liquid pressure drop in the liquid transportation line is [2.100]

$$\Delta P_{l,tl} = F_{l,tl} L_{tl} Q_{CL} \quad [4-32]$$

where,  $L_{tl}$  is the length of the liquid transportation line (m);  $F_{l,tl}$  is the liquid frictional coefficient in the liquid transportation line, defined as

$$F_{l,tl} = \frac{4\mu_l}{\pi D_{l,tl}^2 \rho_l h_{fg}} \quad [4-33]$$

where,  $D_{l,tl}$  is the diameter of liquid core in the liquid transportation line (m).

The liquid pressure gradient in the three-way feeding structure ( $\Delta P_{l,tl}$ ) can be similarly carried out through equations [4-32] and [4-33] by substituting the

length and diameter of the liquid line with the respective characteristic parameters of the three-way fitting.

iii. *Liquid Pressure Drop in the Evaporator ( $\Delta P_{l,e}$ )*

The liquid pressure drop in the evaporator is written as [2.100]

$$\Delta P_{l,e} = F_{l,e} L_e Q_{CL} \quad [4-34]$$

where,  $F_{l,e}$  is the liquid frictional coefficient in absorbing pipe, given as

$$F_{l,e} = \frac{\mu_l}{K_p A_w \rho_l h_{fg}} \quad [4-35]$$

where,  $A_w$  is the cross sectional area of liquid flow in the wick ( $m^2$ );  $K_p$  is the wick permeability ( $m^2$ ), which varies with different types of wick structures:

For a **compound mesh-screen** wick structure, the cross area of the liquid flow and its permeability can be determined by the inner screen layer, given by [4.3]

$$A_w = \pi(D_{iwi,in}^2 - D_{v,e}^2) / 4 \quad [4-36]$$

where,  $D_{iwi,in}$  is the diameter of inner screen layer in the absorbing pipe (m).

$$K_p = \frac{D_{iwi,ms}^2 \varepsilon_{iwi,ms}^3}{122(1 - \varepsilon_{iwi,ms})^2} \quad [4-37]$$

where,  $\varepsilon_{iwi,ms}$  is the porosity of inner mesh screen layer, written as

$$\varepsilon_{iwi,ms} = 1 - \frac{1.05\pi N_{iwi,ms} D_{iwi,ms}}{4} \quad [4-38]$$

For a *sintered powder* structure, the equation for calculating the liquid flow area at the evaporator is the same as that for a heat pipe with a mesh-screen wick, while its permeability is different from the mesh-screen wick, given by

$$K_p = \frac{D_{po,sp}^2 \varepsilon_{sp}^3}{150(1 - \varepsilon_{sp})^2} \quad [4-39]$$

For an *open rectangular grooves* structure

$$A_w = \pi(D_{v,e} + \delta_g)\delta_g \quad [4-40]$$

where,  $\delta_g$  is the groove depth.

$$K_p = \frac{2\varepsilon_g r_{hl,g}^2}{(f_l Re_l)} \quad [4-41]$$

where,  $\varepsilon_g$  is the porosity of the grooves wick, and can be given by

$$\varepsilon_g = \frac{N_g w_g}{\pi(D_{v,e} + \delta_g)} \quad [4-42]$$

where,  $N_g$  is the groove number and  $r_{hl,g}$  is the groove hydraulic radius (m), which is expressed as

$$r_{hl,g} = \frac{2w_g \delta_g}{w_g + 2\delta_g} \quad [4-43]$$

The  $(f_l Re_l)$  factor is the frictional coefficient in the rectangular channels, which can be obtained from **Fig. 4-3** [2.100].

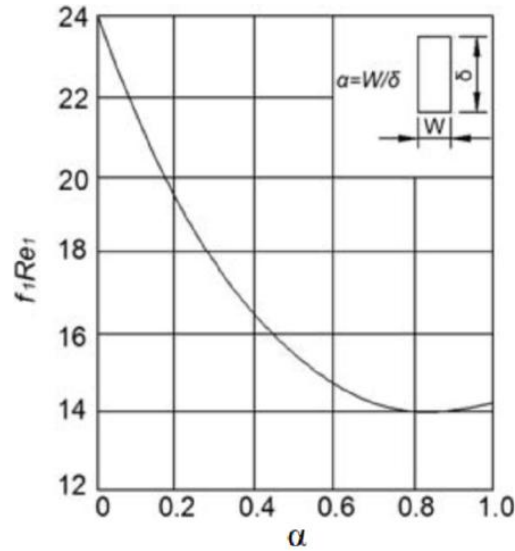


Fig. 4-3: Frictional coefficients in the rectangular pipes

Combining the above equations yields the final expression of the capillary limit

$$Q_{CL} \leq \frac{\Delta P_{c,max} + \Delta P_G}{\left[ \begin{aligned} & \left( F_{v,e} L_e + F_{v,vl} L_{vl} + F_{v,ll} L_{ll} + \frac{F_{v,hx} H_{hx}}{N_{hx} - 2} \right) \\ & + \left( F_{l,e} L_e + F_{l,ll} L_{ll} + F_{l,lr} L_{lr} + \frac{F_{l,hx} H_{hx}}{N_{hx} - 2} \right) \end{aligned} \right]} \quad [4-44]$$

### (5) Boiling Limit, $Q_{BL}$

The boiling limit represents the maximum radial heat density at the evaporator and occurs at an extremely high heat pipe operational temperature, which causes burning out of the liquid at certain areas of the wicks or heat pipe wall. Similarly, a limited heat flux will exist in the condenser (heat exchanger) of the LHP. For the evaporator, the analytical expression is [2.100]

$$Q_{BL,e} = \frac{2\pi L_e k_{wl} T_v}{h_{fg} \rho_v \ln(D_{hp,in} / D_{v,e})} \left( \frac{2\sigma}{r_b} - P_{c,max} \right) \quad [4-45]$$

where,  $r_b$  is the radius of the bubbles, which could be assumed at  $2.54 \times 10^{-7}$  m for the general estimation of a normal heat pipe performance;  $P_{c,max}$  is the



maximum capillary power (Pa), which can be ignored by comparing with the value of  $2\sigma / r_b$ ;  $k_{wi}$  is the effective thermal conductivity of the liquid-saturated wick (W/m-K), for the outer **mesh screen** layer in cylindrical geometry, which is given by

$$k_{wi} = \frac{k_l \left[ (k_l + k_{s,ms}) - (1 - \varepsilon_{owi,ms}) (k_l - k_{s,ms}) \right]}{\left[ (k_l + k_{s,ms}) + (1 - \varepsilon_{owi,ms}) (k_l - k_{s,ms}) \right]} \quad [4-46]$$

where,  $k_l$  and  $k_{s,ms}$  are the thermal conductivities of liquid and outer screen layer (W/m-K). The effective thermal conductivity of the inner screen layer can be similarly obtained from above equation, thus the overall wick effective conductivity is simply expressed as

$$k_{s,ms} = (k_{owi,ms} + k_{iwi,ms}) / 2 \quad [4-47]$$

For the **sintered metal** wick,  $k_{wi}$ , is given [2.100]

$$k_{wi} = \frac{k_l \left[ (2k_l + k_{s,sp}) - 2(1 - \varepsilon_{sp}) (k_l - k_{s,sp}) \right]}{\left[ (2k_l + k_{s,sp}) + (1 - \varepsilon_{sp}) (k_l - k_{s,sp}) \right]} \quad [4-48]$$

For the **rectangular grooves** wick,  $k_{wi}$ , is given [2.100]

$$k_{wi} = \frac{(w_f k_l k_{s,g} \delta_g) + w_g k_l (0.185 w_f k_{s,g} + \delta_g k_l)}{(w_g + w_f) (0.185 w_f k_{s,g} + \delta_g k_l)} \quad [4-49]$$

where,  $w_f$  is the groove fin width, written as

$$w_f = \frac{\pi (D_{v,e} + D_{hp,in})}{2n_g} - w_g \quad [4-50]$$

For the boiling limit within the heat exchanger ( $Q_{BL,hx}$ ), the same equations can be used from [4-45] to [4-50] by substituting the evaporator's parameters (diameter, vapour core space) with the equivalent inner diameter and vapour space of the heat-exchanger plate. Thus, the smaller limit value between the evaporator and the heat exchanger will be the ultimate entrainment limit ( $Q_{BL}$ ), determined by

$$Q_{BL} = \min(Q_{BL,e}, Q_{BL,hx}) \quad [4-51]$$

### (6) Liquid Filling Mass Limit, $Q_{FL}$

The liquid filling mass limit is the minimum liquid level required to be filled into the loops, which affects the heat transportation capacity using liquid gravity force. This limit reflects the minimum amount of liquid that is fully circulated in the heat pipe loop with the assistance of gravity at a certain height. The liquid filling mass limit for the evaporator is [4.6]

$$Q_{FL,e} = \left( \frac{m_f}{xL_e} \right)^3 \frac{k_l g h_{fg}}{3\pi^2 \mu_l \rho_l D_{hp,in}^2} \quad [4-52]$$

where,  $m_f$  is the filled liquid mass (kg);  $x$  is the parameter relating to the filled liquid mass, which is assumed at 0.8 for pipes with wick structure and 1.0 for those sections without wick.

### 4.2.3 Method and Algorithm for the LHP Heat Transfer Model Development and Operation

The algorithm for analysing the above six limits is indicated in **Fig. 4-4**, which gives a flow chart illustrating the computer programming process. The iterative method was applied, especially in calculating the capillary limit.

- (i) Given the geometry of the LHP system components, the technical parameters can be obtained from **Tables 3-1** and **3-2**.
- (ii) Given certain system operating temperatures/pressures, the thermodynamic

properties of the working fluids can be obtained from **Table 3-3**.

- (iii) Calculate the viscous limits at appropriate regions, taking the minimum value as the ultimate viscous limit using equations [4-1] and [4-2].
- (iv) Calculate the sonic limits at appropriate regions, taking the minimum value as the ultimate sonic limit using equations [4-3] to [4-5].
- (v) Calculate the entrainment limits at the wicked absorbing pipes and heat exchanger, taking the smaller value as the ultimate entrainment limit using equations [4-6] to [4-10].
- (vi) Run a numerical iteration to calculate the capillary limit,  $Q_{CL}$ , using equations [4-11] to [4-44]:
  - a. Given an initial value of  $Q_{CL}$ ;
  - b. Capillary pressure,  $\Delta P_{CL}$ , can be obtained by equations [4-12] to [4-15];
  - c. Gravity pressure,  $\Delta P_G$ , can be obtained by equations [4-16] to [4-18];
  - d. Vapour pressure drop,  $\Delta P_v$ , can be obtained by equations [4-19] to [4-28];
  - e. Liquid pressure drop,  $\Delta P_l$ , can be obtained by equations [4-29] to [4-43];
  - f. If  $[(\Delta P_{CL} + \Delta P_G) - (\Delta P_v + \Delta P_l)] / (\Delta P_{CL} + \Delta P_G) < -0.1\%$  (error allowance), then decrease  $Q_{CL}$  by 10, and return to step 'b' for re-calculation;
  - g. If  $[(\Delta P_{CL} + \Delta P_G) - (\Delta P_v + \Delta P_l)] / (\Delta P_{CL} + \Delta P_G) > 0.1\%$  (error allowance), then increase  $Q_{CL}$  by 10, and return to step 'b' for re-calculation;
  - h. If  $-0.5\% \leq [(\Delta P_{CL} + \Delta P_G) - (\Delta P_v + \Delta P_l)] / (\Delta P_{CL} + \Delta P_G) \leq 0.1\%$  (error allowance), heat balance is achieved and the real value of  $Q_{CL}$  can be obtained;
- (vii) Calculate the boiling limits at the wicked evaporator and the heat exchanger, taking the smaller value as the ultimate boiling limit using equations [4-45] to [4-51];
- (viii) Calculate the liquid filling mass limit at the evaporator using equation [4-52];
- (ix) Take the minimum value of the above six limits as the governing limit of the whole operation.
- (x) Program stops.

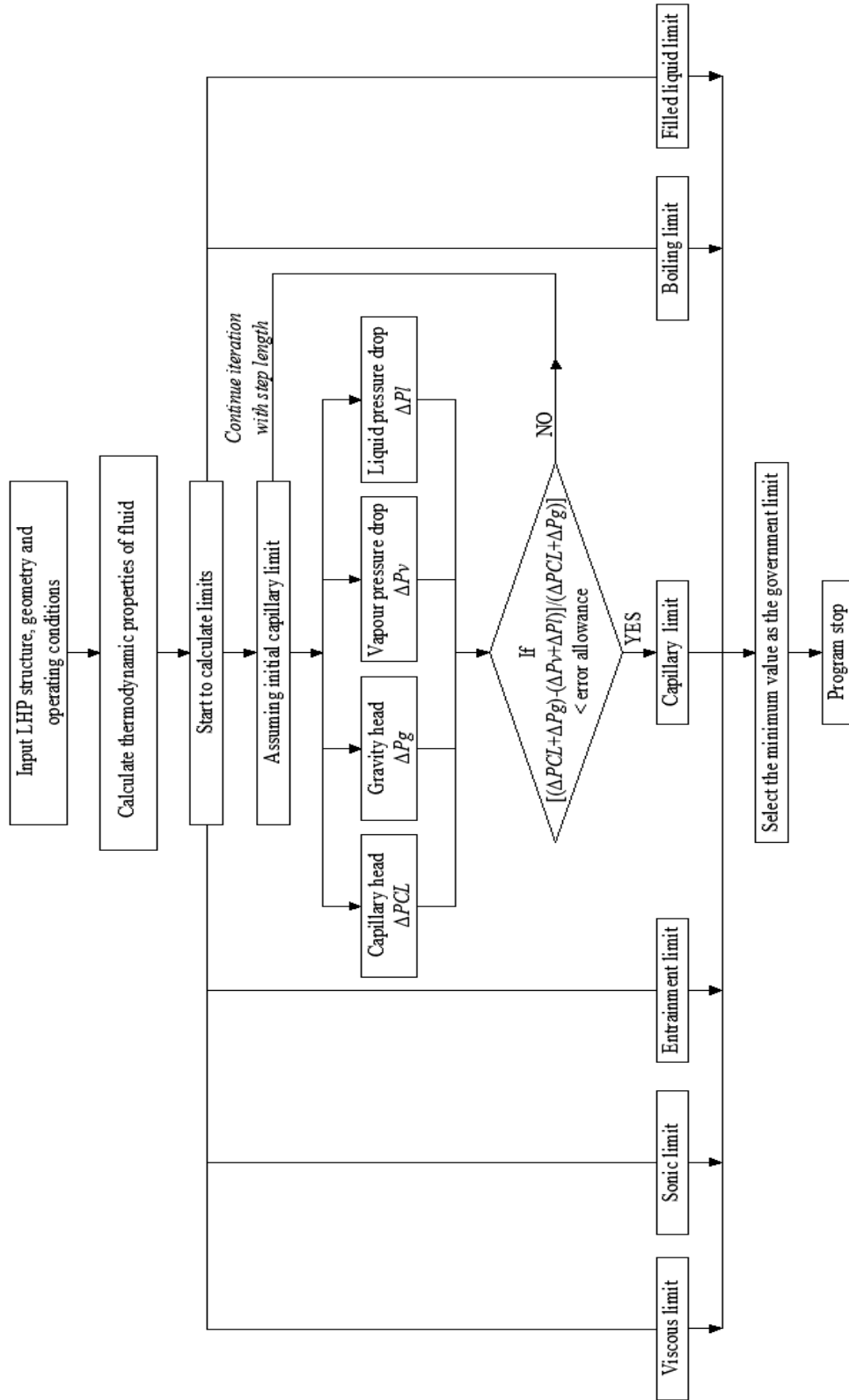


Fig. 4-4: Flow chart for calculating the LHP heat transfer limits

#### 4.2.4 Statistical Analysis

To analyse the difference between the theoretical and experimental results (published or later test data), the correlation coefficient ( $r$ ) and the root mean square percentage deviation ( $e$ ) were applied and defined by

$$r = \frac{n\sum X_e X_s - (\sum X_e)(\sum X_s)}{\sqrt{n\sum X_e^2 - (\sum X_e)^2} \sqrt{n\sum X_s^2 - (\sum X_s)^2}} \quad [4-53]$$

$$e = \sqrt{\frac{\sum [100 \times (X_e - X_s) / X_e]^2}{n}} \quad [4-54]$$

where,  $n$  is the number of experiments implemented; and  $X_e$  and  $X_s$  represent the experimental and simulation results, respectively.

#### 4.2.5 Validation of LHP Heat Transfer Model by the Published Results

The analytical model developed for the LHP device was validated for accuracy by comparing it with previously published experimental results of an LHP with a double-layer wick structure. Wu et al. [4.7] developed the double-layer wick in order to improve the structural strength and heat transfer of the LHP device. The outer layer of such a double-layer wick is a bi-porous wick, which has two different pore sizes: the larger-sized pores are designated for vapour transportation and the smaller-sized ones for liquid transportation. The inner layer of such a double-layer wick is a mono-porous wick, which performs two functions: enhancing the capillary force and increasing the overall wick strength. **Fig. 4-5** shows schematically the experimental rig used, and **Table 4-1** summarises the figures for the geometric and operational parameters relating to the LHP. The gravitational head in this test was considered to be zero, as the LHP evaporator was laid horizontally. The condensation (sink) temperature was maintained at 10 °C during the whole measurement process, which enabled development of the correlation between the LHP evaporator temperature and the heat load applied. The three different wicks for the experiments of the heat

transfer measurements of the heat pipes were mono-porous, bi-porous, and double-layer wicks.

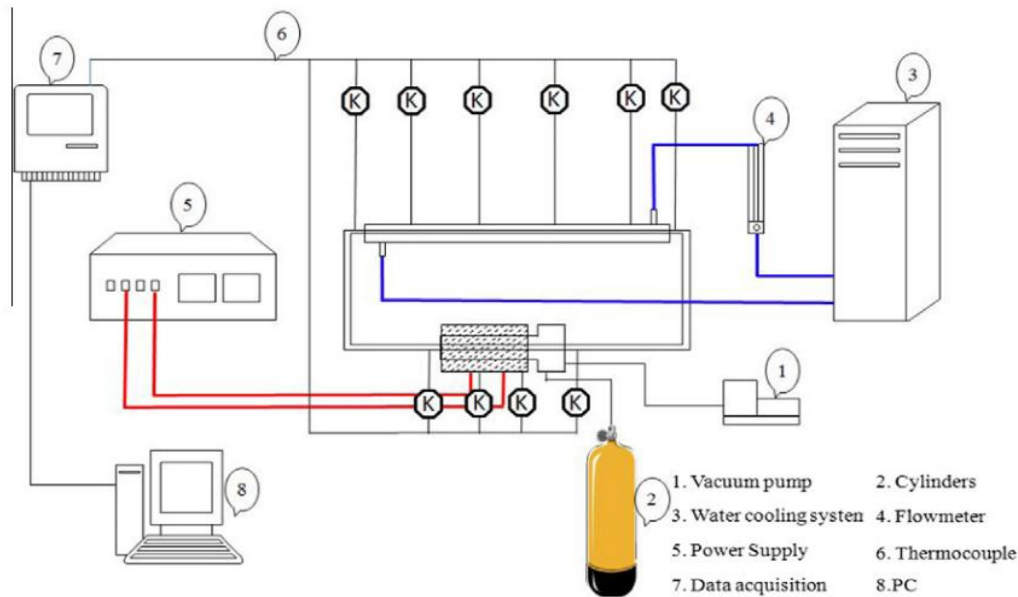
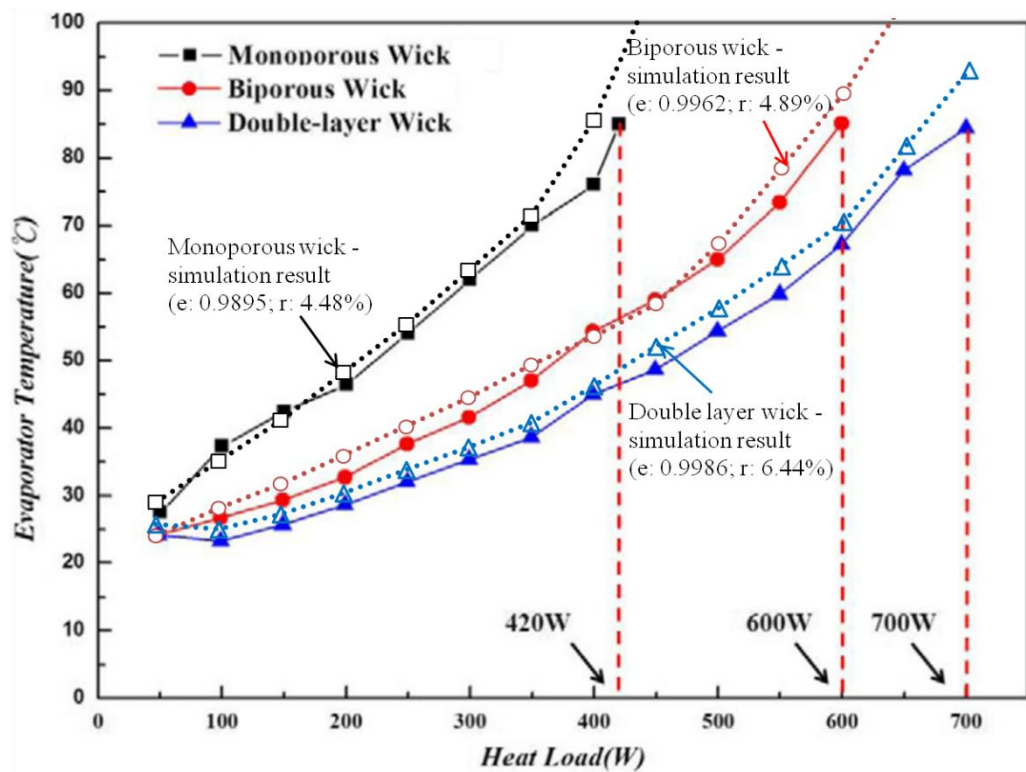


Fig. 4-5: Referenced rig for the LHP thermal measurement [4.7]

Table 4-1: Design and operation parameters of the referenced LHP [4.7]

Design parameters	Value	Design parameters	Value
<u>Capillary evaporator</u>		<u>Vapour line</u>	
Total length (mm)	65	Outer/inner diameter (mm)	6/5
Active length (mm)	40	Length (mm)	470
Outer/inner diameter (mm)	16/12.5	<u>Liquid line</u>	
Material	Stainless steel	Outer/inner diameter (mm)	6/4.5
<u>Sintered nickel powder wick</u>		Length (mm)	583
Outer/inner diameter (mm)	12.5/9	<u>Condenser</u>	
Mono-porous particle size ( $\mu\text{m}$ )	2.2-2.8	Outer/inner diameter (mm)	6.4/5
Mono-porous porosity level	0.55-0.65	Length (mm)	800
Bi-porous particle size ( $\mu\text{m}$ )	32-48	<u>Working fluid</u>	
Mono-porous porosity level	0.75-0.85	Ammonia	
Conductivity (W/k-m)	90.9	<u>Air temperature (<math>^{\circ}\text{C}</math>)</u>	
<u>Compensation chamber</u>		20	
Outer/inner diameter (mm)	29/24	<u>Sink temperature (<math>^{\circ}\text{C}</math>)</u>	
Length (mm)	118	10	
		<u>Mass flow rate (l/min)</u>	
		8	
		<u>Operate temperature (<math>^{\circ}\text{C}</math>)</u>	
		10- 85	
		<u>Heat load (W)</u>	
		50-700	

**Fig. 4-6** presents the correlation between the LHP evaporator temperature and the applied heat load derived from the computer modelling, which was obtained by inputting the design and operation parameters of the referenced LHP experiment. In the simulation model, the compensation chamber was considered equivalent to the three-way vapour-liquid separation structure. The correlation coefficients ( $r$ ) between the modelling and the experimental results for the mono-porous, bi-porous, and double-layer wicked heat pipes were 0.9895, 0.9962 and 0.9986, respectively. The root mean square percentage deviation ( $e$ ) for the modelling and testing of the three wicked heat pipes was 4.48%, 4.89% and 6.44%, respectively. The reason for error generation may be attributed to the utilisation of simplified assumptions and empirical formulas, the inaccurate estimation of heat exchange in the condenser, and ignorance of the heat loss to the surrounding environment. However, the accuracy degree achieved by this simulation model was considered to be acceptable from the engineering point of view, and could be applied to predict the LHP thermal performance and give appropriate recommendations for further system fabrication and operation.



**Fig. 4-6:** Comparison between the LHP simulation results and the published test data

#### 4.2.6 Model Operation and Result Discussion of LHP Heat Transfer Limit

The LHP's heat transfer capacity is a factor that depends upon its several operational and geometric parameters, i.e., working temperature, wick type, evaporator diameter/length, evaporator inclination angle, vapour column diameter in the three-way fitting, liquid filling level, and evaporator elevation above the condenser. The impacts of these parameters on LHP heat transfer capacity are presented in the following sections and the results are then discussed to address important recommendations for the follow-on system fabrication and testing. As the subsequent experiment would be carried out in Shanghai, China, the maximum heat transfer capacity required by the LHP absorber should be over  $730 \text{ W/m}^2$ . This figure is treated as the baseline for the LHP simulation.

##### (1) Impact of Operational Temperature

Each vapour pressure figure within the LHP will be coupled with a corresponding saturated vapour temperature, termed as the operational temperature. Water vapour pressure in the LHP is considered as a function of temperature and can be determined with Clausius–Clapeyron relation [4.8]

$$P = 133.32 \exp \left[ 20.386 - \frac{5132}{(T + 273.13)} \right] \quad [4-55]$$

where,  $T$  and  $P$  are the corresponding temperature (K) and vapour pressure (Pa) of water at certain thermodynamic status.

Taking consideration of the design parameters, i.e., the compound mesh screen as the wick structure, the evaporator internal diameter of 19.6 mm, the evaporator length of 1.5 m, the evaporator inclination angle of  $30^\circ$ , the vapour column diameter of 14 mm in the three-way fitting, the liquid filling mass of 0.03 kg, and the evaporator-to-condenser height difference of 0.3 m, the above analytical computer model was run to obtain the results. The relation between the heat pipe operational temperature and the heat transfer limits was simulated



and the results are presented in **Fig. 4-7**. It was found that the boiling limit decreased with an increase in temperature, while the other five limits increased when the operational temperature grew higher. The capillary limit was found to be the governing limit. A linear correlation between the capillary limit and the operating temperature was found to exist. The viscous limit in the three-way feeding structure was observed as being far larger than the LHP limitation.

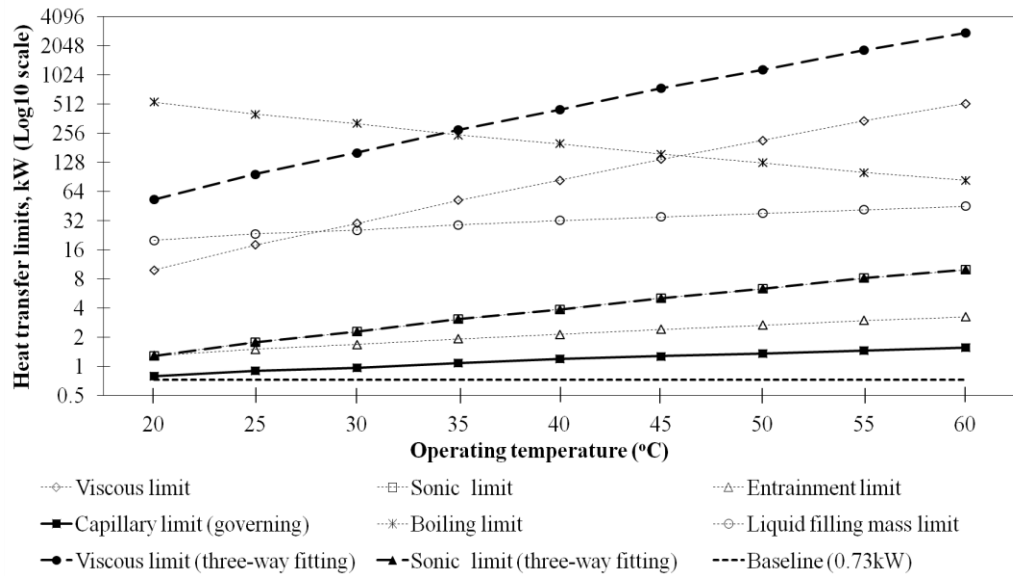


**Fig. 4-7: Impact of operational temperature on the heat transfer performance of the LHP**

This phenomenon could be explained in that at the higher operational temperatures, an enhanced evaporation rate of the liquid occurred and, as a result, the heat transport capacity of the LHP was increased. Increasing the operational temperature would lead to a change in the thermodynamic properties of the working fluid and this would further create increased fluid turbulence (the Reynolds number) within the piping, which would then lead to an increased viscous limit. When the operational temperature rises, the sonic limit (occurring in the three-way fitting) would become higher due to the increased vapour density and the larger amount of vapour circulation mass in the loop. The entrainment limit would also grow larger as a lower shear force would occur at the vapour-liquid boundary within the wicked absorbing pipes. Sufficient vaporisation enabled a higher heat transport capacity within the heat pipes to overcome the vapour flow resistance and, furthermore, the liquid return resistance was also lowered owing to the lower liquid flow viscosity

while the temperature rose. This behaviour immediately strengthened the overall capillary force. As the heat transfer in the heat pipes dominated the boiling limit, when the overall liquid vaporisation increased with the operating temperature, the dry-out danger of the heat pipe appeared and the boiling limit decreased. The higher latent heat of the liquid vaporisation helped to raise the liquid filling mass limit.

However, the operating temperature of the loop heat pipe should be counterbalanced against the required PV temperature to a certain scope while their working efficiency and capacity vary in an opposite way with temperature.

## (2) Impact of Wick Structure

While keeping all other operating and design parameters the same, changing the wick structure in the evaporator from screen mesh, sintered powder to an open rectangular groove led to a variation in the LHP heat transfer limit, and the correlation between these two variables is presented in **Table 4-2**.

**Table 4-2: Impact of wick structure on the heat transfer performance of the LHP**

Wick type	$Q_{VL}$	$Q_{SL}$	$Q_{EL}$	$Q_{CL}$	$Q_{BL}$	$Q_{FL}$	$Q_L$
Screen mesh (kW)	17.93	1.77	1.50	<b>0.90</b>	401.29	23.26	<b>0.90</b>
Sintered powder (kW)	17.93	1.77	2.12	<b>0.64</b>	337.71	23.26	<b>0.64</b>
Open groove (kW)	17.93	1.77	<b>0.86</b>	6.92	702.43	23.26	<b>0.86</b>

It was found that the screen-mesh wick could obtain the highest heat transport capacity (operating limit) over the other two wicks in this case. The critical limits were respectively observed as the entrainment limit for the groove wick and the capillary limit for the other two wicks. The groove wick had the largest capillary and boiling limit but the smallest entrainment limit. The other three limits, i.e., viscous, sonic and liquid filling mass limits, were the same for all the wicks. This phenomenon could be explained in that a groove wick structure usually has the lowest liquid frictional force and radial heat transfer resistance in a gravity-assisted operation and, therefore, should have a much higher capillary limit at the same working conditions. The groove wick has a relatively larger pore hydraulic radius and higher wick effective thermal

conductivity than the other two wicks, which would consequently result in a higher boiling limit but a relatively lower entrainment limit. Depending on the definitions of the viscous, sonic, and liquid filling limits, the wick structure will not impose an influence on these three limits when having a fixed design and operational parameters, e.g., loop geometry, vapour core space, operational temperature, and working fluid.

### (3) Impact of Evaporator Diameter

While the other loop operating and design parameters remained the same, the correlation between the evaporator diameter and the LHP heat transfer limit is presented in **Fig. 4-8**.

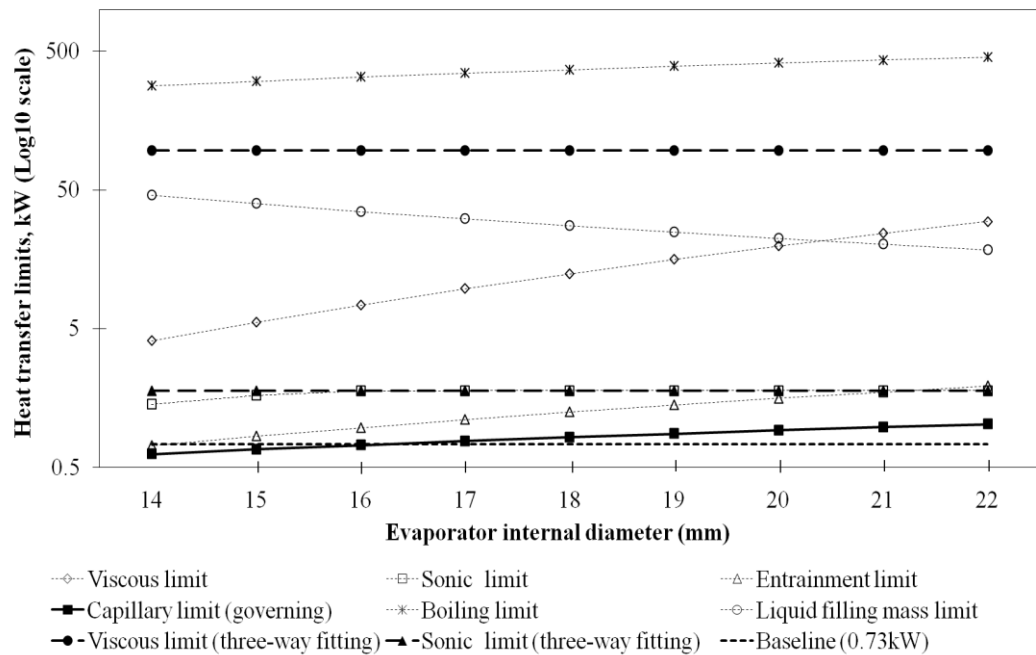


**Fig. 4-8: Impact of evaporator diameter on the heat transfer performance of the LHP**

In this case, only the liquid filling mass limit fell, while the other five limits increased with an increase in the evaporator diameter. The capillary limit was found to be the governing limit for this operation, and a linear relation between the capillary limit and the evaporator diameter was found to exist. This phenomenon could be explained in that increasing the evaporator diameter would result in a higher Reynolds number, a greater rate of liquid evaporation, a broader fluid flow space, a lower vapour flowing velocity, and a larger

amount of liquid to be evaporated within the evaporator. These trends of variation will consequently assist in increasing the values of viscous, sonic, entrainment, capillary, and boiling limits of the LHP. However, the sonic limit originally occurred in the evaporator when its diameter was less than 15 mm and later began to appear in the three-way fitting constantly; changing the evaporator diameter would not affect this limit any more. As the internal evaporating space was inversely proportional to the liquid filling mass limit, an increased evaporator diameter would require more liquid to fill it and, with the current liquid volume, this limit would, therefore, decrease.

#### (4) Impact of Evaporator Length

While the other loop operating and design parameters remained the same, the correlation between the evaporator length and the LHP heat transfer limit is given in **Fig. 4-9**.

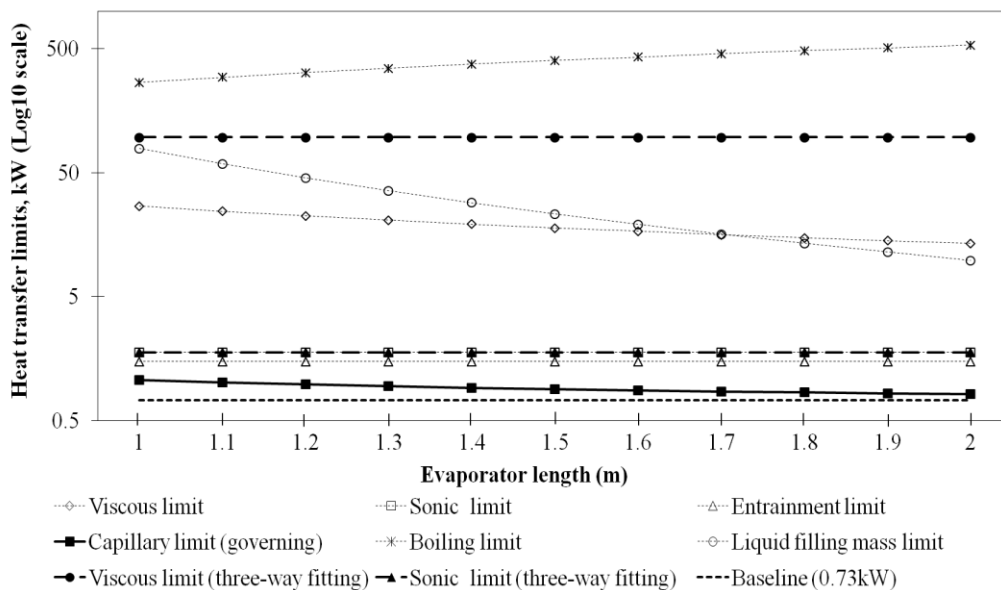


**Fig. 4-9: Impact of evaporator length on the heat transfer performance of the LHP**

In this circumstance, the viscous, capillary and liquid filling mass limits decreased as the evaporator length increased, while the boiling limit varied in the opposite trend, and the other two limits remained constant. The capillary limit was also found to be the critical limit. This phenomenon could be explained in that the increased evaporator length represented an increased fluid

flow distance, leading to increased fluid frictional resistance and possibly decreased volume flow rate (a smaller Reynolds number), which thus led to decreased viscous and capillary limits. Since an increased evaporator space would require more liquid to fill it, at the current liquid level, the liquid filling mass limit was thereby reduced. During this process, the boiling limit became larger as the increased evaporator length led to an increase in the overall loop volume, the evaporation rate of the water and the operational temperature. For the other limits, no interrelation is found between them and the evaporator length and, therefore, caused no impact upon them.

**(5) Impact of Evaporator Inclination Angle**

While the other loop operating and design parameters remained the same, the correlation between the evaporator inclination angle and the LHP heat transfer limit is illustrated in Fig. 4-10.

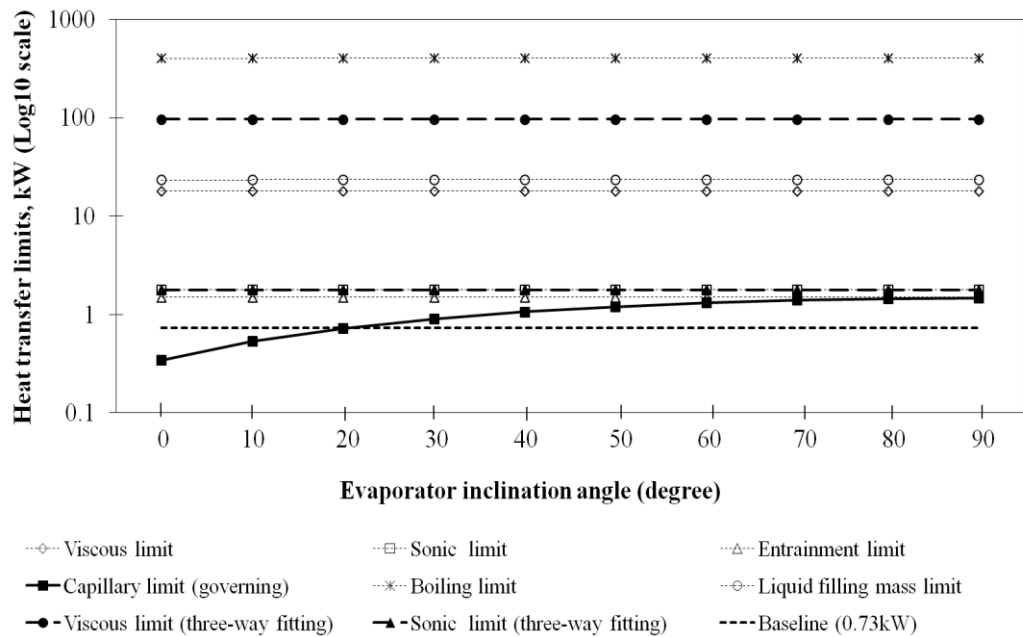


**Fig. 4-10: Impact of evaporator inclination angle on the heat transfer performance of the LHP**

The capillary limit was observed as the primary limit in this case, which increased with the evaporator inclination angle, while the other five limits remained constant. A smooth logarithmic relation between the capillary limit and the evaporator inclination angle exists due to the effect of gravity. The

capillary limit significantly increased when the inclination angle varied from  $0^\circ$  to  $60^\circ$ , but then gently grew to its maximum value. A higher inclination angle led to greater hydrostatic force, which improved the system's capability in returned liquid flow, and thus led to increased heat flux, while the other limits had no internal relationship with this factor.

### (6) Impact of Vapour Column Diameter

While the other loop operating and design parameters remained the same, the correlation between the vapour column diameter in the three-way fitting and the LHP heat transfer limit is shown in Fig. 4-11.

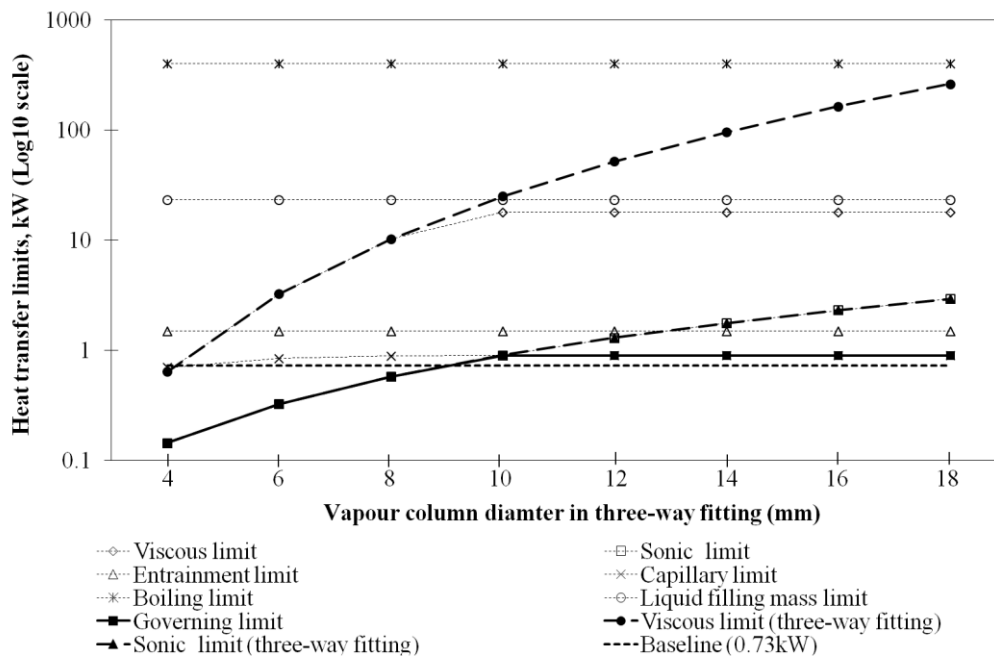


**Fig. 4-11: Impact of vapour column diameter on the heat transfer performance of the LHP**

It was found that the viscous, sonic and capillary limits increased with a larger vapour column diameter in the three-way fitting, whereas the other limits remained constant. The system viscous limit occurred in the three-way fitting when the vapour column diameter was below 9 mm. In this case, the governing limit varied with the different diameter level in the vapour column. The sonic limit, occurring in the three-way fitting, was initially found to be the critical limit, while the vapour column diameter was below 10 mm, whereas the

capillary limit became the governing limit when the column diameter was above 10 mm. Through this observation, it was concluded that the minimum vapour column diameter in the three-way fitting should be no less than 10 mm for this LHP operation in order to avoid the overall heat transfer ability being weakened.

### (7) Impact of Liquid Filling Mass

While the other loop operating and design parameters remained the same, the correlation between the liquid filling mass and the LHP heat transfer limits is displayed in **Fig. 4-12**. It was found that the liquid filling mass limit increased with an increase in liquid mass, whereas the other limits remained constant. The governing limit was first observed to be the liquid filling mass when the mass level was below 0.01 kg, but it became the capillary limit when the mass level was above 0.01 kg. On the basis of this phenomenon, it was concluded that the minimum liquid filling mass should be more than 0.01 kg for the screen-mesh wick; otherwise, a surface dry-out state would occur within the evaporator.

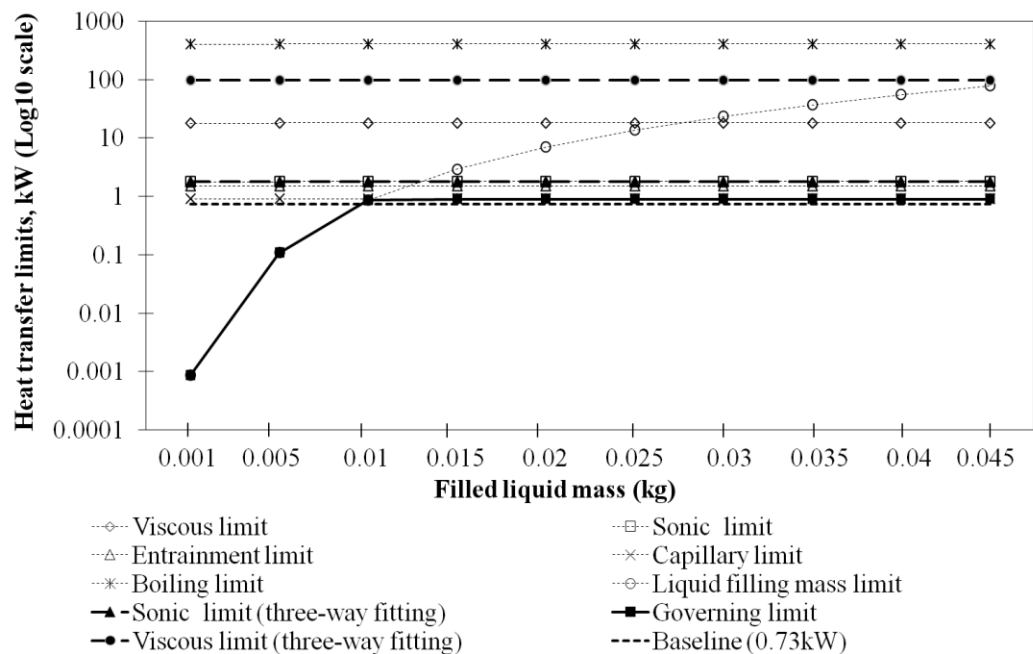


**Fig. 4-12: Impact of liquid filling mass on the heat transfer performance of the LHP**

### (8) Impact of Evaporator-to-condenser Height Difference

While the other loop operating and design parameters remained the same, the correlation between the heat pipe evaporator-to-condenser height difference and the LHP heat transfer limit is described in **Fig. 4-13**. In this circumstance, the capillary limit increased with the evaporator-to-condenser height difference, while the other five limits all remained the same. The capillary limit dominated the heat transfer when the height difference was below 1.1 m, while the entrainment limit (occurring in the heat exchanger) became the governing factor when the elevation difference was above 1.1 m. A linear relation between the capillary limit and the height difference was found to exist owing to the effect of gravity. A greater height difference brought on higher hydrostatic force, which enhanced the system's capability to deliver the returned liquid flow, and, therefore, transfer more applied heat load. The other limits showed no relation with this parameter and remained constant.

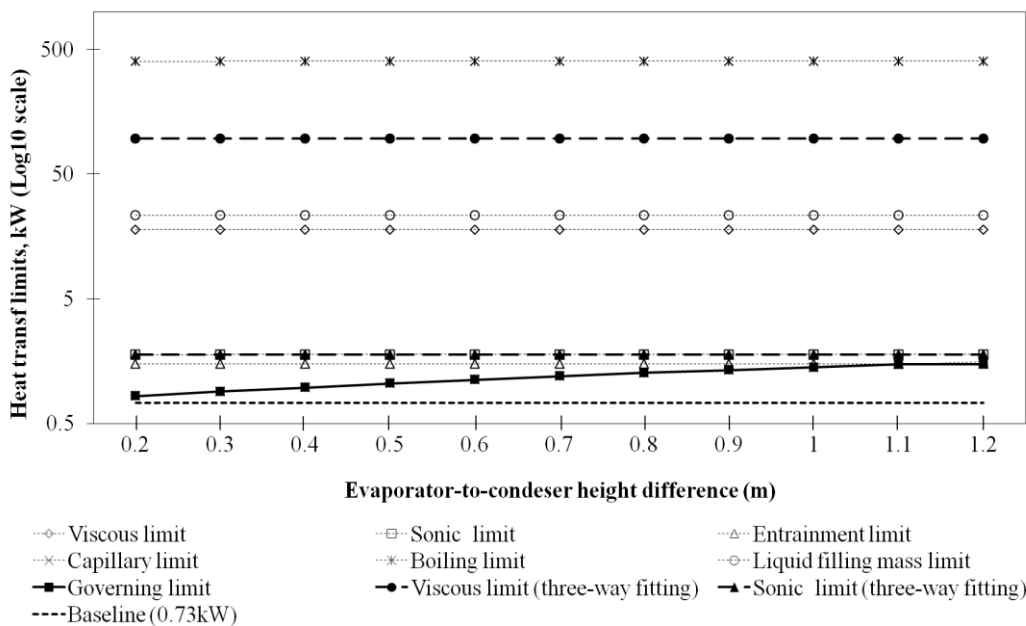


**Fig. 4-13: Impact of evaporator-to-condenser height difference on the heat transfer performance of the LHP**

In summary, the maximum heat transfer capacity required by the LHP absorber in Shanghai is about  $730 \text{ W/m}^2$  (illustrated as the baseline), a single LHP can then meet such heat removal demand for a unit solar collecting area when its maximum heat transfer capacity is nearly 900 W at the specific design and



operating conditions, e.g., a compound mesh screen wick structure, an evaporator internal diameter of 19.6 mm, an evaporator length of 1.5 m, an evaporator inclination angle of  $30^\circ$ , a vapour column diameter of 14 mm in the three-way fitting, a liquid filling mass of 0.03 kg, and an evaporator-to-condenser height difference of 0.3 m.

### 4.3 Steady-state Model for the Characterisation of System Performance

#### 4.3.1 Modelling Objective for the System Steady-state Performance

The purpose of developing a steady-state numerical model was to characterise the performance of the integrated PV/LHP heat pump system under laboratory-controlled conditions, which would enable (a) determination of the system performance against different variables, (b) determination of the optimum system configuration, and (c) recommendations for the appropriate system design and operational parameters. All the analytical results are directly useful for further system prototype fabrication and operation.

#### 4.3.2 Thermal Fluid Theory and the Associated Mathematical Equations of the System Steady-state Model

For a steady-state PV/LHP heat pump system, the solar energy conversion and transfer includes four processes (as shown in **Fig. 4-14**): ① absorbing part of the striking solar radiation and dissipating the rest into the surrounding air; ② converting part of the absorbed energy into electricity using the PV cells; ③ transporting the remaining part of the absorbed energy into the passing refrigerant via the LHP; and ④ upgrading the refrigerant heat to higher-grade heat using a heat pump. These processes are interlinked and finally achieve a balance under the steady-state operation.

To simplify the energy model, the following hypotheses were made:

- a. The system operates under a quasi-steady condition.
- b. The ohm electrical losses within the solar cells and PV module are ignored.
- c. The transmittance of the EVA layers is considered to be 100%.

- d. Heat losses across the module insulation layers are negligible.
- e. Heat losses through the heat pipe transportation lines are ignored.

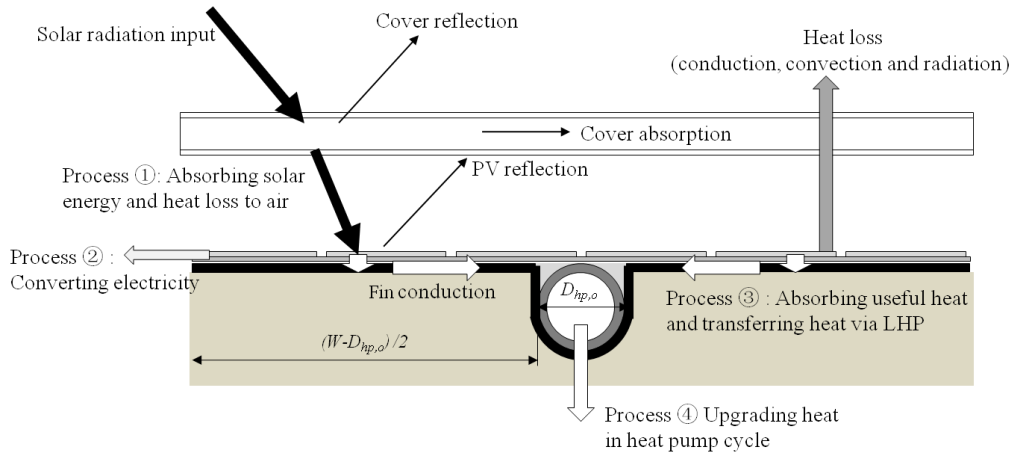


**Fig. 4-14: Schematic of steady-state solar energy conversion and transfer processes**

### (1) Absorbing Useful Solar Radiation and Heat Dissipation

When the solar radiation passes across the top covers and strikes the surface of the PV/LHP module, a small percentage of the radiation energy will be dissipated into the surroundings owing to the occurrence of directional/diffusive reflection and conductive/convective heat transfer, while the remaining radiation energy will be converted into electricity and heat using the PV/LHP settings. Under steady-state operating conditions, the useful energy obtained by the module is equal to the energy reaching the PV surface minus the associated direct or indirect heat losses, which refers to the heat dissipation from the module surface to the surrounding air through conduction, convection and infrared radiation.

The solar energy received by the PV module is a function of the solar radiation striking the module, the transmittance of the glazing cover and the absorptance of the PV surfaces, which can be given by [2.9, 4.9]

$$Q_{abs} = \tau_c^{N_c} \tau_{g,pv} \left[ \alpha_p \beta_p + \alpha_b (1 - \beta_p) \right] A_m I \quad [4-56]$$

where,  $\tau_c$  and  $\tau_{g,pv}$  are the visual transmittances of cover plate and the glazing layer of PV lamination respectively;  $N_c$  is the number of cover plates;  $\alpha_{abs}$  and  $\alpha_b$  are the absorption ratios of the PV layer and its baseboard;  $\beta_p$  is the packing factor of PV layer;  $A_m$  is the collector area of the module ( $m^2$ ).

Owing to the temperature difference between the PV surface and the surrounding air, a certain amount of the absorbed energy will be transferred into the surrounding air through the top cover; while back and edge heat transfers could be ignored if super insulation at those directions is provided. Under the steady-state condition, the heat loss from a double-glazed module will experience (1) heat transfer from the PV absorber surface to the inner glazing cover; (2) heat transfer from the inner cover to the outer cover; and (3) heat transfer from the outer glazing cover to the surrounding air [4.9]. As shown in Fig. 4-15, the three forms of heat transfer are laid in a series and achieve a balance.

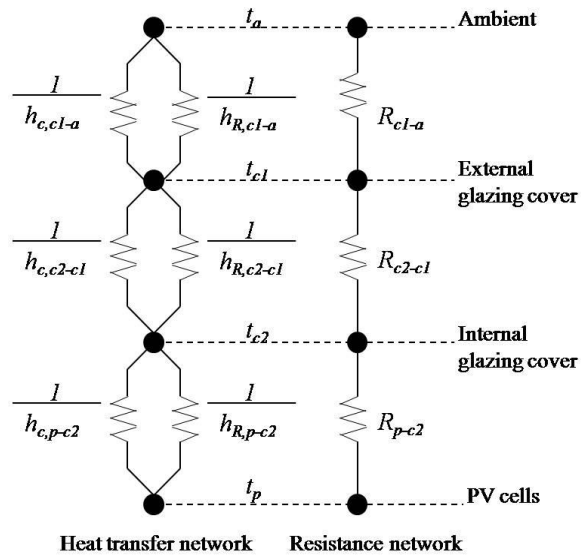


Fig. 4-15: Thermal network of heat loss for a typical double-cover module

Therefore, the total heat loss is written as [4.9]

$$Q_L = U_L A_m (T_p - T_a) \tag{4-57}$$

where,  $Q_L$  and  $U_L$  are respectively the total heat loss (W) and the heat loss coefficient ( $W/m^2-K$ );  $T_p$  and  $T_a$  are the average temperatures of PV layer and the ambient air (K).

Where the  $U_L$  is the overall heat transfer coefficient and could be written

$$U_L = \left( \frac{1}{h_{c,p-c2} + h_{R,p-c2}} + \frac{1}{h_{c,c2-c1} + h_{R,c2-c1}} + \frac{1}{h_{c,c1-a} + h_{R,c1-a}} \right)^{-1} \quad [4-58]$$

where,  $h_{c,p-c2}$ ,  $h_{c,c2-c1}$  and  $h_{c,c1-a}$  are respectively the convective heat transfer coefficients ( $W/m^2-K$ ) of PV layer ( $p$ ) to inner cover surface ( $c_2$ ), inner cover surface ( $c_2$ ) to external cover surface ( $c_1$ ) and external cover surface ( $c_1$ ) to ambient air ( $a$ );  $h_{R,p-c2}$ ,  $h_{R,c2-c1}$  and  $h_{R,c1-a}$  are the radiative heat transfer coefficients ( $W/m^2-K$ ) of PV layer ( $p$ ) to inner cover surface ( $c_2$ ), inner cover surface ( $c_2$ ) to external cover surface ( $c_1$ ) and external cover surface ( $c_1$ ) to ambient air ( $a$ ) respectively.

### ***I. Heat Transfer from the PV Absorber Surface to the Inner Glazing Cover***

In this case, a relatively steady convective air layer exists between the PV absorber surface and the inner glazing cover. Its associated convective heat transfer coefficient,  $h_{c,p-c2}$ , is termed as [4.9]

$$h_{c,p-c2} = \frac{k_{a,p}}{\delta_{a,p}} \left\{ \begin{array}{l} \left[ 1 + 1.446 \left( 1 - \frac{1708}{Ra_{a,p} \cos \theta} \right)^+ \left[ 1 - \frac{1708 \sin(1.8\theta)^{1.6}}{Ra_{a,p} \cos \theta} \right] \right] \\ + \left[ \left( \frac{Ra_{a,p} \cos \theta}{5830} \right)^{0.333} - 1 \right]^+ \end{array} \right\} \quad [4-59]$$

where,  $k_{a,p}$  is thermal conductivity of air gap at the average temperature of PV layer and inner cover surface ( $W/m-k$ );  $\delta_{a,p}$  is the PV layer to glazing cover distance (m);  $\theta$  is the collector slop (degree); the bracket with plus means zero and positive values only;  $Ra_{a,p}$  is the Rayleigh number of the air gap at PV layer and inner cover surface, given by

$$Ra_{a,p} = \frac{g(T_p - T_{c2})\delta_{a,p}^3}{\nu_{a,p}^2 T_{a,m}} Pr_{a,p} \quad [4-60]$$

where,  $g$  is the gravity acceleration ( $m/s^2$ ) and  $\nu_a$  is kinematic viscosity of air at the PV and inner cover surface ( $m^2/s$ );  $Pr_{a,p}$  is the Prandtl number of the air gap at PV layer and inner cover surface, which is assumed to be independent of temperature and taken equal to 0.7;  $T_{a,m}$  is the average air temperature of PV layer and inner cover surface which is

$$T_{a,m} = (T_p + T_{c2})/2 \quad [4-61]$$

where,  $T_p$  and  $T_{c2}$  are respectively the average temperatures (K) of PV layer and inner cover surface.

Converting the radiation transfer into the equivalent convective one, a radiation-relevant factor,  $h_{r,p-c2}$ , is expressed by

$$h_{R,p-c2} = \frac{\sigma(T_p + T_{c2})(T_p^2 + T_{c2}^2)}{(1/\epsilon_p) + (1/\epsilon_{c2}) - 1} \quad [4-62]$$

where,  $T_{c1}$  is the average temperature of external cover surface (K);  $\epsilon_p$  and  $\epsilon_{c2}$  are emissivity of the PV layer and inner cover surface;  $\sigma$  is the Stefan–Boltzman constant ( $5.6679 \times 10^{-8} W/m^2 \cdot K^4$ ).

## ***II. Heat Transfer from the Inner Glazing Cover to the Outer Cover***

Similarly, heat transfer from the inner glass to the outer glass can be calculated using equations [4-59] to [4-62] to substitute corresponding parameters, including temperature, air properties, and emissivity.

### III. Heat Transfer from the Cover's Outer Surface to the Surrounding Air

For a surface exposed to the outside wind, the convective coefficient could be calculated using the Klein equation [4.10], addressed below

$$h_{c,c1-a} = \frac{8.6V^{0.6}}{L^{0.4}} \quad [4-63]$$

where,  $V$  is the wind speed (m/s);  $L$  is the characteristic length of the collector (m). The minimum convective coefficient for a wind-exposed surface is considered to be  $5 \text{ W/m}^2\text{-k}$  [4.10]; if the above calculation gives a lower value, this should be replaced by the minimum value of 5.

Since the temperature of the sky has little impact on the calculation result, it is usually represented by the air temperature, thus

$$h_{r,c1-a} = \varepsilon_{c1} \sigma (T_{c1} + T_a) (T_{c1}^2 + T_a^2) \quad [4-64]$$

For modules with single glazing or with no glazed cover, the items addressed in sections (II) or sections (I)-(II) should be removed. In such cases, the heat transfer from the inner glass to the outer glass will not be counted, or only the heat loss between the module surface and the ambient air is considered.

#### (2) Converting Part of the Absorbed Energy into Electricity

The PV cells' electrical efficiency is adversely proportional to their surface temperature and this dependency can be written as

$$\eta_e = \eta_{rc} [1 - \beta_{PV} (T_p - T_{rc})] \quad [4-65]$$

The overall electricity output is, therefore, given as

$$Q_e = \eta_e \beta_p \alpha_p \tau_c^{N_c} \tau_{g,pv} I A_m \quad [4-66]$$

The module's solar electrical efficiency could be calculated through

$$\eta_e = \frac{Q_e}{IA_m} \quad [4-67]$$

### (3) Transferring the Remaining Absorbed Energy into the Heat Pump Refrigerant

Under the steady-state condition, the rate of useful heat delivered by the module equals the rate of the absorbed energy minus the overall heat loss and converted electricity, expressed as

$$Q_{th} = Q_{abs} - Q_L - Q_e \quad [4-68]$$

This part of the heat will eventually be converted into the heat received by the refrigerant, which is denoted by  $Q_u$ . In this case, the module's thermal efficiency can be defined by

$$\eta_{th} = \frac{Q_{th}}{A_m I} = \frac{Q_u}{A_m I} \quad [4-69]$$

The module's overall solar efficiency,  $\eta_o$ , would be the sum of both the electrical and thermal efficiencies

$$\eta_o = \eta_e + \eta_{th} \quad [4-70]$$

At the heat pipe's evaporation section, part of the solar energy is converted into heat ( $Q_{th}$ ), which leads to the evaporation of heat pipe working fluid. This vapour fluid, via the vapour transportation line, moves forward to the condensing heat exchanger, where the evaporated fluid is condensed and transfers the condensation heat into the adjacent refrigerant flow, thus leading to the evaporation of refrigerant at the next channel of the heat exchanger. The

condensed fluid in the heat pipe, via the liquid transportation line, then returns to the heat pipe evaporation section to retain heat, thus forming a complete heat transportation cycle, as depicted in **Fig. 4-16**. This process involves a number of thermal resistances that result in changing the working fluid temperature, which is detailed as follows. The resistances of the silicon sealant and liquid-vapour interface at the wicked surface are ignored owing to their significantly smaller values compared to the others [2.99].

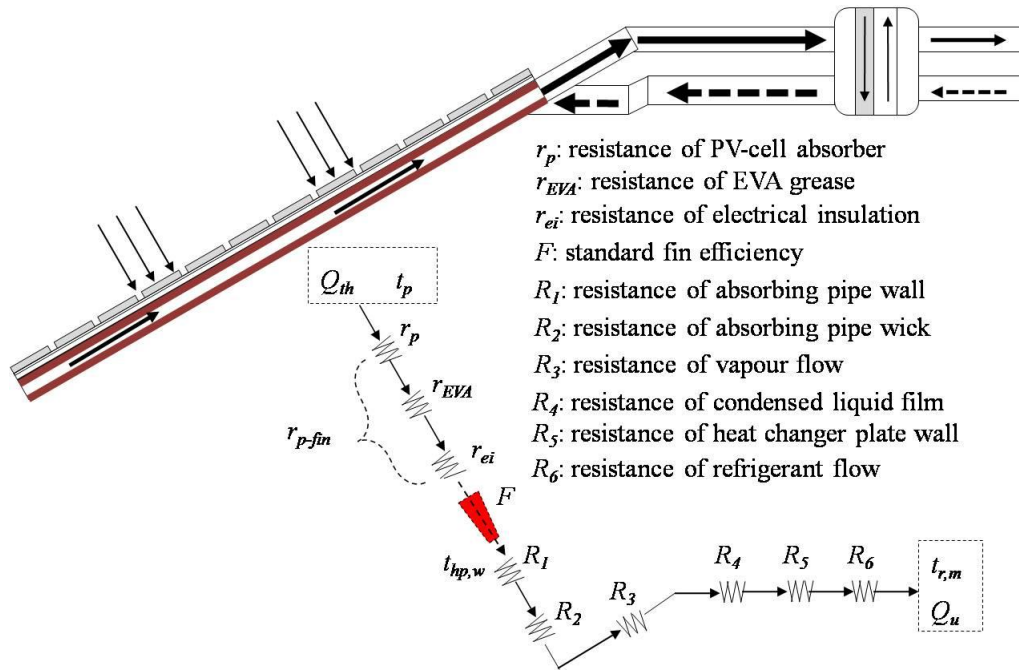


**Fig. 4-16: Temperature drops and equivalent thermal resistances along the heat transfer path**

Heat transfer between the PV module and heat pipe fins is a conventional one-dimensional multi-layer heat conduction process and its associated thermal resistance is [4.11]

$$r_{p-fin} = r_p + r_{EVA} + r_{ei} = \frac{\delta_p}{k_p} + \frac{\delta_{EVA}}{k_{EVA}} + \frac{\delta_{ei}}{k_{ei}} \quad [4-71]$$

where,  $r_{p-fin}$ ,  $r_p$ ,  $r_{EVA}$  and  $r_{ei}$  are respectively the thermal resistances per unit area ( $m^2$ -K/W) of PV cells to fin sheet, PV cells, EVA layer and electrical



insulation;  $k_p$ ,  $k_{EVA}$ ,  $k_{ei}$ ,  $\delta_p$ ,  $\delta_{EVA}$ , and  $\delta_{ei}$  are respectively the thermal conductivity (W/m-K) and thickness (m) of PV layer, EVA layer and electrical insulation.

**I. Thermal Resistance across the Fin Length**

Heat absorbed by the fin will be conducted to the heat pipe wall along its width direction, by leading the heat flow to travel through the cross-sectional fin area. This is considered a one-dimensional heat transfer process starting from the fin end ( $x = 0$ ) and finishing at the fin base [ $x = (W/N_{hp}-D_{hp,o})/2$ ]. **Fig. 4-17** indicates the heat flow simulation process using the finite element approach, which takes  $dx$  as the step length of the numerical calculation.

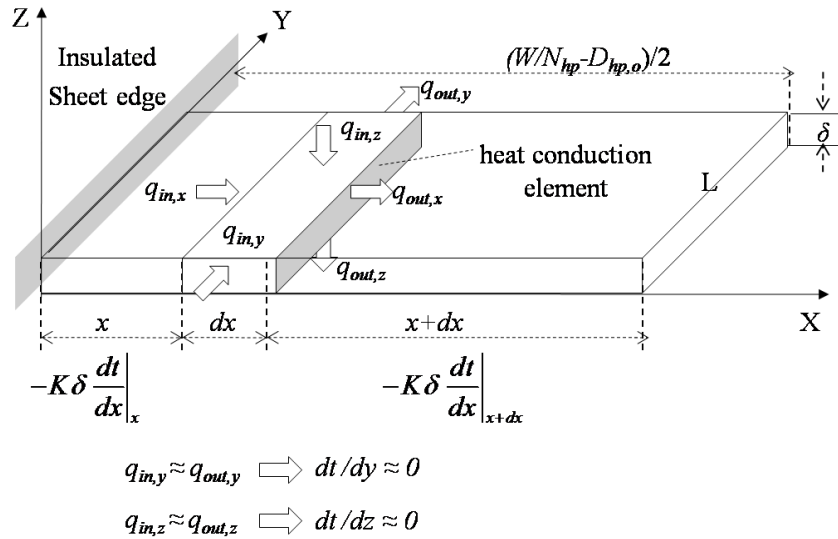


**Fig. 4-17: Heat flow pattern at the elemental length ‘dx’ on the fin sheet**

For a controlled finite element per unit width, the following energy conversion equation can be applied

$$\left[ \frac{q_{abs} - U_L(T - T_a) - q_e}{1 + r_{p-fin} U_L} \right] dx + \left( -k_f \delta_f \frac{dT}{dx} \right)_x - \left( -k_f \delta_f \frac{dT}{dx} \right)_{x+dx} = 0 \tag{4-72}$$

where,  $q_{abs}$  and  $q_e$  are the absorbed solar energy and produced electricity rate at per unit length of the PV/LHP module ( $W/m^2$ );  $k_f$  and  $\delta_f$  are the thermal conductivity (W/m-K) and thickness (m) of the fin sheet.

Along the heat pipe evaporation section, no temperature gradient exists along its length owing to even heat input. The overall useful solar heat conducted through the Hottel-Whillier model [2.9, 4.9] from the fin to the heat pipe is

$$Q_u = LWF_{th} [q_{abs} - U_L(T_{r,m} - T_a) - q_e] \quad [4-73]$$

where,  $L$  and  $W$  are respectively the length (m) and width (m) of the fin sheet;  $T_{r,m}$  is the mean temperature of refrigerant in the heat pump;  $F_{th}$  is the collector thermal efficiency factor, defined as

$$F_{th} = \frac{1/U_L}{\frac{LW}{N_{hp}} \left\{ \frac{1}{LU_L \left[ (W/N_{hp} - D_{hp,o})F_f + \frac{D_{hp,o}}{1+r_{p-fin}U_L} \right]} + \sum_{i=1}^6 R_i \right\}} \quad [4-74]$$

where,  $N_{hp}$  is the number of heat pipes;  $\sum R_i$  is the overall thermal resistance from the fin sheet to the refrigerant (W/m-K). The standard fin efficiency,  $F_f$ , is defined as

$$F_f = \frac{\tanh \left[ m(W/N_{hp} - D_{hp,o})/2 \right]}{m(W/N_{hp} - D_{hp,o})/2} \quad [4-75]$$

where, the variable,  $m$ , is given by [2.9, 4.9]

$$m = \sqrt{\frac{U_L}{k_f \delta_f (1+r_{p-fin}U_L)}} \quad [4-76]$$

In terms of the physical implication,  $F_{th}$  represents the ratio of the system's actual useful heat gain to the overall converted solar heat at a certain working fluid temperature. The system's thermal efficiency factor is a constant figure

under the fixed physical and operating condition. However, this factor's value varies in the following ways: it decreases with increasing fin width, increases with increasing material thickness and thermal conductivities, decreases when there is an increase in the overall heat loss coefficient, and increases with decreases in the overall system heat transfer resistance.

## ***II. Thermal Resistances from the Heat Pipe Wall to its Working Fluid***

### *i. Heat Pipe Wall, $R_1$*

Heat transfer through the heat pipe wall is a typical steady-state conduction process, and its thermal resistance can be written as

$$R_1 = \frac{\ln(D_{hp,o} / D_{hp,in})}{2\pi L_{hp,e} k_{hp}} \quad [4-77]$$

where,  $D_{hp,o}$ ,  $D_{hp,in}$ ,  $L_{hp,e}$  and  $k_{hp}$  are the outer diameter (m), inner diameter (m), length (m) and thermal conductivity of the absorbing heat pipe (W/m-K).

### *ii. Thermal Resistance of the Wick Structure, $R_2$*

The inner surface of the heat pipe wall is attached to the mesh wick, which causes a certain resistance in heat transfer; this part of the resistance is addressed as

$$R_2 = \frac{\ln(D_{hp,in} / D_{v,e})}{2\pi L_{hp,e} k_{wi}} \quad [4-78]$$

where,  $k_{wi}$  is the effective thermal conductivity of wick structure (W/m-K), whose expression can be derived from equations [4-38], [4-46] and [4-47].

### *iii. Thermal Resistance of the Vapour Flow, $R_3$*

Vapour flow from the evaporation section to the condensing heat exchanger experiences a certain pressure loss and, consequently, a temperature drop. This creates a resistance in the heat transfer which could be written as [2.99]

$$R_3 = \frac{T_v^2 R_0 \Delta P_v N_{hp}}{Q_u h_{fg} P_v} \quad [4-79]$$

where,  $T_v$  is the average temperature of vapour (K);  $h_{fg}$  is the latent heat of vaporisation (J/kg);  $R_0$  is the universal gas constant per unit mole ( $R_0 = 8314\text{J/kg}\cdot\text{K}$ );  $P_v$  is the corresponding pressure at certain temperature (Pa);  $N_{hp}$  is the number of loop heat pipes;  $\Delta P_v$  is the total pressure drops (Pa) from the heat pipe evaporation section to condensation section, which should be the sum of the pressure drops in four regions: (i) the absorbing pipe  $\Delta P_{v,e}$ , (ii) the three-way fitting  $\Delta P_{v,f}$ , (iii) the vapour transportation line  $\Delta P_{v,tl}$ , and (iv) the heat exchanger channels (vapour side)  $\Delta P_{v,hx}$ .

$$\Delta P_v = \Delta P_{v,e} + \Delta P_{v,f} + \Delta P_{v,tl} + \Delta P_{v,hx} \quad [4-80]$$

The expressions of the vapour pressure drop in the evaporator, three-way fitting, vapour transportation line and condensation section can be referred to using equations [4-20] to [4-28].

#### *iv. Thermal Resistance of the Condensed Liquid Film, $R_4$*

The condensed liquid film is evenly distributed on the surface of the condensing heat exchanger (on the heat pipe side) and its associated flow resistance is [4.11]

$$R_4 = \frac{\ln \left[ D_{hx,in} / (D_{hx,in} - 2\delta_{lf}) \right]}{2\pi L_{lf} k_{lf} (N_{hx} / 2 - 1)} \quad [4-81]$$

where,  $\delta_{lf}$ ,  $L_{lf}$  and  $k_{lf}$  are the thickness (m), length (m) and thermal conductivity (W/m-K) of the liquid film;  $D_{hx,in}$  is the internal hydraulic diameter of heat exchanger (m);  $N_{hx}$  is the number of heat exchanger plates.

v. *Thermal Resistance of the Heat-exchanging Plate,  $R_5$*

The equivalent thermal resistance of the heat-exchanging plate is derived as

$$R_5 = \frac{\ln(D_{hx,o} / D_{hx,in})}{2\pi(H_{hx} / 2)k_{hx}(N_{hx} / 2 - 1)} \quad [4-82]$$

where,  $k_{hx}$  is the thermal conductivity of heat exchanger plate (W/m-K).

vi. *Thermal Resistance of the Heat Pump Refrigerant,  $R_6$*

The refrigerant in the heat pump cycle passes across the channels of the condensing heat exchanger (on the refrigerant side), where it is evaporated into vapour. This process involves turbulent and forced convection heat transfer, and its associated thermal resistance is [4.11]

$$R_6 = \frac{1}{h_r A_{hx,r} (N_{hx} / 2)} \quad [4-83]$$

where,  $A_{hx,r}$  is the internal surface area of refrigerant flow in each heat-exchanging channel (m<sup>2</sup>);  $h_r$  is the heat transfer coefficient (W/m<sup>2</sup>-K) of two-phase refrigerant flow for each heat-exchanging channel, which is given by

$$h_r = h_{r,l} \left[ (1 - x_r)^{0.8} + \frac{3.8x_r^{0.76} (1 - x_r)^{0.04}}{\text{Pr}_r^{0.38}} \right] \quad [4-84]$$

where,  $x_r$  is the saturation of refrigerant;  $h_{r,l}$  is heat transfer coefficient of the liquid refrigerant (W/m<sup>2</sup>-K).

$$h_{r,l} = \frac{Nu_r k_{r,l}}{D_{hx,in}} \quad [4-85]$$

where,  $k_{r,l}$  is the thermal conductivity of liquid refrigerant (W/m-K). The Nusselt number of refrigerant can be derived from the Dittus-Boelter equation

$$Nu_r = 0.023 Re_{r,l}^{0.8} Pr_{r,l}^{0.4} \quad [4-86]$$

The Reynolds number of the liquid refrigerant ( $Re_{r,l}$ ) within the channel is

$$Re_{r,l} = \frac{m_r (1-x_r) D_{hx,in}}{\mu_{r,l} (N_{hx}/2) N_{hp} A_{hx,r}} \quad [4-87]$$

where,  $\mu_{r,l}$  and  $m_r$  are respectively the mean dynamic viscosity (kg/m-s) and mass flow rate (kg/s) of liquid refrigerant within each heat-exchange channel.

The Prandtl number of the refrigerant ( $Pr_{r,l}$ ) is calculated using

$$Pr_{r,l} = \mu_{r,l} c_{pr,l} / k_{r,l} \quad [4-88]$$

where,  $c_{pr,l}$  is specific heat of liquid refrigerant at a constant pressure (J/kg-K).

#### (4) Upgrading Solar Heat into Condensation Heat by the Heat Pump

The refrigerant is evaporated at the heat exchanger after it absorbs solar heat. This refrigerant vapour is then upgraded through a compressor to a high-temperature refrigerant vapour, which, at the condenser of the heat pump cycle, is condensed and releases heat to the tank water. [4.12]. This part of heat absorbed by the refrigerant is given as

$$Q_u = Q_{e,t} = m_r A_{cr} (H_1 - H_4) \quad [4-89]$$

where,  $H_1$  and  $H_4$  are the thermal enthalpies (kJ/kg) of refrigerant at point 1 and point 4 in **Fig. 3-3**;  $A_{cr}$  is the cross sectional area in refrigerant tube ( $m^2$ ).

The compressor operation was initially assumed to be an isentropic condition and the heat output of the heat pump ( $Q_{c,t}$ ) can be calculated as

$$Q_{c,t} = m_r A_{cr} (H_{2s} - H_3) = m_w C_{p,w} (T_w^{i+1} - T_w^i) \quad [4-90]$$

where,  $H_{2s}$  and  $H_3$  are the thermal enthalpies (kJ/kg) of refrigerant at point 2s and point 3.

The power input into the heat pump ( $Q_{c,e}$ ) at the ideal isentropic condition is

$$Q_{c,e} = m_r A_{cr} (H_{2s} - H_1) \quad [4-91]$$

Thus, the net electricity generation of the system ( $Q_{e,n}$ ) is

$$Q_{e,n} = Q_e - Q_{c,e} \quad [4-92]$$

Consequently, the net electrical output ratio of the prototype system ( $\eta_{e,n}$ ) is defined as the ratio of net electricity output to overall solar radiation

$$\eta_{e,n} = Q_{e,n} / A_m I \quad [4-93]$$

The basic thermal performance coefficient ( $COP_{th}$ ) of a heat pump system is defined as the ratio of the heating or cooling generated over the electrical energy consumed. However, as such a PV/LHP system yields not only heat, but also electricity, the overall coefficient indicating the thermal and the electrical performance ( $COP_{PV/T}$ ) of the system is mostly as desired. This coefficient converts the electricity into the equivalent thermal energy using the average electricity-generation efficiency (commonly 38% [2.18]) at a coal-fired power plant:

$$COP_{PV/T} = \frac{Q_{c,t} + Q_e / 0.38}{Q_{c,e}} \quad [4-94]^5$$

By taking the compressor's isentropic efficiency into account, the system's advanced performance coefficient during experiment ( $COP_{PV/T-exp}$ ) would be an even lower figure, which could be redefined as [2.18]

$$COP_{PV/T-exp} = \frac{Q_{c,t-exp} + Q_{e-exp} / 0.38}{Q_{c,e} / \eta_s} \quad [4-95]$$

where,  $Q_{c,t-exp}$  and  $Q_{e-exp}$  are respectively the experimental figures of heat output of heat pump (W) and electricity generation of the whole system (W). The compressor's isentropic efficiency ( $\eta_s$ ) is given as

$$\eta_s = \frac{Q_{c,e}}{Q_{c,e-exp}} = \frac{H_{2s} - H_1}{H_2 - H_1} \quad [4-96]$$

where,  $Q_{c,e-exp}$  is the experimental figure of electricity input of heat pump (W).

### 4.3.3 Method and Algorithm for the Steady-state Model Development and Operation

The heat transfer processes eventually achieve an energy balance when the system operates at the steady-state condition and each part of the system establishes a certain temperature when in operation. The algorithm used for modelling the set-up is shown schematically in **Fig. 4-18** and illustrates as the followings:

- (i) Input external weather conditions, system design and operating parameters;

---

<sup>5</sup> The  $COP_{PV/T}$  will be preliminarily used in this section to characterise the system performance comprehensively, while an overall assessment of the heat pump cycle, including both the basic thermal  $COP_{th}$  and  $COP_{PV/T}$ , will be applied in practice during the next section.



- (ii) Assume the refrigerant mass flow rate  $m_r$  and the refrigerant evaporating heat gain, calculating  $Q_{e,t}$  using equation [4-89];
- (iii) Assume the cell temperature  $t_p$ , and commence the following analysis:
  - A. Heat balance of the glazing cover could be analysed using equations [4-57] to [4-68], which results in determination of the heat loss,  $Q_L$ ;
  - B. Heat balance of the PV cells could be analysed using equations [4-56], [4-69], [4-70] and [4-72], which results in determination of the converted solar electricity,  $Q_e$  and heat,  $Q_{th}$ ;
  - C. Heat transfer from the PV cells to the heat pump evaporator could be analysed by equations [4-75] to [4-92], which results in determination of the useful heat gain,  $Q_u$ ;
  - D. If  $(Q_{th} - Q_u) / Q_{th} > 0.1\%$  (error allowance), then increase  $t_p$  by  $0.1\text{ }^\circ\text{C}$  and return to step (iii) for re-calculation;

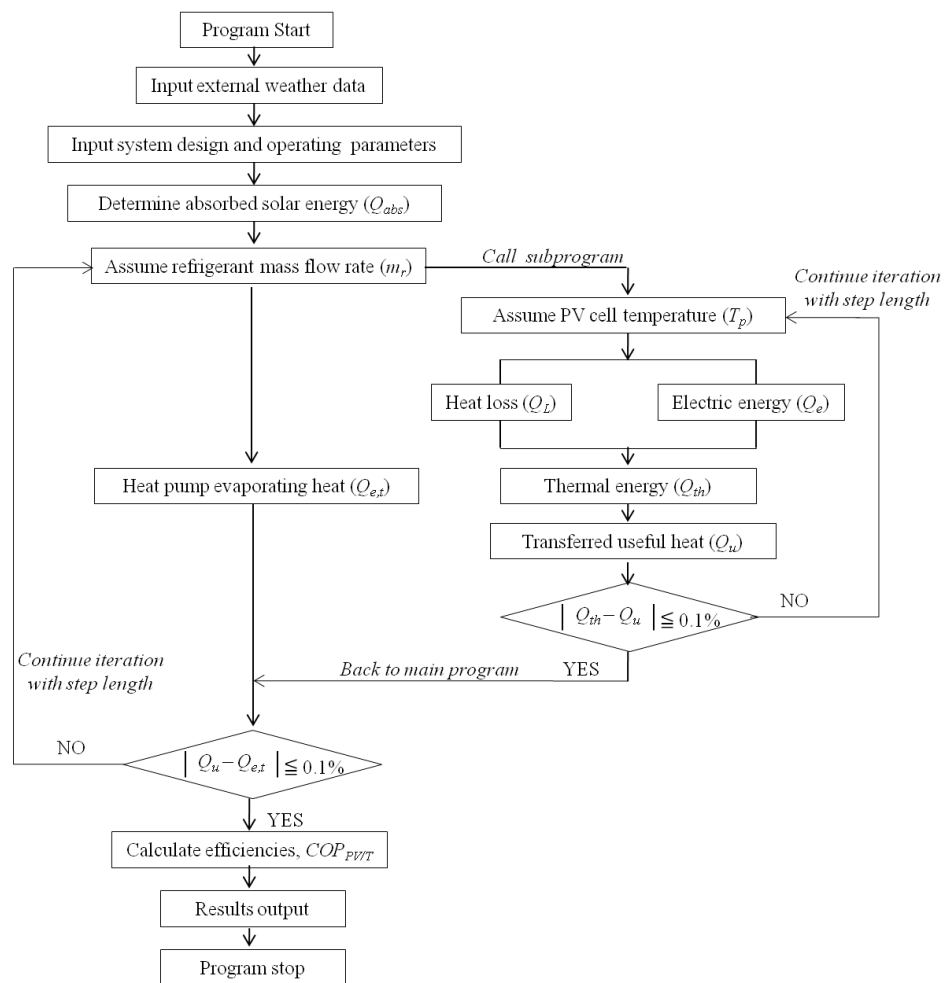


Fig. 4-18: Flow chart for the calculation of steady-state system performance

- E. If  $(Q_{th} - Q_u) / Q_{th} < -0.1\%$  (error allowance), then decrease  $t_p$  by  $0.1\text{ }^\circ\text{C}$  and return to step (iii) for re-calculation;
- F. If  $-0.1\% \leq (Q_{th} - Q_u) / Q_{th} \leq 0.1\%$ , the system achieves heat balance;
- (iv) If  $(Q_u - Q_{e,t}) / Q_u > 0.1\%$  (error allowance), then increase  $m_r$  by  $0.001\text{ kg/s}$  and return to step (ii) for re-calculation;
- (v) If  $(Q_u - Q_{e,t}) / Q_u < -0.1\%$  (error allowance), then decrease  $m_r$  by  $0.001\text{ kg/s}$  and return to step (iii) for re-calculation;
- (vi) If  $-0.1\% \leq (Q_u - Q_{e,t}) / Q_u \leq 0.1\%$ , the system achieves heat balance;
- (vii) Calculate the module's energetic efficiencies, system work-back ratio and the advanced performance coefficient of  $COP_{PV/T}$  using equations [4-71], [4-73], [4-74] and [4-93] to [4-96];
- (viii) Finally determine  $T_p$  and the program stops.

#### 4.3.4 Validation of the System Stead-state Model by the Published Data

The steady-state model for the whole system was validated for its suitability and accuracy by comparing the modelling results with the published experimental data for a PV/solar-assisted heat pump/heat pipe (PV-SAHP/HP) system developed by Fu et al. [4.13]. They attached groups of PV cells to a flat-plate heat pipe thermal collector and a direct-expansion evaporator in a heat pump for hot water generation. There were three operating modes during their testing, and the heat pipe operating mode with the greatest similarity to the proposed PV/LHP system was selected to validate the steady-state model. **Fig. 4-19** schematically shows the testing rig, while **Table 4-3** displays the design and operational parameters of the reference system. The system performance indicators are defined congruously according to the mathematical descriptions in this section. For the heat pipe operating mode, heat pipes are regarded as exchanging heat with the tank water directly. The correlation coefficient ( $r$ ) and the root mean square percentage deviation ( $e$ ) defined in equations [4-53] and [4-54] were applied to analyse the difference between the theoretical and the published experimental results.

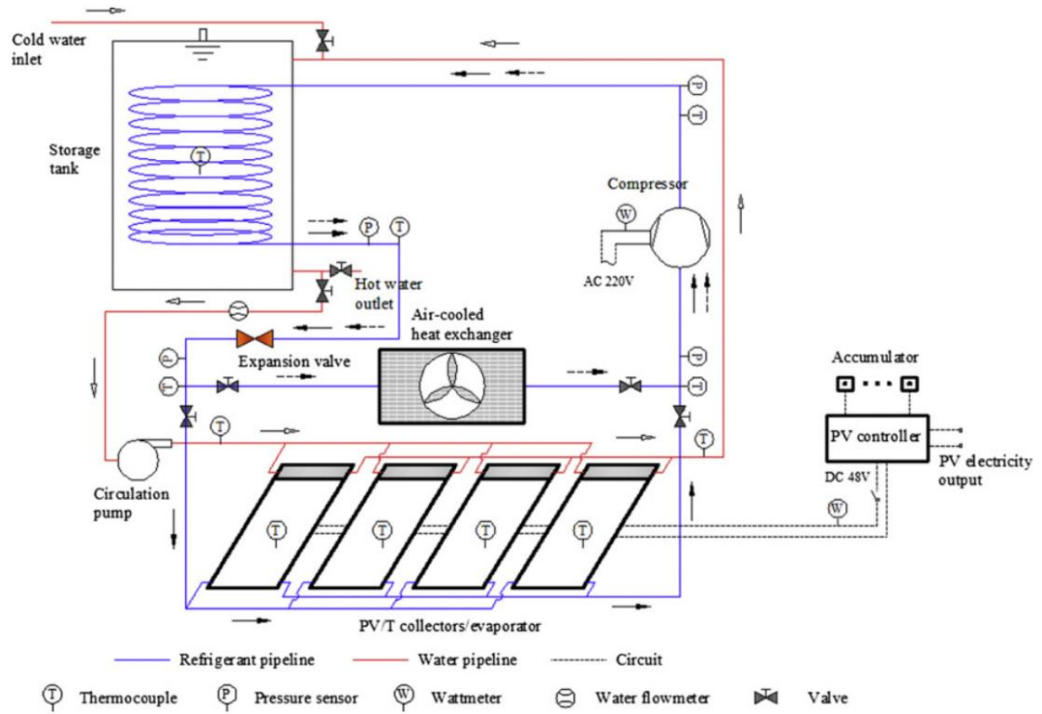


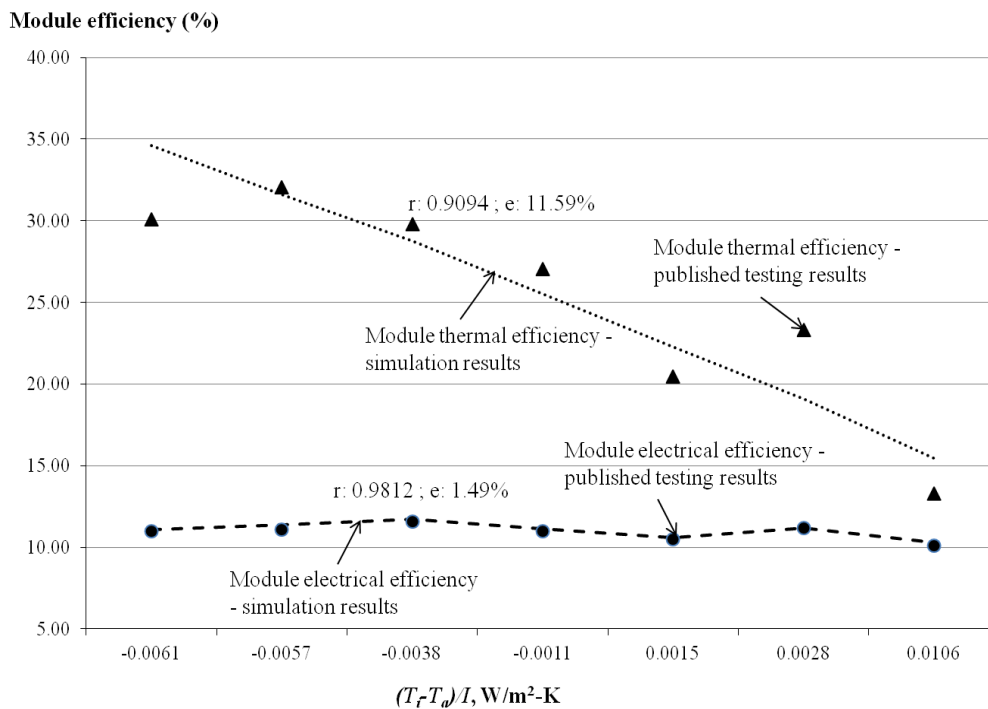
Fig. 4-19: Schematic of the referenced PV-SAHP/HP test rig [4.13]

Table 4-3: Design and operation parameters of the referenced PV-SAHP/HP system [4.13]

Design parameters (unit)	Value
<u>Glazing cover</u>	
Tempered glazing	Single cover
<u>PV layer</u>	
Thickness of transparent TPT cover (mm)	0.2
EVA thickness (mm)	0.5
Type of PV cells	mono-crystalline silicon
Standard efficiency of PV cells (%)	15.8
Thickness of TPT baseboard (mm)	0.2
Cell area of single module (m <sup>2</sup> )	0.728
Total PV area (m <sup>2</sup> )	2.912
<u>Fin sheet</u>	
Aluminium plate (length × width × thickness, mm)	1260 × 962 × 1.16
<u>Heat pipe</u>	
Pipe dimension (diameter × thickness × length, mm)	8 × 0.7 × 1000
Distance between two adjacent heat pipes (mm)	140
Number of heat pipes	9
<u>Heat pipe condenser</u>	
Pipe dimension (diameter × thickness × length)	24 × 1 × 120

Design parameters (unit)	Value
<u>Water flow cycle</u>	
Water pump power (W)	46
Water flow rate (l/min)	7.35
Water tank capacity (litres)	560
<u>Collecting area</u>	
Single module area (m <sup>2</sup> )	1.167
Total module area (m <sup>2</sup> )	4.688

**Fig. 4-20** presents the steady-state simulation results of the module efficiencies against external weather parameters by inputting the design, operation and weather conditions of the referenced PV-SAHP/HP experimental rig. The correlation coefficients ( $r$ ) and the root mean square percentage deviation ( $e$ ) for modelling and testing the module electrical/thermal efficiencies were 0.9812/0.9094 and 1.49%/11.59%, respectively.



**Fig. 4-20: Comparison of steady-state simulation results with the published testing data**

The reason for errors may exist in the utilisation of the simplified assumptions/empirical formulas, and an inaccurate estimation of the heat loss coefficient due to a lack of wind data. However, the accuracy achieved by this steady-state model was acceptable from the engineering point of view, and

could be therefore applied to characterise the system performance and recommend appropriate parameters for further system fabrication and operation. In addition, this steady-state model was further verified for accuracy by the dedicated experiments described in the next chapter.

#### **4.3.5 Model Operation and Result Discussion of the System Steady-state Performance**

Through the established steady-state model, parametric studies of the PV/LHP heat pump system could, therefore, be conducted under a series of laboratory-controlled conditions, including the impacts of solar radiation, air temperature, air velocity, heat pump evaporation temperature, glazing cover, and the number of heat-absorbing pipes. A detailed discussion will be presented in the next chapter for a straightforward parallel comparison between the modelling and test results of the fabricated prototype system, thus leading to verification or modification of the steady-state model for system performance characterisation.

### **4.4 Dynamic Model for the Evaluation of System Performance**

#### **4.4.1 Modelling Objective for the System Dynamic Performance**

The dynamic modelling had the aim of evaluating the performance of the integrated PV/LHP heat pump system in real climatic operational conditions, which are simultaneously affected by several critical factors, i.e., solar radiation, air temperature, air velocity and operating time. This modelling enabled (a) a prediction of system performance in real climatic operational conditions, (b) a forecast of seasonal system performance, and (c) a recommendation for an appropriate climate region suitable for the operation of such a PV/LHP heat pump system. The results derived from the dynamic modelling were utilised in the system's socio-economic analysis, which will be conducted in Chapter 7.

#### 4.4.2 Thermal Fluid Theory and the Associated Mathematical Equations of the System Dynamic Model

For the PV/LHP module-based heat pump water heating system, the transient operational model involved six energy balance equations (as illustrated in **Fig. 4-21**): ① a heat balance equation for the glazing cover; ② a heat balance equation for the PV layer; ③ an one-dimensional unsteady-state heat conduction of the fin sheet; ④ a heat balance equation for the LHP operation; ⑤ heat balance equations for the heat pump cycle and ⑥ the water tank. To simplify the energy model, the following hypotheses were made:

- The vertical temperature gradient over the glazing cover was ignored.
- The ohm electrical losses in the solar cells and PV module are negligible.
- The heat capacities of the EVA filler (the adhesive for connecting the PV cells and PV glass during lamination) were not included, treating the PV layer as a uniform temperature variation.
- Heat conduction in the longitudinal direction of the fin sheet was ignored.
- An isentropic efficiency up to 88% was assumed for the calculation of the compressor power consumption.

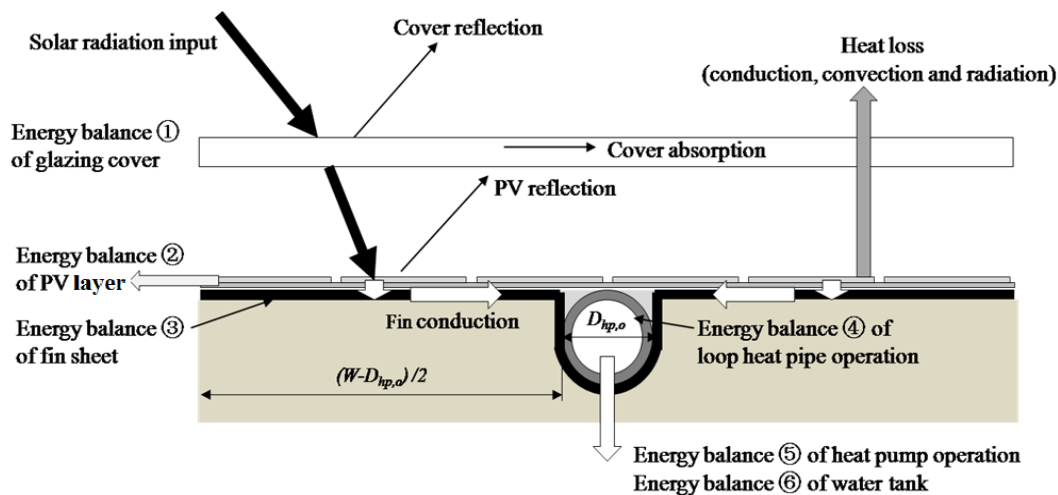


**Fig. 4-21:** Schematic of the transient energy balances in the system

### (1) Heat Balance of the Glazing Cover

To describe the time dependence of the heat flows on a single glazing cover, the corresponding energy balance equation is given by [4.11]

$$\rho_c c_c \delta_c \frac{\partial T_c}{\partial t} = I \alpha_c + (h_{c,p-c} + h_{R,p-c})(T_p - T_c) - (h_{c,c-a} + h_{R,c-a})(T_c - T_a) \quad [4-97]$$

where,  $\rho_c$ ,  $c_c$  and  $\delta_c$  are respectively the density ( $\text{kg/m}^3$ ), specific heat capacity ( $\text{J/kg-K}$ ) and thickness (m) of the glazing cover;  $t$  is the operation time (s);  $T_c$  and  $T_a$  are respectively the temperatures (K) of glazing cover and ambient air;  $h_{c,p-c}$  and  $h_{c,c-a}$  are respectively the convective heat transfer coefficients ( $\text{W/m}^2\text{-K}$ ) from PV layer to cover and from cover to ambient air; while  $h_{R,p-c}$  and  $h_{R,c-a}$  are respectively the radiative heat transfer coefficients ( $\text{W/m}^2\text{-K}$ ) from PV layer to cover and from cover to ambient air. The corresponding convective heat transfer coefficients can be derived from equations [4-59] to [4-64].

### (2) Heat Balance of the PV Layer

The energy balance equation for the combined PV lamination is [4.11]

$$\rho_p c_p \delta_p \frac{\partial T_p}{\partial t} = \left[ I (\tau_c \alpha)_b (1 - \beta_p) + I (\tau_c \alpha)_p \beta_p - Q_e \right] - (T_p - T_f) / R_{p-f} A_p - (h_{c,p-c} + h_{R,p-c})(T_p - T_c) \quad [4-98]$$

where,  $\rho_p$ ,  $c_p$  and  $\delta_p$  are respectively the average density ( $\text{kg/m}^3$ ), specific heat capacity ( $\text{J/kg-K}$ ) and thickness (m) of the PV layer;  $T_p$  and  $T_f$  are average the temperatures (K) of PV layer and fin sheet;  $(\tau_c \alpha)_b$  and  $(\tau_c \alpha)_p$  are the respectively the transmittance-absorption coefficients of baseboard and PV layer;  $\beta_p$  is the packing factor of PV layer;  $R_{p-f}$  is the overall thermal resistances ( $\text{K/W}$ ) from PV cells to fin sheet;  $A_p$  is the absorbing area of PV layer ( $\text{m}^2$ ).

The overall transient solar transmittance for a single cover becomes [4.9]

$$\tau_c = \frac{\tau_{c,\alpha}}{2} \left\{ \frac{1-r_{\parallel}}{1+r_{\parallel}} \left[ \frac{1-r_{\parallel}}{1-(r_{\parallel}\tau_{c,\alpha})^2} \right] + \frac{1-r_{\perp}}{1+r_{\perp}} \left[ \frac{1-r_{\perp}}{1-(r_{\perp}\tau_{c,\alpha})^2} \right] \right\} \quad [4-99]$$

In above equation, the transmittance due to absorption,  $\tau_{c,a}$  is written as

$$\tau_{c,\alpha} = e^{\left( \frac{K\delta_c}{\cos(\theta_2)} \right)} \quad [4-100]$$

And the refraction angle of direct solar beam,  $\theta_2$  (rad), is given

$$\theta_2 = \sin^{-1} \left( \frac{\sin \theta_1}{n_g} \right) \quad [4-101]$$

where,  $n_g$  is the ratio of the refraction index and is typically 1.526 for glass.  $\theta_1$  is the incidence angle (rad) striking the glazing surface, and for a south-facing tilted plane in the Northern Hemisphere, the expression for the incidence angle is given by [4.9]

$$\cos(\theta_1) = \sin(L_m - \theta) \sin(\delta_m) + \cos(L_m - \theta) \cos(\delta_m) \cos(h_m) \quad [4-102]$$

The thermal resistance from PV cells to the fin sheet is calculated as

$$R_{p-f} = R_p + R_{EVA} + R_{ei} = \frac{\delta_p}{k_p A_p} + \frac{\delta_{EVA}}{k_{EVA} A_p} + \frac{\delta_{ei}}{k_{ei} A_p} \quad [4-103]$$

where,  $R_p$ ,  $R_{EVA}$  and  $R_{ei}$  are respectively the thermal resistances (K/W) of PV cells, EVA layer and electrical insulation;  $k_p$ ,  $k_{EVA}$ ,  $k_{ei}$ ,  $\delta_p$ ,  $\delta_{EVA}$ , and  $\delta_{ei}$  are respectively the thermal conductivities (W/m-K) and thickness (m) of PV layer, EVA layer and electrical insulation.



The corresponding electricity output per unit area,  $q_e$  (W/m<sup>2</sup>), is defined by

$$q_e = I(\tau_c \alpha)_p \beta_p \eta_{rc} [1 - \beta_{PV}(T_p - T_{rc})] \quad [4-104]$$

### (3) Heat Balance of the Fin Sheet

The time-dependent heat conductance of the PV-based fin sheet can be tackled as a typical one-dimensional unsteady-state heat transfer on an infinite flat plate. The fin sheet can be divided into various small segments depending on the specific sheet size and differential step space, shown in **Fig. 4-22**. The temperature profile is thereby assumed to be symmetrical with respect to the LHP evaporator location and its heat balance equations are expressed as [4.11]

$$\left\{ \begin{array}{l} \rho_f c_f \delta_f \frac{\partial T_f}{\partial t} = k_f \delta_f \frac{\partial^2 T_f}{\partial x^2} + (T_p - T_f) / R_{p-f} A_p \\ - (T_f - T_a) / (R_{f-a} A_{fs} + 1 / h_a A_{fe}) \end{array} \right. \quad [4-105]$$

$$\left\{ \begin{array}{l} \rho_f c_f \delta_f \frac{\partial T_{f,11}}{\partial t} = (T_{p,11} - T_{f,11}) / R_{p-f} A_p \\ - (T_{f,11} - T_{hp,w}) / R_{f-hp} A_{fc} - (T_{f,11} - T_a) / R_{f-a} A_{fs} \end{array} \right. \quad [4-106]$$

where,  $\rho_f$ ,  $c_f$  and  $\delta_f$  are respectively the average density (kg/m<sup>3</sup>), specific heat capacity (J/kg-K) and thickness (m) of fin sheet;  $T_f$  and  $T_{hp,w}$  are the average temperatures (K) of fin sheet and heat-pipe wall surface;  $T_{p,11}$  and  $T_{f,11}$  are the temperatures (K) of PV layer and fin sheet at the 11 node;  $k_f$  is the thermal conductivity of fin sheet (W/m-K);  $x$  is the length along the fin width direction (m);  $R_{f-a}$  and  $R_{f-hp}$  are the overall thermal resistances (K/W) from fin sheet to ambient air and from fin sheet to heat pipe;  $h_a$  is the convective coefficient of surrounding air (W/m<sup>2</sup>-K);  $A_{fc}$ ,  $A_{fs}$  and  $A_{fe}$  are respectively the central fin area (m<sup>2</sup>), insulation areas around fin sheet (m<sup>2</sup>) and the edge area of fin sheet (m<sup>2</sup>).

The initial temperature and boundary conditions are described as

$$\begin{cases} T(x, 0) = T_{f,i}^0, t = 0 \\ -k_f \frac{\partial T}{\partial x} \Big|_{x=0} = h_a (T_{f,0} - T_a), t > 0 \\ T\left(\frac{W}{2}, t\right) = T_{f,11}, t > 0 \end{cases} \quad [4-107]$$

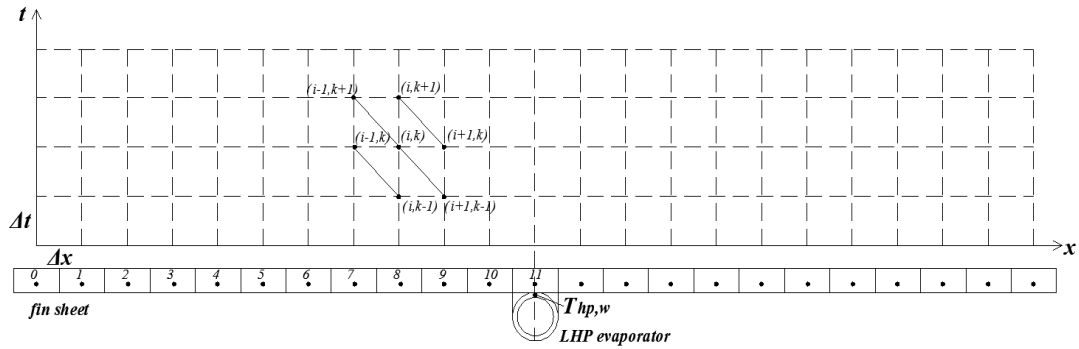


Fig. 4-22: Grid meshing for the fin sheet along the width

The thermal resistances of the insulation bodies separating the fins from the air and beneath the fins are, respectively, written as

$$R_{f-a} = \frac{\delta_{fs}}{k_{fs} A_{fs}} \quad [4-108]$$

$$R_{f-hp} = \frac{\delta_f}{k_f A_{fc}} \quad [4-109]$$

where,  $k_{fs}$  and  $\delta_{fs}$  are the thermal conductivity (W/m-K) and thickness (m) of the insulation around fin sheet respectively.

#### (4) Heat Balance of the LHP

The time-dependent heat transfer variation within the loop heat pipe is [4.11]

$$\frac{1}{4}\pi(D_{hp,o}^2 - D_{hp,in}^2)\rho_{hp}c_{hp}L_{hp}\frac{\partial T_{hp,w}}{\partial t} = (T_{f,11} - T_{hp,w})/R_{f-hp}A_{fc} - (T_{hp,w} - T_{r,m})/R_{hp-r} - (T_{hp,w} - T_a)/R_{hp-a} \quad [4-110]$$

where,  $\rho_{hp}$ ,  $c_{hp}$  and  $\delta_{hp}$  are respectively the average density (kg/m<sup>3</sup>), specific heat capacity (J/kg-K) and thickness (m) of LHP evaporation section;  $T_{r,m}$  is the mean temperature (K) of refrigerant;  $R_{hp-a}$  is the thermal resistance between the heat pipe transportation line and the ambient air (K/W), given by

$$R_{hp-a} = \frac{\ln(D_{hp,o}/D_{hp,in})}{2\pi L_{hp}k_{hp}} + \frac{1}{h_a A_{hp}} \quad [4-111]$$

Thermal resistance between the LHP evaporation section and the heat-pump refrigerant,  $R_{hp-r}$  (K/W), is considered as the overall value that occurring in different components, including heat pipe wall ( $R_{hp,w}$ ), wick structure ( $R_{wi}$ ), liquid film ( $R_{lf}$ ), heat exchanger ( $R_{hx}$ ) and refrigerant flow ( $R_r$ ). Other resistances, such as those of the liquid-vapour interface at the wick structure and the vapour flow in the vapour line, can be ignored due to their much smaller values calculated in the previous section. The relative expressions of the thermal resistances can be derived from equations [4-77] to [4-88].

$$R_{hp-r} = R_{hp,w} + R_{wi} + R_{lf} + R_{hx} + R_r \quad [4-112]$$

### (5) Heat Balances of the Heat Pump and Water Tank

The solar heat delivered to the heat pump operation is theoretically given by

$$\frac{\partial(M_r H_{r,e})}{\partial t} = (T_{hp,w} - T_{r,m})/R_{hp-r} - (T_{hp,w} - T_a)/R_{hp-a} \quad [4-113]$$

where,  $M_r$  is the mass of refrigerant (kg);  $H_{r,e}$  is the enthalpy of refrigerant in the evaporation section (J/kg);

With consideration of the additional compressor work input, the condensation heat expelled from the heat pump is defined as [4.12, 4.14]

$$M_w c_w \frac{\partial T_w}{\partial t} = \frac{\partial (M_r H_{r,c})}{\partial t} - (T_w - T_a) / R_{w-a} \quad [4-114]$$

where,  $M_w$  and  $c_w$  are the mass (kg) and special heat capacity (J/kg-K) of water;  $H_{r,c}$  is the enthalpy of refrigerant in the condensation section (J/kg);  $T_w$  is the mean temperature of water in the tank (K);  $R_{w-a}$  is the equivalent thermal resistance between the water and the ambient air (K/W). This amount of heat is fully transported into the tank water.

$$R_{w-a} = \frac{\ln(D_{ws,o} / D_{ws,in})}{2\pi L_{ws} k_{ws}} + \frac{1}{h_a A_{ws}} \quad [4-115]$$

where,  $D_{ws,o}$ ,  $D_{ws,in}$ ,  $L_{ws}$ ,  $k_{ws}$  and  $A_{ws}$  are respectively the outer/inner diameters (m), length (m), thermal conductivity (W/m-K) and surface area (m<sup>2</sup>) of water-tank insulation.

Once the evaporation and the condensation temperatures are set constantly, the mass flow rate is considered as the primary parameter that determines the thermodynamic process in the heat pump, which can be congruously treated as a special variable in despite of using of the fixed or variable speed compressor: (1) the fixed speed compressor varies the mass flow rate by simply switching on or off during a certain operational period; (2) the variable speed compressor adjusts its motor speed automatically to affect the mass flow rate transiently.

## (6) Grouped differential equations set-up

To resolve the above equations using a numerical method, the differential equations can be rewritten in the formats of the MATLAB's "ode15s" and "pdepe" solvers using an implicit backward difference formula and the finite element methods (FEM) and [4.15]. The MATLAB "pdepe" solver is normally applied for the initial-boundary value problems to solve the parabolic and

elliptic partial differential equation (PDE) systems in one space variable “ $x$ ” and time “ $t$ ”. This solver converts the PDE into ordinary differential equation (ODE) using a second-order accurate spatial discretization based on a set of nodes, which is recognised as a classical FEM method. The time integration is completed with the “*ode15s*” solver, which is a variable order solver to resolve the algebraic equations according to the backward differentiation formulas.

To use the “*ode15s*” solver, the grouped ODEs is needed to be rewritten in below format [4.15]

$$\left\{ \begin{aligned} dy &= [T_c; T_p; T_{f,11}; T_{hp,w}; m_r; T_w] = [y(1); y(2); y(3); y(4); y(5); y(6)] \\ dy(1) &= \left\{ I\alpha_c + (h_{c,p-c} + h_{R,p-c})[y(2) - y(1)] - (h_{c,c-a} + h_{R,c-a})[y(1) - T_a] \right\} / \rho_c c_c \delta_c \\ dy(2) &= \left\{ \begin{aligned} &[I(\tau_c \alpha)_b (1 - \beta_p) + I(\tau_c \alpha)_p \beta_p - Q_e] \\ &- [y(2) - y(3)] / R_{p-f} A_p - (h_{c,p-c} + h_{R,p-c})[y(2) - y(1)] \end{aligned} \right\} / \rho_p c_p \delta_p \\ dy(3) &= \left\{ \begin{aligned} &[y(2) - y(3)] / R_{p-f} A_p - [y(3) - y(4)] / R_{f-hp} A_{fc} \\ &- [y(3) - T_a] / R_{f-a} A_{fs} \end{aligned} \right\} / \rho_f c_f \delta_f \\ dy(4) &= \left\{ \begin{aligned} &\frac{4}{\pi} [y(3) - y(4)] / R_{f-hp} A_{fc} \\ &- [y(4) - T_{r,m}] / R_{hp-r} - [y(4) - T_a] / R_{hp-a} \end{aligned} \right\} / (D_{hp,o}^2 - D_{hp,in}^2) \rho_{hp} c_{hp} L_{hp} \\ dy(5) &= \left\{ [y(4) - T_{r,m}] / R_{hp-r} - [y(4) - T_a] / R_{hp-a} \right\} / H_{r,e} \\ dy(6) &= \left\{ y(5) H_{r,c} - [y(6) - T_a] / R_{w-a} \right\} / M_w c_w \end{aligned} \right. \quad [4-116]$$

To use the “*pdepe*” solver, the PDE function, initial and boundary conditions should satisfy the forms below [4.15]

$$\left\{ \begin{array}{l} C \left( x, t, T, \frac{\partial T}{\partial x} \right) \frac{\partial T}{\partial t} = x^{-m} \frac{\partial}{\partial x} \left[ x^m f \left( x, t, T, \frac{\partial T}{\partial x} \right) \right] + s \left( x, t, T, \frac{\partial T}{\partial x} \right) \\ T(x, t_0) = T_0(x) \\ p(x, t, T) + q(x, t) f \left( x, t, T, \frac{\partial T}{\partial x} \right) = 0 \\ t \in [t_0, t_f], x \in [a, b] \end{array} \right. \quad [4-117]$$

In this case, the dedicated PDE can be rewritten as follows

$$\left\{ \begin{array}{l} \rho_f c_f \delta_f \frac{\partial T_f}{\partial t} = k_f \delta_f x^0 \frac{\partial}{\partial x} \left( x^0 \frac{\partial T_f}{\partial x} \right) + \left[ \begin{array}{l} (T_p - T_f) / R_{p-f} A_p \\ -(T_f - T_a) / (R_{f-a} A_{fs} + 1 / h_a A_{fe}) \end{array} \right] \\ T(x, 0) = T_f^0 \\ h_a (T_{f,0} - T_a) + k_f \frac{\partial T}{\partial x} \Big|_{x=0} = 0 \\ T_{f,11} - T \left( \frac{W}{2}, t \right) = 0 \\ t \in [0, End], x \in \left[ 0, \frac{W}{2} \right] \end{array} \right. \quad [4-118]$$

The time step size,  $\Delta t$ , and the space step size,  $\Delta x$ , are, respectively, given at 1 min and 22 mm. The time step size  $\Delta t$  is chosen at 1/5 of the time interval between two measurements in the following experiment, because a smaller time step would consume much more time to calculate and would not affect the results very much, while a larger time step would lead to an unstable calculation process. The space step size is chosen at 1/23 of the fin width by dividing the fin into 23 segments along its width, because a smaller space step

would have a limited impact on the simulation results and a larger space step would lead to an unstable calculation process. As the temperature profile of the fin sheet is assumed to be symmetrical at two sides of the LHP evaporator in the centre, there are then only considered to be 11 elements from the left-hand edge to the fin centre along the fin width, as shown in **Fig. 4-22**.

### (7) Module Efficiencies and System Performance Indicators

The overall performance of a hybrid PV/T system can usually be assessed from aspects of the engineering, economic and environmental implications. In this chapter, an overall evaluation method, as indicated in **Fig. 4-23**, based upon the thermodynamics, was developed and applied for the technical analysis of the prototype and its associated system. Further research in the next chapter will continue to address the economic/market and environmental impacts.

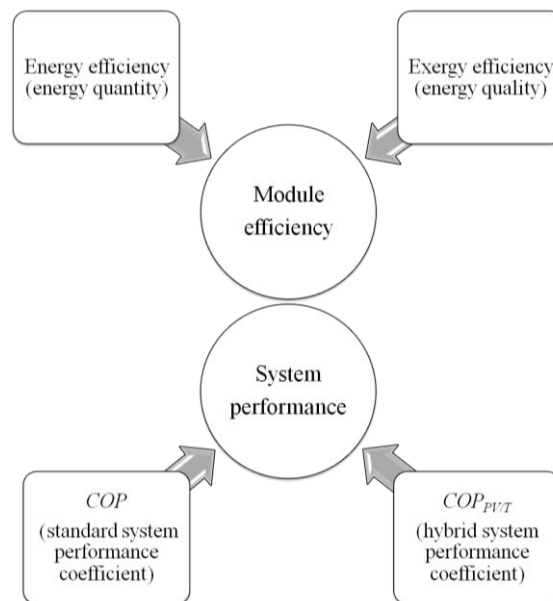


**Fig. 4-23: Technical assessment set-up for the PV/LHP module and its associated system**

#### *I. Assessment Approach for the Module Efficiencies*

##### *i. First-law Thermodynamics Efficiency - Energetic Efficiency*

The overall energetic efficiency is the ratio of the generated electricity and heat to the incident solar radiation striking the module. It is yielded from the first

law of thermodynamics and indicates the percentage of the energy converted from solar radiation. The descriptions of the energetic efficiencies are

$$\eta_e = \frac{\int_{t_0}^{t_{k+1}} Q_e dt}{\int_{t_0}^{t_{k+1}} A_m I dt} \quad [4-119]$$

$$\eta_{th} = \frac{\int_{t_0}^{t_{k+1}} Q_{th} dt}{\int_{t_0}^{t_{k+1}} A_m I dt} \quad [4-120]$$

$$\eta_o = \eta_e + \eta_{th} \quad [4-121]$$

#### ii. Second-law Thermodynamics Efficiency - Exergetic Efficiency

As the electricity and heat generated by a PV/T module are essentially not of the same energy grade (quality), the first-law method may be inadequate for justifying the performance of PV/T systems. However, second-law-based exergetic efficiency takes into account the difference in energy grades between heat and electricity, and involves a conversion of low-grade thermal energy into equivalent high-grade electrical energy using the theory of Carnot cycle. The exergetic efficiency in a solar system is defined as the ratio of total exergy (electricity and heat) output to the total exergy of solar radiation input.

For a conventional PV/T module, exergetic efficiency is defined as the ratio of the module-converted exergetic energy, including electricity ( $Ex_e$ ) and heat ( $Ex_{th}$ ), to the total exergetic energy associated with solar radiation ( $Ex_{sun}$ ). For the proposed PV/LHP module, the overall exergetic efficiency ( $\zeta_o$ ) is the sum of the electrical exergetic efficiency ( $\zeta_e$ ) and the thermal exergetic efficiency ( $\zeta_{th}$ ), which is obtained using following equations [4.16]



$$\xi_e = \frac{\int_{t_0}^{t_{k+1}} Ex_e dt}{\int_{t_0}^{t_{k+1}} Ex_{sun} dt} = \frac{\int_{t_0}^{t_{k+1}} Q_e dt}{\int_{t_0}^{t_{k+1}} Ex_{sun} dt} \quad [4-122]$$

$$\xi_{th} = \frac{\int_{t_0}^{t_{k+1}} Ex_{th} dt}{\int_{t_0}^{t_{k+1}} Ex_{sun} dt} \approx \frac{\int_{t_0}^{t_{k+1}} Q_{th} (1 - T_a / T_{hp,w}) dt}{\int_{t_0}^{t_{k+1}} Ex_{sun} dt} \quad [4-123]$$

$$Ex_{sun} = \left(1 - \frac{T_a}{T_{sun}}\right) IA_m \quad [4-124]$$

$$\zeta_o = \zeta_e + \zeta_{th} \quad [4-125]$$

## II. Assessment Approach for System Performance

The basic thermal performance coefficient ( $COP_{th}$ ) of a heat pump system is defined as the ratio of the heating or cooling generated over the electrical energy consumed. The  $COP_{th}$  provides a measure of the performance of a heat pump that is analogous to the thermal efficiency of power cycles, evaluated by

$$COP_{th} = \frac{\int_{t_0}^{t_{k+1}} Q_w dt}{\int_{t_0}^{t_{k+1}} (Q_w - Q_{th}) dt} \quad [4-126]$$

The advanced overall system coefficient of thermal and electrical performance ( $COP_{PV/T}$ ) is similarly defined as

$$COP_{PV/T} = \frac{\int_{t_0}^{t_{k+1}} (Q_w + Q_e / 0.38) dt}{\int_{t_0}^{t_{k+1}} (Q_w - Q_{th}) dt} \quad [4-127]$$

In the meantime, if part or all of the PV electricity is applied to drive the heat pump compressor, the system net electricity output could be calculated. Thus, the ratio of system net electricity generation is defined as the ratio of the net electricity output to the total absorbed solar energy

$$\eta_{e,n} = \frac{\int_{t_0}^{t_{k+1}} [Q_e - (Q_w - Q_{th})] dt}{\int_{t_0}^{t_{k+1}} A_m I dt} \quad [4-128]$$

In some potential cases, the system is operated in a climate of weak solar radiation but a warm air temperature. Where PV electrical generation is insufficient to drive the compressor, the ratio of the system net electricity output would become negative, which means there is an additional desire to input electricity into the system.

#### 4.4.3 Method and Algorithm for the Dynamic Model Development and Operation

An initial temperature distribution ( $t = 0$ ) from the module cover to the water in the tank is desired before starting the iteration. The corresponding initial and boundary conditions, i.e., solar radiation, air temperature, wind speed and water temperature, were obtained from the experimental records. The algorithm is presented in a flow diagram in **Fig. 4-24**, which is also interpreted as follows:

- (i) Assign the basic system design and operating parameters into code.
- (ii) Input the external boundary conditions from the testing records.
- (iii) Assume the initial parameters' values,  $T_c^0, T_p^0, T_f^0, T_{hp,w}^0, T_{r,m}^0, T_w^0, m_r^0$ .
- (iv) Set up the time step size,  $\Delta t$ , and space step size,  $\Delta x$ , and start the calculation.
- (v) Establish the ODE system by carrying out heat analysis on each module/system component and rewriting them in the required format of the “ode15s” solver. For a single time point of  $t$ , the system energy balance can be determined by the integration of the following equations:

- (a) Analyse the heat balance on the glazing cover using equation [4-97], during which the cover surface temperature  $T_c^{t+\Delta t}$  and PV lamination temperature  $T_p^{t+\Delta t}$  are treated as variables.
- (b) Analyse the heat balance in PV lamination equations [4-98] to [4-104], during which the cover surface temperature  $T_c^{t+\Delta t}$ , PV lamination temperature  $T_p^{t+\Delta t}$ , and fin sheet temperature  $T_f^{t+\Delta t}$  are treated as variables.
- (c) Analyse the heat balance on the central fin sheet (node  $i = 11$ ) using equations [4-105] to [4-109], during which the PV temperature  $T_p^{t+\Delta t}$ , fin central temperature  $T_{f,11}^{t+\Delta t}$ , and LHP wall temperature  $T_{hp,w}^{t+\Delta t}$  are treated as variables.
- (d) Analyse the heat balance of the LHP using equations [4-110] to [4-112], during which the fin central temperature (node  $i = 11$ )  $T_{f,11}^{t+\Delta t}$  and heat pipe external wall temperature  $T_{hp,w}^{t+\Delta t}$  are treated as variables.
- (e) Analyse the heat balance of the heat pump evaporator using equation [4-113], during which the heat pipe external wall temperature  $T_{hp,w}^{t+\Delta t}$  and mass flow rate  $m_r^{t+\Delta t}$  are treated as variables.
- (f) Analyse the heat balance of the heat pump condenser and water tank using equations [4-114] and [4-115], during which the mass flow rate  $m_r^{t+\Delta t}$  and water temperature  $T_w^{t+\Delta t}$  are treated as variables.
- (g) Group the ODEs in the “*ode15s*” solver as equation [4-116] and solve them as a column vector ( $Y$ ).
- (h) Calculate the ODE results accuracy using the iteration number ( $n$ ):
- If  $\|y^{(n)} - y^{(n-1)}\| > \varepsilon$  (error allowance: 0.1%), then the convergence criteria cannot be achieved and return to step (iv) to decrease the time step by 1 s and the space step by 1 mm for recalculation.
  - If  $\|y^{(n)} - y^{(n-1)}\| \leq \varepsilon$ , then the iteration steps (mesh size) are small enough to achieve the convergence criteria.
- (vi) Rewrite the PDE of the fin sheet in the required format of the “*pdepe*” solver using equations [4-117] and [4-118].
- (vii) Input the boundary condition of the fin sheet (central temperature:  $T_{f,11}^{t+\Delta t}$ ) into the PDE and analyse the transient heat conductance on the fin sheet.
- (viii) Calculate the PDE results accuracy using the iteration number ( $n$ ):

- If  $\|T_f^{(n)} - T_f^{(n-1)}\| > \epsilon$ , then the convergence criteria cannot be achieved and return to step (iv) to decrease the time step by 1 s and the space step by 1 mm for recalculation.
  - If  $\|T_f^{(n)} - T_f^{(n-1)}\| \leq \epsilon$ , then the iteration steps (mesh size) are small enough to achieve the convergence criteria.
- (ix) Carry out the performance calculation using equations [4-119] to [4-128],  $\eta_e, \eta_{th}, \eta_o, \xi_o, COP_{th}, COP_{PV/T}$  and  $\eta_{e,n}$ .
- (x) Complete the operation of the program until time end and export the results.
- (xi) Program stops.

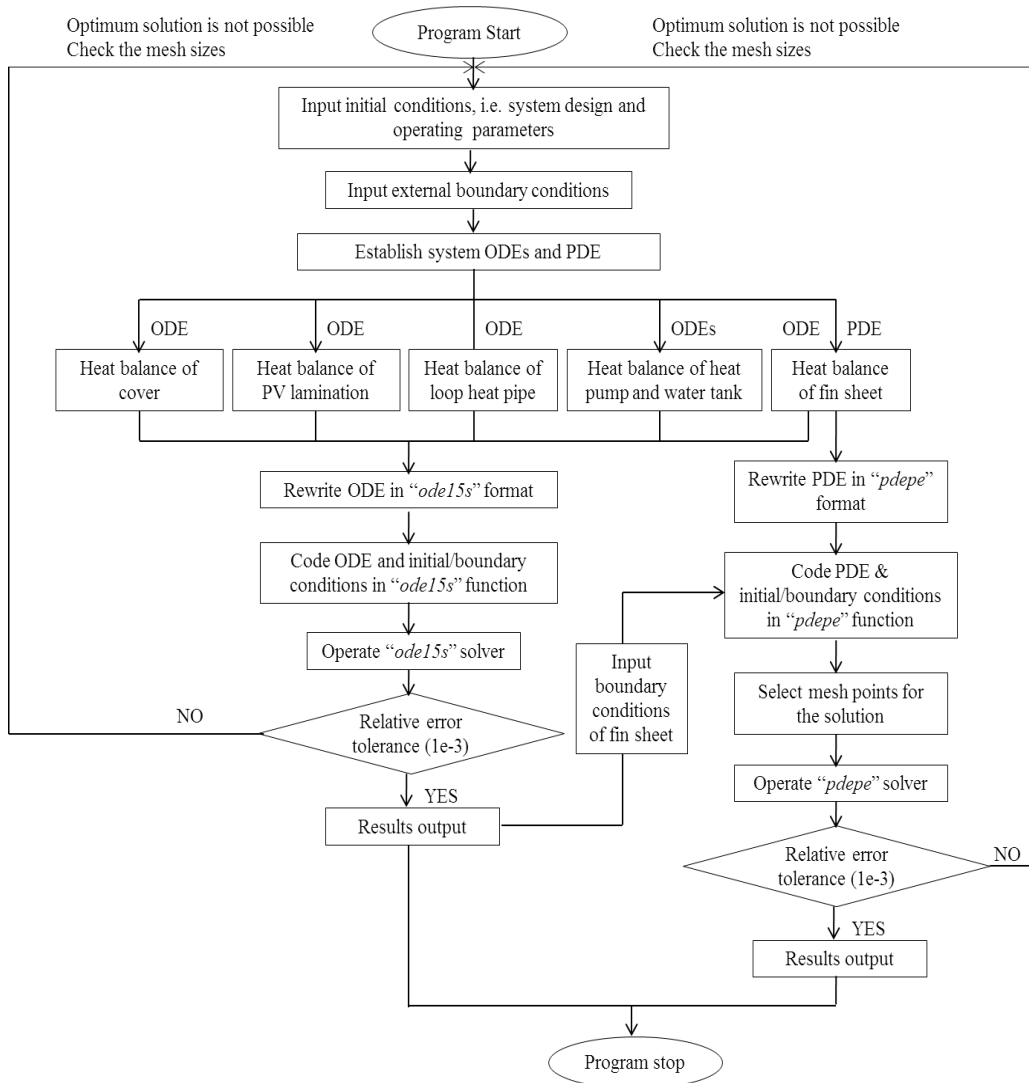


Fig. 4-24: Flow chart for the calculation of the dynamic system performance

#### 4.4.4 Validation of the System Dynamic Model by the Published Data

The dynamic model for the whole system was validated for its suitability and accuracy by comparing the modelling results with the published experimental data of the PV-SAHP/HP system mentioned previously in **Fig. 4-19** and **Table 4-3** [4.13]. The real-time system performance on 8<sup>th</sup> November 2010 in the heat pipe operating mode was adopted to validate the dynamic model. The correlation coefficient ( $r$ ) and the root mean square percentage deviation ( $e$ ) defined in equations [4-53] and [4-54] were applied to analyse the difference between the theoretical and published experimental results.

**Fig. 4-25** presents the transient simulation results of the module outputs against operating time by inputting the design, operation and weather conditions of the referenced PV-SAHP/HP experimental rig. The correlation coefficients ( $r$ ) and the root mean square percentage deviation ( $e$ ) for the modelling and testing of the module electrical/thermal outputs were 0.9938/0.9973 and 4.95%/12.87%, respectively. The reason for errors may exist in the utilisation of simplified assumptions/ empirical formulas, and an inaccurate estimation of the heat loss coefficient due to a lack of wind data. However, the accuracy achieved by this dynamic simulation model was acceptable from the engineering point of view, and could, therefore, be applied to evaluate the system performance in real climates and for recommending appropriate regions for operation. In addition, the accuracy of this dynamic model will be further verified using the dedicated experiments outlined in Chapter 6.

#### 4.4.5 Model Operation and Results Discussion of the System Dynamic Performance

Through the established dynamic model, evaluation of the PV/LHP heat pump system could, therefore, be conducted in real climate conditions. A detailed discussion will be presented in Chapter 6 for a straightforward parallel comparison between the modelling and test results of the fabricated prototype system, thus leading to verification or modification of the dynamic model for further system performance prediction.

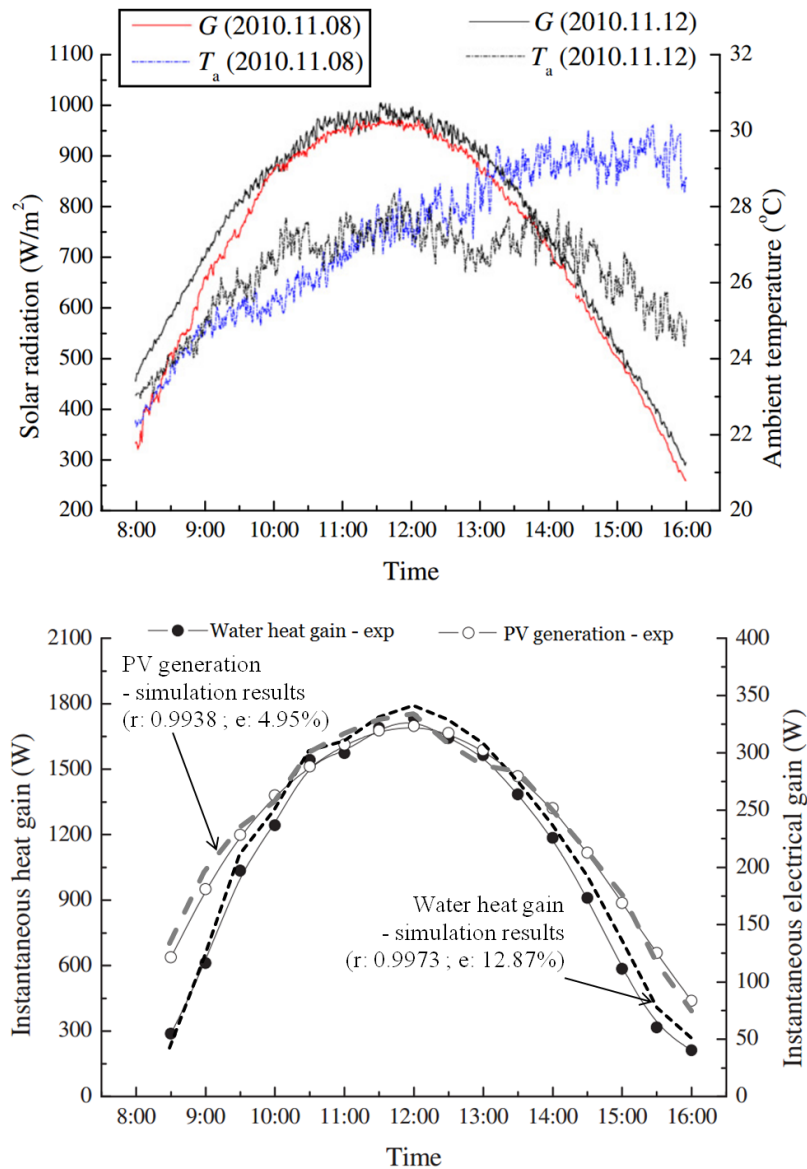


**Fig. 4-25: Comparison of the dynamic simulation results with the published testing data**

## 4.5 Chapter Summary

This chapter investigated the theory behind the LHP and the PV/LHP heat pump system. Three computer simulation models were built for the LHP heat transfer capacity and for the system steady-state/dynamic performance. These simulation models were preliminarily validated by the published test results with a reasonable accuracy in predicting LHP/system performance.

In the LHP analytical model, six operational limits were considered, including viscous, sonic, entrainment, capillary, boiling and liquid filling mass. The

impact of several of the operational and geometric parameters of the LHP on its heat transfer limits was investigated. It was found that such an LHP with a dedicated vapour-liquid separation structure could achieve a maximum heat transport capacity of about 900 W at a specified operational condition. To maintain a high heat transfer coefficient for the LHP for the entire system, the simulation results recommend: (1) maintaining an appropriate operational temperature of lower than 30 °C after counterbalancing the LHP performance and the required PV temperature; (2) adopting a compound mesh-screen wick structure rather than sintered powder and groove; (3) increasing the evaporator diameter appropriately, e.g., to 22 mm; (4) decreasing the evaporator length appropriately, e.g., to 1.2 m; (5) increasing the evaporator inclination angle to 30-60° after counterbalancing the LHP performance and the absorption of solar radiation; (6) increasing the vapour column diameter in the three-way fitting from 10 mm; (7) filling a proper liquid volume to more than 0.01 litre; and (8) raising the heat pipe condenser at least 0.3 m above its evaporator. With the above recommendations, the LHP device could meet the heat-removal demand, especially in Shanghai where the experiment will be conducted.

Through the established steady-state model, parametric studies of the PV/LHP heat pump system could, therefore, be conducted under a series of laboratory-controlled conditions, including the impacts of solar radiation, air temperature, air velocity, heat pump evaporation temperature, glazing cover, and the number of heat-absorbing pipes. More detailed discussion will be expanded in the next chapter for a straightforward parallel comparison between the modelling and test results of the fabricated prototype system, thus leading to verification or modification of the steady-state model for system performance characterisation.

Through the established dynamic model, evaluation of the PV/LHP heat pump system could, therefore, be conducted in real climate conditions. A detailed discussion will be provided in Chapter 6 for a straightforward parallel comparison between the modelling and test results of the fabricated prototype system, thus leading to verification or modification of the dynamic model for further system performance prediction.

## CHAPTER 5: PROTOTYPE FABRICATION, LABORATORY SCALE MEASUREMENT AND STEADY-STATE MODEL VALIDATION

### 5.1 Chapter Introduction

This chapter introduces the specific process for the fabrication and laboratory experiment of the PV/LHP heat pump prototype system. The major works completed in this chapter are presented as follows:

- (1) The fabrication methods for the primary system components, such as the LHP, and the integrated PV/LHP module are described in detail.
- (2) Based on the previous simulation results and the established experimental prototype, a group of laboratory-controlled experiments were conducted to enable characterisation of the electrical and thermal performance of the prototype system.
- (3) A number of impacting factors, including the Al-alloy-based PV layer, solar radiation, air temperature, air velocity, heat pump evaporation temperature, glazing cover and the number of LHPs, were investigated in terms of their correlation with the system's solar efficiency and COP.
- (4) An equivalent comparison between the modelling and the experimental results under the selected experimental conditions was conducted, thus enabling validation of the steady-state simulation model.

The established experimental rig was further tested under the real climatic conditions outlined in the next chapter. The verified steady-state model could be applied to later optimisation of integrated PV/LHP heat pump systems in practice.

### 5.2 Fabrication of the Prototype System

The prototype system was fabricated at the Shanghai Pacific Energy Centre in China. The fabrication process and method for the prototype PV/LHP heat



pump system were detailed with four major aspects, such as the Al-alloy-based PV layer, the LHP, the PV/LHP module and the assembly of the integrated system.

### 5.2.1 Aluminium-alloy-based PV Layer

An anodic-oxide filming method was applied to coat 20  $\mu\text{m}$  black film on a 0.5 mm thick Al-alloy sheet (5052), which not only serves as an electrical insulation device, but also protects the baseboard from corrosion during its life-cycle operation. **Fig. 3-2 (b)** and **Fig. 5-1** show the configuration and fabrication of the Al-alloy-based PV layer, which consists of clean tempered glass on the top, a group of PV cells in the middle, a treated Al-alloy sheet at the back, and two layers of EVA sealant for use in connecting the three components. In addition, pieces of the polyester films were placed under the electrodes for the purpose of preventing a potential short circuit. Whilst all these layers were positioned in sequence, they were placed into a laminator for integration under a 140 °C operational condition. The laminated PV layer was then cooled by the quenching method, which is a rapid cooling process using air. The reason for such a special cooling technique is that the Al-alloy sheet has a much higher thermal expansion coefficient than any other component within the PV layer, and may be bent into an arc (instead of a flat plate) if this process took place under free cooling conditions. **Table 5-1** presents the characteristic parameters of a PV panel under standard testing conditions (1000  $\text{W}/\text{m}^2$  of solar radiation, 25 °C of cell temperature, AM 1.5 solar spectrum).



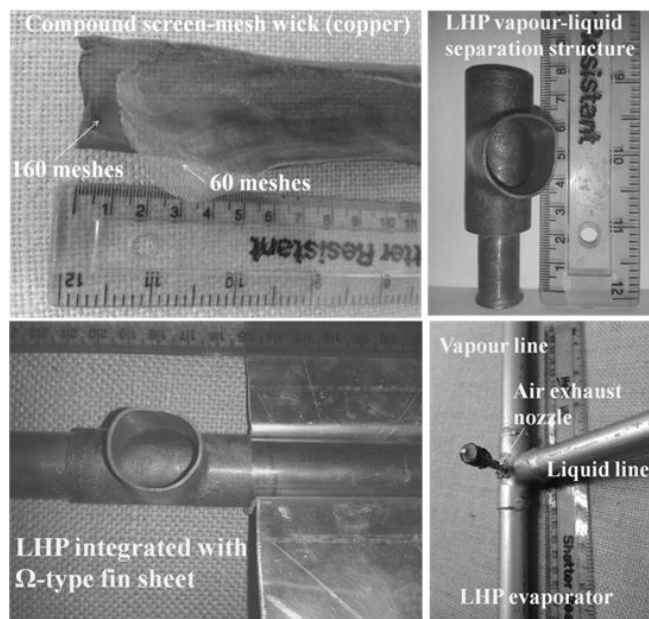
**Fig. 5-1: Fabrication process of the Al-alloy-based PV layer**

**Table 5-1: Photovoltaic characteristics under standard testing conditions**

At short-circuit current	$I_{SC} = 5.54 \text{ A}$ , $V_{SC} = 0 \text{ V}$
At open-circuit voltage	$I_{OC} = 0 \text{ A}$ , $V_{OC} = 22.32 \text{ V}$
At the maximum power point	$I_{mp} = 4.89 \text{ A}$ , $V_{mp} = 18.23 \text{ V}$ ( $P_{mp} = 89.1 \text{ W}$ , $\eta_o = 16.8\%$ )

### 5.2.2 Loop Heat Pipe

The LHP fabrication method is shown in **Fig. 5-2**. A refined three-way copper fitting was internally welded with a piece of '⌘'-type copper tube (smaller diameter), using the oxygen-acetylene welding approach. It was then welded together with the other LHP components, i.e., the LHP evaporator, vapour/liquid lines, and the flat-plate heat exchanger, thus enabling the creation of a closed loop with separate fluid flow channels. Compound copper meshes (160 x 60) were fitted into the heat pipes (evaporation section) to act as the mesh-screen wick structure. The entire loop was filled with 75 ml of water/glycol mixture (95%/5%), which, as a working fluid, is capable of preventing the potential freezing problem. The essential vacuum within the LHP was achieved through the boiling method. The air exhaust nozzle was positioned at the end furthest away from the boiling point, i.e., the end of the liquid line, which enabled the discharge of non-condensed gas.

**Fig. 5-2: Fabrication/connection process of the LHP vapour-liquid separation structure**

### 5.2.3 Integration of the PV/LHP Module

Fabrication of the PV/LHP module is presented in **Fig. 5-3**. The LHP evaporator was placed into an aluminum  $\Omega$ -type fin sheet and attached to the rear surface of the PV layer using thermal-conductive silicon sealants. All the components, including the single tempered glazing, PV layer, LHP evaporator, fin sheet and a polystyrene board for thermal insulation, were integrated together into an AL-alloy casing via clamping and argon-arc welding approaches. The PV/LHP module was fixed to a  $30^\circ$  tilted frame, where the tilt angle was intended to be in accordance with the latitude of the location of the experiment. The overall fabrication process of the PV/LHP module was involved early, at the PV lamination film stage, which is summarised in **Fig. 5-4**. A PV/LHP module has as many manufacturing processes as a typical PV panel, the only changes being the inclusion of a treated Al-alloy baseboard and a number of additional thermal elements. A group of solar cells were wired together and positioned between the clean tempered glass and the coated Al-alloy sheet with two layers of EVA sealant for lamination. The critical thermal components, such as the fin sheet, LHP, insulation and top glazing cover, were then integrated with the PV part to form a hybrid module.

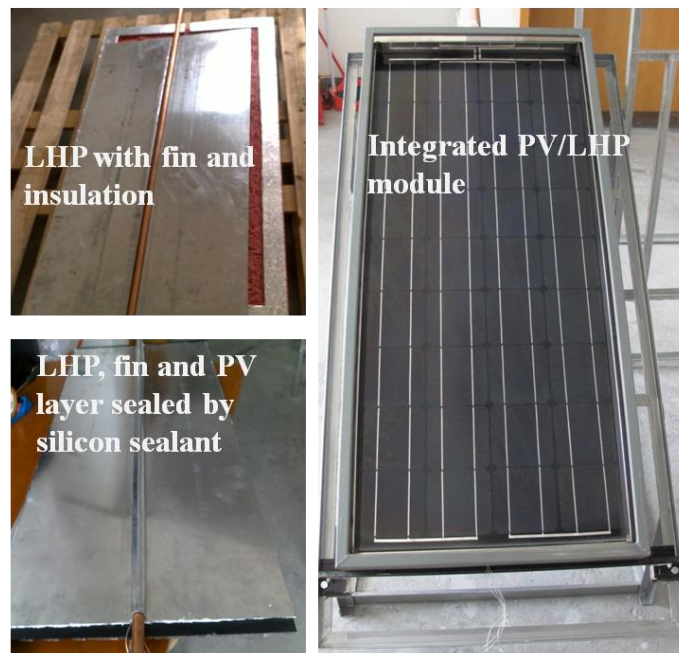


**Fig. 5-3: Fabrication process of the PV/LHP module**

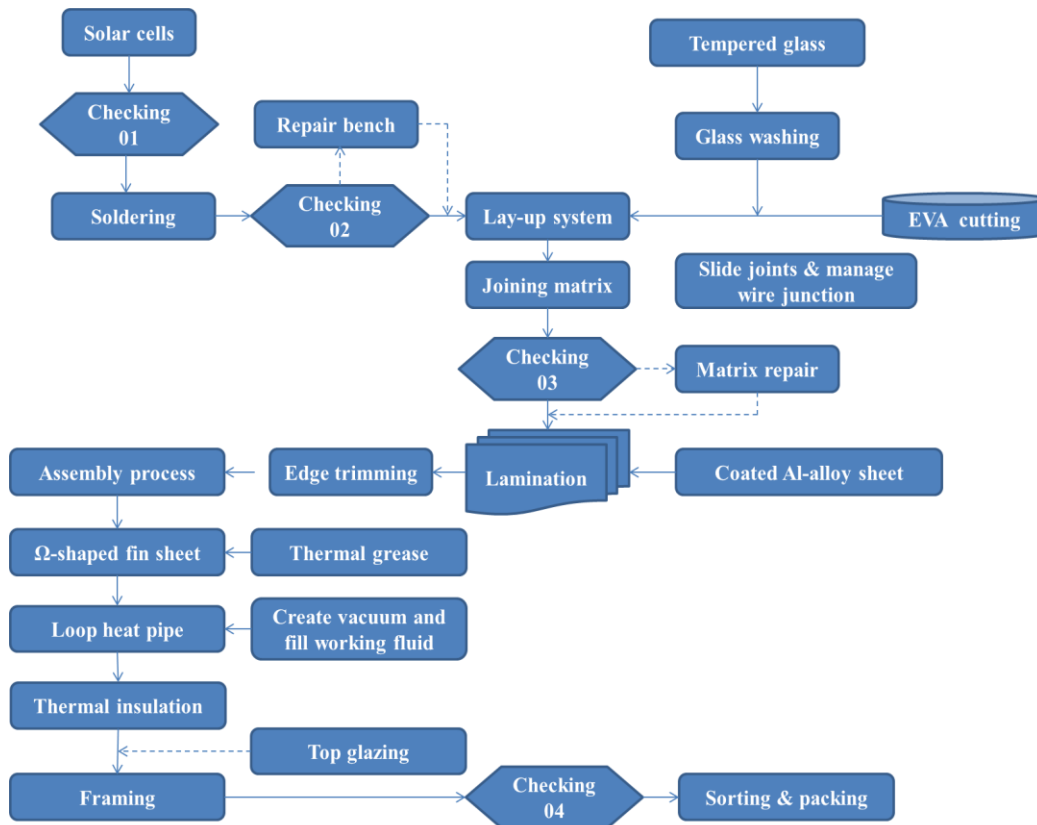
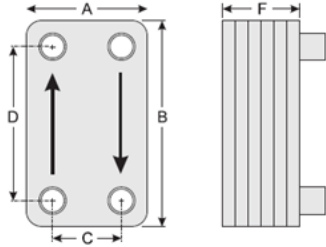







Fig. 5-4: Flow chart indicating the fabrication process of the PV/LHP module

### 5.2.4 System Assembly and Connection

The system employed a 735 W-rated heat pump charged with 300 g of R134a refrigerant. The evaporation and condensation temperatures were set at 10 °C and 55 °C, respectively. A 35-litre water tank with built-in copper heat exchanging coils was connected to the heat pump, acting as its condenser and hot water storage. The system electrical parts included a 12 V (10 A) controller, an 800 W DC/AC inverter, a 100 AH (12 V) battery, and some connection wires. Several insulation materials, including the polyurethane foam for piping and a polystyrene board for the exchangers, were also utilised to minimise the heat loss from the system components. The whole of the piping in the PV/LHP module, heat pump and water tank was finally connected using the oxygen-acetylene welding technique. **Table 5-2** displays the model/capacity of the other primary system components, which are commercially available products and can be directly purchased and assembled into the prototype system.

Table 5-2: Model/capacity of the primary system components

Component Name	Data and dimensions	Value
<b>Flat-plate heat exchanger –</b> <b>Model: BL14-20</b> 	Cooling capacity range CC [kW]	1-4
	Operating pressure [bar]	vacuum -45
	Min/max design temp [ $^{\circ}$ C]	-160/225
	Maximum mass flow rate [ $\text{m}^3/\text{h}$ ]	5
	Dimension, A/B/C/D/F [mm]	76/206/42/172/55
	Plate pack length [mm]	2.3
	Plate number	20
	<b>Heat pump compressor –</b> <b>Model: CAJ4511Y</b>	Nominal capacity [W]
	Primary refrigerant	R134a
	Displacement [ $\text{cm}^3$ ]	32.7
	Oil charge quantity [ $\text{cm}^3$ ]	887
	Voltage 50 Hz nominal [V]	220-240
<b>Electrical expansion valve –</b> <b>Model: TN2</b>	Ambient temperature	-50 to 50 $^{\circ}$ C
	Inlet size [in]	3/8''
	Outlet size [in]	1/2''
	Max. working pressure [bar]	52
	MOPD [bar]	18
<b>Solar controller – Model:</b> <b>HBSC10I</b>	Rated voltage	12/24 V
	Rated current	10 A
	Over voltage protection	30 V
	Full charge cut	27.2 V
	Low voltage cut	21-22 V
<b>Inverter – Model: 12V/800W</b>	Rated power [W]	800
	DC input voltage	10-15
	Convert efficiency	$\geq 95\%$
	Output AC voltage [V]	220
<b>Battery – Model: 12V/100AH</b>	Operating voltage [V]	12
	Charging capacity [AH]	100

## 5.3 Experimental Set-up under Laboratory Conditions

### 5.3.1 Experimental Instrumentation

Apart from the system fabrication, the measurement instruments were also selected and installed in the appropriate positions in the system to enable laboratory-based measurement. The four major parameters to be measured were temperature, power, solar irradiation and air velocity. The thermal detectors were placed, respectively, at the baseboard of the PV lamination, the fin sheet, the heat-absorbing pipe, the end of the fluid transporting lines, the refrigerant inlet and the outlet of the heat exchanger and the water tank. A sensor was also accommodated to record the surrounding air temperature. The electrical output of the PV cells was monitored by a power sensor. A solar photometer and anemoscope were used to record the instant solar irritation and surrounding air velocity. All the measurement sensors were linked to a DT500 data logger and a computer for data recording. **Table 5-3** displays the measurement instruments and their functions during the test process, while **Fig. 5-5** provides a schematic illustration of the experimental rig.

**Table 5-3: List of the experimental testing and monitoring devices**

Device	Specification	Quantity	Location/application
Solar simulator	Tungsten halogen lamps (300 W)	8	Above PV/LHP module
Pyranometer	TQB-2 (Jinzhou Sunlight, China)	1	Module bracket
Anemometer	EC-8SX (Jinzhou Sunlight, China)	1	Near PV/LHP module
Power sensor	WB1919B35-S and WBP112S91 (Weibo, China)	2	PV module output (DC), compressor input (AC)
Flow meter	R025S116N (MicroMotion, USA)	1	Compressor outlet
Resistance temperature detector (RTD)	PT100 RTD probes (China)	10	PV module baseboard, LHP, heat exchanger inlet/outlet, water tank
Thermometer	Testo 605-H1 (Germany)	1	Room temperature
Data logger	DT500 (DataTaker, Australia)	1	Record data

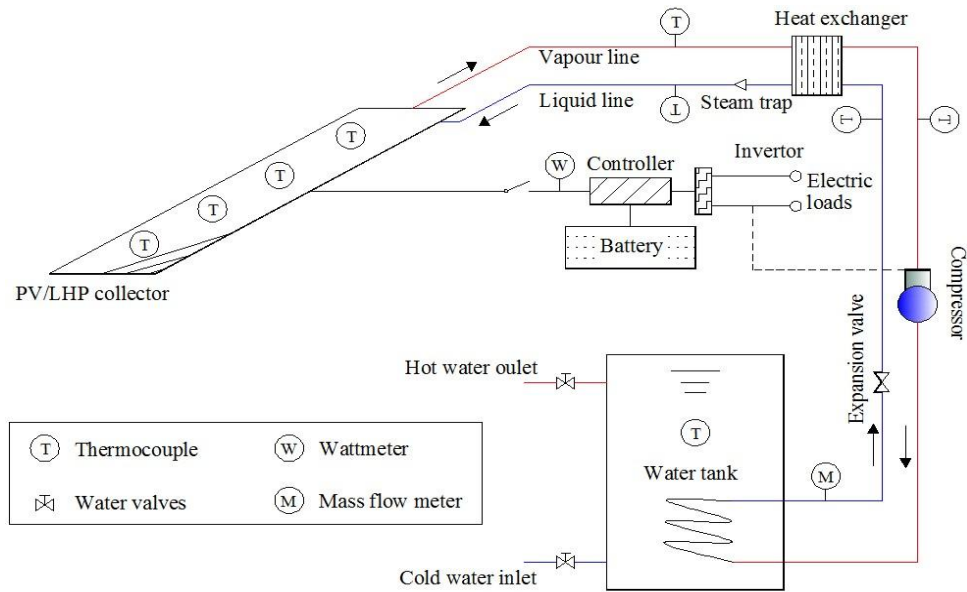


**Fig. 5-5: Experiment rig of the PV/LHP heat pump solar water heating system**

The temperature of the PV cells ( $T_{pv}$ ) was simply considered equivalent to the inner surface of the baseboard and was calculated using the following equation:

$$T_{PV} = \frac{h_{cv,a}}{h_{cd,b}} (T_b - T_a) + T_b \quad [4-129]$$

where,  $h_{cd,b}$  is the conductive coefficient of the PV baseboard ( $2.88 \times 10^5 \text{ W/m}^2\text{-K}$ ),  $T_b$  is the weighted mean temperature of the PV baseboard;  $h_{cv,a}$  is the convective coefficient of the air, given by equation [4-63].

### 5.3.2 Experimental Procedure

#### □ Experiment for the Characterisation of the PV Baseboard

The laboratory testing focused on the impact of the PV baseboard, as shown in **Fig. 5-6**. Both the Al-alloy- and TPT-based PV layers were fixed onto a frame with a detached wooden layer under their rear space. This was to simulate the different mounting solutions of the PV layers in practice, i.e., an on-roof or ground-mounted type. Parallel experiments for these two PV layers were conducted under a series of controlled indoor conditions:  $200\text{-}600 \text{ W/m}^2$  of solar radiation,  $10\text{-}25 \text{ }^\circ\text{C}$  of air temperature, and  $0.5\text{-}5 \text{ m/s}$  of air flow. Each test

was run for a sufficient number of hours to achieve a steady-state status and the acquired data were recorded at 1-minute intervals.

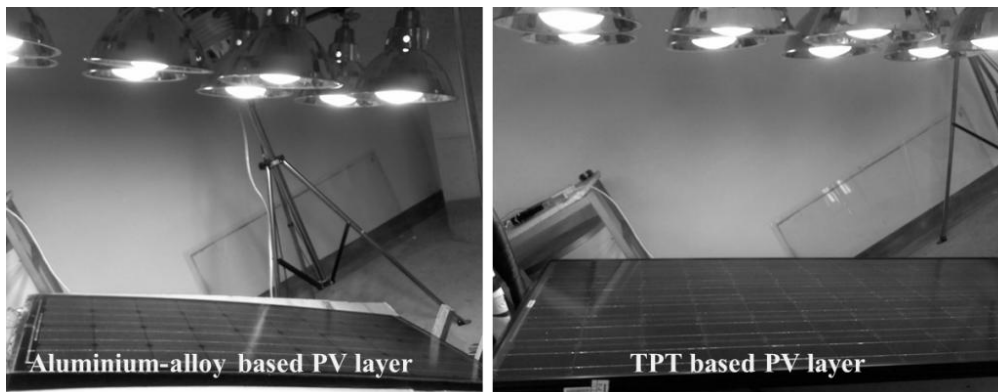


Fig. 5-6: Laboratory testing rigs of the aluminium-alloy- and TPT-based PV layer

#### □ Experiment for the Characterisation of the Integrated PV/LHP Heat Pump System

To enable characterisation of the PV/LHP heat pump system, a series of experiment sets, as shown in **Table 5-4**, were conducted over the period from 8<sup>th</sup> November to 9<sup>th</sup> December 2011 under controlled laboratory conditions. All the sensors/instruments were placed in the positions shown in **Table 5-3**. Each of the tests started at 9:00 am and ran for a sufficient number of hours to obtain the steady-state data. During the tests, the acquired data were recorded at 10-second intervals. The on-site image of the indoor testing is presented in **Fig. 5-7**.

Table 5-4: List of laboratory experimental testing modes

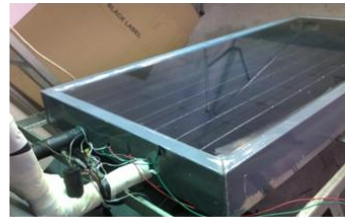
Test mode	$I$ (W/m <sup>2</sup> )	$T_a$ (°C)	$V_a$ (m/s)	$T_{e,hp}$ (°C)	$N_C$	$N_{hp}$
(1)	200 ± 20, 300 ± 20, 400 ± 20, 500 ± 20 600 ± 20	20 ± 2	1 ± 0.2	10	1	1
(2)	600 ± 20	10 ± 2, 15 ± 2, 20 ± 2, 25 ± 2,	1 ± 0.2	10	1	1



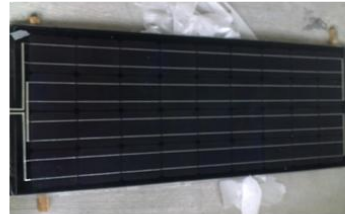
Test mode	$I$ (W/m <sup>2</sup> )	$T_a$ (°C)	$V_a$ (m/s)	$T_{e, hp}$ (°C)	$N_C$	$N_{hp}$
(3)	600 ± 20	20 ± 2	1 ± 0.2, 3 ± 0.2 5 ± 0.2, 7 ± 0.2	10	1	1
(4)	600 ± 20	20 ± 2	1 ± 0.2	5, 10, 15, 20	1	1
(5)	600 ± 20	20 ± 2	1 ± 0.2	10	0, 1, 2	1
(6)	600 ± 20	20 ± 2	1 ± 0.2	10	1	0, 1, 2



(a) PV/LHP module with single heat absorbing pipe



(b) PV/LHP module with double heat absorbing pipe



(c) Aluminium-alloy based PV lamination with no heat absorbing pipe



(d) Detachable glazing cover

Fig. 5-7: Laboratory-based testing rig for the characterisation of the whole system

## 5.4 Results and Discussion

### 5.4.1 Characterisation of the PV Layer with Different Baseboards using the Experimental Results

#### (1) Impact of Operating Time

In the test mode of solar radiation at 600 W/m<sup>2</sup>, air temperature at 20 °C, air velocity at 0.5 m/s, and an on-roof mounting solution, variations in the

performance of the two PV layers versus operating time were conducted, as shown in **Fig. 5-8**. It was found that the Al-alloy-based PV layer achieved a steady state more quickly than the TPT-based PV layer, showing an instant adaptive ability to a dynamic environment during practical operation. The temperature of the Al-alloy-based PV cells was observed at about 62.4 °C, which was 5.2 °C lower than that of the TPT-based PV cells, and its corresponding PV efficiency was about 9.18%, nearly 0.26% higher than the TPT-based type. This is because aluminium alloy has a much higher thermal conductivity than TPT and the accumulated solar heat is, therefore, dissipated more easily to the surroundings, resulting in lower PV temperature and higher PV efficiency. Although the increase in PV efficiency was limited, it was nonetheless meaningful for a PV system that has a relatively low operating efficiency (only around 10% [5.1]) in practice.

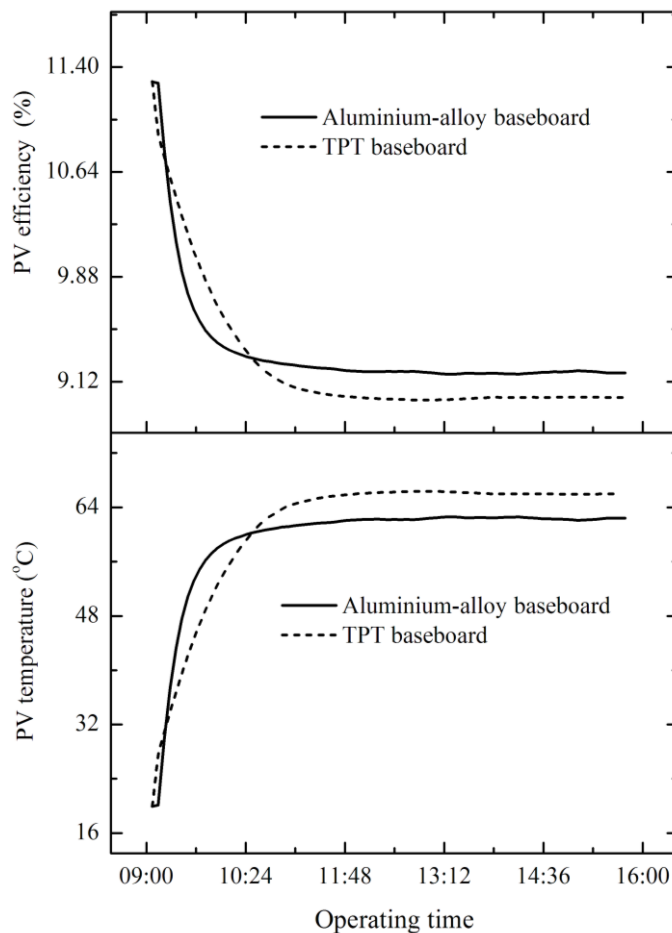


**Fig. 5-8: Impact of operating time on PV layer with different baseboards**

## (2) Impact of Solar Radiation

Varying the solar radiation from  $200 \text{ W/m}^2$  to  $600 \text{ W/m}^2$  while keeping the other external variables constant, i.e., air temperature at  $20 \text{ }^\circ\text{C}$ , air velocity at  $0.5 \text{ m/s}$ , and an on-roof mounting solution, the parallel characterisation of the PV layers with two different baseboards was conducted and the results displayed in **Fig. 5-9**.

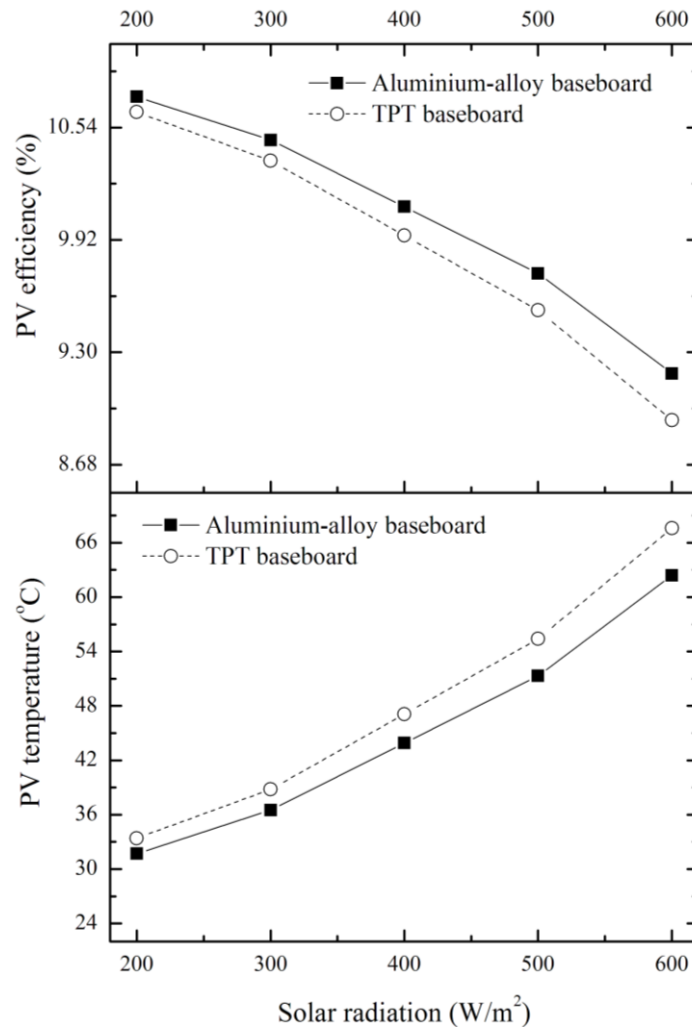


**Fig. 5-9: Impact of solar radiation on PV layer with different baseboards**

It was found that increasing the solar radiation led to a significant increase in the temperatures of both types of PV layer and their rising gradients were greater with the increase in solar radiation. The temperatures at the Al-alloy-based PV cells changed from  $31.7 \text{ }^\circ\text{C}$  to  $62.4 \text{ }^\circ\text{C}$ , while the temperatures at the TPT-based PV cells varied from  $33.4 \text{ }^\circ\text{C}$  to  $67.6 \text{ }^\circ\text{C}$ , resulting in a temperature

difference of 1.7 °C to 5.2 °C between these two PV types. It was seen that the higher the solar radiation, the larger the temperature difference between these two PV types. Such temperature variation determines an opposite changing trend in PV efficiency. The Al-alloy-based PV efficiency was in the range of 10.71% to 9.18% due to different levels of solar radiation, causing a higher PV efficiency than the TPT-based type from 0.08% to 0.26% accordingly. This is because higher solar radiation brings more instant heat to the PV layer, resulting in an increase in its temperature and a decrease in efficiency. Such differences in the temperature and the PV efficiency between the two baseboards were mainly owing to their different thermal attributes.

### (3) Impact of Air Temperature

Varying the air temperature from 10 °C to 25 °C while the other external variables remained constant, i.e., solar radiation at 600 W/m<sup>2</sup>, air velocity at 0.5 m/s, and an on-roof mounting solution, the parallel characterisation of these two PV layers was carried out and the test results illustrated in **Fig. 5-10**. It was found that the higher air temperature accumulated more heat for dissipation, causing the higher temperature and lower efficiency of both PV types. The temperature of the Al-alloy-based PV cells rose from 53.2 °C to 67.8 °C as the surrounding air temperature increased, and was about 3.6 °C to 6.8 °C lower than that of the TPT-based PV cells. The corresponding PV efficiency was about 9.64% to 8.92% for the Al-alloy-based PV layer, which was 0.34% higher than the TPT-based type. The differences in temperature and efficiency between the two PV types became greater with an increase in air temperature. This is because a higher air temperature weakens the overall amount of heat transfer from the PV layer to the surroundings, leading to a rise in temperature and a reduction in efficiency.

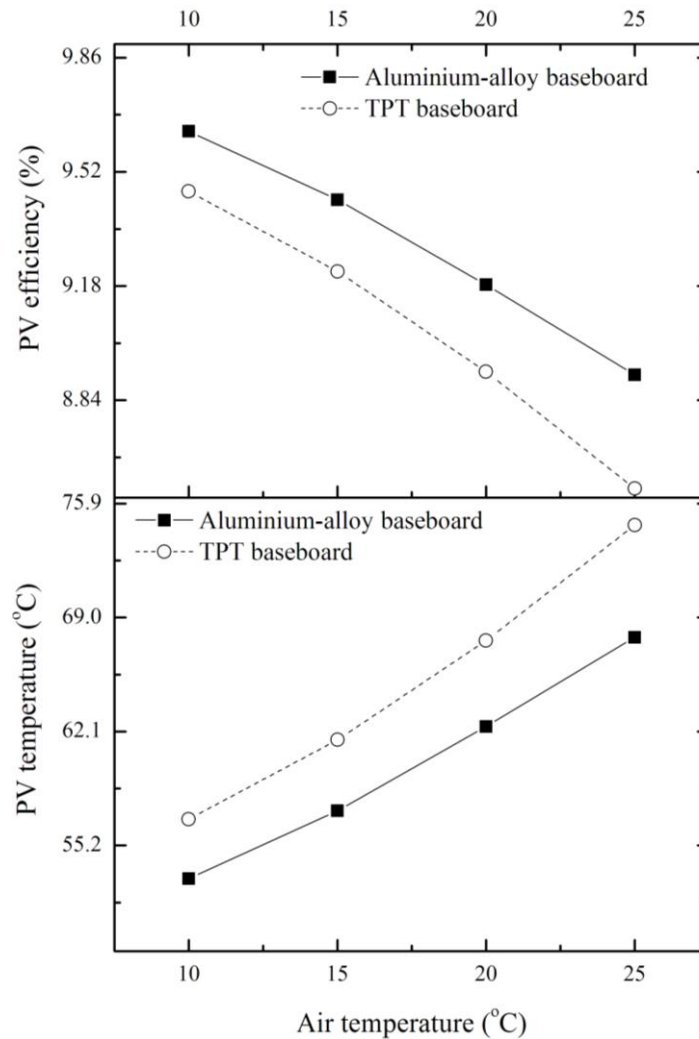


Fig. 5-10: Impact of air temperature on PV layer with different baseboards

#### (4) Impact of Air Velocity

Varying the air velocity from 0.5 m/s to 5 m/s and holding the other external variables constant, i.e., solar radiation at  $600 \text{ W/m}^2$ , air temperature at  $20 \text{ }^\circ\text{C}$ , and an on-roof mounting solution, a parallel comparison of these two PV layers was carried out. The test results are given in **Fig. 5-11**. It was found that increasing the air velocity led to a slight decrease in the temperature of the PV cells and a limited increase in PV efficiency. The temperature of the Al-alloy-based PV cells varied from  $62.4 \text{ }^\circ\text{C}$  to  $55.9 \text{ }^\circ\text{C}$ , which was about  $5.2 \text{ }^\circ\text{C}$  to  $7.4 \text{ }^\circ\text{C}$  lower than that of the TPT-based PV cells. The corresponding PV efficiency was about 9.18% to 9.51% for the Al-alloy-based PV layer, which was about 0.26% to 0.37% higher than the TPT-based type. The differences in temperature and efficiency between these two PV types increased with the air

velocity. This is because a higher air velocity increases the convective heat transfer coefficient from the PV to the surroundings, resulting in a decrease in temperature and an increase in efficiency. However, the impact of air velocity on the eventual heat transfer coefficient was limited, as it is determined not only by the convection of the air, but also by the conductivity of the PV baseboard. The simulated on-roof mounting mode may be another reason for the limited impact of air velocity, as it only allowed a small amount of free air to pass through the rear surface of the PV layer.

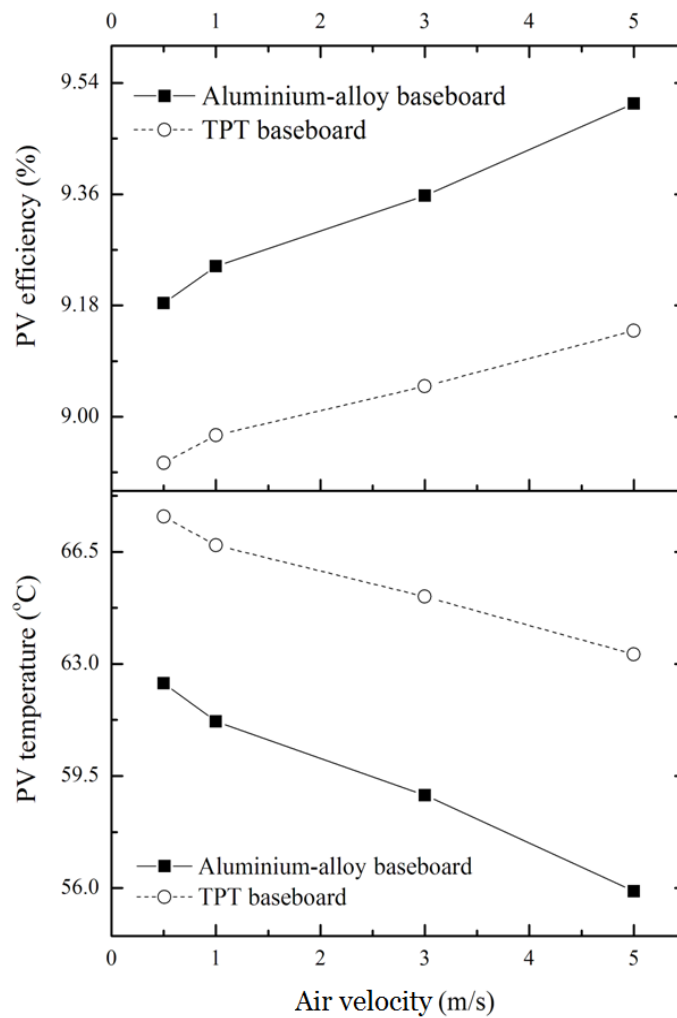
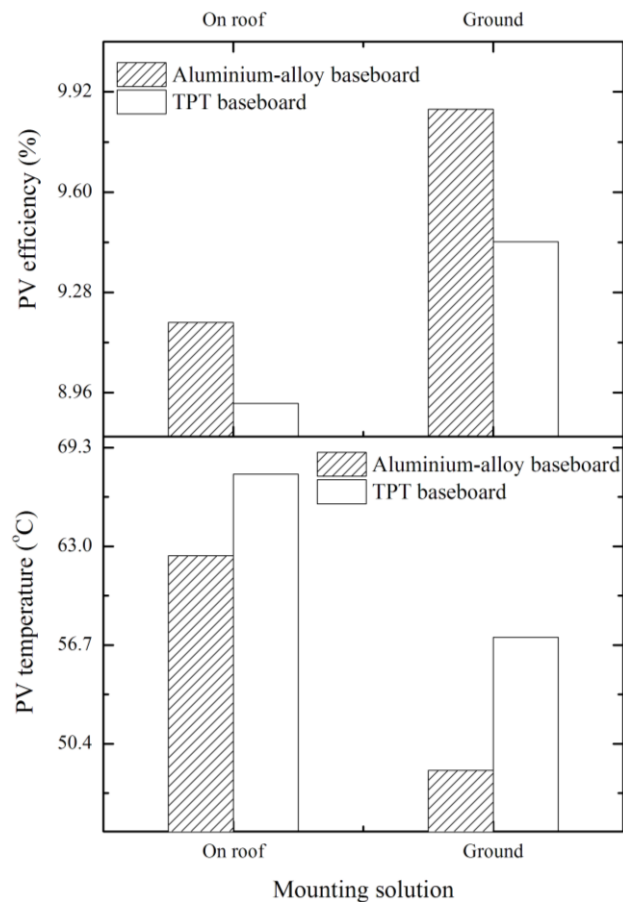


Fig. 5-11: Impact of air velocity on PV layer with different baseboards

### (5) Impact of Mounting Solution

The impact of different mounting solutions, i.e., on-roof and ground, on the PV layers was also investigated by placing or removing the wooden layer under the

rear surface of the PV layer, and the results are shown in **Fig. 5-12**. The other external parameters remained constant, i.e., solar radiation at  $600 \text{ W/m}^2$ , air temperature at  $20 \text{ }^\circ\text{C}$ , and air velocity at  $0.5 \text{ m/s}$ . It was clear that the ground-mounted PV layers achieved lower PV temperatures and higher electrical performance than the on-roof mounted types. The temperature of the Al-alloy-based PV cells decreased from  $62.4 \text{ }^\circ\text{C}$  to  $48.7 \text{ }^\circ\text{C}$ , whilst changing the mounting method from on-roof to the ground led to an increase in efficiency from  $9.18\%$  to  $9.86\%$ . The TPT-based PV layer only increased efficiency from  $8.93\%$  to  $9.44\%$  due to a lower temperature decrease from  $67.6 \text{ }^\circ\text{C}$  to  $57.2 \text{ }^\circ\text{C}$ . The reason is that the ground-mounting solution allows more air to pass through the PV rear surface, which enhances the convective heat transfer coefficient and assists heat dissipation from the PV layer to the surroundings. The ground-mounting solution also seemed more beneficial than the Al-alloy-based PV type as aluminium alloy has much greater thermal conductivity than TPT, which led to a higher overall heat transfer coefficient for the PV layer.



**Fig. 5-12: Impact of mounting solution on PV layer with different baseboards**

## 5.4.2 Characterisation of the Prototype PV/LHP Heat Pump System and the Steady-state Model Validation

Through both the established computer model and the testing rig, parametric studies of the PV/LHP heat pump system were conducted under the preset operational conditions. This allowed a parallel comparison of the modelling and test results of the prototype system, thus leading to verification or modification of the model accuracy in performance prediction. Further, the impacts of the operational parameters (e.g., solar radiation, air temperature/velocity, heat pump evaporation temperature, glazing cover, number of heat-absorbing pipes and PV module baseboard) on system performance (e.g., the efficiencies of the PV/LHP module and system  $COP_{PV/T}$ ) were investigated individually.

### (1) Impact of Solar Radiation

By varying the solar radiation from  $200 \text{ W/m}^2$  to  $600 \text{ W/m}^2$  while the other parameters remained constant, i.e., air temperature at  $20 \text{ }^\circ\text{C}$ , air velocity at  $1 \text{ m/s}$ , heat pump evaporating temperature at  $10 \text{ }^\circ\text{C}$ , single-glazing cover and fixed single heat-absorbing pipe for mode (1) operation, a simulation was carried out using the established computer program. The modelling results were then compared with the test results obtained under the same operational conditions, which yielded the comparison diagram displayed as **Fig. 5-13**. Good agreement between the modelling and experimental results was observed with a correlation coefficient and root mean square percentage deviation of 0.984 and 2.04% for electrical efficiency, and 0.982 and 4.43% for thermal efficiency. It was found that increasing the solar radiation led to a significant increase in the temperature of the PV absorber (from  $31 \text{ }^\circ\text{C}$  to  $41.8 \text{ }^\circ\text{C}$ ) and in the module's thermal efficiency (from 32.4% to 39.6%), and slight decreases in the module's electrical efficiency (from 10.8% to 10.1%) and in the system's advanced performance coefficient (from 9.6 to 8.7). The phenomena could be explained as follows: a higher solar radiation yielded an enhanced solar heat transfer, which helped improve the solar heat gain and the module's thermal efficiency. Meanwhile, the heat gain accumulated in the PV modules owing to the established thermal resistance of the LHP cycle; this led to an increase in



the PV cells' temperature and a decrease in the module's solar electrical efficiency. To remove this amount of heat, the heat pump operated at a high electrical power condition, thus leading to a reduced advanced performance coefficient in the system.

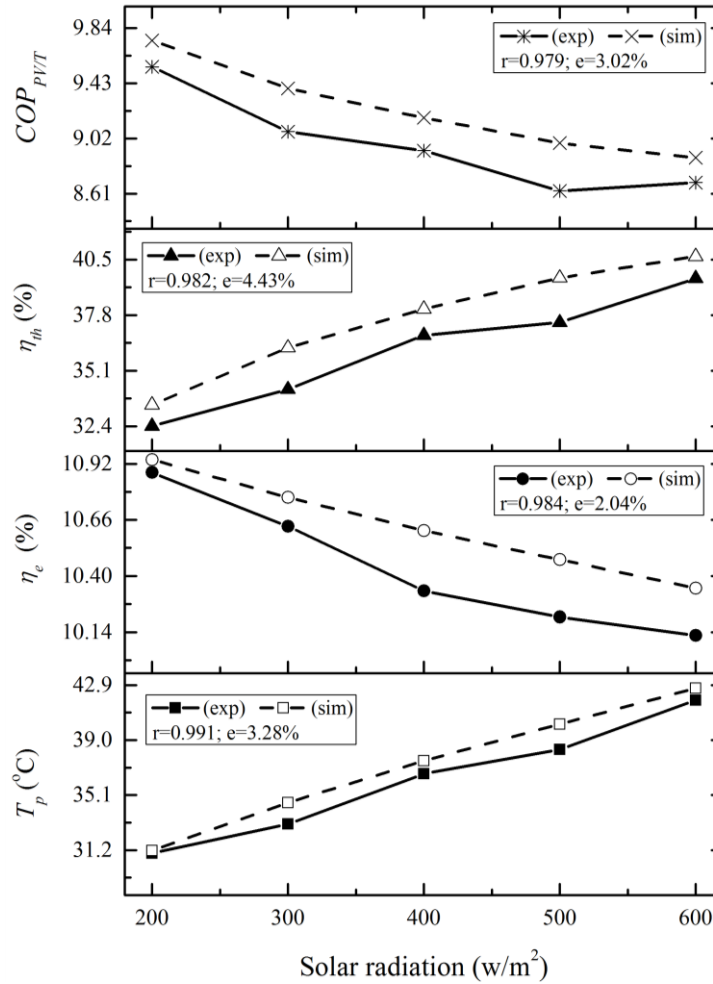


Fig. 5-13: Impact of solar radiation on the PV/LHP heat pump system

## (2) Impact of Air Temperature

By varying the surrounding air temperature from 10 °C to 25 °C while the other parameters remained constant for mode (2) operation, a simulation was carried out using the established computer program. The results of the simulation were then examined in parallel against the experimental data, thus giving the comparison image shown in **Fig. 5-14**. Good agreement was found between these two sets of results, giving a correlation coefficient and root mean square percentage deviation of 0.976 and 1.96% for electrical efficiency, and 0.996

and 4.64% for thermal efficiency. It was found that increasing the surrounding air temperature resulted in an increase in the PV cells' temperature (from 38.7 °C to 42.3 °C) and in associated thermal efficiency (from 31.5% to 42.4%), and a decrease in the module's electrical efficiency (from 10.3% to 10.1%) and in the system's advanced performance coefficient (from 9.3 to 8.3). The phenomena could be explained as follows: the higher surrounding air temperature reduced the module's heat loss and thus increased the useful heat gain, resulting in an increase in the system's thermal efficiency. This, however, also led to increased PV temperature, resulting in reduced system electrical efficiency and net electricity generation. Consequently, the system's advanced performance coefficient fell.

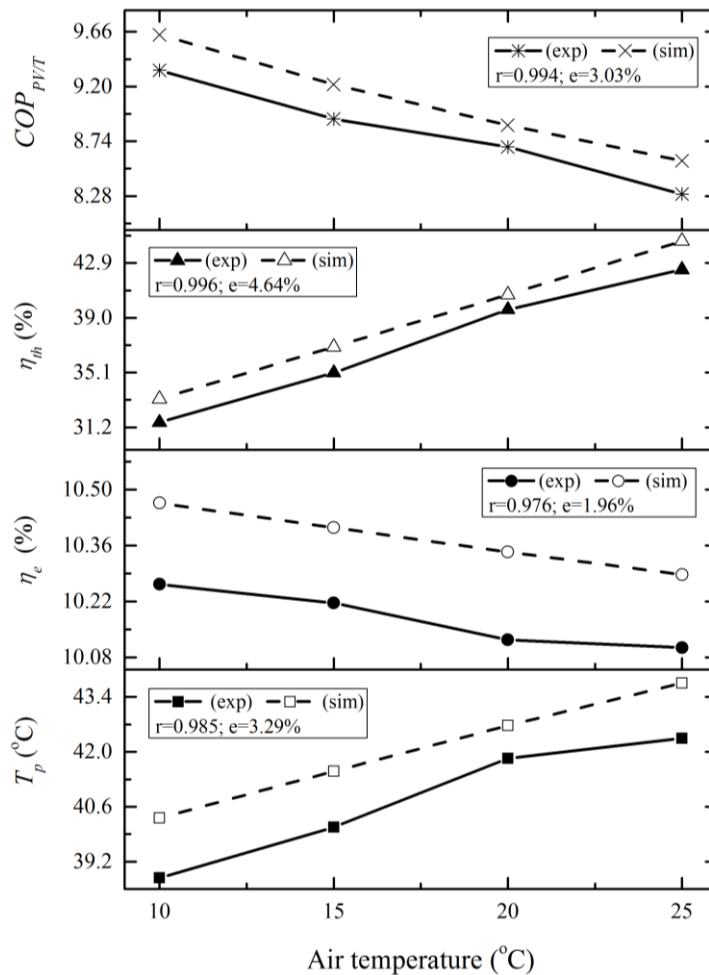
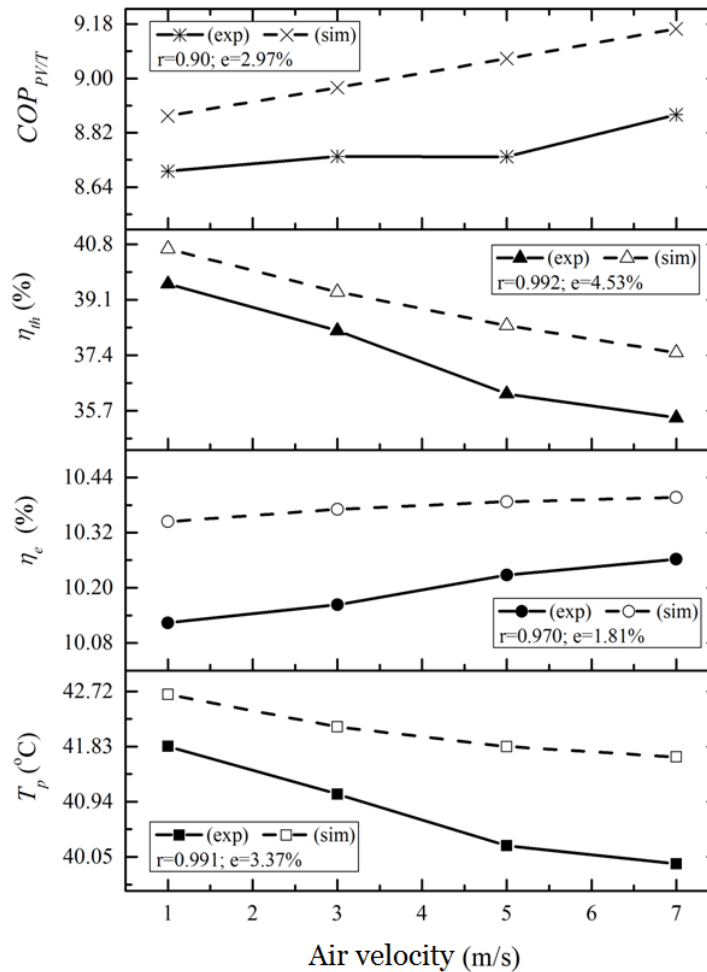


Fig. 5-14: Impact of air temperature on the PV/LHP heat pump system

### (3) Impact of Air Velocity

By varying the surrounding air velocity from 1 m/s to 7 m/s while the other parameters remained constant for mode (3) operation, a simulation was carried out using the established computer program. The results of the simulation were then examined in parallel against the experimental data, giving the comparison image shown in **Fig. 5-15**.



**Fig. 5-15: Impact of air velocity on the PV/LHP heat pump system**

The correlation coefficient and root mean square percentage deviation were found to be 0.970 and 1.81% for electrical efficiency and 0.992 and 4.53% for thermal efficiency, indicating that a good agreement between the simulation and the experiment had been achieved. It was found that increasing the air velocity led to a slight decrease in the temperature of the PV absorber (from 41.8 °C to 39.9 °C) and in the module's thermal efficiency (from 39.6% to

35.5%), and an increase in the module's electrical efficiency (from 10.34% to 10.39%) and in the system's advanced performance coefficient (from 8.7 to 8.9). The phenomena could be explained as follows: the higher air velocity caused increased heat loss and reduced thermal efficiency. It also, however, lowered the temperature of the PV modules, leading to an increase in the module's electrical efficiency. Consequently, the system's advanced performance coefficient was higher.

#### **(4) Impact of Heat Pump Evaporation Temperature**

By varying the heat pump's evaporation temperature from 5 °C to 20 °C while the other parameters remained constant for mode (4) operation, a simulation was carried out using the established computer program. The results of the simulation were then assessed in parallel against the experimental data, thus giving an image for comparison as shown in **Fig. 5-16**. The correlation coefficient and root mean square percentage deviation were found to be 0.979 and 1.56% for electrical efficiency and 0.999 and 5.07% for thermal efficiency, indicating that a good agreement had been achieved between the simulation and the experiment. It was found that increasing the evaporation temperature led to an increase in the temperature of the PV absorber (from 38.9 °C to 52.1 °C) and in the system's advanced performance coefficient (from 7.6 to 11.6), but a decrease in the module's electrical efficiency (from 10.4% to 9.7%) and in the module's thermal efficiency (from 43% to 30%). The phenomena could be explained as follows: the higher evaporation temperature reduced the temperature difference between the PV/LHP absorber and the condensing heat exchanger, thus resulting in a reduced heat transfer across the LHP and reduced module thermal and electrical efficiency. However, the higher evaporation temperature lowered the temperature difference between the condensation and evaporation processes, which led to less compressor power in the heat pump operation. As a result, the system's advanced performance coefficient was much higher.

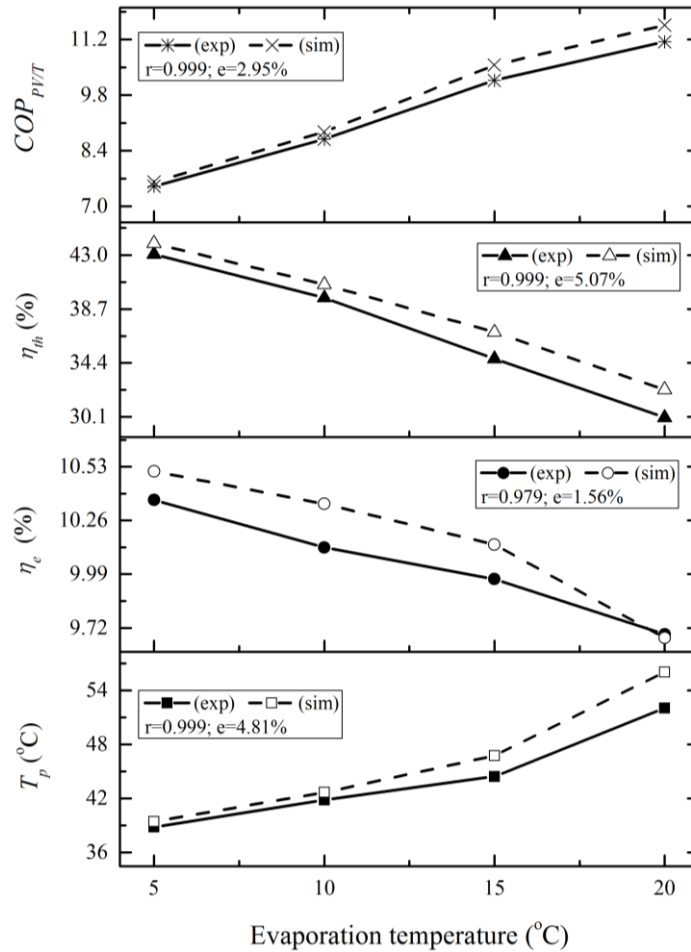


**Fig. 5-16: Impact of heat pump evaporation temperature on the PV/LHP heat pump system**

### (5) Impact of Top Glazing Covers

By varying the number of top glazing covers from 0 to 2 while the other parameters remained constant for mode (5) operation, a simulation was carried out using the established computer program. The simulation results were then put into parallel comparison against the experimental data, thus giving a comparison image as shown in **Fig. 5-17**. It was found that increasing the number of glazing covers led to an increase in the PV absorber temperature and in thermal efficiency, and a decrease in electrical efficiency and in the system's advanced performance coefficient. This is because adding more glazing covers helped to reduce the overall heat losses and the amount of absorbed solar energy due to its reflection and reduced transmittance; as a result, the module's thermal efficiency and the PV absorber temperature rose, and the module's

electrical efficiency and the system's advanced performance coefficient fell. To minimise heat loss and maximise solar energy intake, the single-glazing cover was considered to be the most appropriate option.

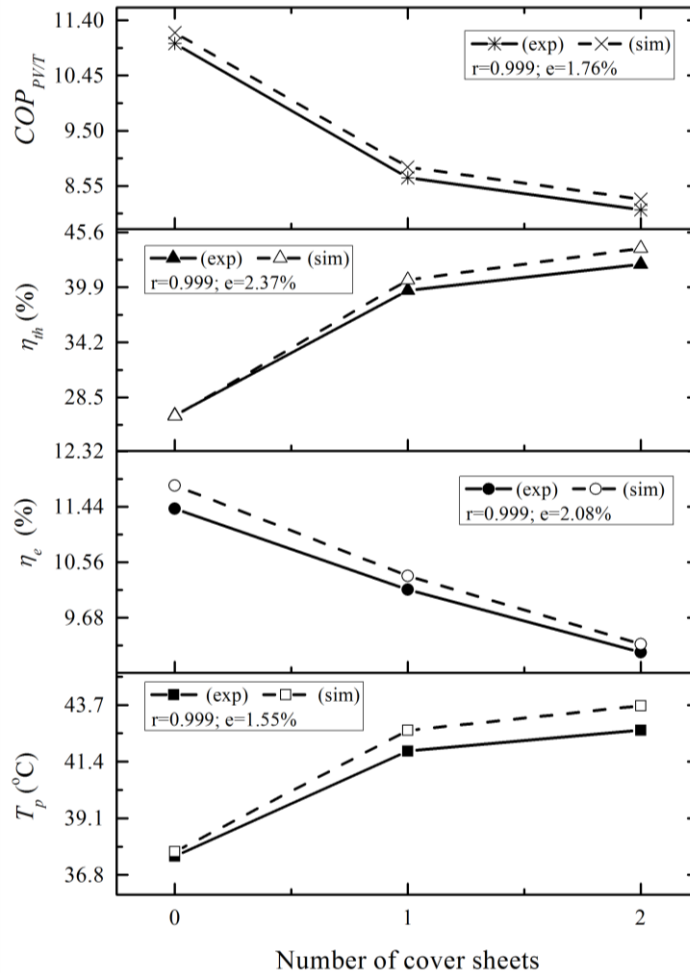


Fig. 5-17: Impact of top glazing covers on the PV/LHP heat pump system

### (6) Impact of the Number of Heat-absorbing Pipes

By varying the number of heat-absorbing pipes behind the PV layer from 0 to 2 while the other parameters remained constant for mode (6) operation, a simulation was carried out using the established computer program. The results were then put into parallel comparison against the experimental data, thus providing the image shown in **Fig. 5-18**. It was found that increasing the number of heat-absorbing pipes led to an increase in all the indicative parameters of the system, including thermal and electrical efficiencies, and  $COP_{PVT}$ . Applying more heat-absorbing pipes underneath the PV laminations

increased the standard fin efficiency, which enabled reduced PV surface temperature, increased solar heat gain, and enhanced thermal and electrical efficiencies; the advanced system performance was enhanced.

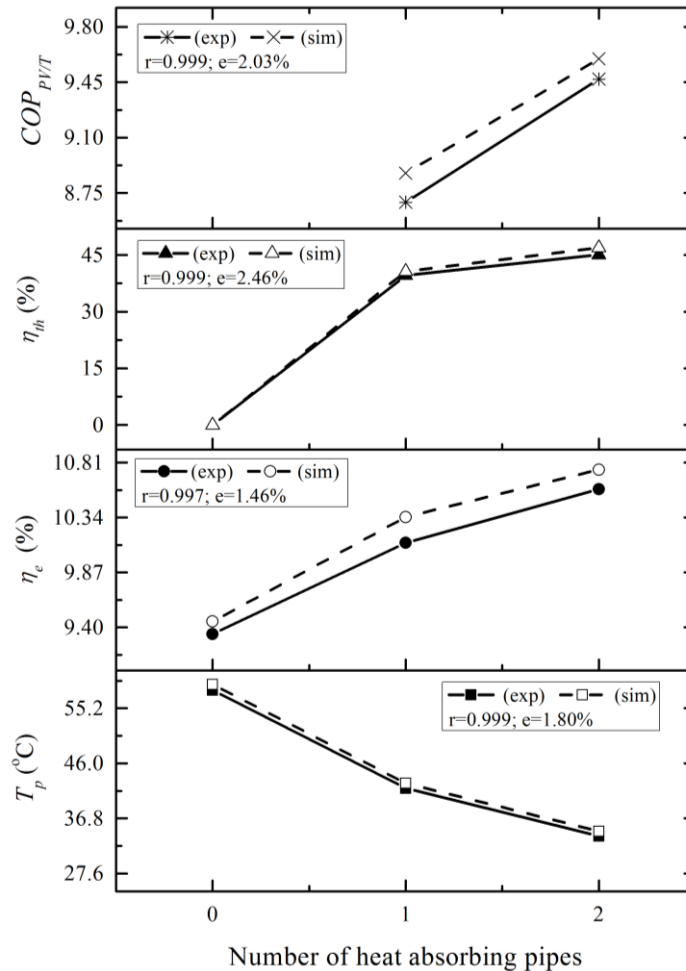


Fig. 5-18: Impact of LHP number on the PV/LHP heat pump system

### (7) Ratio of Net Electrical Output

Given the test conditions, solar radiation at  $600 \text{ W/m}^2$ , air temperature at  $20 \text{ }^\circ\text{C}$ , air velocity at  $1 \text{ m/s}$ , heat pump evaporating temperature at  $10 \text{ }^\circ\text{C}$ , a single-glazing cover and a fixed single heat-absorbing pipe, the consumption of electricity by the compressor reduced the PV electrical output, while the net ratio of system electricity generation ( $\eta_{e,n}$ ) was about 1.51%. This means the system was able to output additional electricity after fulfilling its own power demands under the specific test condition. Such evaluation results will help to develop a fully solar-driven heat pump water heating system in the future.

### **(8) Error analysis**

It was found that certain differences existed between the modelling and test results. For all sets of comparison, the mean deviations were no greater than 5%, which are acceptable in terms of general engineering applications and indicate that the established model can predict system performance at a reasonable level of accuracy. The minor differences in existence may be due to simplified assumptions, the utilisation of empirical formulas, and measurement errors. In particular, owing to the isentropic efficiency of the heat pump compressor ( $\eta_s$  up to about 88%), the practical system performance coefficients were all found to be lower than the theoretical values when more electrical power was consumed in the actual compression process.

### **5.5 Chapter Summary**

This chapter presented the detailed fabrication process and method of the prototype PV/LHP heat pump system, the experimental set-up and test process, as well as dedicated results analysis and steady-state computer model validation.

The coated Al-alloy-based PV layer was characterised against the conventional TPT-based PV type in the laboratory. The whole prototype system was then tested to examine its characteristic performance under a series of controlled laboratory conditions. Parallel comparisons between the modelling and experimental results were carried out, which indicated that these two sets of data were in good agreement. Thus, the established steady-state model was able to predict system performance to a reasonable level of accuracy (average error less than 5%). As the heat pump compressor's isentropic efficiency (up to about 88%) existed in practice, it slightly reduced the practical performance coefficient over the theoretical figure. The electrical, thermal and overall efficiencies of the PV/LHP module under the given laboratory conditions were around 10%, 40% and 50%, respectively. In the case of the basic laboratory conditions, the consumption of electricity by the compressor reduced the PV electrical output, while the net ratio of system electricity generation was



calculated at about 1.51%, which means the system is fully able to output electricity after fulfilling its own power demands in the specific testing environment. The characterisation results will help to develop a fully solar-driven heat pump water heating system further in the future.

The Al-alloy-based PV layer showed much better electrical performance and could adapt to the surroundings more promptly than the TPT-based PV type. The external weather variables, i.e., weaker solar radiation, lower air temperature, higher wind speed, and a ground-mounting solution (rather than an on-roof mode), were favourable in terms of the electrical performance of both PV types. In the test mode of solar radiation at  $600 \text{ W/m}^2$ , air temperature at  $20 \text{ }^\circ\text{C}$ , wind speed at  $0.5 \text{ m/s}$ , and an on-roof mounting solution, the temperature of the Al-alloy-based PV cells was observed at  $62.4 \text{ }^\circ\text{C}$ , which was  $5.2 \text{ }^\circ\text{C}$  lower than that of the TPT-based PV cells, and the PV efficiency was about 9.18%, nearly 0.26% higher than the TPT type. Although the PV efficiency increase was limited, it was meaningful for a PV system with a relatively low operating efficiency in practice.

Relations between the system's characteristic parameters (thermal and electrical efficiencies and  $COP_{PV/T}$ ) and operational/geometric conditions were individually studied under different test modes. The steady-state results indicated the following: lower solar radiation, lower air temperature, higher air velocity and a smaller number of covers led to enhanced electrical efficiency but reduced thermal efficiency of the module; whereas, a lower heat pump evaporation temperature and a larger number of heat-absorbing pipes gave rise to both thermal and electrical efficiencies for the module. In general, to achieve a better operational performance for the PV/LHP heat pump system, construction of further PV/LHP modules should be made by (1) using single glazing in the cover of the module; (2) fixing two heat pipes underneath the PV layer; and (3) employing an aluminium-alloy sheet as the PV baseboard. During the system operation, the evaporation temperature of the heat pump is suggested to be set up to  $20 \text{ }^\circ\text{C}$ . Moreover, the system performed better at moderate solar radiation (e.g.,  $400\text{-}600 \text{ W/m}^2$ ), a mild surrounding air temperature (e.g.,  $15\text{-}20 \text{ }^\circ\text{C}$ ), and a lower air velocity (e.g.,  $0\text{-}1 \text{ m/s}$ ).

This chapter provided a method for fabricating the dedicated PV/LHP heat pump system and examined its characteristic performance, which provided useful clues for the further development of large-scale systems and how to achieve the best possible system performance in terms of appropriate configuration parameters and favourable operational conditions.

## CHAPTER 6: PROTOTYPE PERFORMANCE EVALUATION IN REAL CLIMATIC OPERATIONAL CONDITIONS AND DYNAMIC MODEL VALIDATION

### 6.1 Chapter Introduction

This chapter continues the evaluation of the prototype PV/LHP heat pump system in real climatic conditions. An experimental rig was set up and assessed under real-time outdoor weather conditions by recording a number of parameters, e.g., solar radiation, PV power generation, temperature, and heat pump compressor consumption. The main works are listed as follows:

- (1) The prototype system was measured over a consecutive period for about one week in real climatic conditions.
- (2) The test results were used to validate the dynamic simulation model established in Chapter 4. Through parallel comparison between the modelling and test results, the dedicated dynamic computer model was validated as being able to predict system performance to a reasonable level of accuracy.

As a result of the above, the prototype system was proven to have repeatable and reliable performance in real climatic conditions. Such a dedicated dynamic simulation model is thus regarded as being reliable in predicting the annual system performance for the socio-economic analysis in the next chapter.

### 6.2 Experiment Set-up in Real Climatic Conditions

#### 6.2.1 Real-time Experiment – Daily Based

The outdoor experimental rig for the whole system was continuously operated and recorded over the short term in sunny or cloudy weather conditions from 21<sup>st</sup> to 28<sup>th</sup> November 2011 in Shanghai in China (31°11'N and 121°29'E). The

testing was fully operated for about eight hours daily and all the instruments were fixed in the positions shown in **Table 5-3**. The test data were recorded at 5-minute intervals. The outdoor experimental rig is displayed as **Fig. 6-1**.



**Fig. 6-1: On-site outdoor experimental rig**

### 6.2.2 Real-time Experiment – Hourly Based

The test results from 21<sup>st</sup> November 2011 were chosen as an instance for analysing the real-time performance of the prototype system and the accuracy/reliability of the dynamic computer model. The real-time variation in solar radiation and air temperature is in **Fig. 6-2**. The initial tank water temperature was measured at 14.38 °C and the testing was operated from 08:40 to 16:20.

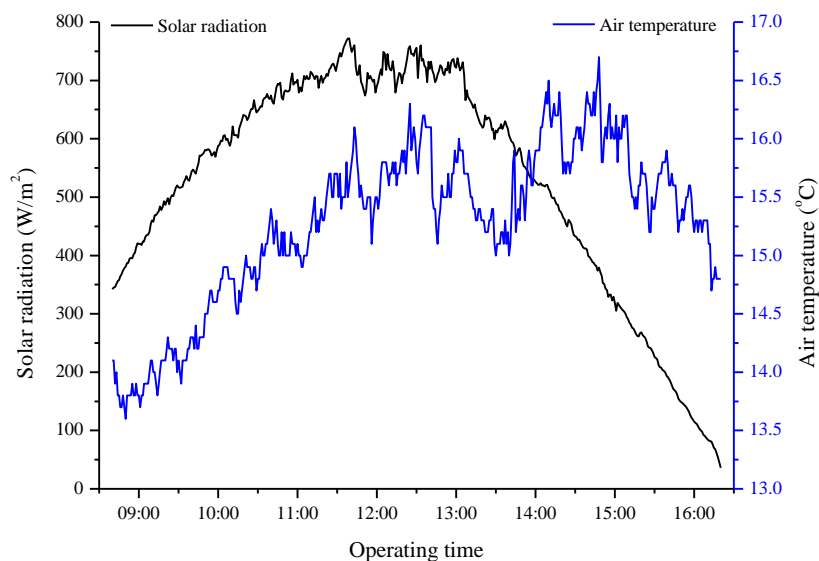


**Fig. 6-2: Real-time variation in solar radiation and air temperature**

## 6.3 Results and Discussion

### 6.3.1 Real-time Measurement – Daily Based

The experimental rig was continuously operated and recorded over the short term in sunny or cloudy weather conditions. The test results, as shown in **Table 6-1**, indicate the system had a steady, consistent and reliable operating performance in real climate conditions. During the test period, the mean daily PV temperature was approximately 40 °C. The water temperatures in the tank rose about to 40 °C, while the ultimate water temperatures reached over 54 °C. The daily average electrical and thermal efficiencies of the PV/LHP module were 9.13% and 39.25%, respectively, resulting in overall energetic and exergetic efficiencies of nearly 48.37% and 15.02%. The average  $COP_{th}$  and  $COP_{PVT}$  values were calculated at 5.51 and 8.71, respectively. The mean net electricity output ratio was measured at 1.38% daily, indicating that this prototype system can be fully operated by itself and output an additional amount of power in the meantime.

**Table 6-1: Test results over a consecutive period in real climate conditions**

Date	$I$ (W)	Temperature (°C)				Efficiency (%)				Performance (%/-)		
		$T_a$	$T_{p,m}$	$T_w^0$	$T_w$	$\eta_e$	$\eta_{th}$	$\eta_o$	$\zeta_o$	$\eta_{e,n}$	$COP_{th}$	$COP_{PVT}$
21.11	321.44	15.28	40.66	14.38	54.29	9.12	38.13	47.24	14.92	1.42	5.51	8.81
22.11	298.56	15.78	39.23	14.72	53.57	9.13	38.91	48.04	15.04	1.38	5.50	8.73
23.11	330.65	15.33	40.85	14.47	54.37	9.11	38.26	47.37	14.88	1.44	5.52	8.85
24.11	336.74	15.36	40.96	14.53	54.42	9.10	38.33	47.43	14.87	1.44	5.52	8.88
25.11	287.78	16.04	38.69	14.91	54.68	9.14	39.69	48.83	15.09	1.35	5.51	8.62
26.11	270.63	18.36	38.24	15.29	54.84	9.15	40.63	49.78	15.17	1.25	5.50	8.51
27.11	292.81	18.47	39.07	15.42	54.91	9.13	40.77	49.90	15.18	1.39	5.51	8.58
Mean	305.52	16.37	39.67	14.82	54.44	9.13	39.25	48.37	15.02	1.38	5.51	8.71

As a type of solar thermal system, the module thermal efficiency can alternatively be derived from the following semi-empirical efficiency model to correlate with external weather and operational conditions [6.1]:

$$\eta_{th} = \eta_{th}^* - U_L (T_r - \bar{T}_a) / I \quad [6-1]$$

where,  $\eta_{th}^*$  is the characteristic module thermal efficiency and can be interpreted when the refrigerant temperature ( $T_r$ ) equals the mean ambient air temperature ( $T_a$ );  $U_L$  is the overall heat loss coefficient of the module ( $W/m^2-K$ ). With the measured weather and operational conditions, the values of  $\eta_{th}^*$  and  $U_L$  for a specific solar collecting system can be determined by linear regression analysis. A larger  $\eta_{th}^*$  and a lower  $U_L$  will result in a more efficient solar thermal module.

According to the test results in **Table 6-1**, the plot of  $\eta_{th}$  against the external weather and operational parameters  $(T_r - T_a)/I$  can be determined by the linear fit method, as shown in **Fig. 6-3**. The regression result is presented in the following expression with a correlation coefficient ( $r$ ) of 0.9296:

$$\eta_{th} = 35.53 - 107.15(T_r - T_a)/I \quad [6-2]$$

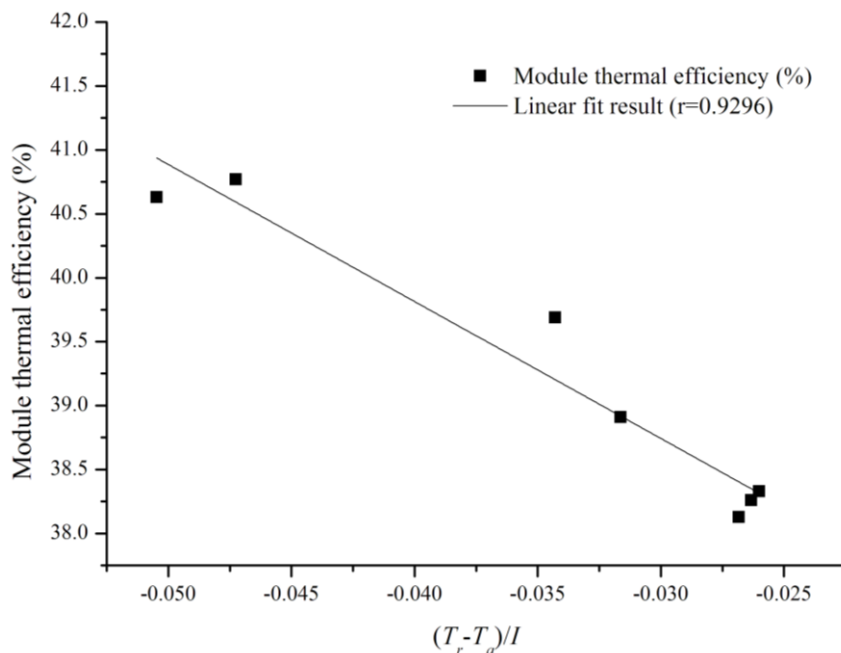


**Fig. 6-3:** Graphic plot of the experimental results for module thermal efficiency

### 6.3.2 Comparison between the Prototype System and Conventional Solar Energy Systems

The average test results over the period from 21<sup>st</sup> to 28<sup>th</sup> November 2011 were compared with those of conventional solar/air energy systems, shown in **Fig. 6-4**. It can be observed that the mean overall efficiency of the PV/LHP module

was more than 48.37%, which was higher than the average operating values of the independent PV panels (about 10% in practice [5.1]) and the standard solar thermal collectors (averaging 40% in practice [6.2]). Owing to the extra thermal energy capture, the overall exergetic efficiency (equivalent to the overall electrical conversion ratio) of the module was high at nearly 15%, which was almost a 3-5% increase in comparison with the standard PV panels [5.1] in practice. The system performance indicators ( $COP_{th}$  and  $COP_{PV/T}$ ) were nearly 1.5 to 4 times those of conventional air-/ground-source heat pump (ASHP/GSHP) systems for hot water generation [6.3], whilst being 1.5 to 2 times above the integral-type solar-assisted heat pump system [6.4].

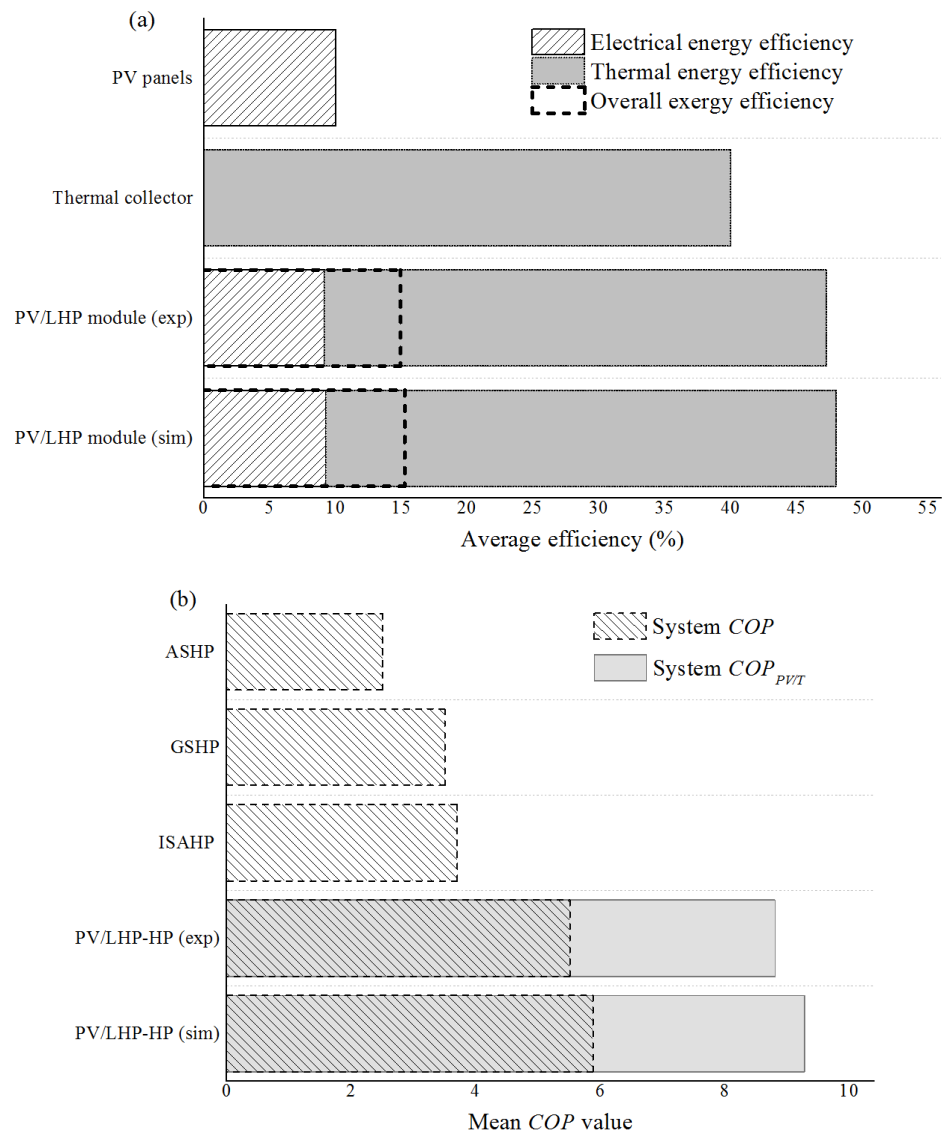


**Fig. 6-4: Comparisons between the PV/LHP heat pump system and (a) independent solar systems and (b) conventional heat pump water heating systems**

### 6.3.3 Real-time Measurement – Hourly Based and the Dynamic Model Validation

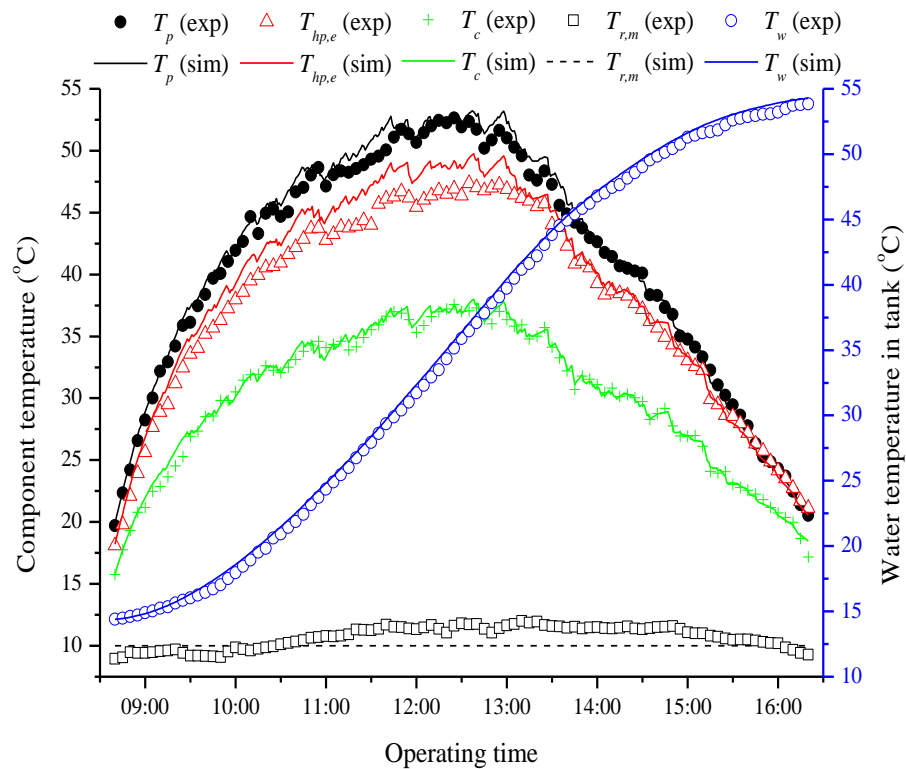
To enable a parallel comparison between the simulation and experimental results, the computer model was adjusted and operated at conditions identical to those of the outdoor weather data and the system's geometric/operational parameters, thus producing numerous sets of simulation results. These results were then compared with the corresponding test data to analyse the accuracy of the model. Further dedicated analysis and discussions of the modelling/test results were conducted.

#### (1) Temperature Distribution

Variations in the temperature in different system components over the test duration are presented in **Fig. 6-5**. Good agreement between modelling and testing can be observed, with mean temperatures of 30.20/29.93 °C for the glazing cover, 41.36/40.66 °C for the PV layer, 38.81/37.54 °C for the LHP evaporator, 10/10.71 °C for the heat pump evaporator, and 35.52/35.01 °C for the water in the storage tank, while the corresponding deviations for the above components were 1.71%, 1.82%, 3.54%, 10.11% and 1.81%, respectively. It was found that all temperature values for the glazing cover, PV layer, heat pipe and heat pump evaporator presented a similar variation trend, giving an upward-rising trend in the morning and a downward-falling trend in the afternoon, while the temperature of the tank water grew continuously throughout the test duration, starting at 14.38 °C and ending at 54.29 °C. The temperature of the PV layer varied in the range from 19.71 °C to 52.64 °C with a mean value of 40.66 °C. The temperature difference between the PV layer and the heat pipe was about 2 °C to 5 °C in the morning, and reached a maximum value of around 6 °C at noon. This temperature difference was subsequently decreased in the afternoon and, as a result, the heat pipe temperature exceeded the temperature of the PV layer in the late afternoon. This phenomenon occurred owing to variations in the solar radiation and the incidence angle of the solar beams, which presented stronger irradiation and a smaller incidence angle in the morning and at noon. This enabled the PV cells to absorb a larger amount of energy during this time period, thus leading to a



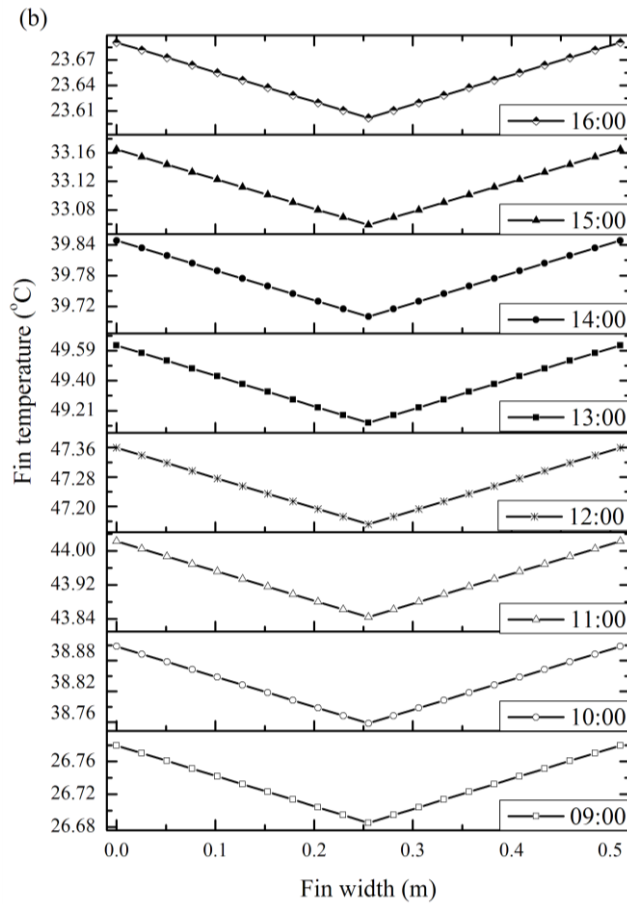
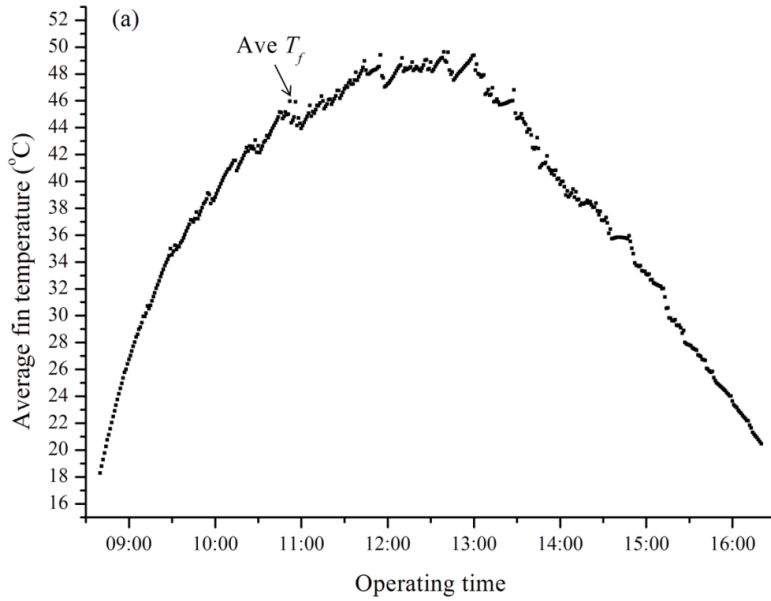
fast rise in temperature. Conversely, the higher air temperature in the afternoon resulted in a smaller heat loss from the module to the air and a lower temperature reduction speed, thus causing a reduced temperature difference between the PV layer and the heat pipe. A similar explanation of the temperature variation could also be related to the glazing cover. Since the heat pump compressor worked intermittently to control its evaporation temperature, a temperature fluctuation existed and was influenced by both the transient solar radiation and the air temperature.



**Fig. 6-5: Real-time temperature distribution of the system components**

The variation in the fin's mean temperature over the test duration is presented in **Fig. 6-6 (a)**. It was found that the fin's mean temperature varied according to a similar trend to that for the PV layer and heat pipe temperatures, which were all influenced by the weather conditions. At a single time point, the temperature variation along the fin width tended to have a 'V' shape, with the minimum value occurring at the central line and the maximum value at the fin edge line, as shown in **Fig. 6-6 (b)**. A temperature difference of around  $0.49\text{ }^{\circ}\text{C}$  was found to exist between the edge and the centre at 13:00 in the early afternoon. This phenomenon occurred owing to the fact that the central line

(nodes) of the fin is situated in the area sticking to the evaporation section of the loop heat pipe, where the temperature was at the lowest level due to the evaporative effect of the heat pipe fluid. As a result, the heat flow was directed from the fin's edges to its central line. A 3D temperature distribution for the fin sheet against the fin width and the operating time is displayed in **Fig. 6-6 (c)**, achieved by running the dynamic simulation model.



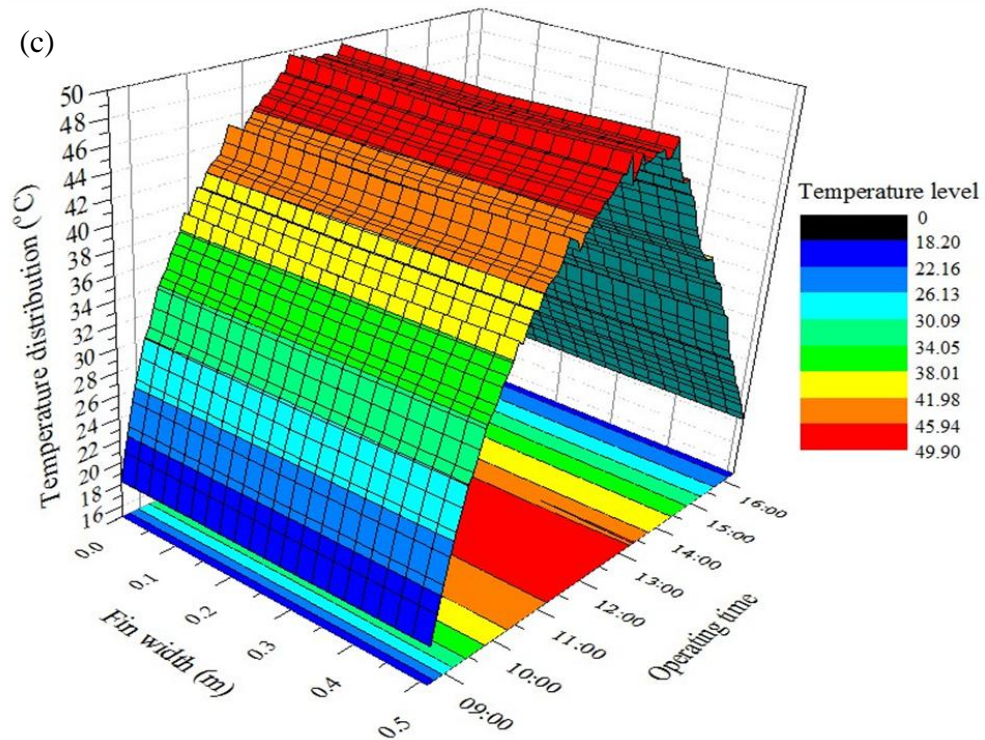


**Fig. 6-6:** (a) real-time mean temperature of the fin, (b) real-time fin temperature versus fin width, and (c) 3D fin temperature versus both fin width and operating time

## (2) Photovoltaic Power Output and Module Electrical Efficiency

**Fig. 6-7** provides a comparison between the modelling and test results of the PV/LHP module electrical output and its corresponding solar electrical efficiency. The average electrical outputs and the corresponding solar electrical efficiencies from the simulation and testing were 29.91 W/29.45 W and 9.23%/9.12%, respectively, giving an excellent mutual agreement with the mean deviation of 1.45%. The variation in the module's electrical output was found to be similar to that of the solar radiation, presenting a gradually increasing trend in the morning and a decreasing trend in the afternoon, while the peak electrical output occurred at noon. The solar electrical efficiency was found to increase slowly in the morning, significantly decrease in the late afternoon, and remain at a relatively stable state for the rest of the day. This variation trend was largely affected by solar radiation and the corresponding incidence angle. It is known that greater solar radiation and a smaller incidence solar beam angle will result in enhanced solar energy absorption and thus increase solar electrical output, which was the situation for the noon-time

operation. It is also known that solar electrical efficiency will change to the opposite trend to the solar incidence angle and at a consistent trend with the PV cells' temperature, and the ultimate changing trend in solar electrical efficiency will depend on the weight of the impact of the two factors. During early morning and late afternoon in Shanghai, the PV temperature is reasonably low but the solar incidence angle is significantly higher. This made the solar incidence angle the dominating factor compared to the PV temperature, and led to significantly varying solar electrical efficiency. During other operational periods, the two parameters above exerted the opposite but same amount of influence on the solar electrical efficiency, which emerged as a relatively stable variation trend.

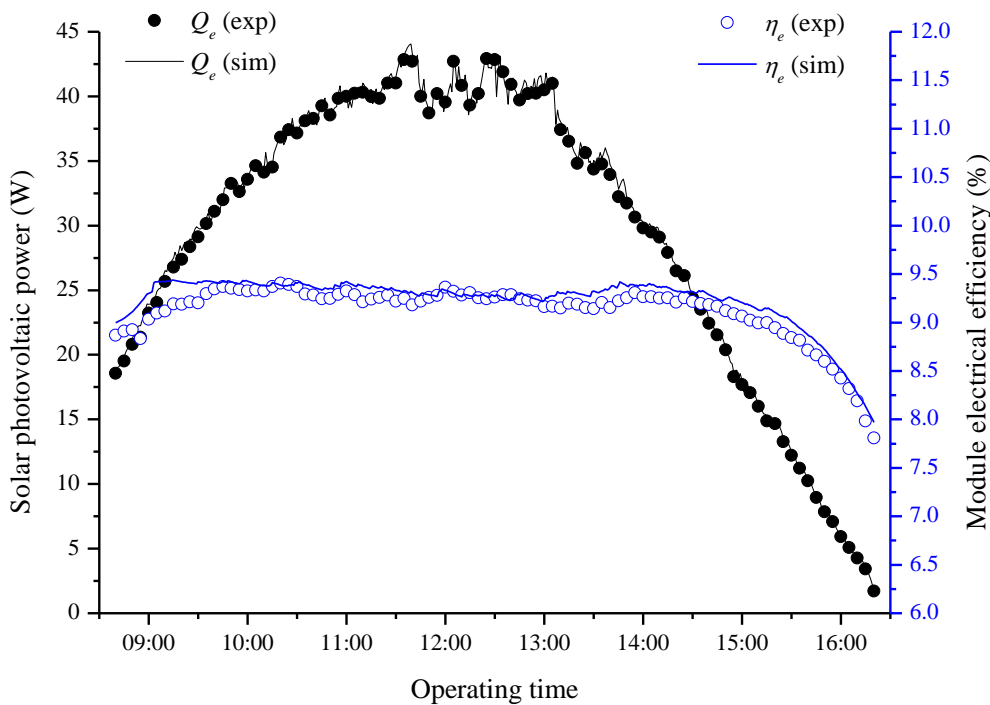
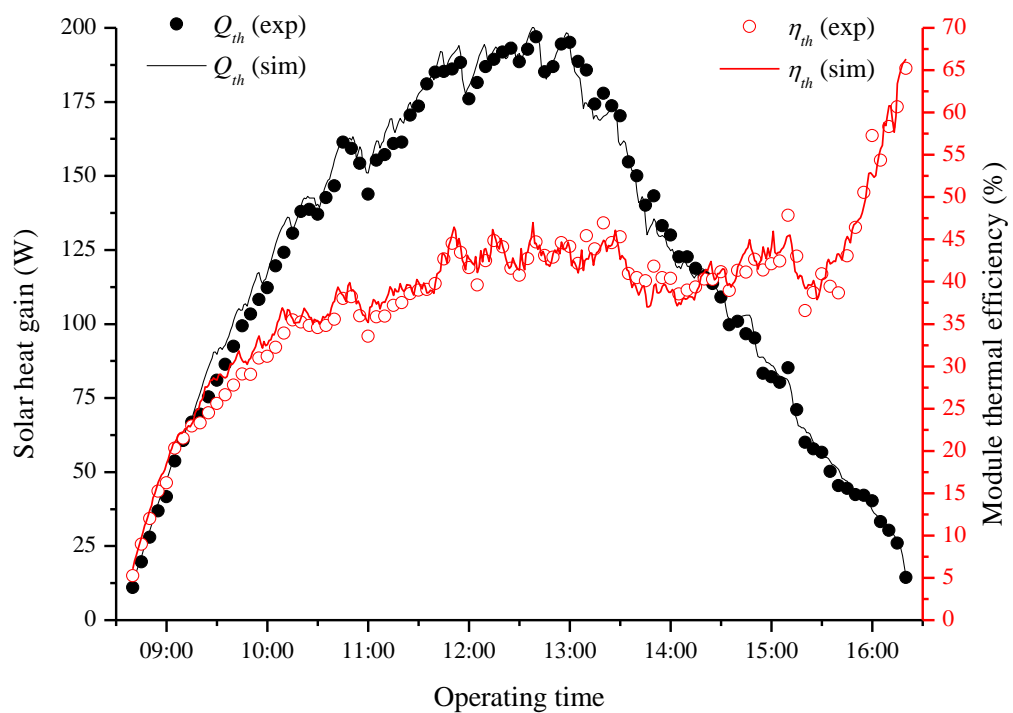


Fig. 6-7: Real-time solar power output and module electrical efficiency

### (3) Solar Heat Gain and Module Thermal Efficiency

Variations in both solar heat gain and module thermal efficiency versus operating time are given in Fig. 6-8. The average solar heat outputs of the module and the corresponding solar thermal efficiencies from the modelling and the experiment were 122.87 W/120.08 W and 38.76%/38.13% respectively, giving reasonable mutual agreement with the mean deviation of 5.20%. The

solar heat output increased quickly in the morning and decreased slowly in the afternoon. Similar to the situation for the solar electrical output, the solar radiation and the incidence angle imposed significant influences on the module's solar heat output. Different from the situation for the solar electrical output, the ambient temperature also became a factor that had an impact on the module's heat output: a higher ambient temperature led to a reduced temperature difference between the module's surface and the ambient air, which caused a smaller heat loss. As the ambient temperature presented a continuously growing trend, the heat loss from the module's surface to the ambient air became less and less during daytime operation and, as a result, the module's net heat output experienced a gentle downward-falling process during the afternoon.



**Fig. 6-8: Real-time solar heat gain and module thermal efficiency**

The module's thermal efficiency was observed to present a sharp variation during both the start-up and ending phases, but remained at a relatively stable condition during the rest of the operational time. During these two phases, the PV/LHP module was subjected to sharp changes in the solar radiation level, which led to a fast temperature build-up and recession within the module, thus

causing sharp changes in the module's solar thermal efficiency. During the rest of the operational time, the solar radiation and the incidence angles presented a slow-changing process and this, along with the stable operational condition established with the heat pump, led to a relatively stable state in terms of the module's solar thermal efficiency.

#### (4) Overall Energetic and Exergetic Efficiencies of the PV/LHP Module

In **Fig. 6-9**, both the overall energetic and exergetic efficiencies of the PV/LHP module are presented against operating time. The average energetic and exergetic efficiencies of the module from the simulation and testing were 47.99%/47.24% and 15.25%/14.92%, respectively, giving reasonable mutual agreement with the mean deviations of 4.00% and 2.73%.

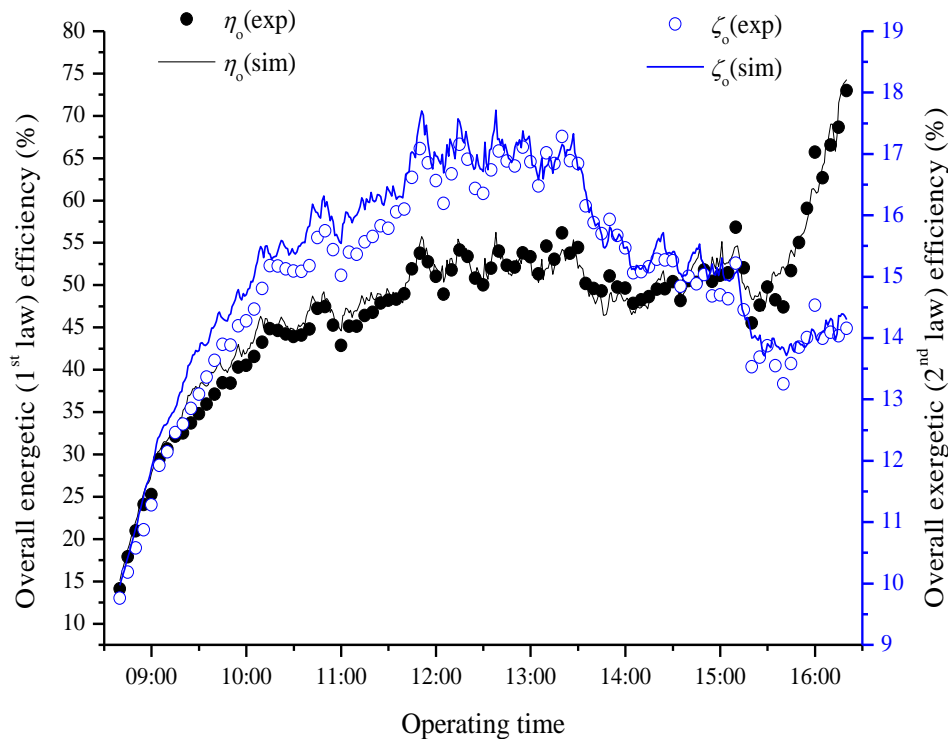


**Fig. 6-9: Real-time module overall energetic and exergetic efficiencies**

For the PV/LHP module, the amount of electrical output was much lower than that of the thermal output, and the overall energetic efficiency was largely impacted by the heat production, and thus presented a similar variation trend to that of the solar thermal efficiency. When taking into account the quality of the energy generations using the exergetic assessment approach, it was found that

around 5.8% of the exergetic efficiency of the module could be attributed to thermal energy collection, while the remaining 9.12% of the exergetic efficiency was due to electrical energy generation. This indicates that the higher grade (quality) electrical energy dominated the overall exergetic efficiency formation, which, therefore, had a similar variation trend to the solar electrical efficiency.

### (5) Heat Pump Condensing Capacity and System COP Performance

**Fig. 6-10** gives the variations in heat pump condensation heat and the basic thermal and advanced system performance coefficients ( $COP_{th}$ ,  $COP_{PV/T}$ ) of the prototype system over the duration of the test. The average water heat gain,  $COP_{th}$  and  $COP_{PV/T}$  of the PV/LHP heat pump system from the simulation and test results were 148.11 W/146.86 W, 5.88/5.51 and 9.28/8.81 respectively, giving reasonable mutual agreement with the mean deviations of 4.58%, 8.80% and 9%. During daytime operation, the heat pump condensation heat presented a similar variation trend to the absorbed solar heat when considering the additional compression work. The basic thermal  $COP_{th}$  value remained almost the same throughout a whole day's operation, during which the evaporation and condensation temperatures of the heat pump operation were constant. The  $COP_{PV/T}$  fell significantly during the first half hour of operation and thereafter remained at a relatively stable level. It was found that during the early half hour of testing, the electrical output imposed a significant impact on the  $COP_{PV/T}$ , leading to an increased  $COP_{PV/T}$  value. Afterwards, the system's heat gain grew quickly and thus became the dominating factor impacting on the heat pump operation. In this circumstance, the  $COP_{PV/T}$  gradually fell to a level close to the COPs. In short, the solar electrical output made a positive contribution to the system's overall performance, contributing to the formation of the difference between the  $COP_{PV/T}$  and  $COP_{th}$ .

It should be noted that as the heat pump compressor is fixed speed, which starts up intermittently once the evaporation temperature is over the settings (10°C) and then shuts down when the evaporation temperature is lower than 10°C. The compressor power consumption was recorded every intermittent period and divided by each interim time length for an average value. In this case, the

measured  $COP_{th}$  and  $COP_{PV/T}$  values for the system were less accurate than the other parameters.

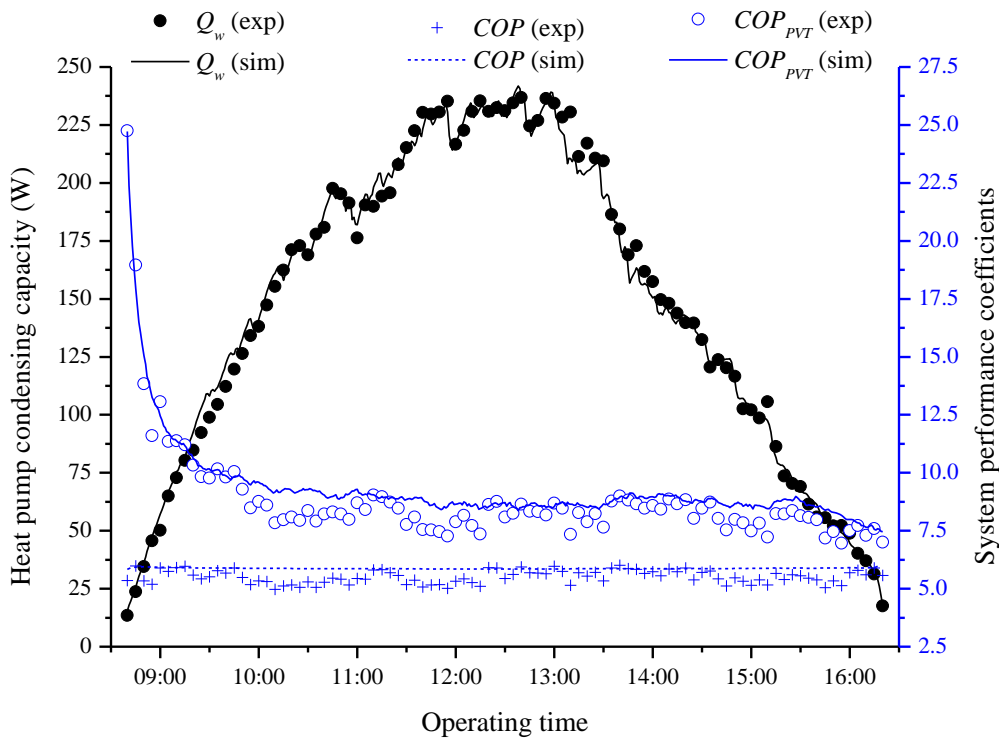


Fig. 6-10: Real-time water heat gain and system performance coefficients

Subtracting the heat pump compressor power from the overall PV electrical generation, the net power output of the PV/LHP heat pump system could be obtained. It was found that the daily mean net electricity output ratio was measured at 1.42%, which implies that the system can not only meet its own power demand, but also provide an additional power output for the measured condition.

## (6) Error Analysis

It was found that certain differences existed between the modelling and test results of the system's characteristic parameters, i.e., the temperatures of the system components, the solar efficiencies, and the system performance coefficients, as indicated in **Table 6-2**. For all sets of comparison, the correlation coefficients were all above 0.9665 and the mean deviations were no larger than 9%, which are acceptable from the point of view of general



engineering applications. The error analysis results indicate that the established dynamic model has a reasonable accuracy and reliability in predicting system performance.

**Table 6-2: Average system performances and error analysis results**

Results	$Q_e$ (W)	$Q_{th}$ (W)	$Q_w$ (W)	$\eta_e$ (%)	$\eta_{th}$ (%)	$\eta_o$ (%)	$\zeta_a$ (%)	$COP$ -	$COP_{PV/T}$ -
EXP	29.45	120.08	146.86	9.12	38.13	47.24	14.92	5.51	8.81
SIM	29.91	122.87	148.11	9.23	38.76	47.99	15.26	5.88	9.28
$r$	0.9998	0.9969	0.9971	0.9665	0.9883	0.9881	0.9896	0.9996	0.9787
$e$	1.45%	5.20%	4.58%	1.45%	5.20%	4.00%	2.73%	8.80%	9.00%

The minor discrepancy could have been caused by both theoretical and measurement errors. For the theoretical analysis, some simplified assumptions and empirical formulas were made and utilised, such as the inappropriate omission of the heat capacities of the two EVA layers, inaccurate calculations of the thermal resistance of the loop heat pipe by neglecting the vapour loss during its transportation, and may have been potential reasons for error generation. For the measurements, factors like insufficient insulation of the heat exchanger, inaccurate instruments/sensors, incorrect installation of detectors, may have caused the deviation in the testing figures with regard to prediction. However, owing to the dedicated rig construction, the selected test devices and the careful preparation/operation, the experiment results seem more reliable and thus there should be further optimisation for the mathematical and computer models.

#### 6.4 Chapter Summary

This chapter reported the dynamic performance of the prototype system operated in real climate conditions over a consecutive period. The overall evaluation approach, based on first-law (energetic) and second-law (exergetic) thermodynamics, was applied for both the quantitative and qualitative analysis of module efficiency. The basic thermal performance coefficient ( $COP_{th}$ ) and the advanced performance indicator ( $COP_{PV/T}$ ) of the system were both considered for a comprehensive assessment of system performance. The mean

daily PV temperature was approximately 40 °C. The daily water temperature rise in the tank was approximately 40 °C, with maximum water temperatures reaching over 54°C. The average electrical and thermal efficiencies of the PV/LHP module were, respectively, above 9.13% and 39% daily, resulting in corresponding overall energetic and exergetic efficiencies of nearly 48.37% and 15.02%. The average  $COP_{th}$  and  $COP_{PV/T}$  values were at 5.51 and 8.71, respectively. The mean net electricity output ratio was measured at 1.38% daily, indicating that this prototype system can fully drive itself and output an additional amount of power in the meantime. The test results indicate that such a prototype system would have a steady and reliable operating performance in real climate conditions.

In comparison with conventional solar collecting devices, the PV/LHP module achieved 3% to 5% higher solar exergetic efficiency than standard PV systems and about a 7% overall performance above independent solar collectors. Compared with conventional solar-/air-/ground-source heat pump systems, the PV/LHP heat pump system achieved a much higher COP figure of 1.5 to 4 times those for conventional heat pumps.

The real-time performance of the prototype system was studied from the aspects of system temperature distributions, module efficiencies and system performance coefficients, which were also applied to verify the established dynamic computer model. Through the parallel comparison of the modelling and test results, the dedicated dynamic model was validated as having a reasonable level of accuracy for predicting system performance (with a mean error less than 9%). It was found that the average water temperature in the storage tank (35 litres) grew gradually from 14.38 °C to 54.29 °C over the duration of the test. The temperature of the PV layer was in the range of 19.71 °C to 52.64 °C during daytime operation, while its mean value was 40.66 °C. The temperature difference between the PV layer and the heat-absorbing pipe was in the range of 2 °C to 6 °C. For the fin sheet, the temperature variations along the fin width presented a 'V' shape and the maximum temperature difference between the fin edges and its central line was around 0.49 °C at 13:00 in the early afternoon. The average electrical/heat

outputs and the corresponding solar efficiencies of the PV/LHP module were measured as 29.45 W/120.08 W and 9.12%/38.13%, respectively. Analysis of the measurement data indicated that the thermal and electrical outputs corresponded to 5.8% and 9.12% for exergetic efficiencies, thus making an overall exergetic efficiency of 14.92% for the PV/LHP module. Further analysis concluded that under daytime test conditions, the average heat pump condensing heat,  $COP_{th}$  and  $COP_{PV/T}$  were 146.86 W, 5.51 and 8.81, respectively. Error analysis was briefly addressed from the theoretical and experimental sides, indicating that the discrepancies were more likely to have come from the theoretical assumptions.

This part of the research will further help to predict system performance over a long-term scheme in different climate regions, and provides the basis for the following socio-economic analysis.

## CHAPTER 7: ENERGY SAVING, ECONOMIC, ENVIRONMENTAL AND REGIONAL ACCEPTANCE ANALYSIS

### 7.1 Chapter Introduction

In this chapter, a feasibility study of the prototype system for use in London, Shanghai and Hong Kong is carried out, involving an annual energy performance prediction, economic analysis and environmental sustainability assessment. The main works involved in this chapter are given as follows:

- (1) The annual energy performance of the prototype system is predicted using the dedicated dynamic simulation model validated in the previous chapter.
- (2) The economic acceptance and environmental benefits of the prototype system are analysed in comparison with conventional water heating systems, e.g., gas boilers and electric heaters.
- (3) This socio-economic analysis is undertaken based on life-cycle assessment methods, including the cost payback period, cost saving and CO<sub>2</sub> emission reduction across the system's life span in the above three regions.

This part of the research develops a socio-economic model that can predict the energy saving, economic and environmental benefits of the prototype PV/LHP heat pump system in three different climatic regions. This can further help suggest the most suitable region for the application of the proposed technology.

### 7.2 Annual Operational Performance

Owing to the good level of agreement achieved between the dynamic modelling and the real-time test results, the established dynamic model is appropriate for predicting the annual operational performance of the PV/LHP heat pump system.

### 7.2.1 Weather Profiles and Operational Conditions

Weather data for the three different climate regions, i.e., London (0.1°W, 51.3°N), Shanghai (121.8°E, 31.2°N) and Hong Kong (114.2°E, 22.2°N), were extracted from EnergyPlus software: ‘037760\_IWEC’ for London, ‘583670\_IWEC’ for Shanghai, and ‘450070\_CityUHK’ for Hong Kong [7.1]. An hourly weather profile of the monthly averages for Shanghai is presented in **Fig. 7-1**, while the monthly diurnal averages for solar radiation and air temperature for these regions are shown in **Fig. 7-2** and **Fig. 7-3**, respectively.

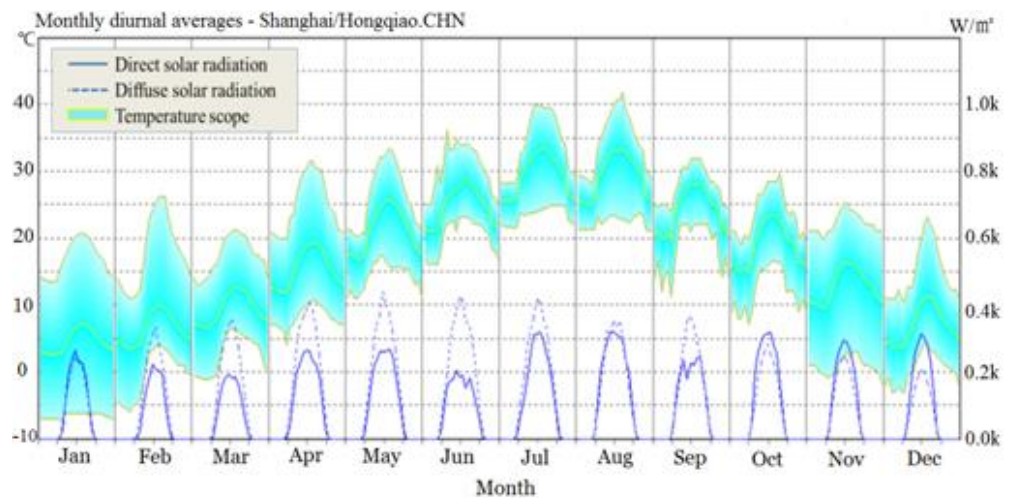


**Fig. 7-1: Hourly weather profile of the monthly averages for Shanghai, China**

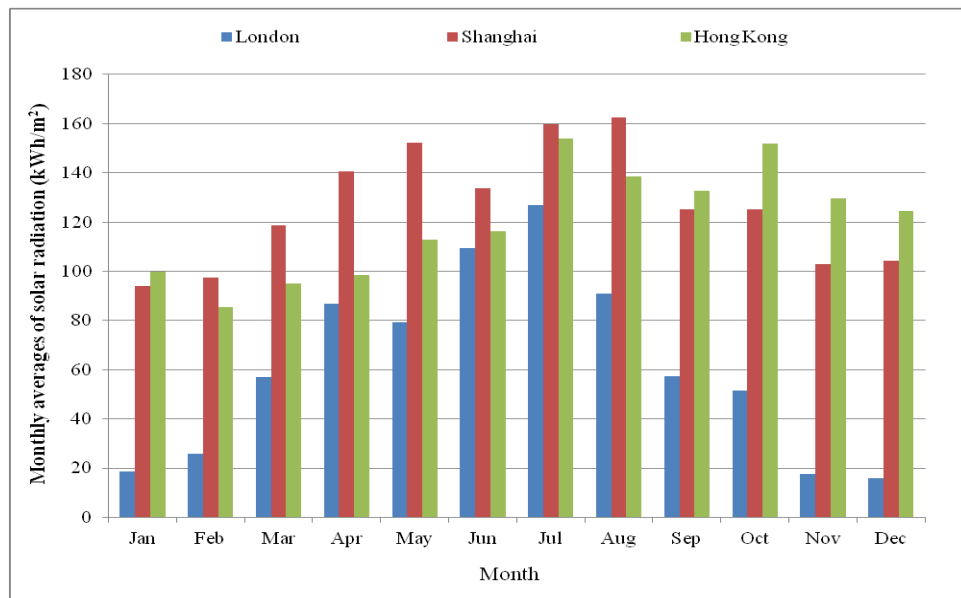


**Fig. 7-2: Monthly averages for solar radiation in three climate regions**

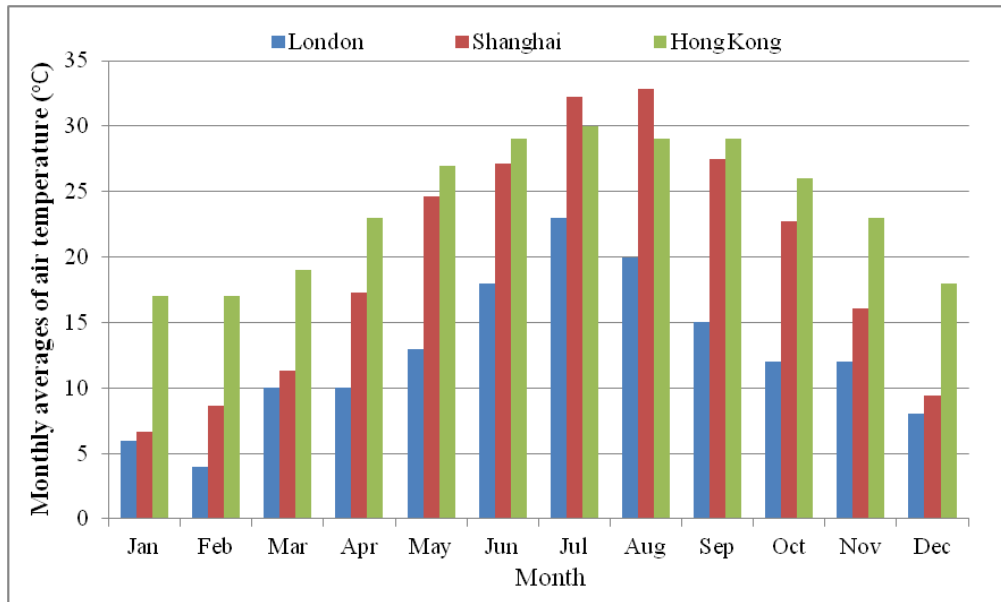


**Fig. 7-3: Monthly averages for air temperature in three climate regions**

**Table 7-1** gives the monthly average weighted wind speed for the three climatic regions. It can be seen that Hong Kong has a medium level of solar radiation, is hot in summer and warm in winter; Shanghai also has a medium level of solar radiation but is hot in summer and cold in winter; while London has a low level of solar radiation, is warm in summer and cold in winter.

**Table 7-1: Monthly averages for wind speed in three climate regions (m/s)**

Location	Jan	Feb	Mar	Apr	May	Jun	Jul	Aug	Sep	Oct	Nov	Dec
London	3.4	2.7	4.6	4.2	2.5	3.2	2.6	3.0	3.1	2.4	2.3	3.2
Shanghai	3.5	3.5	3.5	3.5	3.9	3.7	3.3	3.4	3.6	3.7	3.9	3.8
Hong Kong	3.1	3.7	3.4	3.5	2.8	3.5	3.3	3.3	4.2	3.5	3.3	3.1

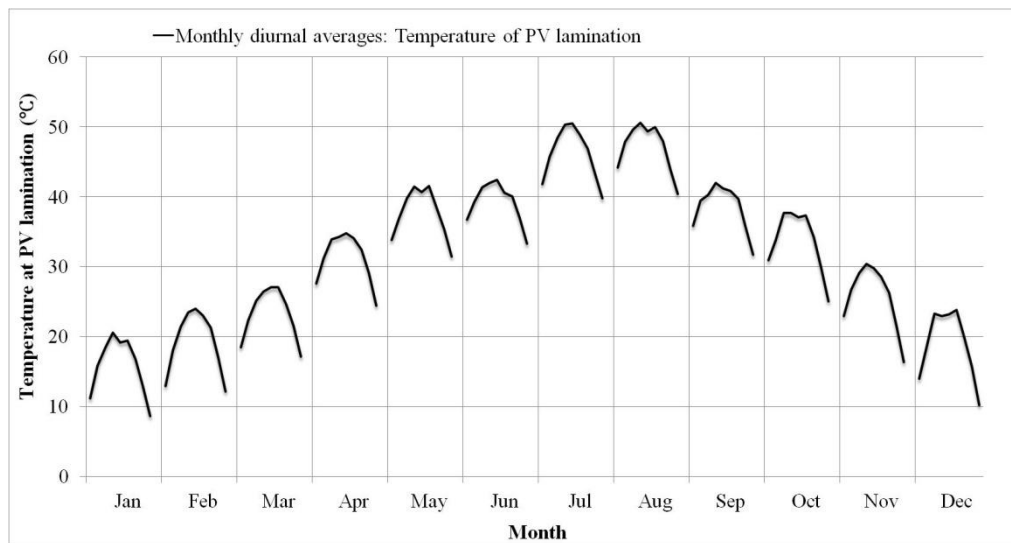
During the simulation, it was assumed that the system starts operation from 08:00 and ends its operation at 16:00 for a single day. The heat pump was considered to operate at 0 °C/55 °C in winter, 10 °C/55 °C in summer, and 5 °C/55 °C in spring and autumn. The PV/LHP panel installation angle was set to the same level as the local altitude in the three selected regions. The initial temperature of the water stored in the tank was considered to be the ground water temperature at a height of 0.5 m below ground level, as in **Table 7-2**. These water temperatures were extracted from the EnergyPlus database [7.1].

Table 7-2: Monthly averages for ground water temperature in three climate regions (°C)

Location	Jan	Feb	Mar	Apr	May	Jun	Jul	Aug	Sep	Oct	Nov	Dec
London	4.2	5.3	7.5	9.6	13.6	15.7	16.2	15.2	12.7	9.7	6.7	4.7
Shanghai	5.5	7.5	11.4	15.2	22.3	26.0	27.0	25.1	20.8	15.3	10.0	6.4
Hong Kong	17.3	18.4	20.5	22.5	26.3	28.3	28.8	27.8	25.5	22.6	19.7	17.8

### 7.2.2 Hourly Predictions of the Prototype System Performance in Shanghai Weather Conditions

By running the established dynamic model, the hourly performance data for the prototype system based in the Shanghai climatic region were derived. **Fig. 7-4** illustrates the average temperature of the PV layer on a typical day during different months. The PV temperature presents the same trend of variation as for the solar radiation and air temperature. Its maximum figure reached over 50 °C during July and August, and the minimum went down to less than 10 °C during December and January.



**Fig. 7-4: Monthly diurnal average variation of temperature at the PV layer**

Owing to the negative effect of temperature on PV electrical output, the PV electrical efficiency presents a contrary trend of variation compared to its temperature. The efficiency reached a level as high as 9.2% in winter and fell to as low as 7.9% in summer, as shown in **Fig. 7-5**. Nevertheless, the hourly PV efficiency during a single day's operation was mainly affected by the solar

incident angle, instead of the PV temperature. As a result, the PV electrical efficiency presented a similar trend of variation to that of the hourly solar radiation, as shown in **Fig. 7-1**.

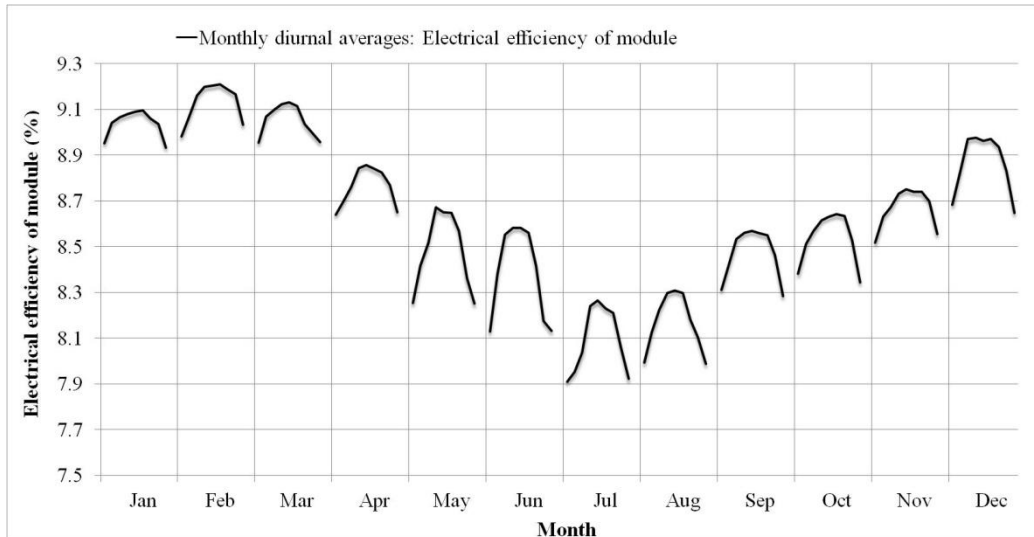


**Fig. 7-5: Monthly diurnal average variation of module electrical efficiency**

**Fig. 7-6** presents the variations in the PV electricity output over different months of a typical year. The electrical output of the PV/LHP module was relatively steady throughout the year, owing to the opposite trend of variation between the solar radiation and the electrical efficiency of the PV/LHP modules.

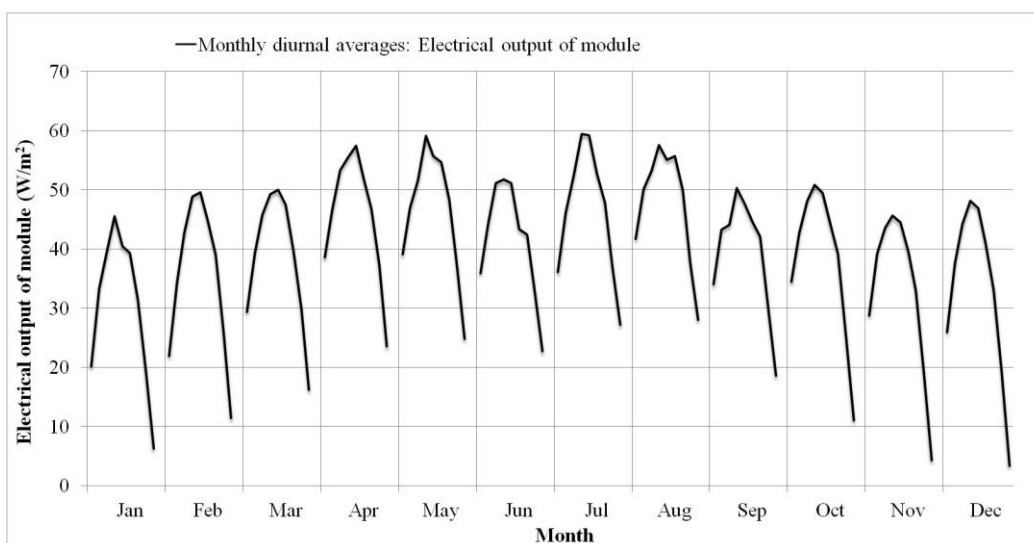


**Fig. 7-6: Monthly diurnal average variations in module electrical output**



The thermal efficiency of the module for monthly diurnal operation is given in **Fig. 7-7**. In a single day's operation, the spontaneous thermal efficiency continued to grow from the morning to the afternoon, owing to the combined effect of lower solar radiation in the morning and higher air temperature in the afternoon, resulting in reduced heat loss and even positive heat absorption from the air. This phenomenon became more obvious in the autumn, leading to significantly higher thermal efficiency up to a level greater than 100%.

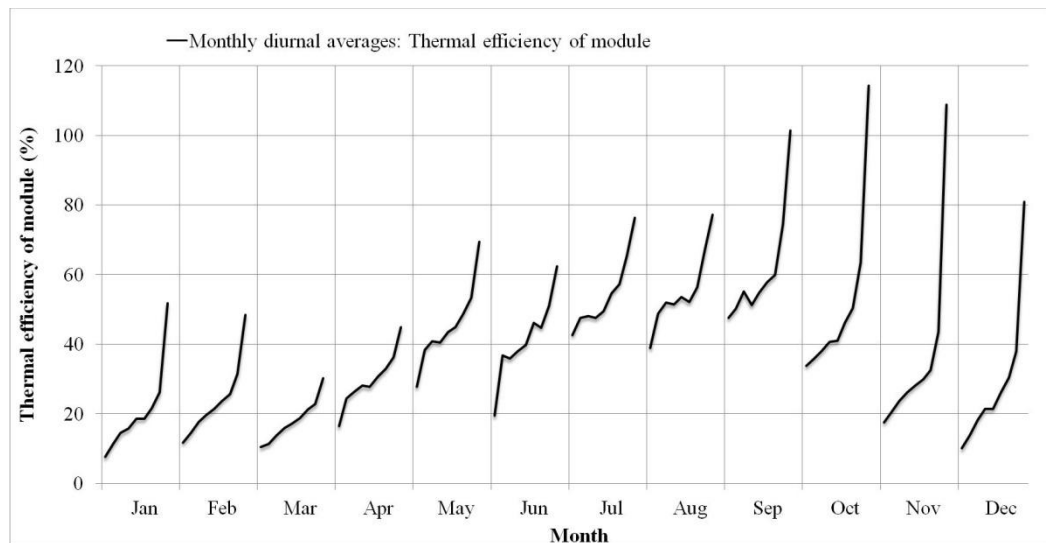


**Fig. 7-7: Monthly diurnal average variations in module thermal efficiency**

**Fig. 7-8** presents the month-to-month variations in the heat output of the module and heat pump condensation capacity during a typical year. It can be seen that the system can absorb more than  $350 \text{ W/m}^2$  of solar heat at its maximum and, consequently, generate more than  $430 \text{ W/m}^2$  of condensation heat using the heat pump.

**Table 7-3** presents variations in the tank water temperature during a single day's operation for different months in a typical year. It was found that from April to October, the water temperatures could achieve a level greater than  $45 \text{ }^\circ\text{C}$ , which would meet the demands of ordinary hot water service. During the remaining months, the water temperature at the end of the day was less than  $45 \text{ }^\circ\text{C}$ , owing to the relatively lower solar radiation, ambient air temperature and initial water temperature. To enable delivery of a suitable water temperature to end users, a back-up heating device, e.g., an electric heater or

gas boiler, should be activated. The highest water temperature that could be achieved in hot seasons reached nearly 55 °C, which is about the same as the condensation temperature of the heat pump. The lowest water temperature was found to be only about 19.45 °C in January. In terms of the temperature rise during a single day's operation, the highest temperature rise was about 39.4 °C, which occurred in October, while the lowest temperature rise was only 14 °C and occurred in January. The area shaded grey in **Table 7-3** indicates the number of months when the temperature of the tank water could not be raised to meet the hot water criterion of 45 °C by only using the prototype system, which consequently indicates that during these months a back-up heater should be brought into operation.

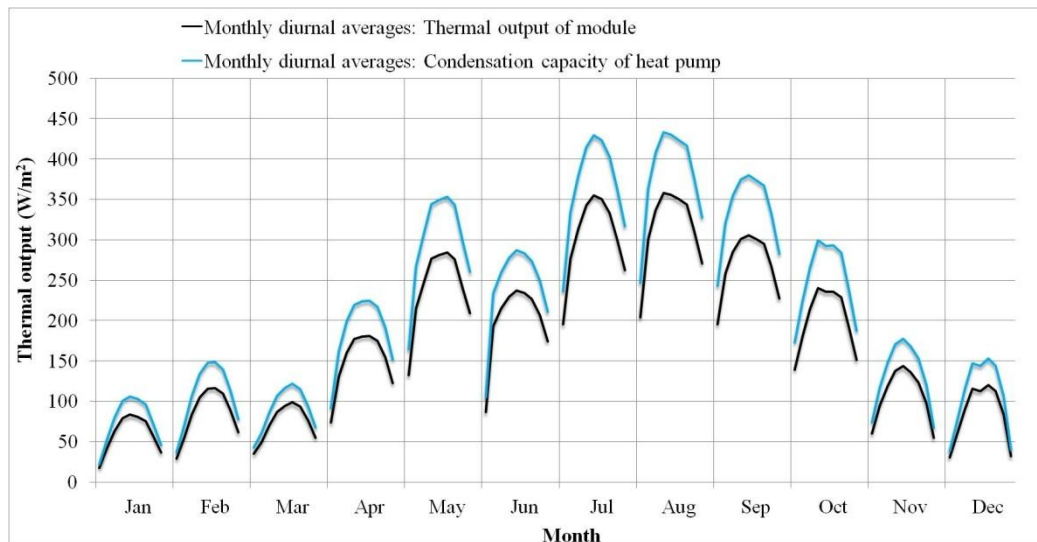


**Fig. 7-8: Monthly diurnal average variations in module thermal output and heat pump condensation capacity**

**Table 7-3: Summary of water temperature in the tank under monthly diurnal averages**

Month	Initial water temperature (°C)	Final water temperature (°C)	Temperature rise over a single day (°C)
Jan	5.45	19.45	14.00
Feb	7.48	26.91	19.43
Mar	11.43	28.52	17.09
Apr	15.17	47.58	32.41
May	22.25	55.00	32.75
Jun	25.97	55.00	29.03

Month	Initial water temperature (°C)	Final water temperature (°C)	Temperature rise over a single day (°C)
Jul	27.00	55.00	28.00
Aug	25.11	55.00	29.89
Sep	20.75	55.00	34.25
Oct	15.31	54.71	39.4
Nov	9.95	32.5	22.55
Dec	6.42	25.76	19.34

**Fig. 7-9** and **Fig. 7-10** provide the overall assessment results of the PV/LHP module only and the integrated PV/LHP heat pump system, respectively. The exergetic efficiency of the module is determined by its thermal efficiency when the PV electrical efficiency only varied in a narrow range. The maximum exergetic efficiency was about 16.6% and occurred in the late afternoons in October, while the minimum exergetic efficiency was only 10.47% and occurred in the early mornings in March.

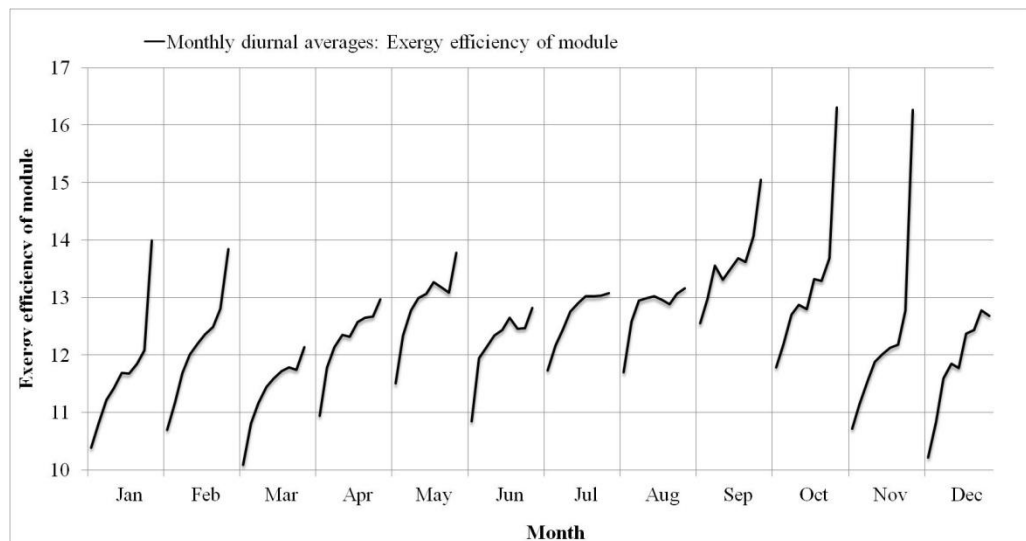


**Fig. 7-9: Monthly diurnal average variations in module exergetic efficiency**

Since the evaporation and condensation temperatures of the heat pump operation have been given for different seasons, the system's thermal performance index ( $COP_{th}$ ) varied seasonally, given as 4.57 in winter, 5.88 in summer, and 5.10 in spring and autumn. The system's overall performance index ( $COP_{PV/T}$ ) was affected by both the electricity and heat generation of the system, and achieved a peak figure of 15.47 in the early mornings in January.

The  $COP_{PV/T}$  figure grew in circumstances of higher electricity generation and lower heat output, which occurred mostly in the cold season (winter) or the early mornings of the other seasons.

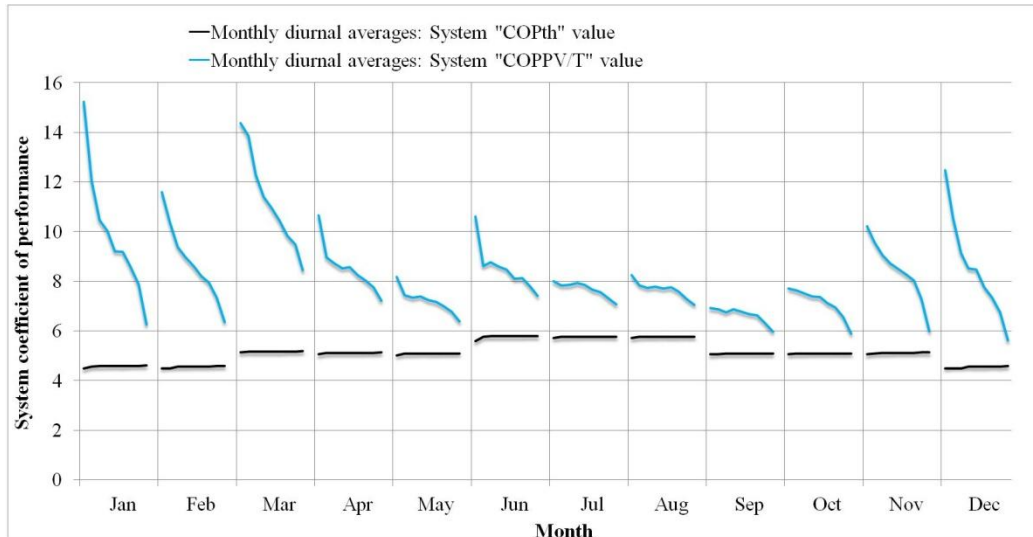
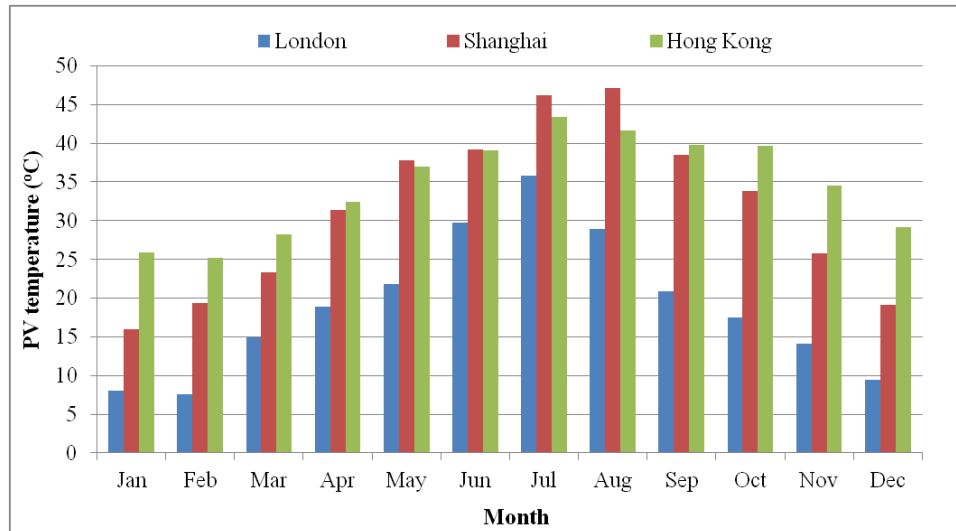


Fig. 7-10: Monthly diurnal average variations in the heat pump  $COP_{th}$  and  $COP_{PV/T}$

### 7.2.3 Monthly Predictions for the Prototype System Performance in Three Climatic Weather Conditions

In order to establish which climate best suits the system, this section investigates the annual operational performances of the prototype system in three climate regions: London, Shanghai and Hong Kong. **Fig. 7-11** presents the monthly average temperatures of the PV layer in the three regions. It was observed that the PV temperature had a similar trend of variation to the solar radiation and air temperature, which achieved a maximum figure in summer and a minimum figure in winter. In London, the monthly PV temperature was in the range from 7.57 °C (in February) to 35.76 °C (in July). In Shanghai, the monthly PV temperature was in the range from 15.93 °C (in January) and 47.12 °C (in August). In Hong Kong, the PV temperature was in the range from 25.23 °C (in February) to 43.41 °C (in July). The PV temperature was the lowest in London and the highest in Hong Kong throughout the year. The annual average PV temperatures in London, Shanghai and Hong Kong were 18.97 °C, 31.45 °C and 34.66 °C, respectively.



**Fig. 7-11: Temperatures of the PV layer in three climate regions**

The monthly electrical efficiencies of the PV/LHP module varied inversely to its temperature, as shown in **Fig. 7-12**, which were in the range from 8.42% to 9.35% in London, 8.02% to 9.08% in Shanghai, and 8.16% to 8.77% in Hong Kong. The annual mean electrical efficiency was highest at 8.94% in London, while it was relatively lower in Shanghai (8.57%) and Hong Kong (8.42%). However, the module's thermal efficiency varied in the opposite manner to its electrical efficiency. The monthly thermal efficiency of the PV/LHP module was in the range from 14.13% to 34.63% in London, 18.06% to 61.41% in Shanghai, and 43.13% to 59.86% in Hong Kong. Operation of the prototype system in Hong Kong was found to be the most stable, with the highest annual average thermal efficiency of the module at about 51.65% owing to the warmest air temperatures existing in this area. In Shanghai and London, the annual average thermal efficiencies of the module were much lower than in Hong Kong at around 38.99% and 26.99%, respectively. After adding the electrical and thermal efficiencies together, the overall energetic efficiencies of the module varied in a similar way to the thermal efficiency, which had annual average values of 35.93%, 47.57% and 60.06% in London, Shanghai and Hong Kong, respectively.

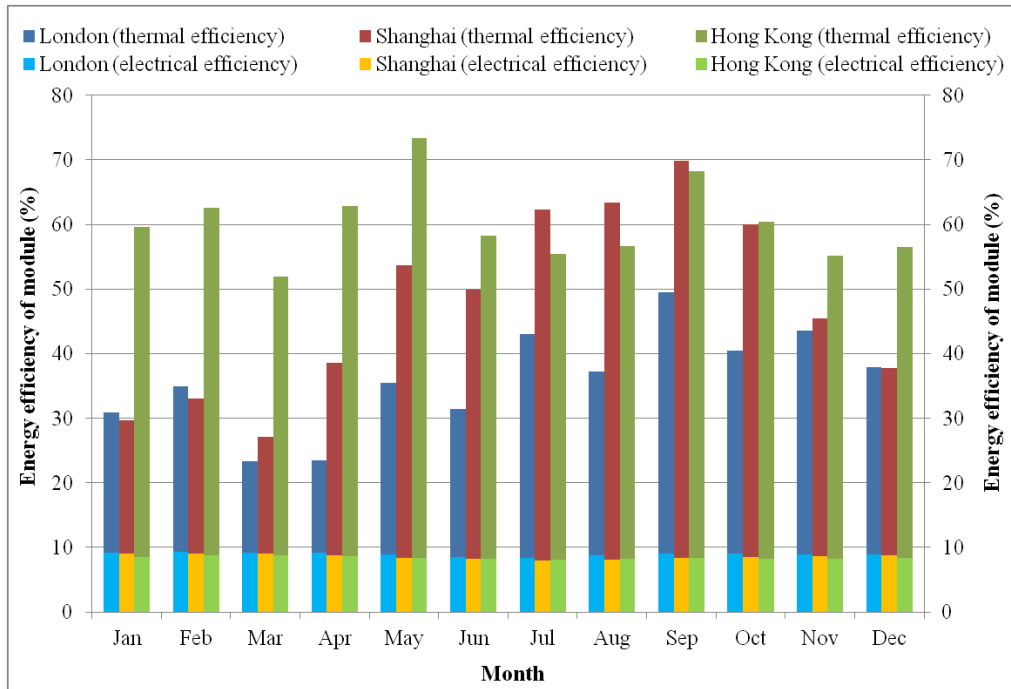


**Fig. 7-12: Energetic efficiencies of the PV/LHP module in three climate regions**

An overall assessment of the PV/LHP module and the associated heat pump system is presented in **Fig. 7-13**. From the module point of view, the exergetic efficiency was relatively stable for all three regions. Owing to the highest thermal output, the annual average exergetic efficiency of the PV/LHP module was highest in Hong Kong at 13.08%, followed by 12.35% in Shanghai, and 11.85% in London. From the integrated system point of view, the annual average  $COP_{PV/T}$  value was highest at 9.44 in London because of the largest ratio of electricity to heat output, while relatively lower  $COP_{PV/T}$  values were found in Shanghai (8.35) and Hong Kong (6.97). It needs to be addressed that as the evaporation and condensation temperatures of the heat pump operation were set up at the same level in all three regions, the seasonal system  $COP_{th}$  value will be the same as that of Shanghai at 4.57, 5.10 and 5.88, respectively, in the winter, transit, and summer seasons.

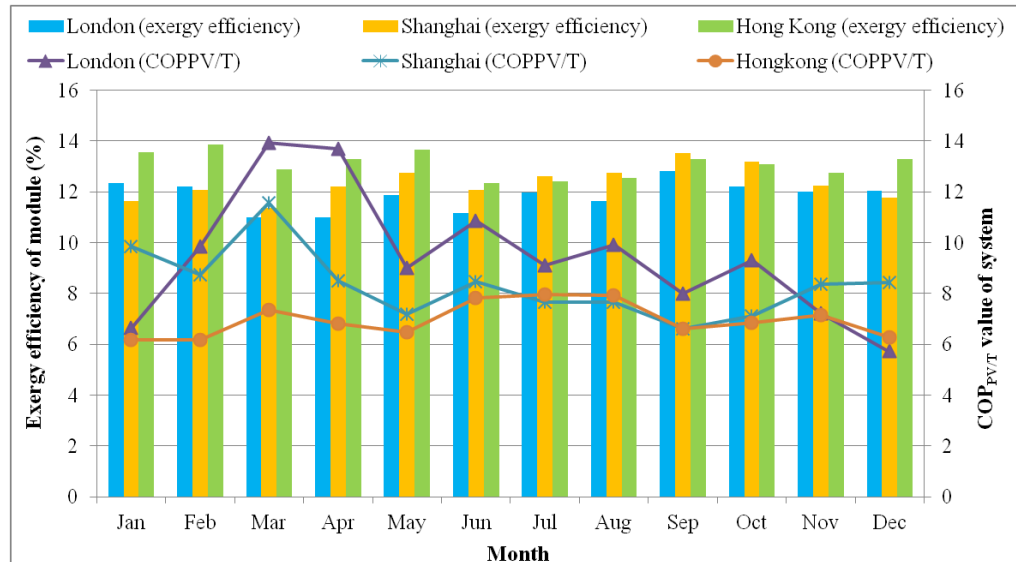


**Fig. 7-13: Overall assessment of the prototype system in three climate regions**

**Fig. 7-14** illustrates the overall energy output of the module. The quantity of the energy output was found primarily to depend on the amount of available solar radiation and the surrounding air temperature in the three regions. The module electricity generation in London varied from 1.42 kWh/m<sup>2</sup> to 10.70 kWh/m<sup>2</sup>, with an average value of 5.43 kWh/m<sup>2</sup>. The monthly electrical output range in Shanghai was from 8.48 kWh/m<sup>2</sup> to 13.15 kWh/m<sup>2</sup>, with an average performance of 10.76 kWh/m<sup>2</sup>. In Hong Kong, the system generated electricity in the range of 7.49 kWh/m<sup>2</sup> to 12.56 kWh/m<sup>2</sup>, with an average value of 10.06 kWh/m<sup>2</sup>. The thermal output ranges of the module were 4.07-43.99 kWh/m<sup>2</sup>, 19.51-89.77 kWh/m<sup>2</sup> and 41.04-79.50 kWh/m<sup>2</sup>, respectively in London, Shanghai and Hong Kong, and their corresponding monthly average values were 16.44 kWh/m<sup>2</sup>, 51.40 kWh/m<sup>2</sup> and 61.82 kWh/m<sup>2</sup>. According to these figures, Hong Kong was found to have the highest energy output for the module, including an almost equivalent electricity output to Shanghai and the highest monthly average heat generation for the three regions.

By adding together the heat pump electrical consumption and the heat output of the module (heat source), the monthly condensation heat outputs (heat sink) of the integrated PV/LHP heat pump system are presented in **Fig. 7-15**, giving a figure in the range from 5.37 kWh/m<sup>2</sup> to 54.96 kWh/m<sup>2</sup> in London, 25.75-112.15 kWh/m<sup>2</sup> in Shanghai, and 52.54-102.28 kWh/m<sup>2</sup> in Hong Kong,

respectively, and the corresponding monthly average figures are 20.89 kWh/m<sup>2</sup> in London, 65.59 kWh/m<sup>2</sup> in Shanghai, and 79.33 kWh/m<sup>2</sup> in Hong Kong.

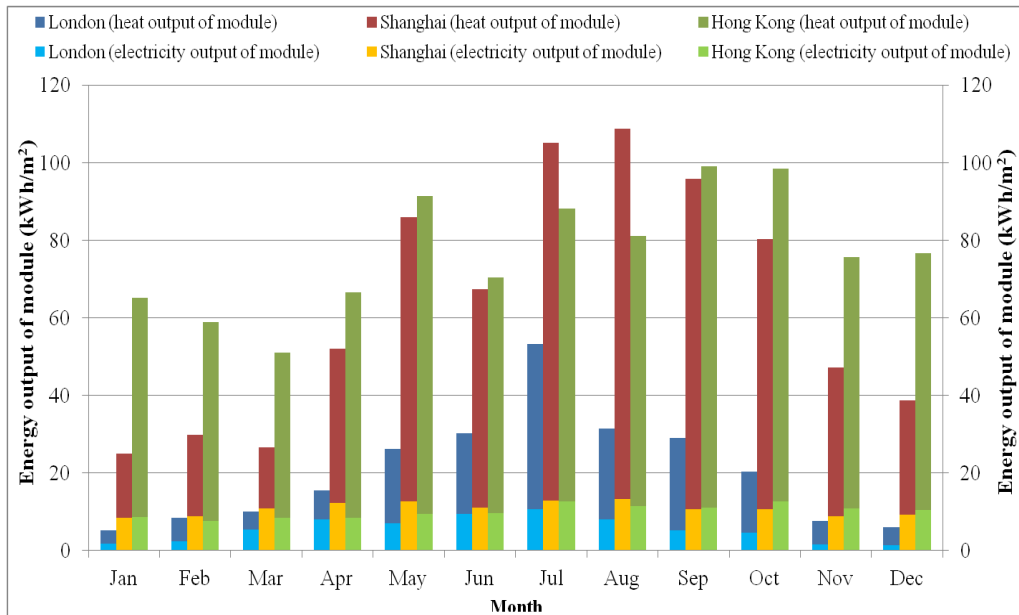


Fig. 7-14: Overall energy output of the PV/LHP module in three climate regions

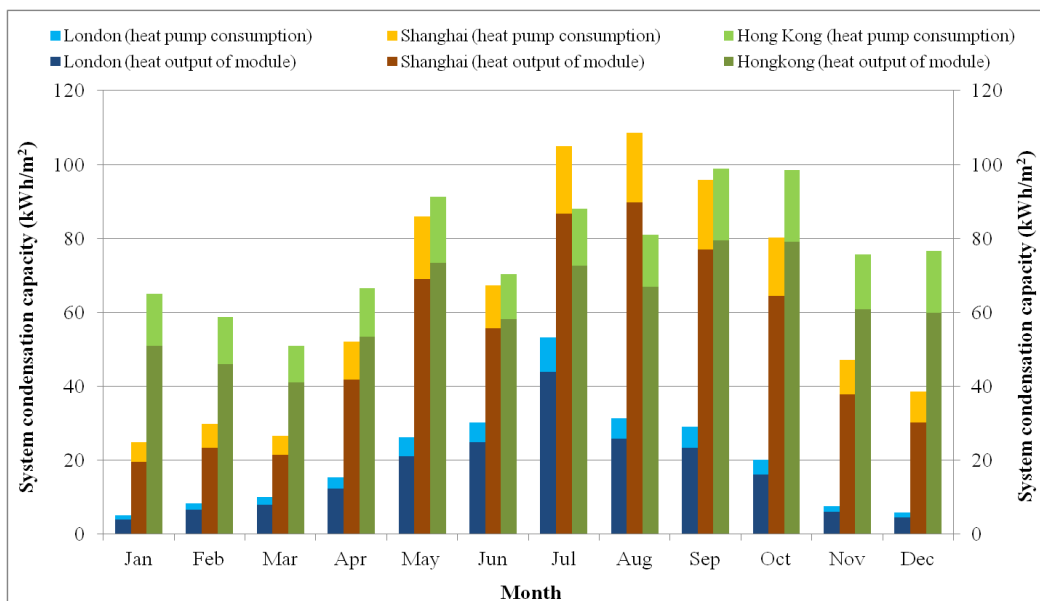


Fig. 7-15: Condensation capacity of the heat pump in three climate regions

Table 7-4 presents the monthly eventual water temperature after a single day’s operation for the three climatic regions. The area shaded grey in the table indicates the months that the temperature of the tank water could not be heated above the hot water temperature criterion of 45 °C by the prototype system



alone. This system could provide hot water service for nearly seven months per year in Shanghai. However, there was only one month in London (July) in which this system could achieve the water temperature criterion. In Hong Kong, this system could reach the required water temperature throughout whole year.

**Table 7-4: Monthly final tank water temperature in three climate regions**

Month	London (°C)	Shanghai (°C)	Hong Kong (°C)
Jan	10.32	19.45	50.73
Feb	9.49	26.91	50.40
Mar	12.67	28.52	47.95
Apr	18.32	47.58	55.00
May	26.31	55.00	55.00
Jun	31.68	55.00	55.00
Jul	47.95	55.00	55.00
Aug	25.01	55.00	55.00
Sep	18.37	55.00	55.00
Oct	16.48	54.71	55.00
Nov	13.97	32.50	55.00
Dec	12.00	25.76	55.00

**Table 7-5** gives the total annual operational output of the prototype system in the three areas. Hong Kong was found to have the highest thermal energy output for the module at 741.85 kWh/m<sup>2</sup>-yr, which was then upgraded to 921.70 kWh/m<sup>2</sup>-yr by inputting electricity at 179.85 kWh/m<sup>2</sup>-yr into the heat pump compressor. After subtracting the solar electricity generation, this system would require additional electricity of 59.11 kWh/m<sup>2</sup>-yr from the grid to meet the heat pump consumption in Hong Kong, which would not need any other auxiliary heater in the system to achieve the hot water demand. Owing to the highest solar radiation level and conspicuous seasonal air temperature in Shanghai, the prototype system could generate the most electricity at 129.14 kWh/m<sup>2</sup>-yr but have a lower heat output than the operation in Hong Kong. In London, this system produced the lowest energy quantity for both electricity and heat, due to the lowest level of solar radiation and the coldest air temperature for the three regions. Although this prototype system produced a net amount of electricity in London, it consumed much more energy from the back-up heater to meet the hot water demand. The simulation results offer the

interpretation that this prototype system would perform best in a subtropical climate, such as the Hong Kong area.

**Table 7-5: Total annual output of the prototype system in three climate regions**

Location	London	Shanghai	Hong Kong
Solar radiation (kWh/m <sup>2</sup> -yr)	737.35	1515.78	1439.26
Solar electricity generation (kWh/m <sup>2</sup> -yr)	65.11	129.14	120.74
Solar heat output of module (kWh/m <sup>2</sup> -yr)	197.23	616.78	741.85
Heat pump work consumption (kWh/m <sup>2</sup> -yr)	45.47	145.29	179.85
Heat pump condensation heat (kWh/m <sup>2</sup> -yr)	242.70	762.07	921.70
System net electricity output (kWh/m <sup>2</sup> -yr)	19.64	-16.15	-59.11

### 7.3 Life-cycle Economic Analysis

#### 7.3.1 Capital Cost

##### (1) Capital Cost of the Prototype PV/LHP Heat Pump System

The capital cost of the prototype PV/LHP heat pump system was estimated by adding together the individual prices of all the system components and taking into account appropriate commercial profits. **Table 7-6** provides a list of cost breakdowns and indicates that the initial cost of such a system is GBP 410.15. Furthermore, the cost details of the different system components are presented in **Fig. 7-16**. The PV/LHP module was the most expensive of the system components, accounting for nearly 44% of the total system cost.

**Table 7-6: Capital cost breakdown of the prototype PV/LHP heat pump system**

No.	Component	Quantity/size	Unit price (CNY)	Cost (CNY)
<b>PV/LHP module</b>				
1	PV layer	1 [89Wp]	850.00	850.00
2	Loop heat pipe	3.2 [m]	160.00	160.00
3	Treated Al-alloy sheet	1 [piece]	150.00	150.00
4	Tempered glazing	1 [piece]	60.00	60.00
5	Aluminium frame	1 [piece]	70.00	70.00
6	Aluminium fin sheet	1 [piece]	110.00	110.00
<b>Other components</b>				
7	Flat-plate heat exchanger	1 [1kW]	150.00	150.00

No.	Component	Quantity/size	Unit price (CNY)	Cost (CNY)
8	Heat pump compressor	1 [1HP]	1,000.00	1,000.00
9	Expansion valve	1 [piece]	50.00	50.00
10	Refrigerant	1 [300g]	60.00	60.00
11	Water tank	1 [35L]	55.00	55.00
12	<u>Solar controller</u>	1 [12V10A]	80.00	80.00
13	Electric wire	1 [coil]	40.00	40.00
14	Battery	1[12V100 AH]	150.00	150.00
<b>Other accessories</b>				
15	Thermal insulation	4 [piece]	60.00	60.00
16	Module bracket	1 [piece]	80.00	80.00
17	Silicon seal	2 [bottle]	30.00	30.00
<b>Subtotal</b>				
Total system fabrication cost (CNY)				3,155.00
Additional profit (30% of total fabrication cost)				946.50
Capital cost (CNY)				4,101.50
Capital cost (GBP)				410.15

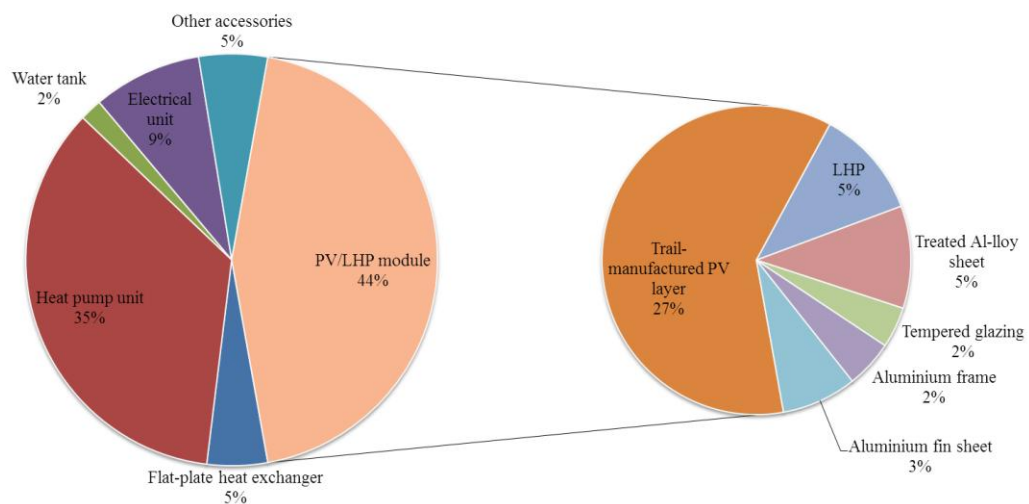


**Fig. 7-16: Cost breakdown of the PV/LHP heat pump prototype system**

## (2) Renewable Earning (RE)

To install a new solar water heating system, it might be possible to receive grants through the government's renewable policy, such as the Renewable Heat Incentive (RHI) scheme in London, which is intended to encourage the uptake of renewable heating technologies within households, communities and businesses through the provision of financial incentives. The financial support available for installing such a solar thermal system in the three regions is given in **Table 7-7** using figures extracted from **Table 7-5** and **Table 7-6** [7.2-7.3].

The final cost of the installation of such a solar prototype system equals the value achieved by subtracting the local incentive amounts for renewable projects from the capital cost.

**Table 7-7: Renewables tariffs for the installation of a solar thermal system**

Location	London	Shanghai	Hong Kong
Tariff	GBP 0.192/ kWh-yr-heat [7.2]	Reduction in 13% of capital cost [7.3]	Not found
Years	7	1	N/A
Total earning (GBP)	199.63	53	N/A

### 7.3.2 Annual Operational Cost and Saving

The initial water temperature in the 35-litre water tank was assumed to be the same as the ground water temperature, as shown in **Table 7-8**. The eventual hot water temperature was considered to be 45 °C. Thus, the annual hot water demand,  $Q_{w,load}$  (W), can be calculated by

$$Q_{w,load} = M_w c_w \Delta T_w \quad [6-1]$$

In the potential case of the unsatisfactory operation of the prototype system in certain terrible weather conditions, an auxiliary heater could be switched on to heat up the water until its temperature achieves the expected 45 °C. A gas boiler and electric heater are, respectively, considered as the auxiliary heater of the prototype system when comparing it with a conventional gas boiler (efficiency of 80%) and a typical electric heater (efficiency of 90%) [7.4]. The annual operating cost of these systems can be estimated as shown in **Table 7-8** and **Fig. 7-17**. It needs to be noted that the total heat (required only to be 45 °C here) produced by the prototype system was estimated to be less than the amount of heat pump condensation heat in **Table 7-5**, because the water was heated up to more than 45 °C in a number of circumstances. The combination of the prototype system with an auxiliary gas boiler was the most economical and, when replacing conventional gas/electric water heaters, such a combined operation could save nearly GBP 10.40/58.75, GBP 8.92/25.28, and GBP

57.17/39.40 per year in the regions of London, Shanghai and Hong Kong, resulting in an annual cost saving ratio of 34.43%/74.79%, 72.03%/88.27%, and 92.95%/90.08%, respectively.

**Table 7-8: Annual operating costs of different water heating systems**

Location	London	Shanghai	Hong Kong
<b>Energy price and demand</b>			
Gas price (GBP/kWh) [7.5-7-7]	0.05	0.02	0.15
Electricity price (GBP/kWh) [7.8-7-10]	0.14	0.06	0.12
Feed-In Tariff (GBP/kWh) [7.11-7-12]	0.15	0.10	0.14
Total heat demand for hot water (kWh/yr)	519.91	431.13	328.04
<b>PV/LHP heat pump system operational performance</b>			
Heat produced from system (kWh/yr)	148.02	317.58	328.04
Energy required from auxiliary heater (kWh/yr)	371.89	113.55	0.00
Total electricity output from module (kWh/yr)	39.85	79.03	73.89
Electricity consumed by heat pump (kWh/yr)	27.84	82.3	110.04
Net electricity output (kWh/yr)	12.01	-3.27	-36.15
<b>Gas water heater (efficiency 80%)</b>			
Required gas energy (kWh/yr)	649.88	538.91	410.05
Operational cost (GBP/yr)	30	12	62
<b>Electric water heater (efficiency 90%)</b>			
Required electricity energy (kWh/yr)	577.68	479.03	364.49
Operational cost (GBP/yr)	79	30	44
<b>PV/LHP heat pump system + auxiliary gas boiler</b>			
Gas required from auxiliary gas boiler (kWh/yr)	464.86	141.94	0.00
Operational cost (GBP/yr)	19.81	3.47	4.34
Annual saving by replacing gas boiler (GBP/yr)	<b>10.40</b>	<b>8.93</b>	<b>57.17</b>
Annual saving ratio by replacing gas boiler (%)	<b>34.43</b>	<b>72.03</b>	<b>92.95</b>
Annual saving by replacing electric heater (GBP/yr)	<b>58.75</b>	<b>26.09</b>	<b>39.40</b>
Annual saving ratio by replacing electric heater (%)	<b>74.79</b>	<b>88.27</b>	<b>90.08</b>
<b>PV/LHP heat pump system + auxiliary electric heater</b>			
Electricity required from auxiliary electric heater (kWh/yr)	413.21	126.17	0.00
Operational cost (GBP/yr)	54.39	7.99	4.34
Annual saving by replacing gas boiler (GBP/yr)	-24.18	4.41	57.17
Annual saving ratio by replacing gas boiler (%)	0.00	35.57	92.95
Annual saving by replacing electric heater (GBP/yr)	24.17	21.57	39.40
Annual saving ratio by replacing electric heater (%)	30.76	72.98	90.08

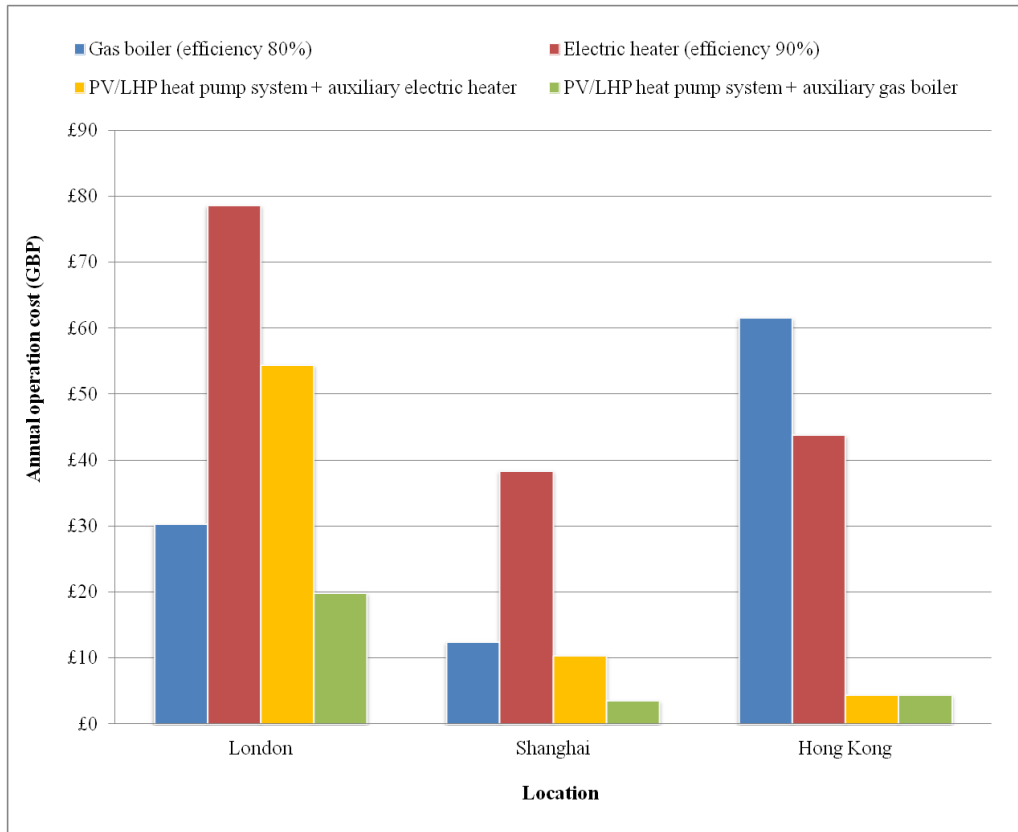


Fig. 7-17: Annual operating costs of different water heating systems

### 7.3.3 Annual Maintenance Cost

The maintenance cost of a solar heating system is normally estimated at 2% of the initial system cost [7.13] due to its low maintenance requirement. The maintenance cost of a gas boiler is estimated at GBP 25/yr, GBP 8/yr and GBP 10/yr, respectively, in the regions of London, Shanghai and Hong Kong [7.14-7.15]. An electric water heater is considered free in terms of its maintenance during its life cycle [7.16].

### 7.3.4 Cost Payback Period and Life-cycle Net Cost Saving

The cost payback period for operating such a prototype system to replace conventional water heaters can be estimated by [7.13]

$$PP_{PV/LHP} = \frac{C_{c,PV/LHP} - C_{RE}}{(C_{o,wh} + C_{m,wh}) - (C_{o,PV/LHP} + C_{m,PV/LHP})} \quad [6-2]$$

where,  $PP_{PV/LHP}$  is the payback period of PV/LHP heat-pump system (year);  $C_{c,PV/LHP}$  and  $C_{RE}$  are respectively the capital cost of PV/LHP heat-pump system and the cost reduction due to renewable earnings (GBP);  $C_{o,wh}$  and  $C_{m,wh}$  are respectively the annual operational and maintenance costs of the conventional water heating system (GBP);  $C_{o,PV/LHP}$  and  $C_{m,PV/LHP}$  are respectively the annual operational and maintenance costs of PV/LHP heat-pump system (GBP).

As a solar photovoltaic system is usually considered to have a life span of 25 years [7.17], the life-cycle net cost saving,  $CS_{PV/LHP}$  (GBP), of this hybrid solar system in energy bills can be determined by

$$CS_{PV/LHP} = (25 - PP_{PV/LHP}) [(C_{o,wh} + C_{m,wh}) - (C_{o,PV/LHP} + C_{m,PV/LHP})] \quad [6-3]$$

**Table 7-9** gives the estimated payback period and life-cycle net cost saving of such a prototype PV/LHP heat pump system when supported by a conventional water heater. When replacing a typical gas heater, this system has the shortest cost payback period of up to 7 years and the highest life-cycle net cost saving of nearly GBP 1,064 in Hong Kong. In London, the cost payback period will be around 8 years with a life-cycle net cost saving of about GBP 469 after considering the renewable award of installing a new solar thermal system. About 41 years (more than its life span) would be required in Shanghai to reclaim the initial investment due to the current lowest gas charging tariff, which indicates that it would be uneconomical to replace a gas water heater with the proposed PV/LHP heat pump system in this area at the moment. When replacing a conventional electric water heater, the system's payback periods were estimated at nearly 5, 20 and 14 years, respectively, in London, Shanghai and Hong Kong owing to the different electricity charging tariffs and governmental support policies. The net cost saving would be around GBP 1,053, GBP 90 and GBP 370 accordingly throughout the system life span.

Table 7-9: Cost payback period and life-cycle net cost saving

Location	London	Shanghai	Hong Kong
<b>Replacing a gas water heater</b>			
Payback period (yrs)	8	41	7
Life-cycle cost saving (GBP)	469	-	1,064
<b>Replacing an electric water heater</b>			
Payback period (yrs)	5	20	14
Life-cycle cost saving (GBP)	1,053	90	370

The analytical results in **Table 7-9** below demonstrate that it would be most cost-effective for such a PV/LHP heat pump system with a backup gas boiler to replace a standard gas water heater in Hong Kong and an electric water heater in London. It would be very uneconomical for the PV/LHP heat pump system to replace either type of conventional water heater in the Shanghai area.

#### 7.4 Life-cycle Environmental Benefits

Environmental benefits can be estimated easily by using the annual CO<sub>2</sub> emission factor when operating this PV/LHP heat pump system with a gas boiler as backup to replace a conventional gas or electric water heater (including the required auxiliary gas energy and the net system electricity consumption) [7.13]. This is given by

$$CR_{PV/LHP} = f_{wh,co_2} Q_{w,load} - f_{gas-co_2} Q_{au,PV/LHP} - f_{el-co_2} Q_{au,PV/LHP} \quad [6-4]$$

where,  $CR_{PV/LHP}$  is the carbon reduction of PV/LHP heat-pump system (kg);  $f_{wh,co_2}$ ,  $f_{gas-co_2}$  and  $f_{el-co_2}$  are respectively the CO<sub>2</sub> emission factors of water-heating system, gas and electric heaters;  $Q_{au,PV/LHP}$  is the required auxiliary gas energy or the electricity consumption by the PV/LHP heat pump system with a gas boiler as backup (W).

The gas-to-CO<sub>2</sub> emission factor is estimated to be the same for the three regions, as gas is directly burned for heat generation. The CO<sub>2</sub> emission factor



of electricity is considered different for the three regions due to the different efficiencies of the national power plants, given in **Table 7-10**.

**Table 7-10: Environmental benefits of the prototype system**

Location	London	Shanghai	Hong Kong
<b>Replacing a gas water heater</b>			
CO <sub>2</sub> emission factor (kg CO <sub>2</sub> /kWh heat) [7.4]	0.260	0.260	0.260
CO <sub>2</sub> emission reduction (kg)	48.11	99.95	76.25
Life cycle CO <sub>2</sub> emission reduction (t)	1.20	2.50	1.91
<b>Replacing an electric water heater</b>			
CO <sub>2</sub> emission factor (kg CO <sub>2</sub> /kWh heat) [7.18-7.20]	0.545	0.997	0.840
CO <sub>2</sub> emission reduction (kg)	193.97	437.43	275.81
Life cycle CO <sub>2</sub> emission reduction (t)	4.85	10.94	6.90

Shanghai was found to have the highest life-cycle CO<sub>2</sub> emission saving of about 2.50 t and 10.94 t when replacing a gas and electric water heater, respectively, with the prototype system, which is mainly owing to the lowest efficiency of its national power plant. In London and Hong Kong, the prototype system has a relatively lower carbon emission reduction of around 1.20 t/4.85 t and 1.91 t/6.90 t to replace gas and electric water heaters, respectively. The analytical results illustrate that the maximum environmental benefits would be achieved by operating the PV/LHP heat pump prototype system in the Shanghai area at the present time.

## 7.5 Chapter Summary

This chapter provided a feasibility study for the use of the prototype PV/LHP heat pump system in three different climatic regions: London, Shanghai and Hong Kong. The overall analysis included a prediction of the annual operational performance, economic rewards, and associated environmental benefits.

Hourly prediction of system performance in Shanghai was conducted and the results indicate that the PV module's electrical efficiency was in the range from 7.9% (in summer) to 9.2% (in winter), while its thermal efficiency was in the range from 7.7% (in winter) to more than 100% (in autumn). The maximum

exergetic efficiency was 16.6%, which occurred in the late afternoons in October, while the minimum exergetic efficiency was 10.47% and occurred in the early mornings in March. The system  $COP_{th}$  varied seasonally with 4.57 in winter, 5.75 in summer, and 5.10 in spring and autumn. The system's overall performance index  $COP_{PVT}$  reached the maximum figure of 15.47 in the early mornings in January, during which time the electricity generation reached the highest level and the heat output fell to the lowest.

The monthly system performance parameters were predicted in the above three regions. The results indicate that the system obtained the highest heat output of 921.70 kWh/m<sup>2</sup>-yr in Hong Kong, which allowed the system to provide sufficiently high water temperatures (above 45 °C) throughout the year by only entering 59.11 kWh/m<sup>2</sup>-yr of grid electricity. In Shanghai, the system obtained a higher volume of electricity but a lower volume of heat compared to Hong Kong. In London, the system provided a lower volume of electricity and heat than both Hong Kong and Shanghai, owing to its low solar radiation and air temperature. As a result, the system, if operated in London, would consume a higher volume of additional energy provided by the backup heaters. The simulation results indicate that the prototype PV/LHP heat pump system would be best suited for use in a subtropical climatic region, such as Hong Kong.

To replace a typical gas water heater, this PV/LHP heat pump prototype system (with a backup gas boiler) has the shortest cost payback period of 7 years and the highest life-cycle net cost saving of nearly GBP 1,064 in Hong Kong. In London, the cost payback period would be 8 years with a life-cycle net cost saving of about GBP 469 after considering the renewable award by installing a new solar thermal system. It was found to be uneconomical to invest in the prototype system in Shanghai, with a payback period of 41 years (more than its life span) due to the low gas charging tariff. To replace a conventional electric water heater, the system's payback periods were estimated at nearly 5, 20 and 14 years, respectively, in London, Shanghai and Hong Kong. The life-cycle net cost saving would, accordingly, be around GBP 1,053, GBP 90 and GBP 370. By considering the different energy charging tariffs and governmental support policies, the analytical results suggest that it would be most cost effective for

such a PV/LHP heat pump prototype system with a backup gas boiler to replace gas water heaters in Hong Kong and electric water heaters in London. It would be very uneconomical for the PV/LHP heat pump system to replace either type of conventional water heater in the Shanghai area at the moment.

The PV/LHP heat pump prototype system could achieve the highest life-cycle CO<sub>2</sub> emission saving of about 2.50 t and 10.94 t in Shanghai when using it to replace gas and electric water heaters, respectively, owing to the lowest efficiency of its national power plant for the three regions at the current stage. In London and Hong Kong, the prototype system would have relatively lower carbon emission reductions of 1.20 t/4.85 t and 1.91 t/6.90 t, respectively, when using it to replace gas and electric water heaters.

## CHAPTER 8: CONCLUSION AND FURTHER WORK

### 8.1 Conclusions

The research has presented an in-depth investigation into a novel PV/LHP heat pump system that was undertaken through a critical literature review, optimal concept design, theoretical analysis, the development of simulation models, prototype construction, laboratory-controlled and field testing, validation of the simulation models, and socio-technical acceptance analysis.

The overall achievements include (1) a full range of computer simulation models based on fundamental thermal-fluid analysis, which were validated by experiment; (2) a prototype PV/LHP heat pump system; and (3) a socio-economic model that can predict the energy saving, economic and environmental benefits of the use of the prototype technology in different climatic regions.

The major conclusions derived from the PhD research are given below.

**LHP heat transfer capacity:** this unique LHP with a dedicated vapour-liquid separation structure can achieve a maximum heat transfer capacity of 900 W in specified operational conditions. To maintain a high heat transfer capacity, the LHP device should (1) remain at an appropriate operational temperature of less than 30 °C; (2) use a compound mesh-screen wick structure, instead of sintered powder and groove; (3) have a relatively larger evaporator diameter, e.g., to 22 mm; (4) have a smaller evaporator length, e.g., to 1.2 m; (5) have an evaporator inclination angle in the range 30-60°; (6) have a relatively larger vapour column diameter in the three-way fitting, e.g., to 10 mm; (7) retain a liquid volume of 0.01 litre; and (8) have a condenser that is at least 0.3 m higher than the evaporator.

**Laboratory measurement and steady-state performance characterisation:** an Al-alloy-based PV layer has much better electrical conversion efficiency

than a TPT-based PV layer and can respond to variations in the ambient environmental conditions more promptly. A number of external parameters, such as solar radiation, air temperature and wind speed, and installation methods were investigated for their impact on the electrical performance of the PV layer. It was found that weaker solar radiation, lower air temperature, higher wind speed, and a ground-mounting solution (rather than an on-roof mode), were positive in terms of the electrical performance of both PV layers. During the test mode of solar radiation at  $600 \text{ W/m}^2$ , air temperature at  $20 \text{ }^\circ\text{C}$ , wind speed at  $0.5 \text{ m/s}$ , and an on-roof mounting solution, the temperature of the Al-alloy-based PV cells was observed at  $62.4 \text{ }^\circ\text{C}$ , which was  $5.2 \text{ }^\circ\text{C}$  lower than that of the TPT-based PV cells, and its PV efficiency was about  $9.18\%$ , nearly  $0.26\%$  higher than the TPT type. Although the PV efficiency increase was limited, it was meaningful for a PV system with a relatively low operating efficiency in practice.

The established steady-state model was verified as being able to predict system performance to a reasonable level of accuracy (average error of less than  $5\%$ ). As the heat pump compressor's isentropic efficiency (up to about  $88\%$ ) exists in practice, this would slightly reduce the practical performance coefficient over the theoretical figure. The electrical, thermal and overall efficiency of the PV/LHP module in the given laboratory conditions was around  $10\%$ ,  $40\%$  and  $50\%$ , respectively. In the case of the basic laboratory condition, the consumption of electricity by the compressor reduced the production of electricity by the PV layer, while the net ratio of system electricity generation was calculated at about  $1.51\%$ , which means the system is fully able to output electricity after fulfilling its own power demands in the specific test environment. The steady research results indicate that lower solar radiation, lower air temperature, higher air velocity and smaller cover number led to enhanced electrical efficiency but reduced the thermal efficiency of the module, whereas a lower heat pump evaporation temperature and a larger number of heat-absorbing pipes gave rise to both thermal and electrical efficiencies for the module.

To achieve a better operational performance for the PV/LHP heat pump system, construction of further PV/LHP modules should be made (1) using single glazing as the module cover; (2) fixing two heat pipes underneath the PV layer; and (3) employing an aluminium alloy sheet as the PV baseboard. During system operation, the evaporation temperature of the heat pump is suggested to be set up to a maximum of 20 °C. Moreover, the system could perform better at moderate solar radiation (e.g., 400-600 W/m<sup>2</sup>), a mild surrounding air temperature (e.g., 15-20 °C), and a lower air velocity (e.g., 0-1 m/s).

**Real-time evaluation in real climatic conditions:** the mean daily PV temperature over a consecutive test period was approximately 40 °C. The daily water temperature rise in the tank was nearly 40 °C with maximum water temperatures reaching over 54 °C. The average electrical and thermal efficiency of the PV/LHP module was, respectively, above 9.13% and 39% daily, resulting in corresponding overall energetic and exergetic efficiencies of nearly 48.37% and 15.02%. The average  $COP_{th}$  and  $COP_{PV/T}$  values were calculated at 5.51 and 8.71, respectively. The mean net electricity output ratio was measured at 1.38% daily, indicating that this prototype system can fully drive itself and output an additional amount of power in the meantime. The test results indicate that such a prototype system would have a steady and reliable operating performance in real climate conditions.

In comparison with conventional solar collecting devices, the PV/LHP module can achieve 3% to 5% higher solar exergetic efficiency than standard PV systems and about 7% overall performance above independent solar collectors. Compared to conventional solar-/air-/ground-source heat pump systems, the PV/LHP heat pump system could achieve a much higher COP figure with 1.5 to 4 times that of conventional heat pumps.

Through a parallel comparison between the modelling and real-time test results, the established dynamic model was validated with a reasonable accuracy to predict system performance (mean error less than 9%). It was found that the average water temperature in the storage tank (35 litres) grew gradually from 14.38 °C to 54.29 °C over the test duration. The temperature of the PV layer was in the range of 19.71 °C to 52.64 °C during daytime operation, while its

mean value was 40.66 °C. The temperature difference between the PV layer and heat-absorbing pipe was in the range of 2 °C to 6 °C. For the fin sheet, the temperature variation along the fin width presented a ‘V’ shape and the maximum temperature difference between the fin edges and its central line was around 0.49 °C at 13:00 in the early afternoon. The average electrical/heat outputs and the corresponding solar efficiencies of the PV/LHP module were measured as 29.45 W/120.08 W and 9.12%/38.13%, respectively. Analysis of the measurement data indicated that the thermal and electrical outputs corresponded to 5.8% and 9.12% exergetic efficiencies, thus enabling an overall exergetic efficiency of 14.92% for the PV/LHP module. Further analysis concluded that under single-day test conditions, the average heat pump condensing heat,  $COP_{th}$  and  $COP_{PV/T}$  were 146.86 W, 5.51 and 8.81, respectively. Error analysis was briefly addressed from the theoretical and experimental sides, indicating that the discrepancies were more likely to have come from the theoretical assumptions.

**Socio-economic assessment:** hourly prediction of the system performance in Shanghai was conducted and the results indicate that the PV module’s electrical efficiency would be in the range from 7.9% (in summer) to 9.2% (in winter), while the thermal efficiency would be in the range from 7.7% (in winter) to more than 100% (in autumn). The maximum exergetic efficiency was 16.6% and would occur in the late afternoons in October, while the minimum exergetic efficiency was 10.47% and would occur in the early mornings in March. The system  $COP_{th}$  would vary seasonally with 4.57 in winter, 5.88 in summer, and 5.10 in spring and autumn. The system’s overall performance index  $COP_{PV/T}$  would reach the maximum figure of 15.47 in the early mornings in January, during which time the electricity generation would reach the highest level and the heat output would fall to the lowest.

The monthly system performance parameters were predicted in the three regions. The results indicate that the system could obtain the highest heat output of 921.70 kWh/m<sup>2</sup>-yr in Hong Kong, which would allow the system to provide sufficiently high temperature water (above 45 °C) throughout the year by only entering 59.11 kWh/m<sup>2</sup>-yr of grid electricity. In Shanghai, the system

could obtain a higher volume of electricity but a lower volume of heat compared to Hong Kong. In London, the system could provide the lowest volume of electricity and heat compared with both Hong Kong and Shanghai, owing to its low solar radiation and air temperature. As a result, the system, if operated in London, would consume a higher volume of additional energy provided by the backup heaters. The simulation results indicate that the prototype PV/LHP heat pump system would be best suited for use in a subtropical climatic region, such as Hong Kong.

To replace a typical gas water heater, this PV/LHP heat pump prototype system would have the shortest cost payback period of 7 years and the highest life-cycle net cost saving of nearly GBP 1,064 in Hong Kong. In London, the cost payback period would be 8 years with a life-cycle net cost saving of about GBP 469 after considering the renewable award by installing a new solar thermal system. It was found to be uneconomical to invest in the prototype system in Shanghai currently with a payback period of 41 years (more than its life span) due to the lowest gas charging tariff of the three regions. To replace a conventional electric water heater, the system's payback periods were estimated at nearly 5, 20 and 14 years, respectively, in London, Shanghai and Hong Kong. The life-cycle net cost saving would be around GBP 1,053, GBP 90 and GBP 370, accordingly. By considering the different energy charging tariffs and governmental support policies, the analytical results suggest that it would be most cost effective for such a PV/LHP heat pump prototype system with backup gas boiler to replace gas water heaters in Hong Kong and electric water heaters in London. It would be very uneconomical for the PV/LHP heat pump system to replace either type of conventional water heater in the Shanghai area at the moment.

The PV/LHP heat pump prototype system could achieve the highest life-cycle CO<sub>2</sub> emission saving of about 2.50 t and 10.94 t in Shanghai when using it to replace gas and electric water heaters, respectively, owing to the lowest efficiency of its national power plant of the three regions at the current stage. In London and Hong Kong, the prototype system would have relatively lower



carbon emission reductions of 1.20 t/4.85 t and 1.91 t/6.90 t, respectively, when using this to replace gas and electric water heaters.

The research results should assist in configuring feasible solutions for PV/T technologies and developing the basis of novel solar-driven heating systems for space heating/cooling, hot water supply and natural ventilation in the future. The core technologies could enable a significant reduction in fossil fuel energy and the associated carbon footprint in a built environment.

## 8.2 Further Opportunities and Challenges

### 8.2.1 Pilot Demonstration Project

Based on the substantial recommendations and conclusions from this research, the optimised PV/LHP heat pump water heating system has been constructed and demonstrated on a pilot scale in Shanghai in China. The PV/LHP modules for demonstration were designed with two absorbing heat pipes beneath the PV module, as shown in **Fig. 8-1**.

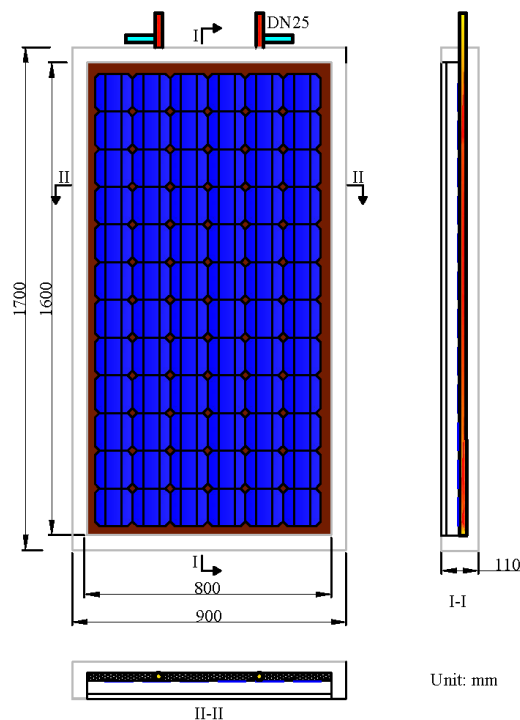


**Fig. 8-1:** Dimensional drawings of the PV/LHP module for the demonstration project

There were four PV/LHP modules in total connected in parallel and each module has an effective absorbing area of  $1.28 \text{ m}^2$ . The modules were fixed to a  $30^\circ$  tilted frame, and fitted with a single-glazing cover on top. The PV cells, consisting of 72 ( $6 \times 12$  array) pieces in total, each with the size of  $125 \times 125 \times 0.3$  (mm  $\times$  mm  $\times$  mm), occupy more than 90% of the absorbing surface. The system employs a 2.25 kW (3 hp)-rating heat pump cycle with evaporation/condensation temperatures of  $10^\circ\text{C}/55^\circ\text{C}$ . A 100-litre water tank with built-in heat-exchanging coils is connected to the heat pump to obtain heat and store the heating water. The electrical parts consist of a 12 V (40 A) controller, an 800 W DC/AC inverter, two 100 AH (12 V) batteries, and connection wires.

The demonstration system was continuously operated and recorded in a real climate over the short term with sunny or cloudy weather conditions from 31<sup>st</sup> July to 6<sup>th</sup> August 2012 in Shanghai ( $31^\circ 11' \text{N}$  and  $121^\circ 29' \text{E}$ ). The testing was fully operated for about six hours daily and the test data were recorded at 30-minute intervals. The on-site project is displayed as **Fig. 8-2**.



**Fig. 8-2: On-site image of the demonstration project in Shanghai, China**

The test results of the experimental rig are given in **Table 8-1**. During the test period, the mean daily PV temperature was approximately  $50^\circ\text{C}$ . The water temperature rise in the tank was about  $30^\circ\text{C}$ , with ultimate water temperatures reaching over  $54^\circ\text{C}$ . The daily average electrical and thermal efficiencies of

the PV/LHP module were 8.99% and 51.14%, respectively, resulting in overall energetic and exergetic efficiencies of nearly 60.13% and 11.03%. The average  $COP_{th}$  and  $COP_{PVT}$  values were about 5.51 and 7.6, respectively. The PV/LHP module generated 2.35 kWh electricity and 13.36 kWh heat daily, while the whole system could produce 16.32 kWh hot water by only inputting an additional 0.61 kWh of electricity.

**Table 8-1: Initial test results for the demonstration project**

Date	Radiation ( $W/m^2$ )	Temperature ( $^{\circ}C$ )			Efficiency (%)		
	$I$	$T_a$	$T_{p,m}$	$\Delta T_w$	$\eta_e$	$\eta_{th}$	$\zeta_o$
2012							
31.07	904	34.50	50.87	30.26	8.95	47.68	11.08
01.08	846	35.10	49.65	29.34	9.00	51.68	11.02
02.08	884	35.70	50.93	30.38	8.94	51.22	11.05
03.08	834	35.20	50.88	29.71	8.95	51.92	11.15
04.08	861	35.40	48.77	30.02	9.03	51.23	10.85
05.08	846	34.90	48.46	30.73	9.04	51.88	10.92
06.08	784	34.60	49.57	30.45	9.00	52.36	11.12
Mean	851	35.06	49.88	30.13	8.99	51.14	11.03
Date	Performance		Energy outputs (kWh)				Energy input (kWh)
2011	$COP_{th}$	$COP_{PVT}$	$Q_e$	$Q_{th}$	$Q_w$	$W_c$	$Q_{e,n}$
31.07	5.51	7.74	2.48	13.24	16.18	2.94	-0.45
01.08	5.50	7.56	2.34	13.43	16.42	2.98	-0.65
02.08	5.52	7.60	2.43	13.91	16.99	3.08	-0.65
03.08	5.52	7.57	2.29	13.30	16.25	2.94	-0.65
04.08	5.51	7.60	2.39	13.55	16.55	3.00	-0.62
05.08	5.50	7.56	2.35	13.48	16.48	3.00	-0.65
06.08	5.51	7.55	2.17	12.61	15.41	2.80	-0.63
Mean	5.51	7.60	2.35	13.36	16.32	2.96	-0.61

Although the demonstration project was tested for about one week, additional testing must be further carried out for long-term schemes to investigate any unpredicted operational problems within the system.

### 8.2.2 PV/LHP Stakeholders

To enable the widespread deployment of such hybrid solar technology, the explicit benefits and challenges for PV/LHP stakeholders have been identified and summarised in **Table 8-2** [1.11], and need to be elaborated to engage them

in the future development of such technology during the coming years. The establishment of an interdisciplinary working group in PV/LHP technology seems necessary, and could attain a sound exchange of information, results and experiences related to R&D, design specifications, design tools, test methods, practical installation barriers, market surveys, policy development, etc. This interdisciplinary cooperation may lead to a clearer understanding of the various problems experienced throughout PV/LHP development.

**Table 8-2: Opportunities and challenges for PV/LHP stakeholders**

PV/LHP stakeholders	Opportunities	Challenges
<b>R&amp;D institutes</b>	Quest for new technological solutions	<ul style="list-style-type: none"> <li>• Performance and reliability standards</li> <li>• Increased module efficiency and system performance</li> </ul>
<b>Engineering Consultants</b>	Innovative and high-profile technology	<ul style="list-style-type: none"> <li>• Commercial design tools development</li> <li>• New system concepts development</li> </ul>
<b>Architects</b>	New solutions for integration	<ul style="list-style-type: none"> <li>• PV/LHP integrated with building design</li> <li>• New building concepts</li> </ul>
<b>Installers</b>	Reduced installation effort	<ul style="list-style-type: none"> <li>• Plug-and-play integration by the available joints</li> <li>• Combination of two professional specialisms</li> </ul>
<b>Building Industry</b>	Increased energy performance	<ul style="list-style-type: none"> <li>• Integration of PV/LHP module into building construction</li> <li>• Prefabrication possibilities</li> </ul>
<b>Manufacturers</b>	Enlarged markets	<ul style="list-style-type: none"> <li>• Cost-effective production</li> <li>• Plug-and-play systems</li> </ul>
<b>Policy makers</b>	More effective path to renewables targets	<ul style="list-style-type: none"> <li>• Relevant building regulations, market and R&amp;D support</li> </ul>

### 8.2.3 Technical Development

Although the characterisation and dynamic evaluation of such technology have been carried out, further technical improvement is still desirable with regard to the following aspects: (1) achieving durable thermal interaction between heat pump controls and solar cells using a variable-frequency compressor; (2) evaluating the economic benefits under different control and operation modes, such as an overnight preheating mode with a low-price electricity tariff; (3) design a double sources heat pump (air and solar PV/LHP) (4) assessing performance with applications in other energy supply systems, such as heating, cooling and processing heat; (5) enhancing the physical contact between the fin sheet and heat pipes for better heat transfer; (6) testing the module structure

strength as a special building facade; and (7) creating feasible options in terms of aesthetics and textures.

#### **8.2.4 Evaluation Standards**

Currently, no published legal standards are found in the PV/T field, while common standards need to be developed as soon as possible. So far, evaluation of PV/T systems in laboratories is conducted according to the researchers' own procedures or standards for solar thermal collectors [1.11]. Neither of these methods is ideal for comparing PV/T with other energy systems equally, for the results will differ from case to case (types of PV cell, testing environment, etc.). As a result, new test procedures should be developed to establish their relevant suitability on the basis of the existing standards of stand-alone PV panels and solar thermal collectors.

#### **8.2.5 Long-term Reliability Measurement**

Although a short-term evaluation of the PV/LHP system in a real climate has been carried out, a long-term (seasonal or annual) scheme is still essential to resolve different uncertainties in practice. This work retains certain challenges, including seasonal dynamic weather conditions, thermal adaptability in different climate zones, and system robustness.

#### **8.2.6 Market Analysis**

Analysis of the market potential is crucial for the development of PV/LHP products. It is well known that solar technology is expected to provide nearly 50% of the low-and-medium temperature heat within the EU [1.8] and 5% of global electricity demand [1.10] by 2030. A market investigation of PV/LHP products is suggested in terms of conducting the following: (1) case studies of existing PV/T products to identify their applicability for end users, climatic regions, market positions, and recommendations; (2) a feasibility study of PV/LHP application in various locations, building types and energy systems; (3) a market survey of customers' preferences; and (4) the establishment of a generic extrapolating methodology for the market analysis of PV/LHP systems.

### **8.2.7 Manufacturing Cost**

Current fabrication of PV/LHP systems is achieved by separate production lines of PV panels and solar thermal collectors. Future large-scale product implementation should combine those two separate manufacturing lines and establish effective upstream/downstream supply chains. Thus, the capital cost would be reduced to some extent. These products also need to be optimised to suit energy specifications, production aspects, and installation and mounting requirements. This part of the work would play an important role in pushing PV/LHP towards the market, while in synergy with market players and local authorities, the PV/LHP manufacturing cost could be further reduced.

### **8.2.8 Dissemination Activities**

In order to motivate the use of PV/LHP technology, more dissemination activities should be presented to the public using various approaches, including the publication of roadmaps, showcases, workshops, on-site visits, open days and conferences. The events should invite both local and national media (television, newspapers, etc.) to conduct live reports throughout the regions, nations and all over the world.

### **8.2.9 Policy Support**

Public energy agencies are the catchers of all the initiatives in building energy saving and environmental pollution reduction, and also connect the actions of the different players. Local authorities and decision makers have a central role in lowering market barriers by proposing public subsidies and financing mechanisms to make PV/LHP solutions competitive with conventional systems. Action should be taken to support PV/LHP development by the integration of local building regulations. The PV/LHP payback time would be significantly reduced if additional policy support came from governments, which we can observe from the case study in London in Chapter 7. However, there is currently no policy issued particularly for this technology. Specific policies should be published to encourage the deployment of such technology and subsidise the corresponding financial benefits for end users.

## APPENDIX: REFERENCES

### References for Chapter 1

- [1.1]. UN Climate Change Conference,  
<[en.wikipedia.org/wiki/Copenhagen\\_Climate\\_Summit](http://en.wikipedia.org/wiki/Copenhagen_Climate_Summit)>, [1/10/2010].
- [1.2]. FIEC – European Construction Industry Federation, < [www.fiec.org](http://www.fiec.org)>, [05/11 /2010].
- [1.3]. EU Energy and transport in figures, statistical pocket book 2007/2008.
- [1.4]. Proposal for a recast of the EPBD, Impact Assessment. COM (2008) 755, SEC (2008) 2821.
- [1.5]. DoE Building Book 2008.
- [1.6]. European Initiative on Energy-efficient Buildings, Scope and Vision, Version 1, January 2009.
- [1.7]. Zekai Şen, Solar energy in progress and future research trends, Progress in Energy and Combustion Science 30 (2004): 367–416.
- [1.8]. Solar Heating and Cooling for a Sustainable Energy Future in Europe (Revised), European Solar Thermal Technology Platform (ESTTP), 2009.
- [1.9]. Solar Thermal Action Plan for Europe: Heating & Cooling from the Sun, European Solar Thermal Industry Federation (ESTIF), 2007.
- [1.10]. Technology Roadmap-Solar photovoltaic energy, International Energy Agency, 2010. <[www.iea-pvps.org](http://www.iea-pvps.org)>, [06.11.2010]
- [1.11]. Photovoltaics/thermal Solar Energy Systems - Status of the technology and roadmap for future development, International Energy Agency, 2002.

### References for Chapter 2

- [2.1]. Roger A. Messenger, Jerry Ventre. Photovoltaic System Engineering, 2nd ed., Florida (USA): CRC Press; 2003, 54-55.
- [2.2]. Brinkworth et al., Thermal regulation of photovoltaic cladding. Solar Energy 1997; 61:169–78.
- [2.3]. Kranter et al., Combined photovoltaic and solar thermal systems for facade integration and building insulation. Solar Energy 1999; 67: 239–48.
- [2.4]. Kalogirou SA, Tripanagnostopoulos Y. Hybrid PV/T solar systems for domestic hot water and electricity production. Energy Conversion and Management 2006; 47: 3368–82.
- [2.5]. J.R.E.C. Kern, M.C. Russell, Combined photovoltaic and thermal hybrid collector systems, In Proceedings of the 13th IEEE PV specialist conference. Washington, DC. 5-8 June 1978, p1153-57.
- [2.6]. H.A. Zondag, D.W. Vries, W.G.J. and A.A. Van Steenhoven, Thermal and electrical yield of a combi-panel, in: Proceedings of ISES Bi-annual Conference on CD-ROM,

- Jerusalem, 1999.
- [2.7]. X. Zhao, X. Zhang, S. B. Riffat, X Su, Theoretical investigation of a novel PV/e roof module for heat pump operation, *Energy Conversion and Management* 2011; 52: 603-614.
- [2.8]. H.C. Hottel, A. Willier, Evaluation of flat-plate solar collector performance *Transactions of the Conference on the Use of Solar Energy*, vol. 2, University of Arizona Press, Tucson, Arizona, 1958.
- [2.9]. J.A. Duffie, W.A. Beckman, *Solar engineering of Thermal Processes*, second ed., John Wiley and Sons Inc., New York, 1991.
- [2.10]. Zondag HA, De Vries DW, Van Helden WGJ, Van Zolingen RJC, Van Steenhoven AA, The yield of different combined PV-thermal collector designs, *Solar Energy* 2003; 74: 253–269.
- [2.11]. Heat pipe, < [heatpipe.nl/index.php?page=heatpipe&lang=EN](http://heatpipe.nl/index.php?page=heatpipe&lang=EN)>, [19.11.2010]
- [2.12]. Yaohua Zhao et al., Photovoltaic cell radiating and combined heat and power system, Patent CN 200820123998 U, 04-Dec-2008.
- [2.13]. Z. Quan, N. Li, Y. Zhao, X. Tang, The experiment research for solar PV/T system based on flat-plate heat pipes, *Proceeding the 17th Chinese national HVAC&R academic conference*, 2010.
- [2.14]. X. Tang, Y. Zhao, Z. Quan, The experimental research of using novel flat-plate heat pipe for solar cells cooling, *Proceeding the Chinese thermal engineering physics of heat and mass transfer conference*. 13-16 November, 2009, p239-241.
- [2.15]. QIAN Jian-feng, ZHANG Ji-li1, MA Liang-dong, Analysis of a New Photovoltaic Thermal Building Integration System and Correlative Technology, *Building Energy & Environment* 2010; 29 (02): 12-16.
- [2.16]. Jili Zhang et al., Closed loop capillary solar photovoltaic thermoelectric board, Patent CN 200810228051 A, 08-Oct-2008.
- [2.17]. S.C. Solanki, Swapnil Dubey, Arvind Tiwari, Indoor simulation and testing of photovoltaic thermal (PV/T) air collectors, *Applied Energy* 2009; 86: 2421–2428.
- [2.18]. Huang B. J., Liu T. H., Hung W. C., Sun F. S., Performance evaluation of solar photovoltaic/thermal systems. *Solar Energy* 2001; 70: 443-448.
- [2.19]. J. Ji et al., Experimental study of photovoltaic solar assisted heat pump system, *Solar Energy* 2008;82: 43–52.
- [2.20]. EN 12975-1:2006 Thermal solar systems and components. Solar collectors. General requirements.
- [2.21]. EN 12975-2:2006 Thermal solar systems and components. Solar collectors. Test methods.
- [2.22]. EN 12976-1:2006, Thermal solar systems and components. Factory made systems. General requirements.
- [2.23]. EN 12976-2:2006, Thermal solar systems and components. Factory made systems. Test methods.
- [2.24]. DD CEN/TS 12977-1:2010, Thermal solar systems and components. Custom built



- systems. General requirements for solar water heaters and combisystems.
- [2.25]. DD CEN/TS 12977-2:2010, Thermal solar systems and components. Custom built systems. Test methods for solar water heaters and combisystems.
- [2.26]. BS EN 12977-3:2008, Thermal solar systems and components. Custom built systems. Performance test methods for solar water heater stores.
- [2.27]. DD CEN/TS 12977-4:2010, Thermal solar systems and components. Custom built systems. Performance test methods for solar combistores.
- [2.28]. DD CEN/TS 12977-5:2010, Thermal solar systems and components. Custom built systems. Performance test methods for control equipment.
- [2.29]. Solar Keymark: The Quality Label for Solar Thermal Products in Europe, <<http://www.estif.org/solarkeymark/>>. [12.12 2010]
- [2.30]. ISO 9806-1:1994, Test methods for solar collectors -- Part 1: Thermal performance of glazed liquid heating collectors including pressure drop.
- [2.31]. ISO 9806-2:1995, Test methods for solar collectors -- Part 2: Qualification test procedures.
- [2.32]. ISO 9806-3:1995, Test methods for solar collectors -- Part 3: Thermal performance of unglazed liquid heating collectors (sensible heat transfer only) including pressure drop.
- [2.33]. MCS 004:2008, Microgeneration Certification Scheme: Product Certification Scheme Requirements: Solar Collectors.
- [2.34]. IEC 61215:2005, Crystalline silicon terrestrial photovoltaic (PV) modules – Design qualification and type approval.
- [2.35]. IEC 61646: 2008, Thin-film terrestrial photovoltaic (PV) modules – Design qualification and type approval.
- [2.36]. IEC 61730-1:2004, Photovoltaic (PV) module safety qualification Part 1: Requirements for construction.
- [2.37]. IEC 61730-2:2004, Photovoltaic (PV) module safety qualification Part 2: Requirements for testing.
- [2.38]. UL 1703:2002, UL Standard for Safety Flat-Plate Photovoltaic Modules and Panels.
- [2.39]. UL 1741:2010, UL Standard for Safety Inverters, Converters, Controllers and Interconnection System Equipment for Use With Distributed Energy Resources.
- [2.40]. UL 4703: 2005, Photovoltaic Wire.
- [2.41]. IEEE 1262:1995, IEEE Recommended Practice for Qualification of Photovoltaic (PV) Modules.
- [2.42]. IEEE 929:2000, IEEE Recommended Practice for Utility Interface of Photovoltaic (PV) Systems.
- [2.43]. What is CE Marking (CE Mark), <[www.ce-marking.org](http://www.ce-marking.org)>.[15.12 2010]
- [2.44]. Miroslav Bosanac, Bent Sørensen, et al, Photovoltaic/thermal solar collectors and their potential in Denmark, Final Report, EFP Project, 2003, 1713/00-0014.
- [2.45]. Huang B. J., Performance rating method of thermosyphon solar water heaters, Solar Energy 1993; 50: 435–440.

- [2.46]. S.A. Kalogirou, Use of TRNSYS for modelling and simulation of a hybrid PV–thermal solar system for Cyprus, *Renewable Energy* 2001; 23: 247–260.
- [2.47]. Tripanagnostopoulos Y, Souliotis M, Battisti R, Corrado A. Energy, cost and LCA results of PV and hybrid PV/T solar systems. *Progress in Photovoltaics: Research and Applications* 2005; 13:235–50.
- [2.48]. T.T. Chow, A review on photovoltaic/thermal hybrid solar technology, *Applied Energy* 2010; 87: 365–379.
- [2.49]. S.D. Hendrie, Evaluation of combined Photovoltaic/Thermal Collectors. In: ISES International Congress and Silver Jubilee, Atlanta, USA, 28 May–1 June 1980, Vol.3, p1865-1869.
- [2.50]. L.W. Florschuetz, Extension of the Hottel–Whillier model to the analysis of combined photovoltaic/thermal flat plate collectors, *Solar Energy* 1979; 22 (04): 361–366.
- [2.51]. Raghuraman P, Analytical prediction of liquid and air photovoltaic/thermal flat plate collector performance. *J. of Solar Energy Engineering*. Vol.103, 1981, p291-298.
- [2.52]. T. Bergene, O.M. Lovvik, Model calculations on a flat plate solar heat collector with integrated solar cells, *Solar Energy* 1995; 55 (6): 453–462.
- [2.53]. K.S. Sopian, H.T. Yigit, H.T. Liu, S. Kakac, T.N. Veziroglu, Performance analysis of photovoltaic/thermal air heaters, *Energy Conversion and Management* 1996; 37 (11): 1657–1670.
- [2.54]. B. Sandnes, J. Rekstad, A photovoltaic/thermal (PV/T) collector with a polymer absorber plate. Experimental study and analytical model, *Solar Energy* 2002; 72 (1): 63–73.
- [2.55]. Tiwari A. and Sodha M. S., Performance evaluation of solar PV/T system: an experimental validation, *Solar Energy* 2006; 80: 751-759.
- [2.56]. Dubey S, Sandhu GS, Tiwari GN. Analytical expression for electrical efficiency of PV/T hybrid air collector. *Applied Energy* 2009; 86: 697–705.
- [2.57]. T.T. Chow, Performance analysis of photovoltaic–thermal collector by explicit dynamic model, *Solar Energy* 2003; 75(02): 143–152.
- [2.58]. C.H. Cox, P. Raghuraman, Design considerations for flat-plate photovoltaic/thermal collectors, *Solar Energy* 1985; 35(03): 227–241.
- [2.59]. Grag H. P., Agarwal R.K., Some aspects of a PV/T collector/forced circulation flat-plate solar water heater with solar cells. *Energy Conversion and Management* 1995; 36: 87-99.
- [2.60]. J.K. Tonui, Y. Tripanagnostopoulos, Performance improvement of PV/T solar collectors with natural air flow operation, *Solar Energy* 2008; 82: 1–12.
- [2.61]. A. Shahsavar, M. Ameri, Experimental investigation and modeling of a direct-coupled PV/T air collector, *Solar Energy* 2010; 84: 1938–1958.
- [2.62]. De Vries DW. Design of a photovoltaic/thermal combi-panel. PhD report, UT, 1998.
- [2.63]. Zondag HA, De Vries DW, Van Helden WGJ, Van Zolingen RJC, Van Steenhoven AA, The thermal and electrical yield of a PV-Thermal collector, *Solar Energy* 2002; 72(02):

- 113–28.
- [2.64]. Chow TT, He W, Ji J. Hybrid photovoltaic-thermosyphon water heating system for residential application. *Solar Energy* 2006; 80: 298–306.
- [2.65]. J. Ji et al., Distributed dynamic modelling and experimental study of PV evaporator in a PV/T solar-assisted heat pump, *International Journal of Heat and Mass Transfer* 2009; 52: 1365–1373.
- [2.66]. Komp R, Reeser T. Design, construction & operation of a PV/Hot air hybrid energy system. In: *ISES Solar World Congress, Hamburg, 1987*.
- [2.67]. Fudholi A, Sopian K, Ruslan MH, Alghoul MA, Sulaiman MY. Review of solar dryers for agricultural and marine products. *Renewable and Sustainable Energy Reviews* 2010; 14:1-30.
- [2.68]. Takashima T, Tanaka T, Doi T et al, New proposal for photovoltaic-thermal solar energy utilization method, *Solar Energy*, Vol.52, 1994, p241-245.
- [2.69]. Moshtegh B., Sandberg M., Investigation of fluid flow and heat transfer in a vertical channel heated from one side by PV elements, Part I—numerical study. *Renewable Energy* 1996; 08: 248 – 253.
- [2.70]. Sandberg M., Moshtegh B., Investigation of fluid flow and heat transfer in a vertical channel heated from one side by PV elements, Part II – experimental study. *Renewable Energy* 1996; 08: 254 – 258.
- [2.71]. Bhargava A. K, Garg H.P, Agarwal R.K, Study of a hybrid solar system-solar air heater combined with solar cells, *Energy Convers. Mgmt.* Vol. 31, 1991, p471-479.
- [2.72]. Prakash J. Transient analysis of a photovoltaic thermal solar collector for cogeneration of electricity and hot air water. *Energy Conversion and Management* 1994; 35: 967–72.
- [2.73]. Kelly N., Strachan P. A., Modelling enhanced performance integrated PV modules. *Proceeding of the 16th European PV solar energy conference, Glasgow, UK, May 1-5 2000: 2025-2028*.
- [2.74]. Tripanagnostopoulos Y, et al., Hybrid photovoltaic thermal solar system. *Solar Energy* 2002; 72: 217-234.
- [2.75]. Tiwari A, Sodha MS. Parametric study of various configurations of hybrid PV/thermal air collector: Experimental validation of theoretical model. *Solar Energy Mater Solar Cells* 2007; 91: 17–28.
- [2.76]. Garg H.P, Ahhikari R.S, Conventional hybrid photovoltaic/thermal (PV/T) air heating collector: steady-state simulation, *Renewable Energy*, Vol.11, p363-385.
- [2.77]. Agarwal R.K, Garg HP. Study of a photovoltaic-thermal system—thermisyphonic solar water heater combined with solar cells. *Energy Convers Manage* 1994; 35(7): 605–20.
- [2.78]. Grag H. P., Agarwal R.K., Some aspects of a PV/T collector/forced circulation flat-plate solar water heater with solar cells. *Energy Conversion and Management* 1995; 36: 87-99.
- [2.79]. T. Bergene, O.M. Lovvik, Model calculations on a flat plate solar heat collector with integrated solar cells, *Solar Energy* 55 1995; 06: 453–462.

- [2.80]. Elswijk MJ, Jong MJM, Braakman JNC, Lange ETN de, Smit WF. Photovoltaic/Thermal collectors in large solar thermal systems. In: 19th EPSEC, Paris, 2004.
- [2.81]. Jie. Ji, Tin-Tai. Chow and Wei. He, Dynamic performance of hybrid photovoltaic/thermal collector wall in Hong Kong, *Building and Environment* 2003; 38: 1327-1334.
- [2.82]. Nishikawa M, Sone T, Ito S. A heat pump using solar hybrid panels as the evaporator. In: ISES Solar World Congress, Budapest, 1993.
- [2.83]. Ito S, Miura N, Wang K. Heat pump using a solar collector with photovoltaic modules on the surface. *JSEE* 1997; 119: 147–151.
- [2.84]. Ito S, Miura N, Wang K. Performance of a heat pump using direct expansion solar collectors. *Solar Energy* 1999; 65(3): 189–196.
- [2.85]. TWINSOLAR, < [www.grammer-solar.com](http://www.grammer-solar.com) >, [20.12 2010].
- [2.86]. SolarVenti, < [www.solarventi.com](http://www.solarventi.com)>, [20.12 2010].
- [2.87]. Solar Wall, <[solarwall.com/en/home.php](http://solarwall.com/en/home.php)>, [20.10 2010].
- [2.88]. PVTWINS, < [www.pvtwins.nl](http://www.pvtwins.nl)>, [20.12 2010].
- [2.89]. MULTI SOLAR PV/T System, < [www.millenniumsolar.com](http://www.millenniumsolar.com)>, [20.12 2010].
- [2.90]. Solar Collector X10, < [www.absolicon.com](http://www.absolicon.com)>, [20.12 2010].
- [2.91]. PV/T examples, <[www.iea-shc.org/task35/examples.htm](http://www.iea-shc.org/task35/examples.htm)>, [11.10. 2010].
- [2.92]. Robles-Ocampo B, Ruiz-Vasquez E, Canseco-Sanchez H, Cornejo-Meza RC, Trapaga-Martinez G, Garcia-Rodriguez FJ, et al. Photovoltaic/thermal solar hybrid system with bifacial PV module and transparent plane collector. *Solar Energy Materials & Solar Cells* 2007; 91:1966–71.
- [2.93]. Anand S. Joshi, Arvind Tiwaria, Energy and exergy efficiencies of a hybrid photovoltaic–thermal (PV/T) air collector, *Renewable Energy* 2007; 32 (13): 2223-2241.
- [2.94]. Jin GL, Ibrahim A et al, Evaluation of Single-Pass Photovoltaic-Thermal Air Collector with Rectangle Tunnel Absorber, *Energy Research Journal* 2010; 1 (1): 1-6.
- [2.95]. Cristofari C, Notton G, Canaletti JL, Thermal behaviour of a copolymer PV/Th solar system in low flow rate conditions, *Solar Energy* 2009;83(8):1123–38.
- [2.96]. Wei He, Tin-Tai Chow, Jie Ji et al., Hybrid photovoltaic and thermal solar-collector designed for natural circulation of water, *Applied Energy* 2006; 83: 199–210.
- [2.97]. Zhennan Liang, Hong Qin and Hui Shen, The experimental study on backplane material influencing the performance of solar cell module, *Proceeding 10<sup>th</sup> China solar photovoltaic conference*, Changzhou, Jiangsu, China, 19<sup>th</sup>-21<sup>st</sup> September 2008; page 988-993.
- [2.98]. Heat pipes, < [www.thermguide.co.il/Heat\\_pipes.html](http://www.thermguide.co.il/Heat_pipes.html)>, [19.10.2010]
- [2.99]. P.D. Dunn, D. A. Reay, Heat Pipes, fourth ed., ELSEVIER science LTD, 1994.
- [2.100]. S.W. Chi, Heat pipe theory and practice: a source book, Washington: Hemisphere Pub. Corp, 1976.
- [2.101]. A. Faghri, Heat Pipe Science and Technology, one ed., Taylor & Francis Group, 1995.
- [2.102]. Hamdan M., Cytrynowicz D., Medis P., Shuja A., Gerner F., Henderson H., Gollhofer E.,

- Mellott K., Moore C., Loop Heat Pipe (LHP) Development by Utilizing Coherent Porous Silicon (CPS) Wicks, Proceedings of the 8th IThERM Conference, May 29-June 2, (2002): 457-465.
- [2.103]. Ji Li, Daming Wang, G.P. Peterson, Experimental studies on a high performance compact loop heat pipe with a square flat evaporator, *Applied Thermal Engineering* 2010; 30: 741–752.
- [2.104]. Xiang-you Lu et al., Thermal analysis of loop heat pipe used for high-power LED, *Thermochimica Acta* 2009; 493: 25–29.
- [2.105]. A.M. Alklaibi, Evaluating the possible configurations of incorporating the loop heat pipe into the air-conditioning systems, *international journal of refrigeration* 2008; 31: 807-815.
- [2.106]. Z. Wang, Z. Duan, X. Zhao, M. Chen, Dynamic performance of a façade-based solar loop heat pipe water heating system, *Solar Energy* 2012;86(05): 1632–1647.

### References for Chapter 3

- [3.1]. Solar compressors, < [www.danfoss.com](http://www.danfoss.com)>, accessed on [15/07/2013].
- [3.2]. S. ZHOU, J. ZHENG, The Diurnal and Seasonal Variation of Solar Radiation at Shanghai City, *Journal of East China Normal University (Natural Science)*, 1992; 02:63-73.
- [3.3]. Operation of Loop Heat Pipes, < [china-heatpipe.net/](http://china-heatpipe.net/)>, [21/10/2010]
- [3.4]. Water properties, <[www.efunda.com/materials/](http://www.efunda.com/materials/)>, [24/09/ 2011].
- [3.5]. Water thermal properties, <[www.engineeringtoolbox.com/](http://www.engineeringtoolbox.com/)>, [24/ 09/2011].
- [3.6]. Plate heat exchanger, <[en.wikipedia.org/wiki/Plate\\_heat\\_exchanger](http://en.wikipedia.org/wiki/Plate_heat_exchanger)>,[24/10/ 2010]
- [3.7]. Insulation Performance: R-value, < [www.house-energy.com](http://www.house-energy.com) >, [24/10/ 2010].

### References for Chapter 4

- [4.1]. C. A. Busse, Theory of ultimate heat transfer limit of cylindrical heat pipes, *International Journal of Heat and Mass Transfer* 1973; 16:169-186.
- [4.2]. Zhuang J et al. *Heat Pipe Technology and Engineering Application* (1st ed). The Press of Chemistry Industry, Beijing, China, 2000.
- [4.3]. Zhao Xiaobao, Analysis and Amendment of Design Factors about Heat Pipe of Screen Wicks, *Journal of Nanjing normal University* 2004; 04(03): 07-10.
- [4.4]. Imura H, Kozai H, Ikeda Y, The effective pore radius of screen wicks [A], Ma Tongze. *Advances in Heat Pipe Science and Technology*[C], Proceedings of the 8th International Heat Pipe Conference, 1992: 113-118.
- [4.5]. Kraus AD, Bar-Cohen A. *Thermal Analysis and Control of Electronic Equipment*. McGraw-Hill, 1983.
- [4.6]. Riffat SB, Zhao X, Doherty PS. Analytical and numerical simulation of the thermal performance of ‘mini’ gravitational and ‘micro’ gravitational heat pipes, *Applied Thermal Engineering* 2002; 22: 1047–1068.

- [4.7]. Shen-Chun Wu et al., Manufacturing and testing of the double-layer wick structure in a loop heat pipe, *International Journal of Heat and Mass Transfer* 2013; 56: 709-714.
- [4.8]. Vapour-temperature function, <[http://en.wikipedia.org/wiki/vapour\\_pressure\\_of\\_water](http://en.wikipedia.org/wiki/vapour_pressure_of_water)>, assessed on [24/09/ 2011]
- [4.9]. Soteris A. Kalogirou, *Solar energy engineering: process and system*, Elsevier Inc., 2009.
- [4.10]. Klein, S.A, Calculation of flat-plate collector heat-loss coefficients, *Solar Energy* 1975; 17(01): 79-80.
- [4.11]. W. Rohsenow, J.Hartnet, Y.Cho, *Handbook of Heat Transfer*, 3<sup>rd</sup> edition, McGraw-Hill, 1998.
- [4.12]. Stephen R. Turns, *Thermodynamics: concepts and applications*, Cambridge University Press, 2006.
- [4.13]. H.D.FU et al., Experimental study of a photovoltaic solar-assisted heat-pump/heat-pipe system, *Applied Thermal Engineering* 2012; 40: 343-350
- [4.14]. Michael J. Moran, Howard N. Shapiro, *Fundamentals of engineering thermodynamics*, 3rd edition, John Wiley and Sons Inc., 1995.
- [4.15]. Jianfei Jiang, Liangjian Hu, Jian Tang, *Numerical analysis and MATLAB experiment*, Siencep press, 2004.
- [4.16]. T.T. Chow, et al., Energy and exergy analysis of photovoltaic–thermal collector with and without glass cover, *Applied Energy* 2009; 86(3):3 10-316.

#### References for Chapter 5

- [5.1]. Solar photovoltaic modules, < [www.solardirect.com/pv/pvlist/pvlist.htm](http://www.solardirect.com/pv/pvlist/pvlist.htm)>, [12-03-2012].

#### References for Chapter 6

- [6.1]. B.J. Huang, S.C. Du, A performance test method of solar thermosyphon systems, *Transactions of the American Society of Mechanical Engineers Solar Energy* 1991; 113: 172-179.
- [6.2]. Solar water heating, < [www.bigginhill.co.uk/solar.htm](http://www.bigginhill.co.uk/solar.htm)>, [12-03-2012].
- [6.3]. Heat pump, < [en.wikipedia.org/wiki/Heat\\_pump](http://en.wikipedia.org/wiki/Heat_pump)>, [12-03-2012].
- [6.4]. B.J. Huang, J.P. Chyng, Performance characteristics of integral type solar assisted heat pump, *Solar Energy*, 2001; 71 (06): 403–414.

#### References for Chapter 7

- [7.1]. Weather profile, < [apps1.eere.energy.gov](http://apps1.eere.energy.gov) >, [17/11/2012]
- [7.2]. Renewable Heat Incentive (RHI), < [www.energysavingtrust.org.uk](http://www.energysavingtrust.org.uk)>, [24/07/2013]
- [7.3]. Solar thermal tariff in China, <[www.sdpc.gov.cn](http://www.sdpc.gov.cn)>, [24/07/2013]
- [7.4]. Energy, < [www.greenspec.co.uk](http://www.greenspec.co.uk)>, [24/07/2013]
- [7.5]. UK gas price, < [www.britishgas.co.uk](http://www.britishgas.co.uk)>, [26/06/2013]
- [7.6]. Shanghai gas price, < [www.shgas.com.cn](http://www.shgas.com.cn)>, [26/06/2013]

- [7.7]. Hong Kong gas price, < [www.towngas.com](http://www.towngas.com)>, [26/06/2013]
- [7.8]. UK electricity price, < [www.britishgas.co.uk](http://www.britishgas.co.uk)>, [26/06/2012]
- [7.9]. Shanghai electricity price,< [www.sh.sgcc.com.cn](http://www.sh.sgcc.com.cn)>, [26/06/2012]
- [7.10]. Hong Kong electricity price, < [www.hkelectric.com/](http://www.hkelectric.com/)>, [26/06/2012]
- [7.11]. Feed-In Tariffs scheme (FITs), < [www.energysavingtrust.org.uk](http://www.energysavingtrust.org.uk)>, [24/07/2013]
- [7.12]. Feed-In Tariffs in China, <[www.sdpc.gov.cn](http://www.sdpc.gov.cn)>, [24/07/2013]
- [7.13]. S. Kalogirou, Economic analysis of solar energy systems using spread sheets, Proceedings of World Renewable Energy Congress IV, Denver, Colorado, US, 1996, 1303-1307.
- [7.14]. Maintenance cost of gas boiler in UK, <[www.britishgas.co.uk](http://www.britishgas.co.uk)>, [28/07/2013]
- [7.15]. Maintenance cost of gas boiler in China, <[www.sdpc.gov.cn](http://www.sdpc.gov.cn)>, [28/07/2013]
- [7.16]. Benefits of electric heating, < [www.dimplex.co.uk](http://www.dimplex.co.uk) >, [26/11/2012]
- [7.17]. R. Kannan et al., Life cycle assessment study of solar PV systems: An example of a 2.7 kWp distributed solar PV system in Singapore, Solar Energy 80 (2006) 555–563.
- [7.18]. 2010 guidelines to Defra/DECC's GHG conversion factors for company reporting, < [www.carbontrust.co.uk](http://www.carbontrust.co.uk) >, [26/11/2012].
- [7.19]. Electricity-to-CO<sub>2</sub> conversion ratio in China, < [www.china5e.com](http://www.china5e.com)>, [26/11/2012]
- [7.20]. Electricity-to-CO<sub>2</sub> conversion ratio in Hong Kong, < [www.clp.com.hk](http://www.clp.com.hk)>, [26/11/2012]